



HAL
open science

Densification and microstructural characterization of ZnO-based ceramics obtained by SPS sintering for thermoelectric application

Precious Manti Radingoana

► **To cite this version:**

Precious Manti Radingoana. Densification and microstructural characterization of ZnO-based ceramics obtained by SPS sintering for thermoelectric application. Materials. Université Paul Sabatier - Toulouse III, 2019. English. NNT : 2019TOU30298 . tel-03103694

HAL Id: tel-03103694

<https://theses.hal.science/tel-03103694>

Submitted on 8 Jan 2021

HAL is a multi-disciplinary open access archive for the deposit and dissemination of scientific research documents, whether they are published or not. The documents may come from teaching and research institutions in France or abroad, or from public or private research centers.

L'archive ouverte pluridisciplinaire **HAL**, est destinée au dépôt et à la diffusion de documents scientifiques de niveau recherche, publiés ou non, émanant des établissements d'enseignement et de recherche français ou étrangers, des laboratoires publics ou privés.



THÈSE

En vue de l'obtention du
DOCTORAT DE L'UNIVERSITÉ DE TOULOUSE

Délivré par l'Université Toulouse 3 - Paul Sabatier

Présentée et soutenue par

Precious Manti RADINGOANA

Le 5 décembre 2019

Titre:

**Densification et caractérisation microstructurale de céramiques à base de ZnO
obtenues par frittage SPS pour application
thermoélectrique**

Ecole doctorale: SDM - SCIENCES DE LA MATIERE – Toulouse

Spécialité: Sciences et Génie des Matériaux

Unité de recherche:

CIRIMAT - Centre Interuniversitaire de Recherche et d'Ingénierie des
Matériaux

Thèse dirigée par

Sophie GUILLEMET-FRITSCH
Claude ESTOURNES

Jury:

Guillaume BERNARD-GRANGER Directeur de Recherche, CEA

Bertrand LENOIR Professeur, Institut Jean Lamour

Bénédicte WAROT Directeur de Recherche, CEMES/CNRS

Sophie GUILLEMET-FRISTCH Directeur de Recherche, CIRIMAT/CNRS

Claude ESTOURNES Directeur de Recherche, CIRIMAT/CNRS

Peter Apata OLUBAMBI Professeur, University of Johannesburg

Jacques NOUDEM Professeur, CRISMAT

Rapporteur

Rapporteur

Examinatrice

Directrice de thèse

Co-directeur de thèse

Invité

Invité

Abstract

The pursuit of better thermoelectric properties using ZnO has been hampered by the high thermal conductivity and low electrical conductivity of this low cost and environmental friendly material. The present study focuses on the synthesis and spark plasma sintering of zinc oxide composites to improve these thermoelectric properties. Pure and Al (2at %) doped ZnO powder were synthesized using co-precipitation followed by calcination. Further, the synthesized Al-doped ZnO powder was mixed with low concentrations of polyaniline (PANI) powder to reduce the thermal conductivity. The powders were sintered using Dr Sinter 2080 unit by varying different parameters: temperature (250-900°C), pressure (100-250 MPa), sintering atmosphere (air and vacuum), point of pressure application, holding time and current isolation. The ceramics were finally annealed at 600°C in air.

The densification and the microstructure properties of pure ZnO ceramics were studied. It was illustrated that SPS can sinter to high densities irrespective of starting powder. The characteristics of the ceramics prepared from both synthetic and commercial ZnO powder were compared. Both could be fully densified above 99% at a temperature as low as 600°C. The sintering atmospheres (air and vacuum) and electric current (with or without) did not affect the densification. However, grain size difference of about 8 μm was observed when sintering with or without current. A guide for controlling the densification and the grain size of ZnO ceramics obtained by spark plasma sintering of dried powders was developed. Annealing at 600°C does not have significant effect on the microstructure of ZnO ceramics, however, affects the oxygen stoichiometry, and hence modified the electrical behaviour such that the resistivity of the pure ZnO ceramics increased by two orders of magnitude. As-sintered ceramics prepared from synthetic powder show the best thermoelectric performance as compared to annealed ceramics with a ZT of 8×10^{-3} at 500°C because of low electrical resistivity and high Seebeck Coefficient. This signifies the importance of the synthesis process in determining the thermoelectric properties.

The thermal conductivity and electrical resistivity of ZnO ceramic were improved by doping with 2 at% Al. The powder grain size reduced from 177 to 75 nm when Al is present. Maximum relative density of 98.9% was achieved at a temperature of 650°C and a pressure of 250 MPa. The grain size of the sintered ceramics reduced from 5.4 μm to $<1 \mu\text{m}$. Secondary phases, ZnAl_2O_4 and Al_2O_3 , are formed because of excess Al when the axial pressure was applied at room temperature and temperatures above 650°C. Al-doped ZnO ceramics

improved in electrical conductivity which caused a decrease in the absolute Seebeck Coefficient as a result of increased carrier concentration. The reduction in the grain size lead to a decrease in the thermal conductivity due to phonon scattering at the grain boundaries. As a result, ZT of 1.5×10^{-3} at 500°C was obtained.

The influence of dispersed PANI in Al-doped ZnO ceramics was investigated. Using SPS, high densification of 98.5% and 97.3 % was achieved at a temperature as low as 250°C for 5wt% and 9wt% PANI, respectively. As a result, the nanostructure of the ceramics was maintained. Thermal conductivity below 6 W/mK was achieved by incorporating PANI into Al-doped ZnO ceramics. The resistivity was also slightly improved and high Seebeck Coefficient was kept, due to energy filtering. Maximum ZT of 0.8×10^{-3} was achieved at 190°C using 9wt% PANI compared to 0.06×10^{-3} for 0 wt% PANI. This study has opened opportunities for development of ZnO based polymer composites at low temperatures using spark plasma sintering.

Keywords: ZnO, Spark plasma sintering, Thermoelectricity, Ceramics, Polyaniline, Aluminium

Acknowledgements

The research associated with this PhD thesis commenced in January 2016 at Centre Inter-Universitaire de Recherche et d'Ingénierie des Matériaux (CIRIMAT) laboratory. In completing this programme I am grateful to many people, who have inspired, encouraged, supervised, supported and helped me over the time of the research, my stay in France and during the writing of this thesis. I would like to extend my warmest gratitude to my supervisors, **Dr Sophie Guillemet-Fritsch and Prof. Claude Estournès**, for their excellent supervision, persistent help, skilful and excellent guidance, positive encouragement and most of all, their unwavering patience in bringing me back to track when occasionally falter.

This programme would not have been possible if it was not to the initiatives of **Prof. P.A Olubambi** to collaborate with the CIRIMAT laboratory. Thank you for having faith in me. I am grateful for your emotional support and the expertise shared in this thesis.

I acknowledge the financial support of **A European and South African Partnership on Heritage and Past+ (AESOP+, Europe) and National Research Fund (NRF, South Africa)** for providing an opportunity to do research studies at CIRIMAT laboratory.

I am thankful to the director of CIRIMAT laboratory, **Prof. Christophe Laurent**, for accepting me in the laboratory to use the facilities towards my research studies. I would also like to thank my colleagues at CIRIMAT laboratory for their friendship and individual help during my time here. I appreciate the technical support of **Marie-Claire, Geoffroy, Benjamin, Jean-Jacques, Christopher, Isabelle, Vincent, and Abdérahmane**. I am thankful for the general logistics and administrative support of **Maryse, Jessie, Nabila** and other administrative staff. I am grateful to my officemates for creating a pleasant working environment, support and assistance towards the research studies of this thesis: **Veronique, Nahum, Elsa, Thi Mong Cam, Vignesh, Thi Ly, Mai Doo and Zifeng**. Also, thanks for the support of **Yohan, Inthunga, Juliano, Juliana, Glenda, David, Driss, Arnaud, Yannick** and other CIRIMAT colleagues.

I am thankful to **Laboratoire de Cristallographie et Sciences des Matériaux (CRISMAT)** for allowing me to do my thermoelectric measurements and other analysis at their laboratory. The members at CRISMAT made the working environment to be pleasant during my stay, it is very much appreciated. I appreciate and acknowledge the technical assistance of **J. Lecourt**

and C. Bilot. Foremost, I am grateful for the short term supervision of **Prof. Jacques Noudem** for all his assistance and expertise.

My dearest friends, **Dr O.M Olabanji, Dr G Chimowa and Dr S Diouf**, are gratefully acknowledged for their contributions towards compilation of this thesis. I am also grateful to **Prof K. Mpofu** for allowing me to using their premises at Tshwane University of Technology during the last part of my thesis.

Apart from work, I am thankful to my friends: **Aluwani, Ntombi, George and Miltia** for making my stay in Toulouse to be such a wonderful experience. I appreciate all your emotional support and positive encouragement; you have made my PhD journey to be bearable. Also, grateful to my friends during my stay in South Africa for the last months of my thesis for all their assistance: **Eddie Thaba and Tshepo Mahanuke.**

I would like to express my heartfelt thanks to **my loving family** for their great support towards my dreams. Thank you for being the pillars of my strength, the encouragement you gave me through this programme is well appreciated.

Finally, I thank the almighty **God** for the strength and wisdom he gave me to conclude this study.

I will forever cherish the experience of studying in France.

Much thanks,

Radingoana Precious Manti

Université Paul Sabatier, Toulouse

26 September 2019

Table of Contents

Abstract	ii
Acknowledgements	iv
List of tables	x
List of figures	xi
List of symbols	xvi
General introduction	2
1. Bibliography	5
1.1 Thermoelectricity fundamentals	5
1.1.1 Thermoelectric effects (Seebeck and Peltier effect).....	5
1.1.2 Performance of thermoelectric materials.....	8
1.2 Current state-of-the-art thermoelectric materials.....	14
1.3 Metal oxide thermoelectric materials	15
1.4 ZnO based thermoelectric materials.....	17
1.4.1 Characteristics and challenges of pure ZnO	17
1.4.2 Challenges with preparing nanostructured pure ZnO ceramics	18
1.4.3 Intrinsic ZnO defects.....	21
1.4.4 Doped and co-doped ZnO TE properties	24
1.4.5 Influence of grain morphology on thermoelectric properties of Al-doped ZnO....	26
1.4.6 Doping of metal oxides with conducting polymers	29
1.4.7 Low temperature sintering of ZnO based ceramics	34
1.5 Summary	37
2. Experimental techniques	39
2.1 Synthesis of pure and Al-doped ZnO powders	39
2.2 Preparation of polymer doped ZnO based powders	40
2.3 Consolidation of ZnO based ceramics	41
2.3.1 Background on spark plasma sintering equipment.....	41
2.3.2 Sintering of pure ZnO	42
2.3.3 Sintering of aluminium and polyaniline doped ZnO composites	46

2.4	Characterization techniques	46
2.4.1	X-ray diffractometer	46
2.4.2	Microscopy analysis.....	46
2.4.3	Particle size and relative density measuring techniques	47
2.4.4	Thermal analysis (TGA-DSC)	48
2.4.5	Spectroscopy analysis.....	48
2.5	Electrical transport properties	48
2.5.1	Resistivity and Seebeck Coefficient measurements.....	48
2.5.2	Thermal conductivity measurement	50
2.5.3	Hall Effect measurements.....	51
2.5.4	Band gap measurements	52
3.	Influence of processing parameters on the densification and the microstructure of pure zinc oxide ceramics prepared by spark plasma sintering	55
3.1	Introduction	55
3.2	Experimental method and procedure.....	57
3.3	Results and discussion.....	57
3.3.1	Characterization of the commercial ZnO powder.....	57
3.3.2	Spark plasma sintering of ZnO ceramics	60
3.4	Conclusions	70
4.	Thermoelectric properties of ZnO ceramics densified through spark plasma sintering	72
4.1	Introduction	72
4.2	Materials and methods.....	72
4.2.1	Synthesis of ZnO particles	72
4.2.2	Densification of ZnO by Spark plasma sintering (SPS)	73
4.2.3	Electrical measurements	73
4.3	Results and discussion.....	74
4.3.1	Characterization of synthetic zinc oxide powders	74
	<i>FTIR and thermal analysis</i>	78

4.3.2	Spark plasma sintering of pure ZnO ceramics	79
4.3.3	Influence of annealing treatment on the microstructure of ZnO ceramics.....	88
4.3.4	Thermoelectric properties of pure ZnO ceramics	90
4.4	Conclusions	98
5	Microstructure and thermoelectric properties of Al-doped ZnO ceramics prepared through spark plasma sintering	100
5.1	Introduction	100
5.2	Materials and methodology	101
5.2.1	Synthesis of Zn _{0.98} Al _{0.02} O powder	101
5.2.2	Spark plasma sintering of the Zn _{0.98} Al _{0.02} O powder	101
5.3	Results and discussion.....	101
5.3.1	Characterization of synthetic Al-doped ZnO powders	101
5.3.2	Spark plasma sintering of Al-doped ZnO powder	105
5.3.3	Thermoelectric properties	114
5.4	Conclusions	118
6	Spark plasma sintering of polyaniline dispersed in Al-doped ZnO ceramics for thermoelectric application.....	121
6.1	Introduction	121
6.2	Materials and methodology	122
6.2.1	Preparation of Zn _{0.98} Al _{0.02} O /Polyaniline powder	122
6.2.2	Spark plasma sintering of Zn _{0.98} Al _{0.02} O /Polyaniline powder	122
6.2.3	Characterization of Zn _{0.98} Al _{0.02} O /Polyaniline powders and ceramics.....	122
6.2.4	Electrical properties of Zn _{0.98} Al _{0.02} O /Polyaniline ceramics.....	123
6.3	Results and discussion.....	123
6.3.1	Characterization of mixed powders of Al-doped ZnO and Polyaniline	123
6.3.2	Characterization of sintered Al-doped ZnO/PANI ceramics	129
6.3.3	Thermoelectric properties of sintered ceramics	134
6.4	Conclusions	140
	Conclusions and recommendations	142
	Conclusions	142

Recommendations	143
References	144
Appendix	164
Appendices A : Heat capacity measurements.....	165
Résumé étendu	167

List of tables

Table 1.1 Thermoelectric properties of pure ZnO ceramics at 700K.....	20
Table 1.2 Chemical structure of few conducting polymers [144].....	30
Table 1.3 Thermoelectric properties of conducting polymers, re-tabulated from Du <i>et al.</i> [144].	30
Table 1.4 Characteristics of ZnO ceramics sintered below 400°C	36
Table 2.1 Sintering conditions of ZnO and ZnA/PANI ceramics	44
Table 3.1 Relative density and grain size of ceramics prepared from commercial ZnO powder for different sintering conditions [Symbols: SC is sintering cycle and RT is room temperature]	61
Table 4.1 Specific surface area and grain size of synthetic and commercial ZnO powders	77
Table 4.2 Relative density and grain size of ceramics prepared from com-ZnO and synthetic ZnO powder for different sintering conditions [Symbols: CCP : ceramics prepared from commercial ZnO powder, CSP : ceramics prepared from synthetic ZnO powder, SC : sintering cycle and RT : room temperature].....	82
Table 4.3 Electrical parameters measured at room temperature of as-sintered ZnO ceramics	92
Table 5.1 Surface area distribution and particle size of pure and Al-doped ZnO powders	104
Table 5.2 Summary of pure and Al-doped ZnO ceramics characteristics for varied SPS parameters (<i>Note: RT-Room temperature, HT- Holding time</i>).....	107
Table 6.1 Relative density of sintered Al-doped ZnO/PANI ceramics	131
Table 6.2 Determined physical properties of Al-doped ZnO/PANI ceramics	136
Table 6.3 Figure of merit of ZnO based polymer composites at 190°C	139

List of figures

Fig. 1.1 Comparison between Seebeck and Peltier effect [5].....	6
Fig. 1.2. Illustration of Seebeck effect [6]: Migration of charge carriers from hot to cold side on n- and p-type (a) and the building up of internal electric field (b).....	6
Fig. 1.3 Typical example of thermoelectric module[14].....	8
Fig. 1.4 Power generation efficiency versus temperature for different energy conversion technologies [15] (Note: org-Organic, CSP-concentrated solar power, PV- photovoltaic, TE-thermoelectric, TI-Thermionic).....	10
Fig. 1.5 Figure of merit and behavior of thermoelectric parameters at varying carrier concentration [21]	11
Fig. 1.6 Effect of thermal conductivity on the figure of merit [14]	13
Fig. 1.7 Effect of grain size on thermal conductivity as a function of temperature on nano-grained Ga-ZnO ceramics [44].....	13
Fig. 1.8 Scattering mechanism of phonons within a nanostructured material [27].....	14
Fig. 1.9 Recent advances of different thermoelectric materials: n-type materials[22] (a), p-type materials [22] (b) and n & p-type of recent thermoelectric materials [66] (c).....	15
Fig. 1.10 Recent progress on thermoelectric properties of metal oxides. ZT versus temperature for (<i>Bi</i> _{0.875} <i>Ba</i> _{0.125} <i>CuSeO</i> [29], <i>Ca</i> _{2.7} <i>Ag</i> _{0.3} <i>CoO</i> ₉ /10wt% <i>Ag</i> [71], <i>Ca</i> _{2.8} <i>Ag</i> _{0.05} <i>Lu</i> _{0.15} <i>Co</i> ₄ <i>O</i> _{9+δ} [70], <i>Na</i> _{1.7} <i>Co</i> ₂ <i>O</i> ₄ [72], <i>Na</i> _{1.7} <i>Co</i> ₂ <i>O</i> ₄ /10wt% <i>Ag</i> [72], <i>Ca</i> _{0.9} (<i>Dy</i> , <i>Yb</i>) _{0.1} <i>MnO</i> ₃ [74], <i>Ca</i> _{0.9} <i>Bi</i> _{0.1} <i>MnO</i> ₃ [75], <i>CaMn</i> _{0.98} <i>Nb</i> _{0.02} <i>O</i> ₃ [76], <i>In</i> _{1.9} <i>Ga</i> _{0.1} <i>O</i> ₃ [77], <i>SrNb</i> _{0.15} <i>Ti</i> _{0.85} <i>O</i> ₃ /3wt% <i>KTO</i> [78], <i>La</i> _{0.08} <i>Dy</i> _{0.12} <i>Sr</i> _{0.8} <i>TiO</i> ₃ [79], <i>Zn</i> _{0.96} <i>Al</i> _{0.02} <i>Ga</i> _{0.02} <i>O</i> [28])	16
Fig. 1.11 Crystal structures of ZnO [92]	17
Fig. 1.12 SEM micrographs of functionally graded ZnO ceramic[31]	21
Fig. 1.13 Ionisation energy of ZnO point defects at room temperature [119].....	22
Fig. 1.14 Concentration of ZnO defects as a function of oxygen partial pressure at room temperature [124]	24
Fig. 1.15 Recent progress on thermoelectric performance of ZnO based ceramics.....	26
Fig. 1.16 SEM micrographs of Zn _{0.98} Al _{0.02} O powders and ceramics prepared by SPS	27
Fig. 1.17 Thermoelectric properties Al-doped ZnO prepared by SPS, for different morphologies	28

Fig. 1.18 Thermoelectric properties of current ZnO/polymer composites a function of temperature: Resistivity (a), Seebeck Coefficient (b), power factor (c), thermal conductivity (d) and figure of merit (ZT) (e)	32
Fig. 1.19 TEM micrograph of Zn _{0.95} Ni _{0.05} O/9 wt% PPP ceramic (a), interface.....	33
Fig. 1.20 Thermoelectric properties of AZO and PANI at room temperature [177]	34
Fig. 1.21 Sintering mechanism of ZnO ceramics sintered with water [184].....	35
Fig. 1.22 Illustration of ZnO/polymer densification process	36
Fig. 2.1 Process block diagram of Al-doped zinc oxide nanoparticles synthesis	40
Fig. 2.2 SPS equipment: Dr. Sinter 2080 unit (SPS Syntex Inc., Japan)	42
Fig. 2.3 SPS chamber setup and sintering process	42
Fig. 2.4 SPS sintering cycles: (a) SC1 for 8mm die (b) SC1 for 20mm and (c) SC2	45
Fig. 2.5 Schematic diagram of the SPS column: (a) Normal setup (b) Current isolation using alumina (c) Sample preparation with alumina	45
Fig. 2.6 Photo of ZEM-3 (Ulvac-Riko).....	49
Fig. 2.7 Illustration of measurement section	50
Fig. 2.8 Schematic diagram of LFA 457 MicroFlash (NETZSCH)[199]	51
Fig. 2.9 Sample preparation for the physical property measurement: (a) Sample holder (b) arrangement of indium contacts on sample.....	52
Fig. 2.10. Typical example of direct band gap estimation using ZnS film [202].....	53
Fig. 3.1 SEM micrograph (a) of commercial zinc oxide powder and corresponding particle size distribution (b).....	58
Fig. 3.2 XRD patterns of zinc oxide powder.....	58
Fig. 3.3 Effect of drying ZnO powder: (a) FTIR and (b) Thermo-gravimetric analysis of commercial ZnO powder.....	59
Fig. 3.4 Thermal behaviour of ZnO ceramics in air and vacuum atmospheres	60
Fig. 3.5 Relative density and grain size as a function of pressure for ceramics prepared from commercial ZnO powder (T= 400°C)	62
Fig. 3.6 XRD patterns of ZnO ceramics sintered at varying pressure.....	63
Fig. 3.7 SEM micrograph of fractured surface of ceramics prepared from commercial ZnO powder at various pressures (T = 400 °C).....	63
Fig. 3.8 Relative density and grain size of ceramics prepared from commercial ZnO as a function of temperature (P = 250 MPa)	64

Fig. 3.9 SEM micrographs of fractured surfaces and pictures of as-sintered ceramics showing the effect of sintering temperature.....	65
Fig. 3.10 (a) SEM micrograph of fractured surfaces (b) grain size distribution of ceramics prepared from commercial ZnO powder for 8 mm and 20 mm die	66
Fig. 3.11 (a) SEM micrograph of fractured surfaces (b) grain size distribution (Image J) of ceramics prepared from ZnO powder (700°C - 250 MPa).....	67
Fig. 3.12 (a) SEM micrograph of fractured surfaces (b) grain size distribution (Image J) of ceramics prepared from ZnO powder (900°C - 100 MPa).....	68
Fig. 3.13 Influence of SPS parameters on the densification and grain size of ZnO ceramics (Note: RT is room temperature and HT is holding temperature).....	69
Fig. 4.1 Characterization of the precipitate (a) XRD patterns and (b) SEM micrographs of zinc oxalate hydrate	75
Fig. 4.2 Differential Thermal and Thermogravimetric Analysis of zinc oxalate hydrate.....	75
Fig. 4.3 XRD patterns of commercial zinc oxide powder and synthetic one, heat-treated at various temperatures (a) and Zoomed 101 peak (b).....	76
Fig. 4.4 SEM micrographs of synthetic ZnO powders obtained at various calcination temperatures	76
Fig. 4.5 Particle size distribution of ZnO powders (ImageJ)	77
Fig. 4.6 FTIR (a) and Thermogravimetric analysis (b) of the different ZnO powders	79
Fig. 4.7 Displacement ratio and displacement during heating of pure commercial and synthetic ZnO powder in air (700°C).....	81
Fig. 4.8 SEM micrograph of fractured surfaces and grain size distribution (Image J) (a) CSP ceramic (b) CCP ceramic (700°C-250 MPa).....	83
Fig. 4.9 Displacement ratio and displacement during heating of pure commercial and synthetic ZnO powder in air (900°C).....	84
Fig. 4.10 SEM micrograph of fractured surfaces and grain size distribution (Image J) (a) CSP ceramics (b) CCP ceramic (900°C -100 MPa-SC2).....	85
Fig. 4.11 Photographs of (a) CSP ceramic (b) CCP ceramic (900°C -100 MPa-SC2)	86
Fig. 4.12 XRD patterns of ZnO ceramics from synthesized powder sintered at 600°C	87
Fig. 4.13 SEM micrograph of fractured surfaces of ZnO ceramics prepared from synthesized powder (P=250 MPa)	87
Fig. 4.14 Photos of as-sintered ZnO ceramics prepared from synthesized powder	88

Fig. 4.15 Thermogravimetric (TGA) analysis of as-sintered CCP ceramic.....	89
Fig. 4.16 SEM micrographs of as-sintered and annealed CCP ceramic.....	89
Fig. 4.17 Resistivity vs Temperature of as-sintered pure ZnO ceramics	91
Fig. 4.18 Seebeck Coefficient vs Temperature of as-sintered pure ZnO ceramics	93
Fig. 4.19 Thermal conductivity vs Temperature of as-sintered pure ZnO ceramics: (a) resistivity (b) Seebeck Coefficient (c) thermal conductivity (d) power factor (e) ZT	95
Fig. 4.20 Performance of as-sintered pure ZnO ceramics with temperature: power factor (a) ZT (b)	96
Fig. 4.21 Thermoelectric properties of annealed 900°C-Vacuum-CSP ceramic: (a) resistivity (b) Seebeck Coefficient (c) thermal conductivity (d) ZT.....	97
Fig. 5.1 XRD patterns of pure and Al-doped ZnO oxalate powder	102
Fig. 5.2 SEM images of pure and Al-doped ZnO oxalate powder.....	102
Fig. 5.3 Thermogravimetric analysis of pure and Al-doped ZnO powder	102
Fig. 5.4 XRD patterns of pure and Al-doped ZnO powder.....	103
Fig. 5.5 SEM micrographs of pure and Al-doped ZnO powder.....	104
Fig. 5.6 Particle size distribution of pure and Al-doped ZnO powder	104
Fig. 5.7 Sintering behavior of pure ZnO and Al-doped ZnO using spark plasma sintering ...	106
Fig. 5.8 Relative density versus temperature of Al-doped ZnO ceramics	108
Fig. 5.9 XRD patterns of Al-doped ZnO ceramics at varying temperature	109
Fig. 5.10 SEM micrographs of 0 at% and 2 at% Al ZnO ceramic sintered at 700°C	110
Fig. 5.11 SEM micrograph of Al-doped ZnO ceramic at different sintering temperatures ...	111
Fig. 5.12 XRD patterns of Al-doped ZnO ceramics sintered at 600C and 650C with a pressure of 250 MPa using RT and HT mode	112
Fig. 5.13 XRD patterns of Al-doped ZnO ceramics sintered at 250 MPa and 500 MPa with a temperature of 600°C using HT mode	113
Fig. 5.14 SEM micrograph of Al-doped ZnO ceramics sintered at 650°C (HT) and 700°C (RT).....	114
Fig. 5.15 SEM micrograph of annealed Al-doped ZnO ceramics sintered at 650°C (HT)....	114
Fig. 5.16 Resistivity versus temperature for annealed pure and Al-doped ZnO ceramics sintered at 650°C (HT)	115
Fig. 5.17 Seebeck Coefficient versus temperature for annealed pure and Al-doped ZnO ceramics sintered at 650°C (HT).....	116

Fig. 5.18 Thermal conductivity versus temperature of annealed pure and Al-doped ZnO ceramics sintered at 650°C (HT).....	117
Fig. 6.1 XRD patterns of polyaniline emeraldine powder	124
Fig. 6.2 SEM micrographs of polyaniline emeraldine powder before (a) and after (b) addition of HCl.....	124
Fig. 6.3 FTIR spectrum of polyaniline powders with inserted table of resistivity at room temperature.....	125
Fig. 6.4 Thermogravimetric analysis of polyaniline powder before and after acid activation	126
Fig. 6.5 XRD patterns of Al-doped ZnO powders and PANI composites.	127
Fig. 6.6 SEM micrographs of Al-doped ZnO powders doped with polyaniline powder	127
Fig. 6.7 FTIR spectrum of Al-doped ZnO powders doped with polyaniline powder	128
Fig. 6.8 Thermogravimetric analysis Al-doped ZnO powders doped with polyaniline powder	129
Fig. 6.9 XRD patterns of pure ZnO, ZnA, ZnA-5PANI and ZnA-ZA9PANI ceramics	132
Fig. 6.10 SEM micrographs of ZnA, ZnA-0,75PANI ZnA-5PANI and ZnA-ZA9PANI ceramics.....	132
Fig. 6.11 TEM micrographs of ZnA-ZA9PANI ceramic.....	133
Fig. 6.12 Raman spectrum of ZnA and ZnA-5PANI ceramics and PANI pellet.....	134
Fig. 6.13 Thermal conductivity of ZnO, ZnA, ZnA-5PANI and ZnA-ZA9PANI ceramics..	135
Fig. 6.14 Illustration of thermal vibrations of ZnA-ZA9PANI ceramic at the interface[150]	135
Fig. 6.15 Resistivity of ZnO, ZnA, ZnA-5PANI and ZnA-ZA9PANI ceramics	136
Fig. 6.16 Arrhenius plot of ZnA-5PANI and ZnA-9PANI	137
Fig. 6.17 Seebeck Coefficient of Al-doped ZnO/PANI ceramics	138
Fig. 6.18 Performance of Al-doped ZnO/PANI ceramics: (a) Power factor (b) Figure of merit	139

List of symbols

Symbol	Definition	Units
S	Seebeck Coefficient	V/K, $\mu\text{V/K}$
V	Voltage	V
G, q	Conductance	S/m
f	Fermi energy	
T	Temperature	K, $^{\circ}\text{C}$
t	time	s,min
E	Fermi level	eV
q	Conductance	S/m
n	Carrier concentration	m^{-3}
m^*	Carrier effective mass	Kg/g
m	mass	Kg/g
h	Planck's constant	$\text{m}^2\text{kg/s}$
ZT	Figure of merit	
e	electrons	
k	Thermal conductivity	W/m.K
L	Lorentz number	$\text{W}\Omega/\text{K}^2$
N_{dc}	Density of defect	-
H	Enthalpy	J
C_p	Heat capacity	J/kg
PF	Power factor	W/m.K^2

k_B	Boltzmann constant	J/K
d	Crystallite size	M
d, ρ	density	kg/m^3
Q	Heat flow	W/m^2
B	Magnetic induction	Tesla
I	Current	A
x	thickness	M
$h\nu$	Energy of photons	V
R	Reflectance	-
TE	Thermoelectric	-
CSP	Ceramic prepared from synthetic powder	-
CCP	Ceramic prepared from commercial powder	-
PANI	Polyaniline	-
SPS	Spark plasma sintering	-
Com-ZnO	Commercial zinc oxide	-
XRD	Xray-diffractometer	-
SEM	Scanning Electron Microscopy	-
EDX	Energy Dispersive X-Ray Spectroscopy	-
TEM	Transmission electron microscopy	-
FTIR	Fourier Transform-Infrared Spectroscopy	-
BET	Brunauer–Emmett–Teller technique	-
DTA	Differential Thermal Analysis	-

TGA	thermogravimetric analysis	-
ICP-AES	inductively coupled plasma atomic emission spectroscopy	-
ICP-OES	inductively coupled plasma optical emission spectroscopy	-

Greek Symbol

Symbol	Definition	Units
Δ	Change/difference	-
μ	Carrier charge mobility	$\text{m}^2/\text{V}\cdot\text{s}$
ρ	Resistivity	$\Omega\cdot\text{m}, \Omega\cdot\text{cm} / \text{g}\cdot\text{m}^{-3}$
α	Diffusivity	m^2/s
	Absorption coefficient	cm^{-1}
σ	Electrical conductivity	$\text{S}/\text{m}, \text{S}/\text{cm}$
π	Relaxation time	
η	efficiency	%

General introduction

General introduction

The global warming due to fossil fuels and the escalating worldwide demand for energy is driving wide investigation and development of sustainable and alternative energy sources. Thermoelectric (TE) devices are considered as an attractive option and are being used for direct conversion of heat to electricity. They are being preferred because of the lack of moving parts, their robustness in harsh environment and also there is no need for high temperature fluids. Currently, the limitations in both heat transfer efficiency and cost of the thermoelectric devices has relegated their application especially for large-scale energy-conversion processes.

At present, much research is focused on improving and developing new thermoelectric materials that are environmentally friendly and inexpensive i.e. containing earth-abundant elements. Hence, the use of metal oxide as TE materials has been thoroughly studied over the past years as green technology materials. In this study, ZnO was chosen because of its high Seebeck Coefficient and carrier mobility which are perfect parameters towards improving thermoelectric performance. However, the main challenge with pure ZnO is the high thermal conductivity and resistivity which reduces the thermoelectric efficiency. Hence, the present study focuses on improving the thermoelectric properties of ZnO by evaluating the processing of ZnO powder and dense ceramics; and also doping and/or incorporation with other materials with an aim to address the mentioned shortfalls.

From literature it was observed that pure ZnO is mostly doped with Group III elements (Al, Ga, In, and B) as source of charge carriers to improve its electrical conductivity. Recently, hybrid structures and nanocomposites are receiving a lot of attention due to the unique properties they possess such as reduction in thermal conductivity. Conducting polymers (such as polythionates, polypropylene, polyaniline, polyacetylene, polypyrrole and polyethylene) are being merged with inorganic composites to create hybrid thermoelectric materials. Polymers have become of interest because they have low thermal conductivity.

The aim of this study was to investigate the dispersion of polyaniline (PANI) in Al-doped ZnO ceramics in order to improve thermoelectric properties of the ceramics prepared through spark plasma sintering (SPS). The successful completion of this project will open new opportunities and important insights on how to produce promising low temperature power generation and cooling systems that can be applied in remote areas. About over a billion

people have no access to electricity, hence, the development of off grid solar energy based technologies will transform lives and also benefit those who are currently not being supplied with adequate electricity.

To achieve this noble goal, low cost and manufacturability of polymers are required, as they can be scalable for large applications. This work focused on understanding the characteristics of synthesized pure and Al-doped ZnO particles and their thermoelectric performance. At first a determination of efficient spark plasma sintering parameters for pure ZnO, Al-doped ZnO and Al-doped ZnO/PANI ceramics was done. This was in order to produce ceramics with preserved nanostructure. Attention was paid on the densification, phase transformation and microstructural evolution. The influence of PANI concentration in Al-doped ZnO ceramics on thermoelectric properties was evaluated.

This thesis is made up of six chapters; **Chapter One** contains theoretical background on thermoelectricity and literature review on state-of-the-art thermoelectric materials, performance of ZnO based ceramics and hybrid/metal oxide ceramics on their thermoelectric properties. The materials and methods used for the experiment are contained in **Chapter two**. **Chapter three** discusses the influence of spark plasma sintering parameters on pure ZnO. The study of ZnO powder quality and spark plasma sintering parameters on thermoelectric properties are discussed in **Chapter four**. **Chapter five** contains synthesis, sintering and thermoelectric properties of Al-doped ZnO. **Chapter six** focuses on the incorporation of polyaniline in the Al-doped ZnO ceramic, the powder preparation, densification and thermoelectric properties are discussed. Conclusions drawn from this study and recommendations made are presented in **the last part**.

Chapter 1

Bibliography

1. Bibliography

This chapter provides extensive literature review on current status of thermoelectric materials. The first section focuses on the basic principles of thermoelectricity and the state-of-the-art of thermoelectric materials. Recent progress of promising n-type and p-type metal oxide thermoelectric materials is reviewed. This includes compilation of important parameters such as resistivity, Seebeck Coefficient and thermal conductivity. In-depth discussion on ZnO based thermoelectric materials is presented. The influence of material properties and underlying transport mechanisms are highlighted. Then, a review on thermoelectric properties of ZnO based polymer composites is discussed. Low temperature sintering mechanism of ZnO composites are also discussed in this chapter. Brief conclusions and outlook for future studies are presented.

1.1 Thermoelectricity fundamentals

1.1.1 Thermoelectric effects (Seebeck and Peltier effect)

As highlighted in general introduction, thermoelectricity is a physical phenomenon that occurs in a conductor or semiconductor when exposed to temperature difference or when current is passed through it. There are three thermoelectric effects that occur in materials: Seebeck, Peltier and Thomson effects [1-5]. Thomson effect is the absorption or evolution of heat when current is passed through unequally heated conductor. Seebeck effect is the flow of current due to temperature gradient between two ends of a material. Peltier effect is an inverse of Seebeck effect; it involves heating or cooling of a material on one side when current is passed through it. The description of Seebeck (power generation mode) and Peltier effect (Refrigeration mode) phenomenon is indicated in Fig.1.1. The thermocouples consist of n-type and p-type materials for both the power generation and refrigeration mode. When there is a heat source a temperature difference occurs between the two semiconducting/conducting materials. As a result, an open circuit voltage called Seebeck Voltage is produced that causes the bulb to glow (Fig.1.1). Whereas, when current is passed through the semiconducting/conducting junctions it is converted into heat on one end of the material while the other end gets cooler, this process is known as Peltier effect. Fig. 1.1 illustrates cooling as a result of the Peltier effect. There is interdependence between electric current and temperature difference between the hot and cold ends. In this thesis, we will only focus on Seebeck effect.

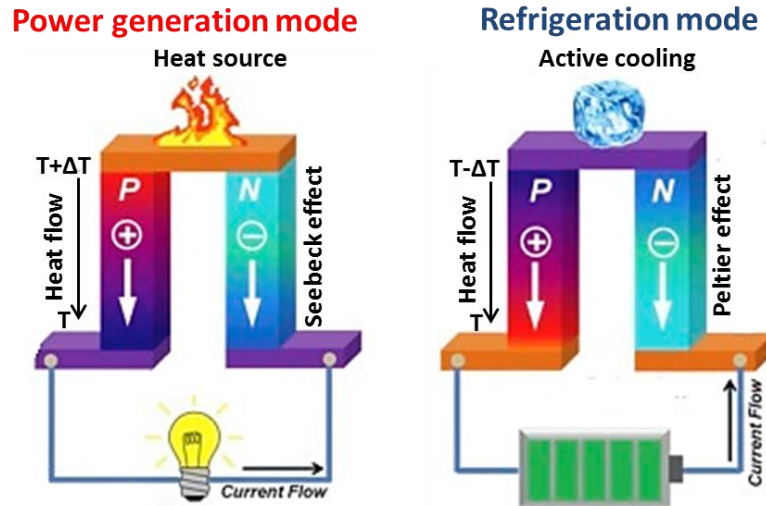


Fig. 1.1 Comparison between Seebeck and Peltier effect [5]

A detailed description of Seebeck effect is given in Fig.1.2. A temperature difference causes charge carriers at hot side to become more active and therefore diffuse to the cold side and then accumulate there (Fig.1.2. (a)), until an internal electrical field (E) is built up that depress further migration (Fig.1.2. (b))[6]. The ratio of the voltage developed to the temperature difference ($\Delta V/\Delta T$) is known as Seebeck Coefficient (S) or thermo-power [2, 6, 7]. If the dominant charge carriers in the material are electrons, the electric field will be opposite to the temperature gradient. Hence, the Seebeck Coefficient will bear a negative sign for electrons (n-type). The reverse is true for holes, a positive sign (p-type) is assigned for Seebeck coefficient [2, 6, 7].

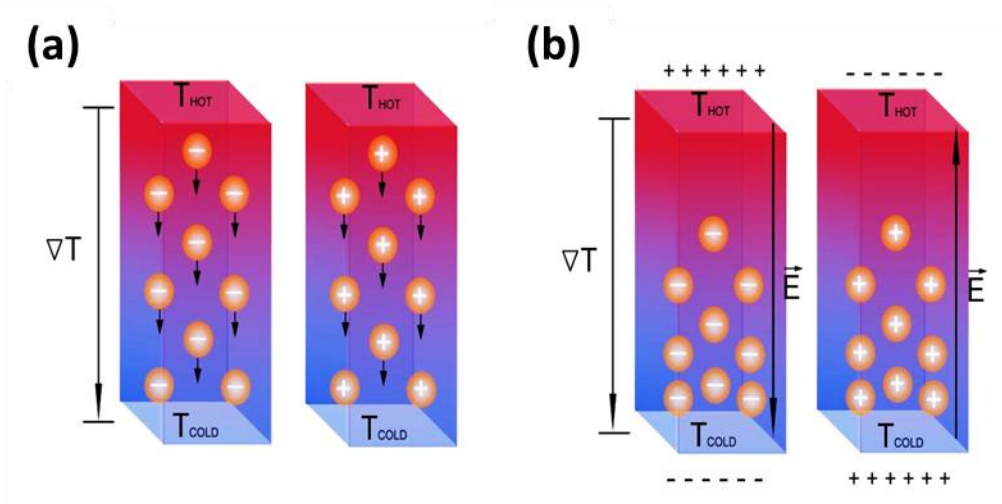


Fig. 1.2. Illustration of Seebeck effect [6]: Migration of charge carriers from hot to cold side on n- and p-type (a) and the building up of internal electric field (b).

The Seebeck Coefficient can be explained from the first principles of Boltzmann's kinetic theory that relates it with thermal conductance [8, 9], see Eq. 1.1-1.3.

$$S = -\frac{\Delta V}{\Delta T} = -\frac{G_s}{G} \quad [1.1]$$

Where G is intrinsic thermal conductance (S/m) and G_s is thermal contact conductance (S/m), ΔV is change in voltage and ΔT is change in temperature

The conductance can be further expressed as follows:

$$G = \int dE \left[-\frac{\partial f}{\partial T} \right] [G(E)] \quad [1.2]$$

$$G_s = \int dE \left[-\frac{\partial f}{\partial T} \right] [G(E)] \frac{E-\mu}{qT} \quad [1.3]$$

Where E is Energy level (eV), f is Fermi function, T is temperature (K), q is conductance (S/m) and μ is mobility ($m^2/V.s$).

Eq. 1.3 shows that the magnitude and sign of Seebeck Coefficient relies on the electronic structure or Fermi function of material [2]. The Fermi energy can be further expressed in terms of effective mass and carrier concentration as shown in Eq. 1.4.

$$E = \frac{\hbar^2}{2m^*} [3\pi^2 n]^{\frac{2}{3}} \quad [1.4]$$

Where h is Planck's constant (m^2kg/s), m^* is carrier effective mass (kg), n is carrier concentration (m^{-3}) and π is pi (3.142).

From the above arguments it follows that a simplified Seebeck Coefficient equation for bulk semiconducting materials is expressed in Eq.1.5 [10].

$$S_{bulk} = \frac{8m^*\pi^2k_b^2}{3eh^2} T \left(\frac{\pi}{3n} \right)^{\frac{2}{3}} \quad [1.5]$$

Where S_{bulk} is Seebeck Coefficient of a bulk material, k_B is Boltzmann constant (J/K) and π is pi (3.142).

It is evident from Equation 1.5 that for high Seebeck Coefficient a large effective mass is required. This explains the high Seebeck Coefficient found in transition metal oxides such as ZnO, MnO₂ etc. [11-13]. It is also predicted that by manipulating the temperature and carrier concentration through doping an optimum Seebeck Coefficient could be obtained.

1.1.2 Performance of thermoelectric materials

Thermoelectric materials are constructed into devices that consist of modules for application purposes. The setup is illustrated in figure 1.3; the top part is the thermoelectric device and the bottom enlarged part is the thermocouple. The thermoelectric device is made of thermoelectric couples that consist of a pair of n and p-type thermoelectric elements connected electrically in series and thermally in parallel. Other parts that make up the device are the substrates for heat adsorption and metal interconnects to contact current. In this study we will only focus on the performance of n-type materials.

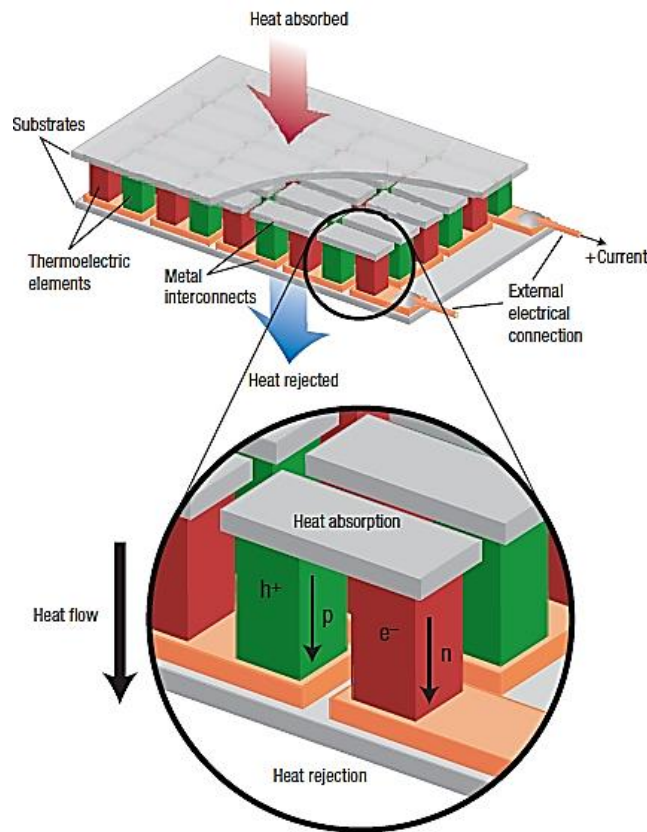


Fig. 1.3 Typical example of thermoelectric module[14]

The conversion efficiency of a thermoelectric generator is determined from the Carnot efficiency:

$$\frac{\Delta T}{T_H} = (T_H - T_C)/T_H \quad [1.6]$$

And reduction factor that takes into account the materials performance (ZT) [2, 5].

$$\eta = \left[\frac{T_H - T_C}{T_H} \right] \left[\frac{\sqrt{1 + ZT_{ave}} - 1}{\sqrt{1 + ZT_{ave}} - \left(\frac{T_C}{T_H} \right)} \right] \quad [1.7]$$

Where η is conversion efficiency (%), T is temperature on Hot (H) and Cold side (C) (K), and ZT_{ave} is average figure of merit from each thermoelectric couple.

A dimensionless figure of merit (ZT) is a central parameter in characterizing the thermoelectric properties of a material; it is determined by the electrical and thermal transport properties of a material (see Eq. 1.8) [5]. It is shown in Eq.1.8 that large **power factor** ($S^2\sigma$ or S^2/ρ) is desired for high figure of merit while maintaining minimal thermal conductivity. Hence, high figure of merit (ZT) can be attained by materials that exhibit high Seebeck Coefficient and electrical conductivity with very low thermal conductivity. It can be seen that the parameters are interrelated and that makes the enhancement of ZT difficult to obtain.

$$ZT = \frac{S^2\sigma T}{k} = \frac{S^2T}{\rho k} \quad [1.8]$$

Where k is thermal conductivity (W/m.K), T is temperature (K), S is Seebeck Coefficient or thermo-power (V/K), σ is electrical conductivity (S/m) and ρ is resistivity ($\Omega.m$).

Different energy conversion technologies and their power generation efficiencies with temperature are given in Fig.1.4. It is presented that improving the ZT value could expand the increasing application of thermoelectric materials. Thermoelectric (TE) materials with $ZT > 1$ are regarded as high-performance materials with potential to be commercialized [1, 15]. The first application of thermoelectricity was in flight space navigation satellites for radioisotope thermoelectric generators (RTGs) carried out by Thor-DM21 Able-Star in 1961 [16]. RTGs have recently been successfully used in deep-space probes launched by NASA for Cassini missions. Nowadays, thermoelectric devices are being installed in vehicles to recover automobile exhaust heat into useful electrical energy and thereby improving fuel efficiency [1, 17]. Solid state refrigerating devices that uses thermoelectric or Peltier effect have been widely used in computers, infrared detectors and optoelectronic devices for cooling [7, 18]. Thermoelectric car seat climate control system are being commercialized [17]. Recent advances include TE-solar hybrid systems for energy conversion and power generation [15].

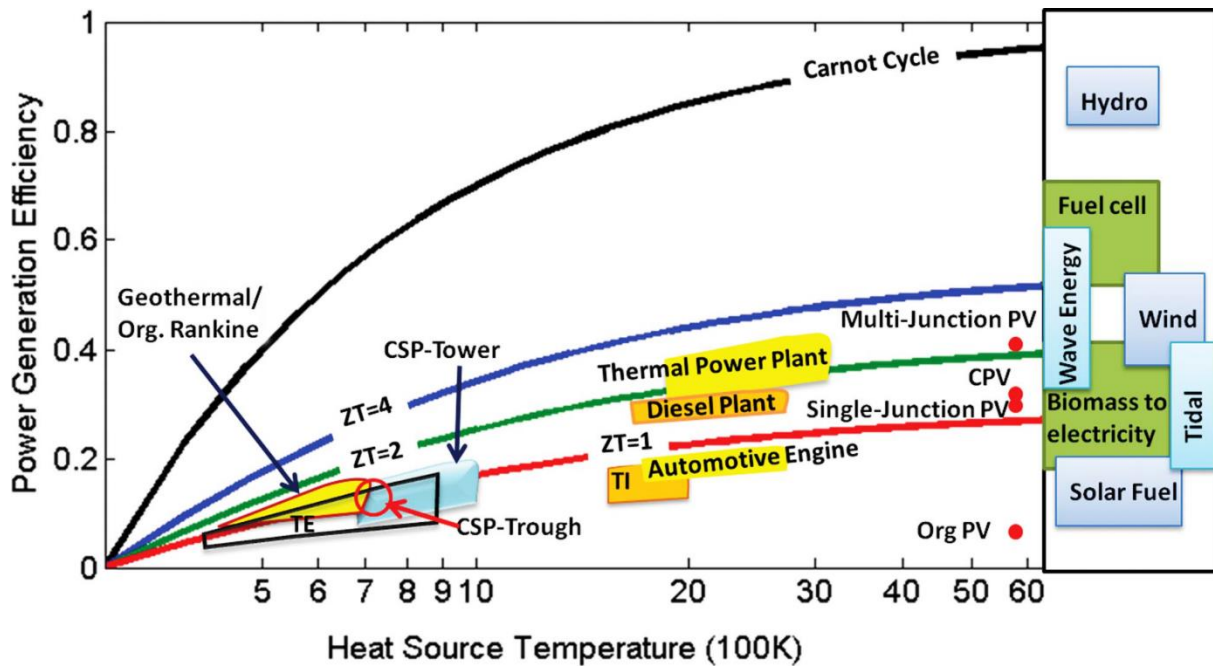


Fig. 1.4 Power generation efficiency versus temperature for different energy conversion technologies [15] (Note: org-Organic, CSP-concentrated solar power, PV- photovoltaic, TE-thermoelectric, TI-Thermionic)

Highest ZT recorded to date is from Cu_2Se and single crystal SnSe (ZT is ~ 2.6) [19, 20], though the mission of the thermoelectric community is to reach ZTs values greater than 3 for large scale application [15]. Hence processing routes and new materials are being explored to improve the performance of thermoelectric materials. However, due to the complexity of thermoelectric materials, only few successful researches have been reported, especially for semiconducting metal oxides and polymers. Therefore, better understanding of the thermoelectric concept is required for altering the parameters.

The relationship between ZT and thermoelectric parameters with carrier concentration is given in Fig 1.5. It is shown that there should be a balance of the carrier concentration with Seebeck Coefficient and electrical conductivity to have improved ZT. The trade-off between electrical conductivity and Seebeck Coefficient can also be understood from the electronic density of states. The electrical conductivity of bulk semiconductors is related to charge carrier concentration (n) and mobility (μ) as shown in Eq. 1.9 [5, 10]. There is a clash amongst the parameters looking into Eq.1.5 and 1.9; high carrier concentration will result in high electrical conductivity whereas a decrease in the Seebeck Coefficient will occur. Also, large effective mass is favored for high Seebeck Coefficient while for the electrical conductivity is not the case. Therefore, a trade-off needs to be done amongst these parameters for increasing the ZT value.

$$\sigma = n(E)e\mu(E) = n(E)e^2 \frac{\pi(E)}{m^*} \quad [1.9]$$

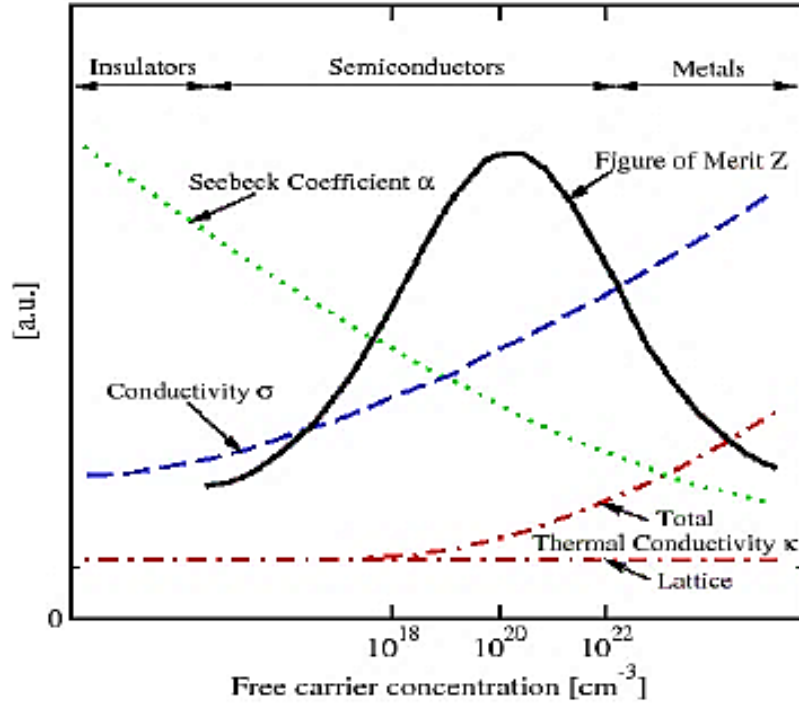


Fig. 1.5 Figure of merit and behavior of thermoelectric parameters at varying carrier concentration [21]

Thermal conductivity also plays an important role when improving thermoelectric performance. Based on the previous successful researches a minimal thermal conductivity of less than 5 W/m.K is required [20, 22]. Fundamentally, both phonons and electronic charge carriers (electrons or holes) are responsible for thermal transport. The corresponding contributions of these are lattice (l) and electronic (e) thermal conductivity (Eq.1.10 and 1.11)[10].

$$k = k_l + k_e \quad [1.10]$$

$$k_e = LTne\mu \quad [1.11]$$

Where L is Lorentz number ($2.4 \times 10^{-8} \text{ W}\Omega/\text{K}^2$)

At high carrier concentration ($n > 10^{20} \text{ cm}^{-3}$), thermal conductivity is increased whereas high electrical conductivity is favored as shown in Fig. 1.5. Several studies have been conducted in order to reduce lattice thermal conductivity by phonon scattering through various ways such as nano-structuring [14, 23-27], material doping [10, 28-30] and morphology manipulation using process techniques such as Spark plasma sintering or microwave sintering etc... [24,

31-34]. In addition to the above other methods such as the creation of nanopores [35, 36], the elaboration of nanoprecipitates [33, 34, 37] and development of complex structures such as skutterudites [38, 39], clathrates [38, 40], half-Heusler [38, 41] etc have been reported for reducing the lattice thermal conductivity. Furthermore, Hicks and Dresselhaus [42] proposed that quantum confinement of charge carriers could increase the power factor, thus improving the ZT. A typical example of how thermal conductivity reduction can enhance the figure of merit is illustrated in Fig. 1.6. Thermal conductivities 0.2 W/mK and 0.8 W/m.K are compared; it could be seen that reducing the thermal conductivity to 0.2 W/mK improves the ZT by two-folds. Reduction in thermal conductivity reduces carrier mobility, as electron scattering will be increased, this will result in high Seebeck Coefficient.

Thus far, nano-structuring has been reported as the most efficient and easier method for reducing the lattice thermal conductivity [14, 23, 43]. The effect of grain size on the thermal conductivity as a function of temperature is given in Fig.1.7 for nano-grained Ga-ZnO ceramics. It is shown that thermal conductivity decreases as the grain size is decreased. Also, as the temperature is increased the thermal conductivity is further reduced. A nanostructured material reduces the phonon mean free path and also offers different phonon scattering modes that could reduce the thermal conductivity. The scattering mechanism that occurs in a nanostructured material is illustrated in Fig.1.8. Mid/Long phonon wavelengths are scattered at the nanoparticles and grain boundaries whereas the short wavelengths are scattered by the atomic defects. At high temperatures the mean free path is decreased due to molecular vibrations. In this work, we will explore the reduction of thermal conductivity by addition of conducting polymers in a transition metal oxide.

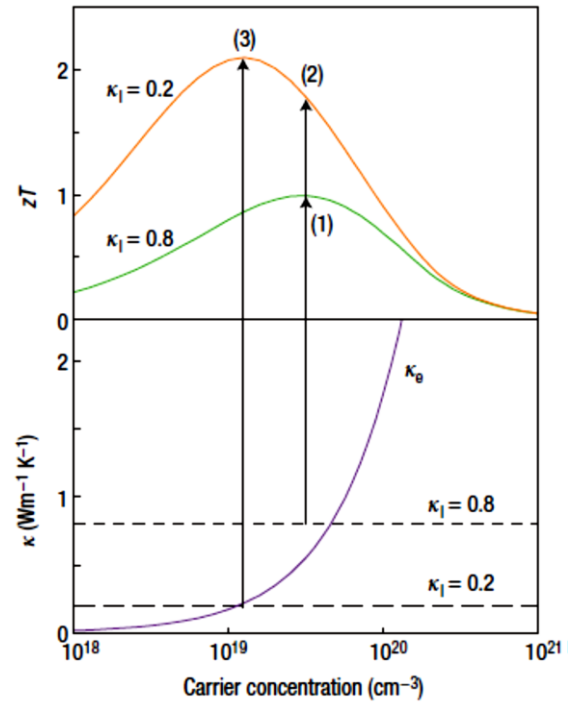


Fig. 1.6 Effect of thermal conductivity on the figure of merit [14]

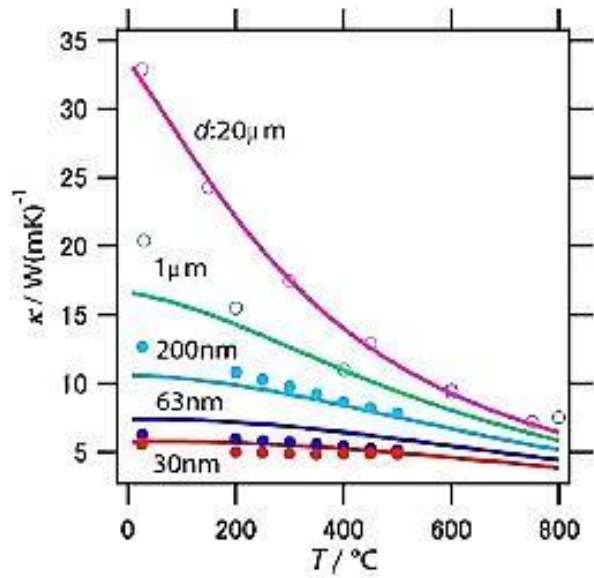


Fig. 1.7 Effect of grain size on thermal conductivity as a function of temperature on nano-grained Ga-ZnO ceramics [44]

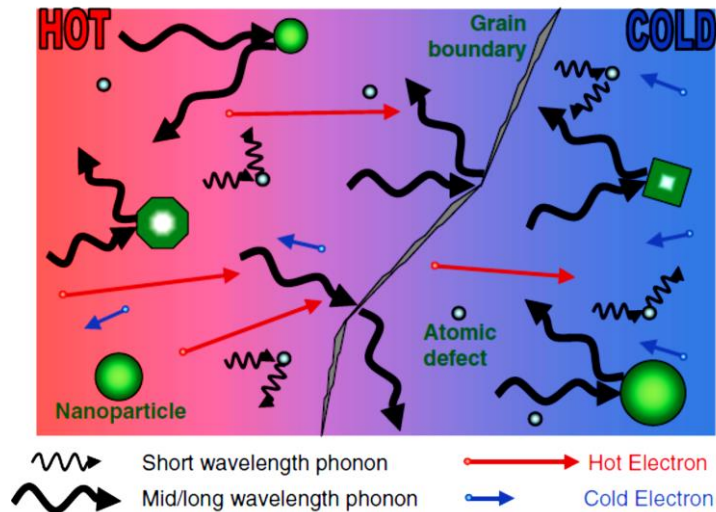


Fig. 1.8 Scattering mechanism of phonons within a nanostructured material [27]

1.2 Current state-of-the-art thermoelectric materials

Previously we have indicated the importance of improving the figure of merit for large scale application and the need to optimize thermoelectric parameters. ZT has been improved enormously over the past decades through intense experimental procedures [1, 45] and theoretical studies on different materials [42, 46, 47]. ZT of different n and p-type thermoelectric materials as a function of temperature are given in Fig.1.9. The classical materials: Bi_2Te_3 [48, 49], PbTe [50-53] and GeSi [54-56] are well known for room temperature ($\sim 300\text{K}$), mid ($300\text{-}700\text{K}$) and high temperature ($>700\text{K}$) applications, respectively. Through band engineering and nano-structuring ZT over 2 was achieved for Na doped SnSe [57], $\text{AgSbTe}_{1.85}\text{Se}_{0.15}$ [58], $\text{Ge}_{0.89}\text{SbIn}_{0.01}\text{Te}$ [59], Na-doped PbTe-SrTe [60] and PbTe-PbS [61] composites (Fig 1.9 (a,b)). Over the years, new materials with unique characteristics (such as the Skutterites (MX_3 , where M is transition metals and X is Phosphorus, Arsenic, Antimony etc..) [62, 63], Clathrate[64], half-heusler [65] etc..) to improve ZT value have been proposed and studied (Fig1.9 (c))[38]. The highest reported ZT to date for bulk materials is 2.66 at 923K from SnSe single crystal measured along the b axis [19, 45] and recently from indium doped Cu_2Se with ZT of 2.6 at 850K [20, 45]. However, the setback of these materials is the restriction for large scale application as their compounds are made up of rare earth (very expensive) and toxic elements. It is vital to use materials which are abundant and environmentally friendly. Hence, metal oxides are the ideal and most recently studied materials since they are made up oxygen and earth friendly elements.

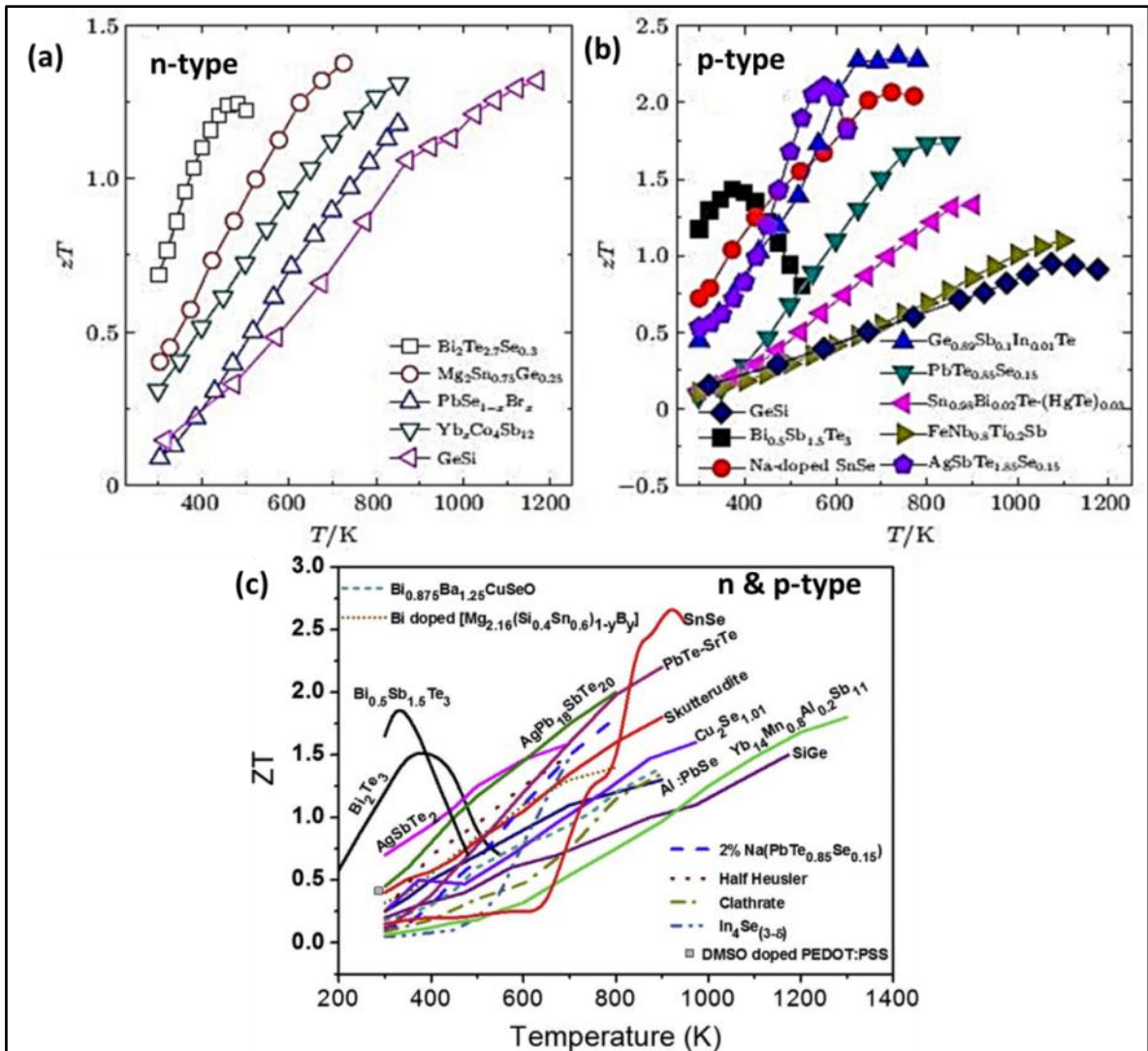


Fig. 1.9 Recent advances of different thermoelectric materials: n-type materials[22] (a), p-type materials [22] (b) and n & p-type of recent thermoelectric materials [66] (c)

1.3 Metal oxide thermoelectric materials

Metal oxides are of interest recently as eco-friendly thermoelectric materials because they are less toxic, inexpensive and have high thermal stability[13]. Thermoelectric devices made from metal oxides are more durable because of their stability in oxidizing environment unlike tellurium, antimony and germanium based compounds. Their electrical properties can be transitioned from insulator to metallic behavior through manipulation of crystal structure, doping/co-doping and chemical compositions [10, 67, 68]. The recent progress on the performance of n-type and p-type metal oxides, in terms of figure of merit vs temperature is given in Fig.1.10. The most promising thermoelectric metal oxides are the p-type layered cobaltite ($\text{Ca}_3\text{Co}_4\text{O}_9$ and Na_xCoO_2)[13]. A single crystal $\text{Ca}_3\text{Co}_4\text{O}_{9+\delta}$ was reported to give ZT of 0.83 at 973K [69]. Whereas, a dually doped polycrystalline $\text{Ca}_3\text{Co}_4\text{O}_{9+\delta}$ with silver and

lutetium gave maximum ZT of 0.61 at 1118K due to drastically reduced thermal conductivity $<1.8\text{W/m.K}$ and enhanced thermopower ($\sim 240\mu\text{V/K}$) induced by Ag nano-inclusions [70, 71]. While, undoped Na_xCoO_2 with Na/Co ratio of 0.85 showed ZT of 0.78 at 950K [72], and after doping with silver, the ZT was increased to 0.91 at 950K. Recent advances on the p-type metal oxides are focused on BiCuSeO oxyselides [73]; pristine BiCuSeO has high Seebeck Coefficient of between 300 and $400\mu\text{V/K}$ at 300-900K with minimal thermal conductivity [29, 68, 73]. As a result, BiCuSeO doped with BaO gave ZT of 1.4 at 900K.

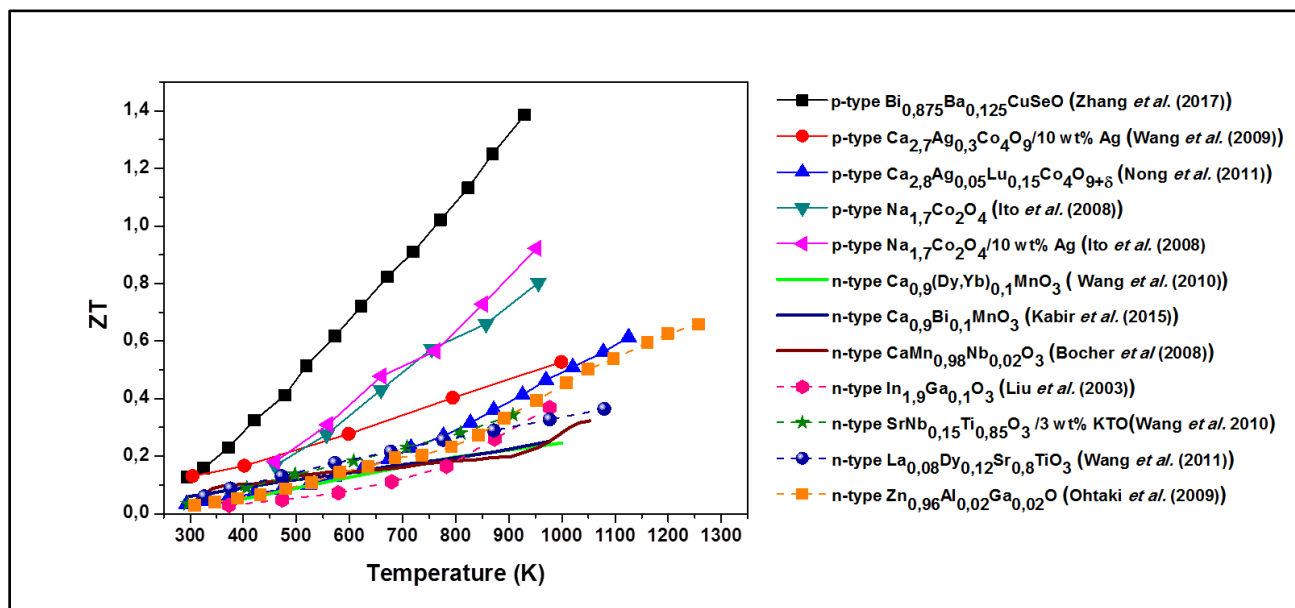


Fig. 1.10 Recent progress on thermoelectric properties of metal oxides. ZT versus temperature for ($\text{Bi}_{0.875}\text{Ba}_{0.125}\text{CuSeO}$ [29], $\text{Ca}_{2.7}\text{Ag}_{0.3}\text{CoO}_9/10\text{wt}\%\text{Ag}$ [71], $\text{Ca}_{2.8}\text{Ag}_{0.05}\text{Lu}_{0.15}\text{Co}_4\text{O}_{9+\delta}$ [70], $\text{Na}_{1.7}\text{Co}_2\text{O}_4$ [72], $\text{Na}_{1.7}\text{Co}_2\text{O}_4/10\text{wt}\%\text{Ag}$ [72], $\text{Ca}_{0.9}(\text{Dy},\text{Yb})_{0.1}\text{MnO}_3$ [74], $\text{Ca}_{0.9}\text{Bi}_{0.1}\text{MnO}_3$ [75], $\text{CaMn}_{0.98}\text{Nb}_{0.02}\text{O}_3$ [76], $\text{In}_{1.9}\text{Ga}_{0.1}\text{O}_3$ [77], $\text{SrNb}_{0.15}\text{Ti}_{0.85}\text{O}_3/3\text{wt}\%\text{KTO}$ [78], $\text{La}_{0.08}\text{Dy}_{0.12}\text{Sr}_{0.8}\text{TiO}_3$ [79], $\text{Zn}_{0.96}\text{Al}_{0.02}\text{Ga}_{0.02}\text{O}$ [28])

The most investigated n-type metal oxides are the perovskite-type such as the strontium titanate (SrTiO_3 (STO) and calcium manganite (CaMnO_3 (CMO))) [10, 13]. The doping process of these materials is promoted by creating an oxygen deficient ceramic [68]. An STO doped with potassium titanate (KTO) and lanthanum-doped barium titanate has shown promising ZT values of about 0.38 at 900K [78, 79]. However, the issue with STO is the easy oxidation of Ti^{3+} ions to Ti^{4+} ions above 650K [13, 80]; oxygen easily diffuses causing the ceramic to be insulating [81]. Thus, CMO are used for high temperatures greater than 1000K due to stability of Mn^{3+} ions at these conditions [82]. Unfortunately, its performance has been poor with ZT below 0.2 when doped with bismuth [75] and co-doping with ytterbium and

dysprosium [74]. A slight improvement in the ZT of the CMOs was observed doping with Niobium on the manganese site [76]. Other reported work on the thermoelectricity of metal oxides includes gallium doping in indium oxide ceramics [77]; ZT of 0.37 at 1000K was achieved. In this work we will focus on zinc oxide (ZnO), a promising n-type metal oxide with better performances at high temperature. Maximum ZT of 0.65 was reported at 1247K on a dually doped with aluminum and gallium[28]. This will be discussed in details in section 1.4.2.

1.4 ZnO based thermoelectric materials

1.4.1 Characteristics and challenges of pure ZnO

Zinc Oxide is an n-type semiconductor with a wide band gap between 3.2 to 3.5eV, hence, has broad applications in optoelectronics, piezoelectric, thermoelectricity, gas sensing and photovoltaic due to its unique chemical and physical properties [83-89]. It has good photo-stability, high chemical and thermal stability, high bond energy and broad range of radiation absorption capabilities. Zn metal has high electronegativity which results in less polarized Zn-O bonds. Crystal structures of ZnO are presented in Fig.1.11. At ambient conditions, ZnO normally crystallizes into a thermodynamically stable phase, hexagonal wurzite structure, space group $P6_3mc$ (Hermann–Mauguin notation) or $C6_v^4$ (Schoenflies notation) with lattice parameters: $a = b = 3.2488\text{\AA}$, $c = 5.2054\text{\AA}$ [90]. Depending on the synthesis conditions other crystal structures can be formed; this includes cubic zinc-blende (tetrahedral, formed at high pressures (>9GPa)) and rocksalt (which is mostly formed at very high pressures) [91, 92].

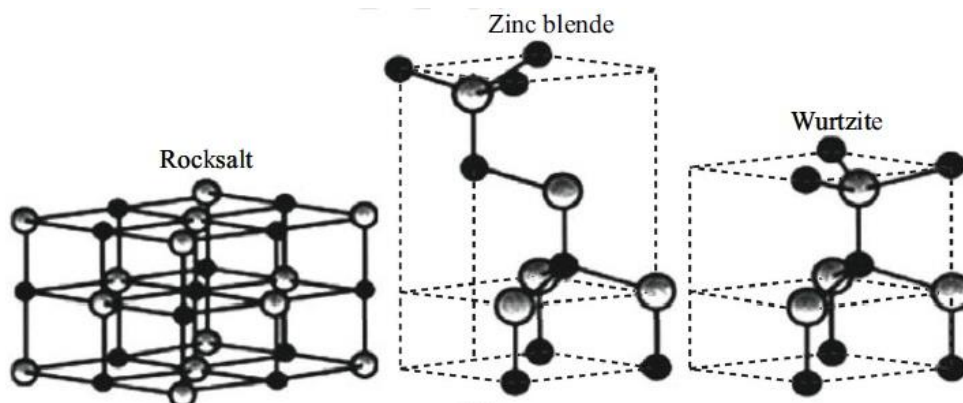


Fig. 1.11 Crystal structures of ZnO [92]

Because of the simple crystal structure and light elemental composition, wurzite ZnO struggles from high thermal conductivity which can go as high as $\sim 100\text{ W/m.K}$ at room temperature [93-95] and $\sim 11\text{ W/m.K}$ at 1000K [95]. This is a setback for the performance of thermoelectric materials. Hence, it is important to find new/upgrade existing processing

methods (including powder synthesis and sintering techniques) and explore different dopants to reduce the thermal conductivity. Even though ZnO is praised for its high Seebeck Coefficient of about $600\mu\text{V/K}$ at room temperature [95], it struggles from low electrical conductivities. Fully annealed sputtered ZnO ceramic with a thickness of 100 nm has resistivity of $10^4 \Omega\cdot\text{cm}$ at room temperature [96]. By introducing dopants and manipulating the stoichiometry of ZnO the resistivity could be reduced towards a metallic behavior, with resistivity ranging between $10^2\text{-}10^3 \Omega\cdot\text{cm}$ [83, 91, 97].

1.4.2 Challenges with preparing nanostructured pure ZnO ceramics

As alluded earlier numerous research studies have been reported on the nanostructuring of thermoelectric materials for improving the ZT by thermal conductivity reduction [23, 26, 27, 42]. Different powder synthesis and sintering techniques have been considered for the reduction of grain size. So, nanometric ZnO powders of varying particle size distribution and grain morphology have been synthesized by chemical precipitation, sol gel, emulsion, hydrothermal and microwave techniques [83, 89]. Though, the challenge in consolidating nanopowder ceramics is obtaining full densification and maintaining the nanostructure. Sintering methods such as microwave and spark plasma sintering have been reported for densifying materials while maintaining the nanostructure [98-100]. Because of the high surface area of nanopowders, grain growth rapidly predominates during sintering due to the diffusion of grain boundaries and Ostwald ripening [101-105]. Therefore, it is crucial to be cautious about sintering techniques to minimize grain size. Spark plasma sintering (SPS) is a recent effective sintering technique for consolidating all kinds of materials. It uses rapid heating and high thermal efficiency, and as a result, it contributes to full densification of materials within minutes with retained nano/microstructure [100, 106, 107].

Retaining the nanostructure of ZnO ceramics can result in lower thermal conductivity to about 10 W/mK at room temperature [31, 32]. Usually thermal conductivity of about $35\text{-}55\text{W/m.K}$ is reported at room temperature because of the micrometre grain sizes [32, 108-111]. The summary of thermoelectric properties of pure ZnO ceramics at 700 K is presented in Table.1.1. Great progress has been done over the past 2 decades in improving the thermoelectric properties of ZnO ceramics. Advancement in the processing techniques resulted in a decrease in the sintering temperature to less than 400°C which caused a decrease in the grain size from $\sim 30 \mu\text{m}$ to less than $10 \mu\text{m}$ [31, 108, 111, 112]. As a result, thermal conductivities of about 12 W/m.K were obtained for fully dense ZnO ceramics. Porosity has been reported as a way to reduce thermal conductivity, however, it has a huge impact on electrical conductivity of ceramics [113]. Virtudazo *et al.* [32] made a macro/nanoporous ZnO

ceramic from nanoporous ZnO powders prepared through double emulsion; lowest thermal conductivity of 4 W/m.K was reported at 700 K due to shortening of phonon mean free path [114]. Thus, ZT of 0.03 was reported for 0.05 Ω .cm of resistivity and -279 μ V/K in Seebeck Coefficient, for ZnO ceramic obtained by spark plasma sintering at 550°C. When ZnO ceramic was spark plasma sintered at 950°C, the highest ZT of 0.06 was obtained when the resistivity was 0.002 Ω .cm, and the Seebeck Coefficient of -123 μ V/K and thermal conductivity was 11 W/mK. Sintering at high temperature resulted in higher concentration of oxygen vacancies that improved the electrical conductivity of the ceramic, hence, the higher ZT. The theoretical background of ZnO intrinsic defects is discussed in section 1.4.3.

Recently, Cramer *et al.* [31] reported on the densification of ZnO nanoparticles using modified graphite mould using and spark plasma sintering to enhance thermoelectric properties through simultaneous improvement of Seebeck Coefficient, electrical conductivity and thermal conductivity through grain size gradation across the ceramic. Relative density of 97% was obtained. The SEM micrograph of the functionally graded material (FGM) is depicted in Fig. 1.12. The grain sizes decreased from the hot to the cold side; 1200 nm to 200 nm. At room temperature the thermal conductivity was 20 W/m.K and 12W/m.K at 700K. It is noticed that the thermal conductivities are in the same range as that of normal sintering at high temperatures. Thermal conductivities of less than 5 W/m.K are required for improvement of the ZT value. The absolute Seebeck Coefficient and resistivity were 180 μ V/K and 0.02 Ω .cm at 700K, respectively, which resulted in a ZT of 0.01.

Lowering the sintering temperature could be used to reduce the thermal conductivity by causing little or no grain growth. There have been reports about sintering of ZnO nanoparticles at low temperatures, less than 600°C [115-118]. Ceramic grain sizes of about 200 nm resulted in reduced thermal conductivity of about 10 W/m.K at room temperature. Unfortunately, this caused an increase in the resistivity to \sim 80 Ω .cm because of scattering of electrons at the grain boundaries and reduction in crystallinity [31]. ZnO being a non-stoichiometric semiconductor, it is easily affected by temperature and sintering atmosphere which has a huge influence on the resistivity. These last points will be discussed in detail in section 1.4.3.

Table 1.1 Thermoelectric properties of pure ZnO ceramics at 700K

Yr.	Technique	Sintering conditions	Powder crystallite size	Ceramic grain size	RD	ρ	S	k	PF	ZT	Ref.
			nm	μm	%	$\Omega.\text{cm}$	$\mu\text{V/K}$	W/m.K	10^{-4}W/m.K^2		
2017	SPS	Differential sintering, 73MPa, 773-1173K	18 (Nanoparticle)	0.18-1.2	97	0.02	-180	12	1.43	0.01	[31]
2017	SPS	3.5kN, Argon	20 (Nanoporous)								[32]
		823K		<10	78	0.05	-279	4	1.73	0.03	
		1023K		~5-25	80	0.006	-195	12	6.79	0.04	
		1223K		~5-30	91	0.002	-123	11	9.53	0.06	
2016	SPS	125MPa, Vacuum, 1173K	- (Nanoparticle)	- (Annealed)	>98	3.64	-600	20	0.1	3.5×10^{-4}	[95]
2015	SPS	Argon 1173K	13.8 (Nanoparticle)	1-2	93	0.13	-300	12	0.68	3.9×10^{-3}	[111]
2013	SPS	1173K	~70	0.1-1 (Annealed)	-	0.3	-374	15	0.47	2.2×10^{-3}	[109]
			~100 (Nanoparticle)	-		4	-	6	-	-	
2011	Hot press	Air 1673K	28 (Nanoparticle)	31	>97	1.25	-280	14	0.06	3.1×10^{-4}	[108]
2005	SPS	Vacuum 1273K	- (Nanoparticle)	<10	99	251	-500	11	0.001	6.3×10^{-6}	[112]
1997	Hot press	Air 1673K	- (Nanoparticle)	-	99	0.1	-325	18	1.06	4.1×10^{-3}	[110]

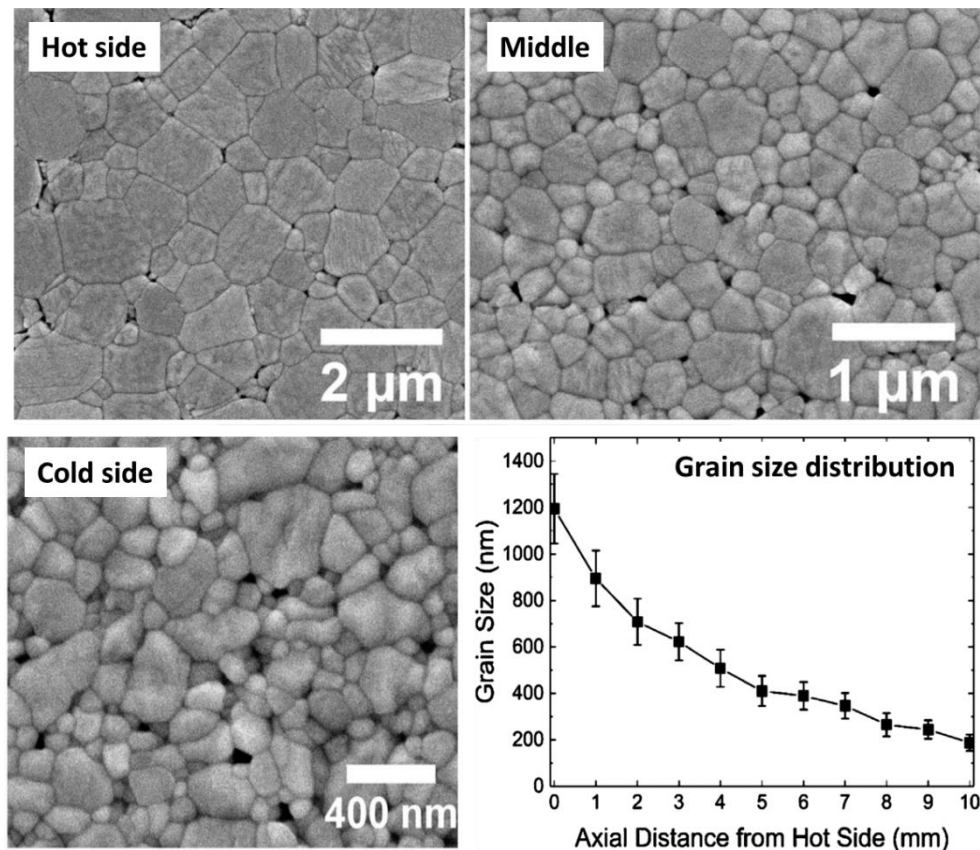


Fig. 1.12 SEM micrographs of functionally graded ZnO ceramic[31]

1.4.3 Intrinsic ZnO defects

Even though ZnO is praised for its high Seebeck Coefficient value ranging between 300-600 μ V/K thanks to the use of SPS technique depending on the concentration of charge carriers, which are controlled by powder synthesis methods, sintering techniques and annealing procedures, it still suffers from low electrical conductivities as highlighted in the previous sections [95, 109, 110, 112]. Through doping and manipulation of stoichiometry of ZnO ceramics the resistivity could be reduced towards metallic behavior. The defects in pristine ZnO play an important role in the electrical properties [91, 119-121]; by controlling operating parameters such as the sintering atmosphere, temperature etc... the concentration of defects could be tuned. There are different defects which can form within the ZnO bandgap. The ionization energy of the defects is shown in Fig. 1.13 [119] : zinc interstitials (Zn_i) close to the conduction band with energies between 0.05-0.15 eV, oxygen vacancies (V_O) with energies between 0.05-2 eV and zinc vacancies (V_{Zn}) close to the valence band with energies between 0.8-2.8 eV.

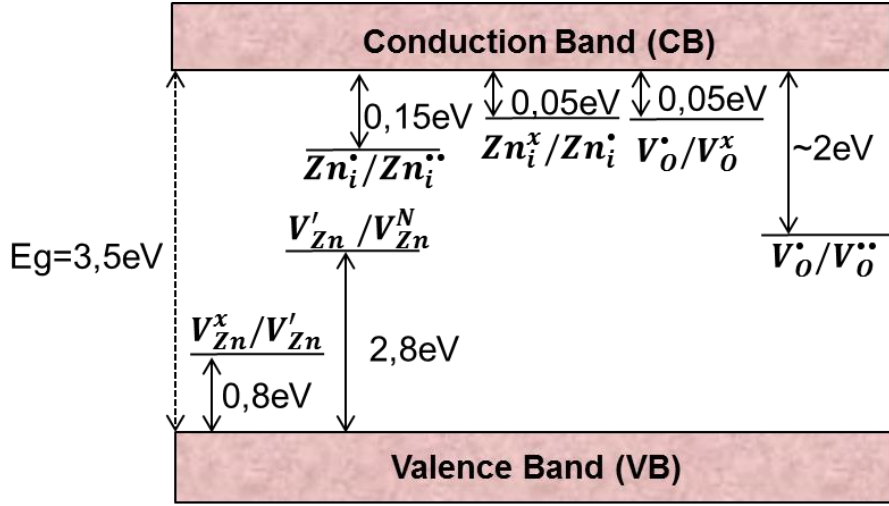


Fig. 1.13 Ionisation energy of ZnO point defects at room temperature [119]

The defects chemistry in ZnO using the Kroger vink notation is presented in Eq. 1.12-1.19, based on the Frenkel and Schottky reactions [119].

Frenkel defect formation reactions: Zinc Interstitials



Schottky defect formation reactions: Oxygen vacancies



Zinc vacancies



Where i is interstitial site, Zn is zinc, O is oxygen, V is vacancy, e^- is electron, h is hole and the superscripted are the charges (a prime indicates negative charge, a dot a positive charge and cross indicates anion site)

The zinc interstitials (Zn_i) always donate 2+ charge electrons to the conduction band in a non-equilibrium n-type ZnO, making them to be shallow donors [122]. The zinc vacancies are

partially filled in their energy orbitals, they can accept additional electrons, and are known to be deep acceptors because of the high transition levels of 0.18-0.87 eV. Oxygen vacancies (V_O) are deep donors with high formation energy, also known to be responsible for the n-type conductivity in ZnO. Whereas, the oxygen interstitials (O_i) can be split into two and acts as a deep acceptor in n-type ZnO and could react with the lattice to form covalent bonds with host oxygen that could be a donor.

The possibility of a defect to contribute to conductivity is determined through the density of defects (N_{de}) in Eq.1.20 [122]. N_{de} depends on the enthalpy of defect formation. The relationship between enthalpy and atomic radius is that, the bigger the atomic radius the higher the enthalpy of defect formation (ΔH) which leads to low N_{de} based on the relationship between ΔH and N_{de} (Eq. 1.20). Oxygen and zinc have Van der Waals radius of 152 and 142 pm [123], respectively. Thus, oxygen will have higher ΔH and low N_{de} , and zinc will have low ΔH and higher N_{de} . This implies that the most vital contributing defects on the conductivity of ZnO are the zinc interstitials and vacancies. Since, zinc interstitials have the lowest energy level compared to zinc vacancies it is the main contributor giving the n-type conductivity in native ZnO.

$$N_{de} \propto \exp\left[-\frac{\Delta H}{k_B T}\right] \quad [1.20]$$

Where N_{de} is the density of defect, H is the enthalpy of defect formation (J), k_B the Boltzmann constant (J/K) and T the temperature (K).

It was previously highlighted that the formation and concentration of ZnO defects depends on the operational parameters. ZnO defects are sensitive to processing atmosphere; Fig.1.14 relates the concentration of ZnO defects with oxygen partial pressure. It is revealed that at low partial pressure of oxygen (reducing atmosphere) the concentration of oxygen vacancies predominates. In stoichiometric conditions, the concentration of oxygen vacancies equals that of oxygen interstitials which is rare for polycrystalline ZnO. The conductivity could be tuned from n-type to p-type depending on the partial pressure of oxygen.

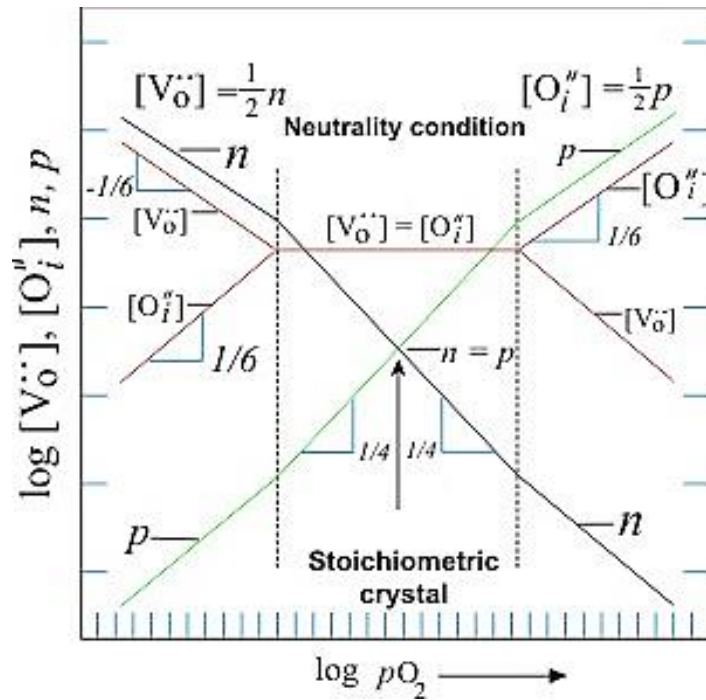


Fig. 1.14 Concentration of ZnO defects as a function of oxygen partial pressure at room temperature [124]

On the electrical properties, the influence of the sintering parameters on the resistivity and Seebeck Coefficient of pure ZnO ceramics are shown in Table.1. The resistivity and Seebeck Coefficient vary between 0.002 to 251 $\Omega \cdot \text{cm}$ and -123 to 600 $\mu\text{V/K}$, respectively; depending on the grain size, relative density and concentration of oxygen vacancies. High power factor (σS^2) of $9.53 \times 10^{-4} \text{ W/m.K}^2$ was achieved with low resistivity of 0.002 $\Omega \cdot \text{cm}$ and Seebeck Coefficient of -123 $\mu\text{V/K}$, whereas ceramics with high Seebeck coefficients of -600 $\mu\text{V/K}$ and resistivity of 3.64 gave low power factors of about $3.5 \times 10^{-4} \text{ W/m.K}^2$. Therefore, it is vital to have very high electrical conductivities for better performance while maintaining the Seebeck Coefficient at moderate level. Several research studies have been done on the addition of substitutional dopants on the zinc side to narrow the band gap with the objective to obtain higher electrical conductivities [125].

1.4.4 Doped and co-doped ZnO TE properties

Zinc oxide is usually doped with the group III elements as they have ionic radius close to that of Zn^{2+} ions (0.074 nm) [126, 127]. The ionic radius of aluminium (Al^{3+}), indium (In^{3+}) and gallium (Ga^{3+}) ions are 0.054, 0.080 and 0.062 nm respectively. These elements act as shallow donors substituting some part of the zinc side giving carrier concentrations higher than 10^{20} cm^{-3} [83]. The recent progress of ZnO based thermoelectric ceramics are given in Fig.1.15. There are several reports on thermoelectric properties of Al-doped ZnO with ZTs

of ~0.17 to 0.47 at 1000K from ceramics prepared through hot press [28, 110, 128, 129], microwave [130] and spark plasma sintering [6, 33, 34, 37, 111, 131]. To date, the highest ZT value reported is 0.65 at 1247K from dual doping with Al and Ga [28]. Gallium was found to improve the solubility of Al in the ZnO crystal. Another factor that improved the properties is the reduced thermal conductivity by nanostructuring. For instance, aluminum hinders grain growth.

Doping with heavy elements like indium (In) leads to promising results because of low thermal conductivities of ~3 W/m.K giving a high power factor of 1230 W.m.K² at 1000K [132]. Further, doping ZnO ceramics with bismuth (Bi) leads to high Seebeck Coefficient of ~500 μ V/k and a decrease in the electrical conductivity was reported due to the segregation of Bi ions at the grain boundaries. Theoretical analysis on antimony (Sb) doping in ZnO nanowires estimated promising ZT of ~0.25 [133]. Transition metal ions such as cobalt [134], nickel [112, 135], zirconium [136], magnesium [137, 138], silver [139], scandium [140], iron [141] etc... were also investigated as grain growth inhibitors. Han *et al.* [140] developed a stable ceramic by dual doping of Sc and Cd; a ZT of ~0.27 was obtained. Recent attempts involved doping of anionic ion sulphur through ZnS compound to tune intrinsic defects in ZnO [142]. Co-doping of Al with reduced graphene oxide (RGO) showed high electrical conductivities of 2000 S/cm at room temperature due to reduced Schottky barriers. Unfortunately, there were no reports about Seebeck and thermal conductivity [143]. Other advancements concerning the inclusion of polymer fillers for thermal conductivity reduction [135] will be discussed in detail in section 1.4.6.

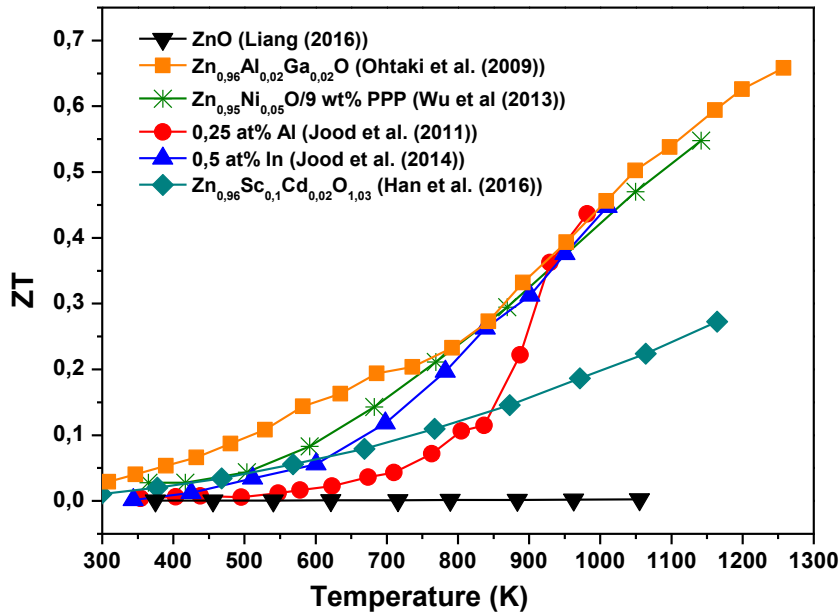


Fig. 1.15 Recent progress on thermoelectric performance of ZnO based ceramics (*ZnO*[95], *Zn_{0.96}Al_{0.02}Ga_{0.02}O* [28], *Zn_{0.95}Ni_{0.05}O/9 wt% PPP*[135], *0.25 at% Al*[130], *0.5 at% In* [132],*ZnSc_{0.1}Cd_{0.02}O_{1.03}* [140])

1.4.5 Influence of grain morphology on thermoelectric properties of Al-doped ZnO

The effects of grain morphology and grain size were highlighted in the previous section on pure ZnO ceramics. Ceramics prepared from nanoparticles, rods, platelets and micro/nano structure powders are compared based on previous reports by Han *et al.* [33] and Zhang *et al.* [34]. The unique morphologies were studied with the aim to minimize thermal conductivity and maximize charge carrier mobility for better electrical conductivities. The SEM micrographs of the Al (2 at%)-doped ZnO powders and ceramics are given in Fig.1.16. The nanoparticles were prepared by hydrolysis whereas the rods, platelets and dual micro/nano microstructure were prepared by hydrothermal techniques. The ceramics were consolidated by spark plasma sintering; relative densities of 80-90% were determined from these ceramics; this is too low for better electrical conductivity. Sintering becomes complicated when complex microstructures and nanometric powders are consolidated. The rods and platelets ceramics have preferential orientation while the ceramics from nanoparticle and micro-nano structured ceramics do not show such behavior. The nanoparticles ceramics had finer grains of less than 1 μ m whereas the micro-nanostructured ceramics had grains of about 3 μ m consisting of small nano-crystallites of about 200 nm. The rods and platelets particles prefer to grow on the miller impedance, <001>, direction while for the nanoparticle and micro-nano particles the <001> growth is prohibited.

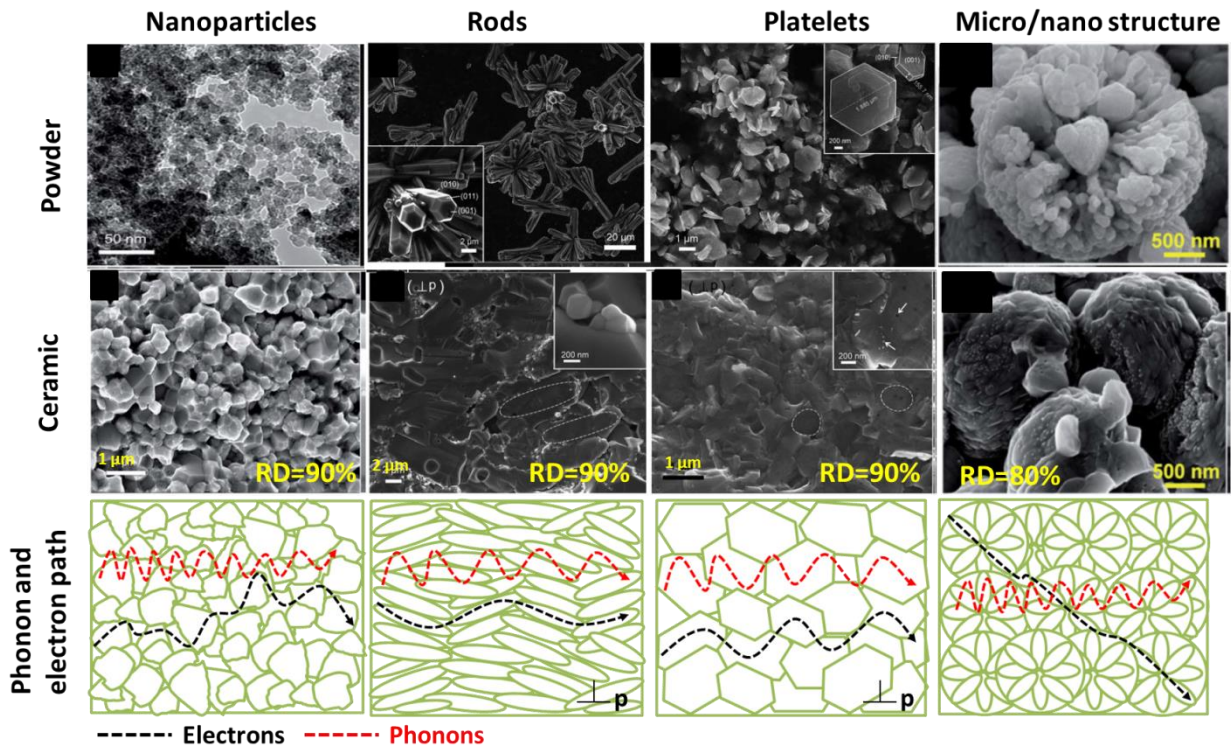


Fig. 1.16 SEM micrographs of $Zn_{0.98}Al_{0.02}O$ powders and ceramics prepared by SPS

(*Nanoparticles, Rods, Platelets [33]; Micro-nano structured [34]*)

The thermoelectric properties of these ceramics are given in Fig.1.17. Ceramics prepared from nanoparticles have high resistivity ($13 \text{ m}\Omega\cdot\text{cm}$) because of many grain boundaries, electrons get scattered at the interface causing reduced flow of charge carriers as illustrated in Fig 1.16 [23]. At room temperature, resistivity of micro-nano structure, platelet and rod ceramic were 0.8 , 0.18 and $0.12 \text{ m}\Omega\cdot\text{cm}$, respectively. The low resistivity was due to increased charge carrier mobility when rod and platelet are measured perpendicular to sintering pressure. A semiconducting behavior was reported in nanoparticles ceramics due to excitation of shallow donors while in rods, platelets and macro-nano structure a metallic behavior with temperature was observed. An average Seebeck Coefficient of $\sim 25 \text{ }\mu\text{V/K}$ was reported for platelets and rods and $\sim 50 \text{ }\mu\text{V/K}$ for nanoparticles and micro-nano structured ceramics at 400K . Due to the simple structure of rods and platelets the thermal conductivity were found to be 35 and 21 W/m.K at 400K , respectively. Both macro-nano structured ceramics showed surprisingly reduced thermal conductivity of $\sim 8\text{W/m.K}$ at 400K . As a result, maximum ZT of 0.37 at 1000 K was determined in micro-nano structured ceramics. The other morphologies did not show significant difference in the ZT.

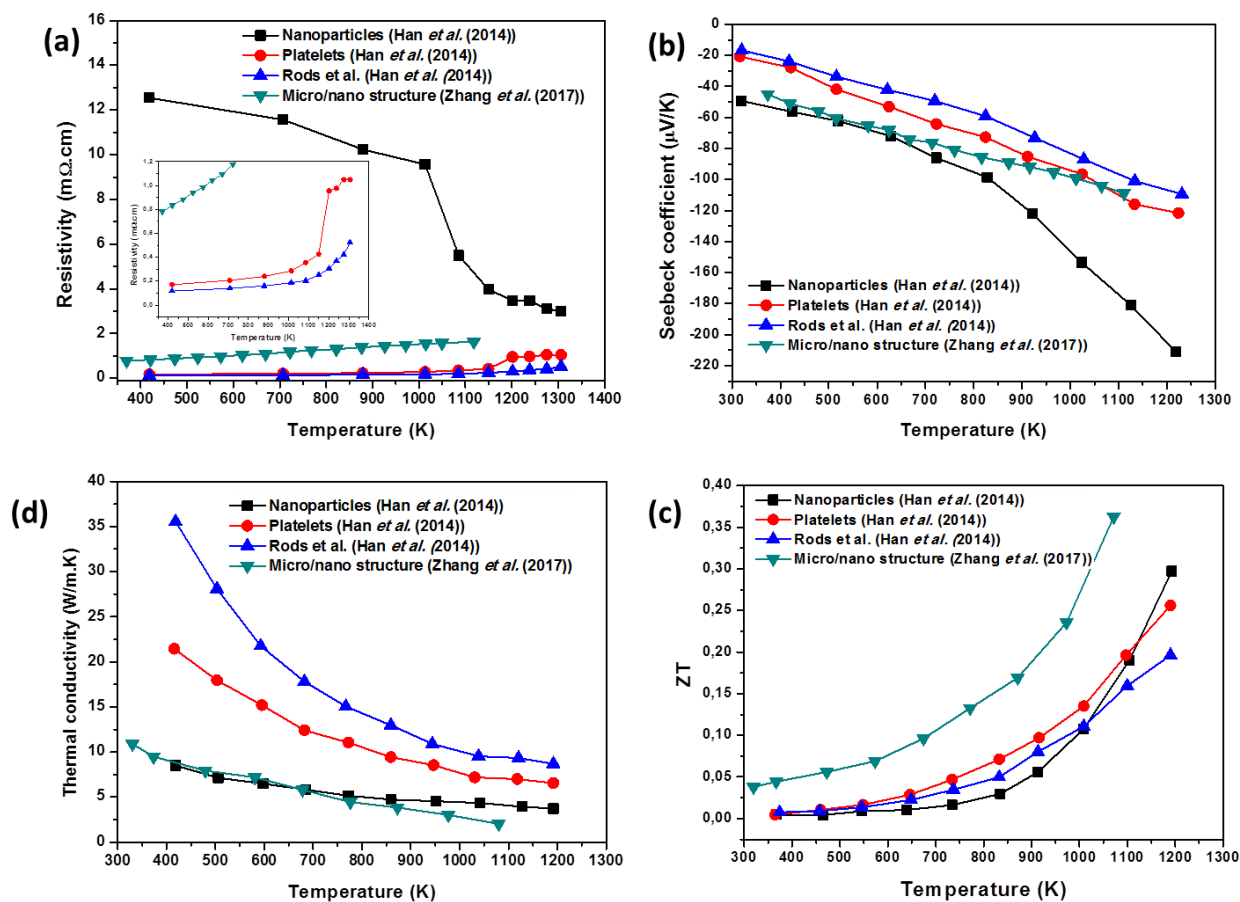


Fig. 1.17 Thermoelectric properties Al-doped ZnO prepared by SPS, for different morphologies

(Nanoparticles, Rods, Platelets [33]; Micro-nano structured [34])

Based on these results it is evident that microstructure has an important effect on the thermoelectric properties of Al-doped ZnO ceramics. It would be beneficial to use the micro-nano structured ceramics; however, the synthesis route for these powders is complicated and expensive. Nanoparticles are easier to produce by chemical techniques such as coprecipitation, sol gel etc... These techniques are cost effective, allows for low temperature synthesis and easy manipulation of crystal size. However, the problem with ceramics from nanoparticles is the high resistivity that draws back its performance. Since the parameters are interconnected it will be difficult to alter one without harming the other. In this manner, it is valuable to search for dopants that will keep the electrical conductivity high while the Seebeck Coefficient is kept moderately around 100-200 $\mu V/K$ at minimal thermal conductivities of less than 5 $W/m \cdot K$. Recently, the doping of conducting polymers are being investigated as promising dopants for ZnO composites as they could give unique electrical properties because of the low thermal conductivities of polymers.

1.4.6 Doping of metal oxides with conducting polymers

Conducting polymers are currently being used for various electrical applications (such as optical, thermoelectricity, sensors etc.) [144-147]. This is because they are flexible, easier to process, cost effective and most importantly have low thermal conductivities than those of inorganic materials. Chemical structure and thermoelectric properties of commonly studied conducting polymers are given in Table 1.2 and 1.3. One can mention: polyaniline (PANI), polythiophene (PTh), polyacetylene (PA), poly (3,4 ethylene dioxythiophene) (PEDOT), polypyrrole (PPy), poly paraphenylene (PPP) and poly (2,7 carbazolylenevinylene) (PC). Intense studies have been done on PEDOT doped with polystyrene sulfonate (PSS) and tosylate (Tos) because of their high electrical conductivity, with a maximum ZT of 0.25 reported at 300K [148]. PANI, PPy, PEDOT: PSS/Tos and PTh were reported to have ZT of $3 \cdot 10^{-4}$ - $1.1 \cdot 10^{-2}$ @ 423K, $2.9 \cdot 10^{-2}$ @423K, $1 \cdot 10^{-2}$ -0.25@ 300K and $7.84 \cdot 10^{-4}$ - $3 \cdot 10^{-2}$ @250K, respectively [144]. The difference is caused by different preparation methods such as the processing techniques, activation reagents etc. PC is becoming of interest recently because of reported high powder factor of $19 \mu\text{W}/\text{mK}^2$ at room temperature [149].

Nowadays, conducting polymers are being incorporated in metal oxide composites to provide unique properties especially for facilitating charge carrier transport and lowering thermal conductivity [147]. The addition of PPP in titanium oxide [150], iron oxide [30] and zinc oxide [135, 139] composites has been investigated.

Table 1.2 Chemical structure of few conducting polymers [144]

Material	Chemical structure	Material	Chemical structure
Polyaniline: leucoemeraldine ($y=1$), emeraldine ($y=0.5$) and Pernigraniline ($y=0$)		Polythiophene	
Poly (3,4 ethylene- dioxythiophene)		Trans- polyacetylene	
Polypyrrole		Poly(paraphenylene)	
Poly (2,7 carbazilylenevin ylene)		Poly(para- phenylenevin ylene)	

Table 1.3 Thermoelectric properties of conducting polymers, re-tabulated from Du *et al.* [144].

Material	T (K)	σ <i>S/cm</i>	S $\mu\text{V/K}$	k <i>W/m.k</i>	ZT
PANI [151-157]	423	$\sim 10^{-7}$ -320	~ 16 -225	~ 0.02 -0.542	$\sim 3 \times 10^{-4}$ - 1.1×10^{-2}
PTh [158-161]	250	$\sim 10^{-2}$ - 10^3	~ 10 -100	~ 0.028 -0.17	$\sim 2.9 \times 10^{-2}$
PEDOT:PSS/Tos [148, 152, 162, 163]	300	6×10^{-4} -945	8-888	~ 0.34 -0.37	1×10^{-2} -0.25
PPy [164-168]	423	0-340	-1-40	0.2	7.84×10^{-4} - 3×10^{-2}
PA [169-171]	423	$\sim 1.53 \times 10^{-3}$ - 2.85×10^4	~ -0.5 -1077	-	-
PC [149, 172]	300	$\sim 4 \times 10^{-5}$ - 5×10^2	4.9-600	-	-
PPP [147]	300	~ 500	-	-	-

The thermoelectric properties of zinc oxide composites doped with PPP are presented in Fig.1.18. The addition of the conducting polymer simultaneously improved both resistivity and Seebeck Coefficient. The resistivity was reduced about 2 folds at 400K as compared to ceramic without polymer; PPP nano-inclusions caused an increase in the carrier concentration [135, 139]. The polymer provides an interconnected network within the ZnO matrix as shown in TEM micrograph in Fig 1.19 (a). Thus, the conductivity is improved because of higher charger carrier mobility due to efficient conduction paths and charge redistribution at the junction of doped-ZnO and PPP[173]. Power factors of 11 and 4.5 W/m.K² (900K) were determined from Ni and Ag doped ZnO ceramics with 9 wt% and 0.15 wt% PPP, respectively. As a result, Ni-doped ZnO, 9 wt% ceramics gave ZT of ~0.27 at 900K and 0.54 at 1150K.

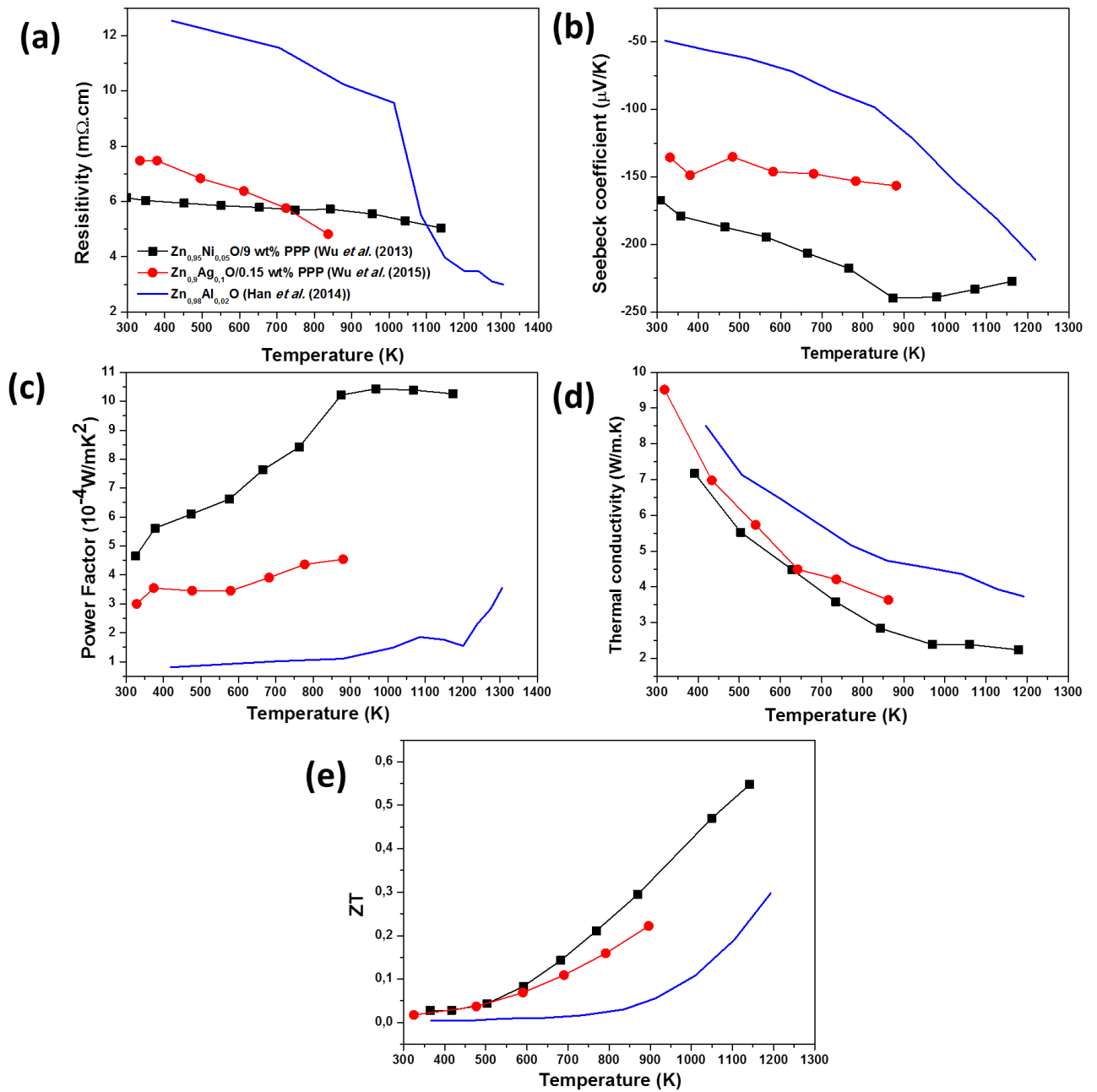


Fig. 1.18 Thermoelectric properties of current ZnO/polymer composites a function of temperature: Resistivity (a), Seebeck Coefficient (b), power factor (c), thermal conductivity (d) and figure of merit (ZT) (e)

($Zn_{0.95}Ni_{0.05}O/9$ wt% PPP [135], $Zn_{0.9}Ag_{0.1}O/0.15$ wt% PPP [139] and $Zn_{0.98}Al_{0.02}O$ [33])

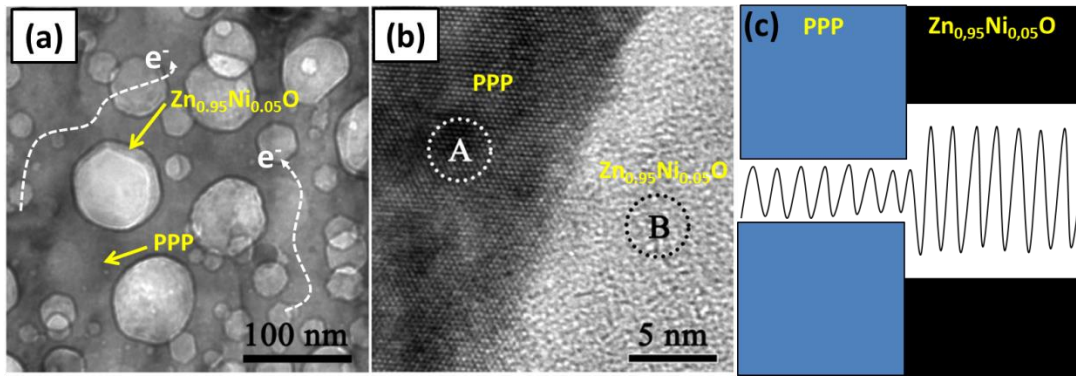


Fig. 1.19 TEM micrograph of $Zn_{0.95}Ni_{0.05}O/9$ wt% PPP ceramic (a), interface image of $Zn_{0.95}Ni_{0.05}O$ and 9 wt% PPP (b) and schematic illustration of vibrational heat conductance (c) [135]

The improved thermoelectric performance is due to high power factor and reduced thermal conductivity of about 7 W/m.K at room temperature caused by mismatch vibrational spectra of metal oxide and polymer [174]. An illustration of vibrational heat conductance is indicated in Fig 1.19 (c); PPP has lower frequencies as compared to the metal oxide which become disturbed at the interface causing overall decrease in the thermal conductivity. Other factors that contribute to the reduction in thermal conductivity is the phonon scattering due to nano-grains and grain boundaries [23, 42, 175].

In this work, an Al-doped ZnO (AZO)/ polyaniline composite was synthesized to minimize the scattering of electrons at the grain boundaries due to nanostructuring. Polyaniline is one of the most stable conjugated polymers, hence, has received much attention over the years. Its electrical conductivity can go as high as 300 S/cm when doped with camphorsulfonic acid (CSA) [176]. Chemically activated polyaniline with 1M HCl lead to a maximum ZT of 3×10^{-4} at 423K [151, 157, 177]. Mitra *et al.* [177] recently reported on thermoelectric properties of AZO nanorods doped with polyaniline (5-25wt%). AZO nanorods doped with 16 wt% polyaniline gave high ZT of 0.0035 at room temperature because of simultaneous improvement in electrical conductivity due to enhanced carrier mobility and Seebeck Coefficient due to scattering of low energy carriers via the energy-filtering effect [178]. The individual performances of the materials are given in Fig.1.20. Polyaniline showed better performance at room temperature compared to AZO with ZT of $\sim 3 \times 10^{-4}$ at room temperature because of high power factor and low thermal conductivity. However, the problem with this polymer is the low degradation temperature of about 300°C [151]. This will make

densification of Al-doped ZnO/PANI composites difficult. In this case, Spark plasma sintering (SPS) technique could help solve the problem since it is well known for lowering the sintering temperature while achieving high densification.

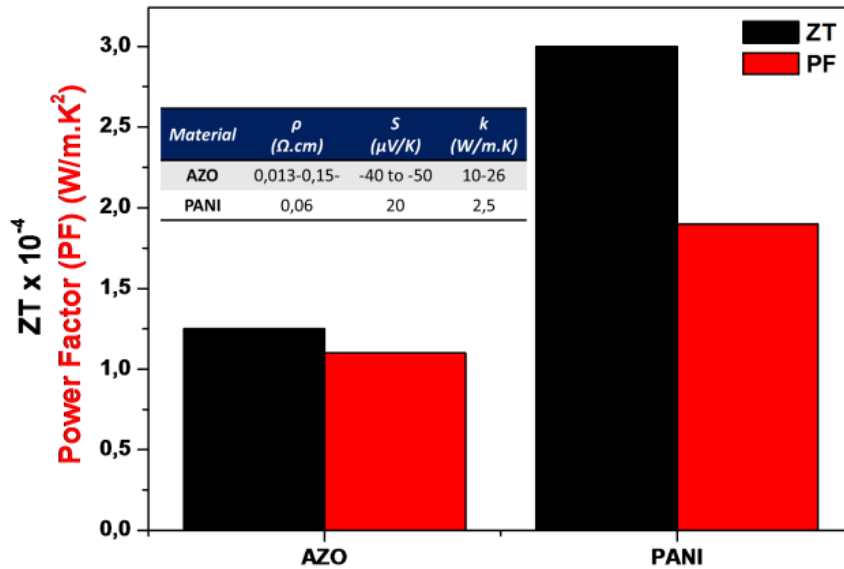


Fig. 1.20 Thermoelectric properties of AZO and PANI at room temperature [177]

1.4.7 Low temperature sintering of ZnO based ceramics

Recent research [116, 118, 179-183] is focusing on the consolidation of ZnO based nanoparticles at low temperatures (less than 400°C) and high pressures (300 to 600 MPa) by adding solvents (such as water, aqueous acetic acid, polymers etc....) to enhance densification. The summary of the low temperature sintered ZnO composites is given in Table 1.4. Dargatz *et al.* [116, 179] were able to get a fully dense ZnO ceramic at 400°C by controlling the heating rates, water content and electric field using SPS. About 99.9% relative density was reported when using 1.6 wt% water, however, anisotropic grain morphology were observed due to diffusion of hydrogen and hydroxide ions into the ZnO crystallite. The sintering mechanism is illustrated in Fig.1.21 [182, 184]; improved densification at such low temperatures is due to the adsorbed water on the surface of the ZnO particles that reduces the inter-particles friction allowing better particle rotation and dissolution of Zn²⁺ and O²⁻ ions on the grain's surface. As a result, the grain boundary area has high defect chemistry that forms high potential. Thus, the activation energy of atomic diffusion becomes reduced leading to full densification at very low temperatures. Gonzalez-Julian *et al.* [180] recently reported the lowest sintering temperature of 250°C using SPS; densification of 97.3% was obtained using aqueous acetic acid that lead to enhanced sintering by pH modification [181, 185].

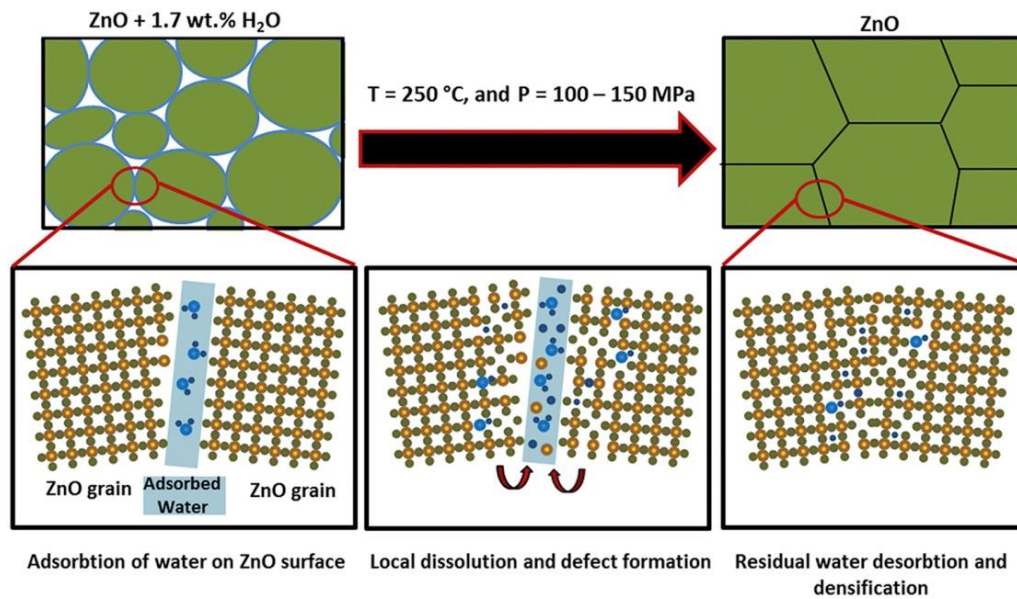


Fig. 1.21 Sintering mechanism of ZnO ceramics sintered with water [184]

Nowadays, most research studies are focusing on the sintering of ceramic-polymer composites as they possess unique properties [186]. Ceramics can be co-sintered with polymers to densifications greater than 90% at temperatures between room temperature to 300°C. Zhao *et al.* [182] lately reported on the cold sintering of ZnO/Polytetrafluoroethylene (PTFE) using hot-press; densification of about 90-95% was obtained sintering at 285°C and 300 MPa. An illustration of the ZnO/polymer sintering mechanism is shown in Fig.1.22. During rearrangement, the PTFE covers the ZnO grains that improves the packing by particle sliding to close pores[187]. Depending on the concentration and the type of second phase/dopant full densification can be attained just by rearrangement. A decrease in the relative density was reported as PTFE concentration was increased from 1 – 40 wt%. Thus, in this work an attempt was made to consolidate Al-doped ZnO ceramics with polyaniline (PANI). PANI decomposes at different stages depending on the moisture content and dopant [188] in the temperature range 400-500°C [188, 189]. Below 400°C, polyaniline glass transitions (T_g) to rubber form, hence, aid with particles rearrangement to obtain a fully dense ceramic.

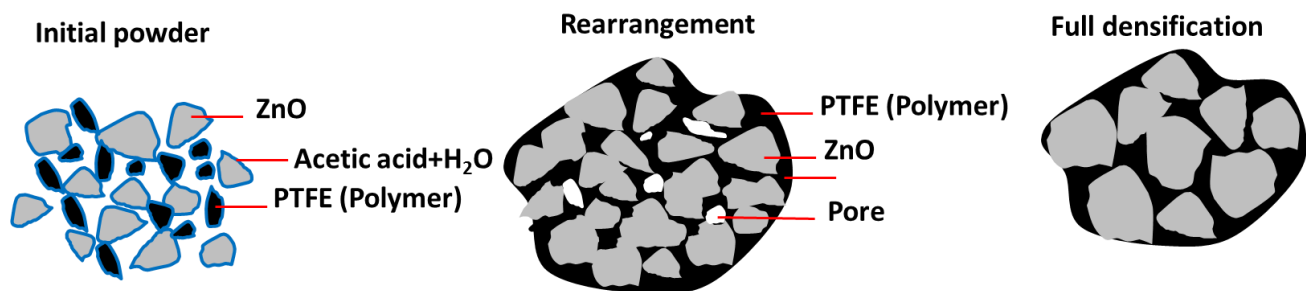


Fig. 1.22 Illustration of ZnO/polymer densification process

Table 1.4 Characteristics of ZnO ceramics sintered below 400°C

Technique	Material	Additive	Sintering conditions	RD (%)	Powder grain size (μm)	Ceramic grain size (μm)	Ref.
Hot press (CSP)	ZnO	1M acetic acid	<300°C, 387 MPa, 1 h	90-98	-	~3	[185]
SPS	ZnO	1.6wt% H ₂ O	250°C, 300 MPa, 5 min	92	-	<0.2	[184]
Hot press (CSP)	ZnO/PTFE	20wt% aqueous acetic acid	285°C, 300 MPa, 1 h	90-95	-	-	[182]
Hot press (CSP)	ZnO/Ti ₃ C ₂ T _x	1.5M acetic acid	<300°C, 250MPa, 1 h	92-98	100-900	1-4	[181]
SPS	ZnO	aqueous acetic acid	250°C, 150 MPa, 5 min	98	-	<0.5	[184]
SPS	ZnO	1.6wt% H ₂ O	400°C, 150 MPa, 10 min	100	-	-	[116]

1.5 Summary

A literature review of thermoelectric principles and properties of different materials has been discussed in detail; the focus was on zinc oxide. The poor ZT in pristine ZnO is as a result of high resistivity and thermal conductivity. Powder quality and sintering techniques play a crucial role in improving the thermoelectric properties of ZnO based ceramics. Nanostructuring is beneficial in reducing the thermal conductivity however has a negative effect on the resistivity which derails the overall performance. Thus far, dual doping of aluminium and gallium has shown high ZT in ZnO ceramics. The interrelated parameters still remains a draw back in improving thermoelectric properties of Al-doped ZnO composites especially between the resistivity and thermal conductivity. The addition of conducting polymers in ZnO composites has shown to simultaneously improve the resistivity and Seebeck Coefficient while the thermal conductivity is kept at a minimal point. Sintering aids and secondary phases could fully densify ZnO composites at temperatures below 400°C.

In this work, focus was on the powder synthesis characteristics of ZnO and the influence of spark plasma sintering parameters (such as temperature, pressure, current insulation, sintering atmosphere and pressure) on densification and thermoelectric performance of ceramics. Performance indicator, ZT, ranging between 4×10^{-4} to 2×10^{-3} could be obtained at 700K by other researchers. The ZnO powder was also doped with Al to improve its electrical properties. The influence of powder synthesis and sintering parameters on thermoelectric properties was evaluated. Thermal conductivity of the Al-doped ZnO ceramics was further reduced by incorporating polyaniline. Sintering below 300°C by using spark plasma sintering technique was investigated. The measurements were done at temperature below the sintering temperature. Polymer/ZnO based ceramics could have ZT of about 0.5 at 500 K. Hence, it was expected that, would be improved ZT as a result of reduced thermal conductivity.

Chapter 2

Experimental Techniques

2. Experimental techniques

This chapter discusses the materials and methods which were used to carry out this research study. The synthesis of the pure and doped ZnO powders using co-precipitation technique followed by calcination is discussed. Spark plasma sintering technique is explained in detail; the parameters which were tested in this study are also indicated. Analytical and electrical property techniques are described.

2.1 Synthesis of pure and Al-doped ZnO powders

Co-precipitation method followed by calcination was used to synthesize pure and Al-doped ZnO particles as it produces high quality powder. Moreover, this technique allows low temperature processing and has high manufacturing yield. The specific route employed in this work was described by Mory *et al.* [190] under the thesis work of Guy [191] at the Centre Inter-Universitaire de recherche et d'ingénierie des matériaux (CIRIMAT). Already there are other published works of using this technique [115]. A schematic illustration of the experimental procedure used for the synthesis of the powders is given in Fig.2.1. High purity chemicals: zinc nitrate hexahydrate ($\text{Zn}(\text{NO}_3)_2 \cdot 6\text{H}_2\text{O}$, 98%) (Sigma-Aldrich), Aluminium nitrate nonahydrate ($\text{Al}(\text{NO}_3)_3 \cdot 9\text{H}_2\text{O}$) (Sigma-Aldrich) and ammonium oxalate monohydrate ($(\text{NH}_4)_2\text{C}_2\text{O}_4 \cdot \text{H}_2\text{O}$, 98%) (Molekula) were used as precursors without any further purification.

For the synthesis of pure ZnO particles, solutions of 4M zinc nitrate hexahydrate, 0.2M and 0.38 M ammonium oxalate monohydrate were separately prepared. At ambient temperature zinc nitrate hexahydrate solution was mixed with 0.2 M ammonium oxalate monohydrate solution to initiate nucleation. At a subsequent time and constant stirring, 0.38 M ammonium oxalate monohydrate solution was added into the mixture to promote particle growth. The final pH was ensured to be between 6.5 and 7 by adjusting with an ammonia solution. A white precipitate was formed which was centrifuged and dried for 22 hrs at 80°C. The dried precipitate was calcined in a furnace to produce ZnO powder. Calcination temperatures ranging between 500°C and 700°C were used to obtain the pure ZnO. The synthesized ZnO powder was compared with commercial zinc oxide (Com-ZnO) of 99.99% purity and <1µm particle size procured from Sigma-Aldrich.

Similar procedure was followed for the Al-doped ZnO powder, aluminium nitrate was mixed with Zinc nitrate at an excess of 10% to ensure final aluminium concentration of 2 mol%. The solubility limit of Al into the ZnO crystal is < 2 mol% and thus far, promising thermoelectric properties have been reported from this concentration [28, 33]. The powder

was calcined using optimum calcination temperature of pure ZnO. Note: All samples were dried at 150°C overnight before sintering.

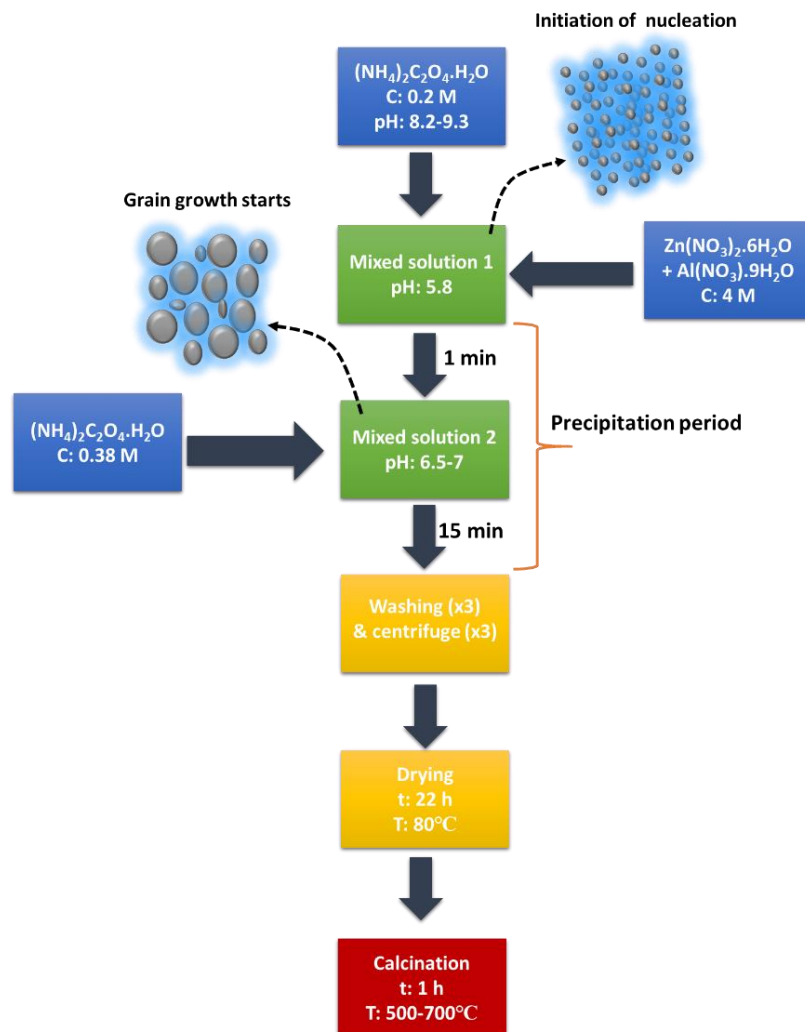


Fig. 2.1 Process block diagram of Al-doped zinc oxide nanoparticles synthesis

2.2 Preparation of polymer doped ZnO based powders

Polyaniline was used as a conducting polymer dopant. It was preferred because it is stable and one of the promising thermoelectric polymer materials. The proposed use of the polymer in this work is to make it as a medium for thermal conductivity reduction by introducing two different vibrational thermal conductance and also to create a conduction path for electrons to improve mobility. Polyaniline emeraldine base with molecular weight of 50000 g/mol was purchased from Sigma-Aldrich. It was converted to a more conducting structure, emeraldine salt, by adding HCl at ratio of 1:4. The mixture was ground in a mortar for an hour, thereafter washed several times to remove excess HCl and dried at 80°C for 15 min. Concentrations of 0.75, 5 and 9 wt% were investigated on the sintering and thermoelectric properties of pure

and Al-doped ZnO ceramics. The ceramic and polymer powders were pre-mixed in a tubular mixer for 15 min and then ballmilled for 4 h 30 min to reduce grain size of polyaniline and to ensure homogeneity.

2.3 Consolidation of ZnO based ceramics

2.3.1 Background on spark plasma sintering equipment

The ZnO based composites were densified with Dr. Sinter 2080 unit (SPS Syntex Inc., Japan) available at the Plateforme Nationale de Frittage Flash (PNF2) located at the Université Toulouse 3 Paul Sabatier (see figure 2.2). The spark plasma sintering equipment is shown in Fig.2.2a; it has a mounted computer to monitor and record sintering processes. The control panel consists of temperature, pressure, gas flow and intensity controllers. Sintering takes place in the SPS chamber; as shown in the enlarged image (see Fig.2.2b). The electrodes charge current through the sample and/or the die (depending on the electrical conductivity of the sample compare to that of the die) and apply axial pressure; whereas the graphite spacers connect the sample to the electrodes through a die. The samples in this work were sintered in an 8 and 20 mm inner diameter tungsten carbide and graphite dies. A schematic diagram of the SPS chamber setup is indicated in Fig.2.3, the cross-section of the die shows the position of the sample and the lining of the mold with 0.2 mm thick graphite foil (PERMA-FOIL®Toyo Tanso). The principle of the spark plasma sintering technique is that sintering occurs through simultaneous application of current and axial pressure on a sample. As shown on the enlarged image of the sample, when electric current is passed through there is spark discharge amongst the grains [192, 193]. In that manner, Joule heating occurs causing mass transport of the grains to form a dense ceramic [106, 107, 192, 193].



Fig. 2.2 SPS equipment: Dr. Sinter 2080 unit (SPS Syntex Inc., Japan)

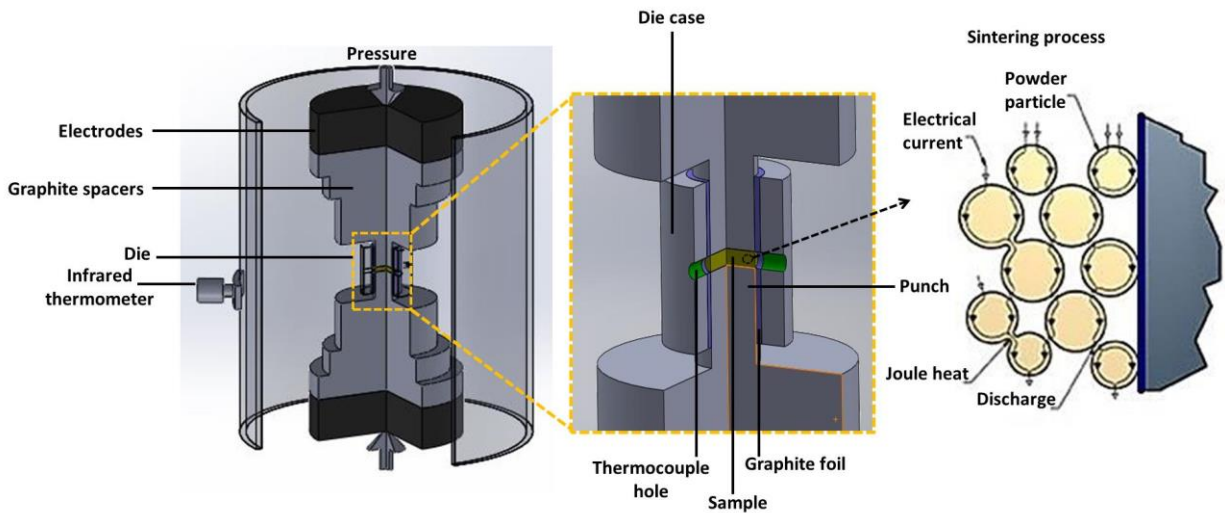


Fig. 2.3 SPS chamber setup and sintering process

2.3.2 Sintering of pure ZnO

Several parameters were varied during the study with the aim to have fully dense pellets with minimal grain growth. The summary of all the parameters altered in this study are given in Table 2.1. Sintering pressure (250-850 MPa), temperature (400 to 700°C), atmosphere (Air and Vacuum), current isolation and sintering cycle were investigated. The sintering cycles (SC) which were compared in this study are shown in Fig.2.4. Sintering cycle 1 (SC1) reported in Fig.2.3 (a; b) was used for all the test work. The cycle in Fig.2.4 (a) was used for 8 mm samples. Uniaxial pressure was applied at room temperature for 2 min followed by temperature increase with a ramp of 100°C/min. The holding time at the temperature setpoint

has been fixed at 6 minutes. The temperature was cooled down to room temperature at a rate of 100°C/min simultaneously with pressure release. For the 20 mm samples the heating rate was reduced to 50°C/min when it approached the temperature setpoint to avoid any overshoot as shown in Fig. 2.4 (b). The other sintering cycle (SC2) in Fig.2.4 (c) entails applying the temperature first and followed by application of axial pressure for 2 min towards the dwell time.

A scheme of the SPS column is illustrated in Fig.2.5. It shows that a part of the total current flows through the sample for “Normal” setup (Fig.2.5 (a)) and “current insulated” using alumina (Fig.2.5 (b)). About 2 g of alumina powder was put on both sides of a sample as shown in Fig. 2.5 (c). It was previously reported that internal current can influence the progress of sintering of ZnO ceramics especially on the grain growth [194, 195].

Table 2.1 Sintering conditions of ZnO and ZnA/PANI ceramics

No.	Temperature (°C)	Pressure (MPa)	Period pressure applied	Holding time (min)	Atmosphere	Insulation	Sintering cycle
Ceramics prepared from commercial ZnO (CCZ)							
1.	400	250-850	RT	6	Air	No	SC1
2.	400-700	250	RT	6	Air	No	SC1
3.	900	100	RT	6	Vacuum	No	SC1
4.	900	100	RT	6	Vacuum	Yes	SC1
5.	900	100	Holding time	6	Vacuum	Yes	SC2
Ceramics prepared from synthetic ZnO (CSZ)							
1.	600-700	250	RT	6	Air	No	SC1
2.	900	100	Holding time	6	Vacuum	Yes	SC2
Zn_{0.98}Al_{0.02}O (ZnA) ceramics							
1.	600-650	250-500	Holding time	6	Air	No	SC2
2.	550-700	250	RT	6	Air	No	SC1
ZnA/PANI ceramics							
1.	150-250	250-500	Holding time, 150°C	10-30	Air	No	-

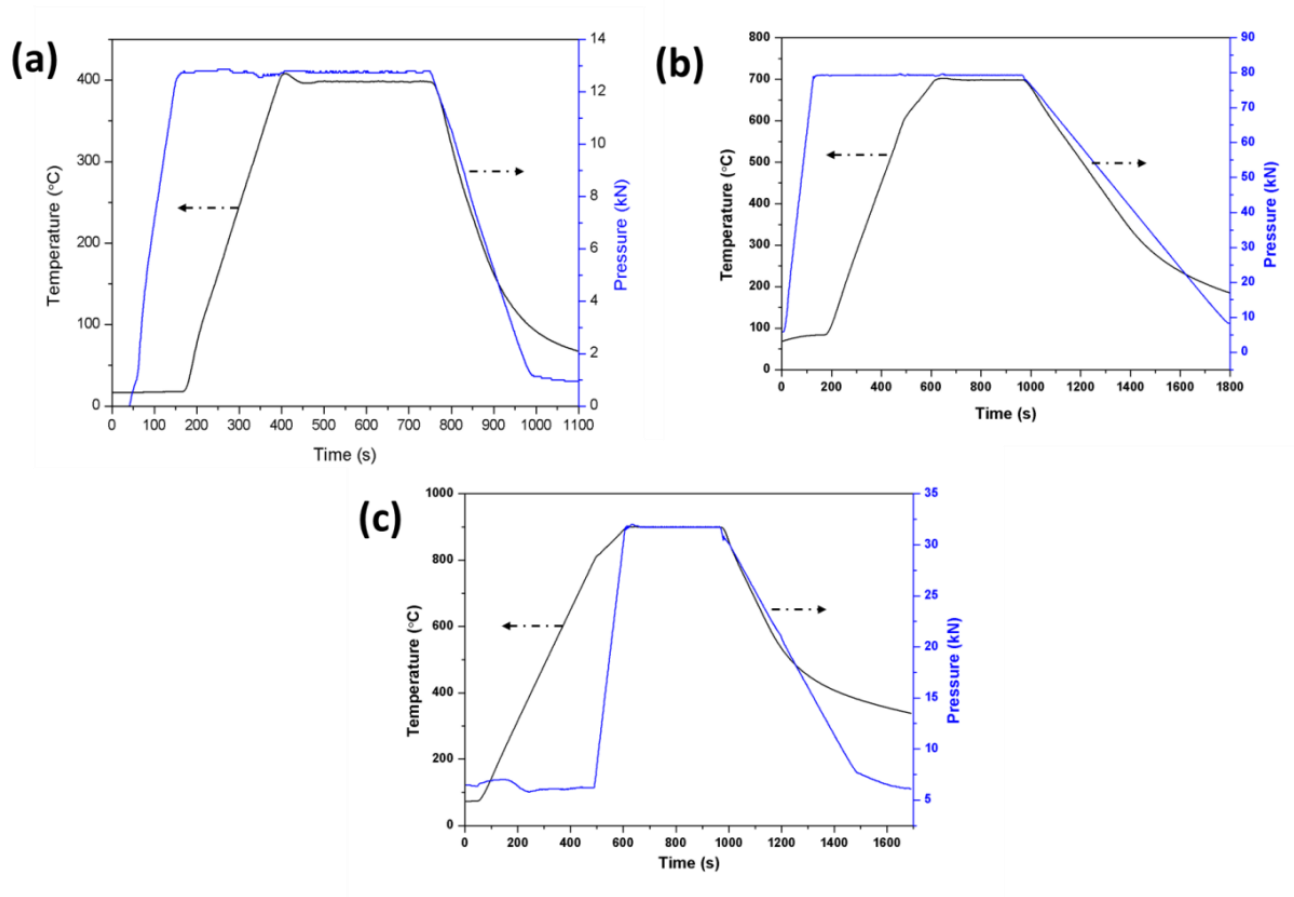


Fig. 2.4 SPS sintering cycles: (a) SC1 for 8mm die (b) SC1 for 20mm and (c) SC2

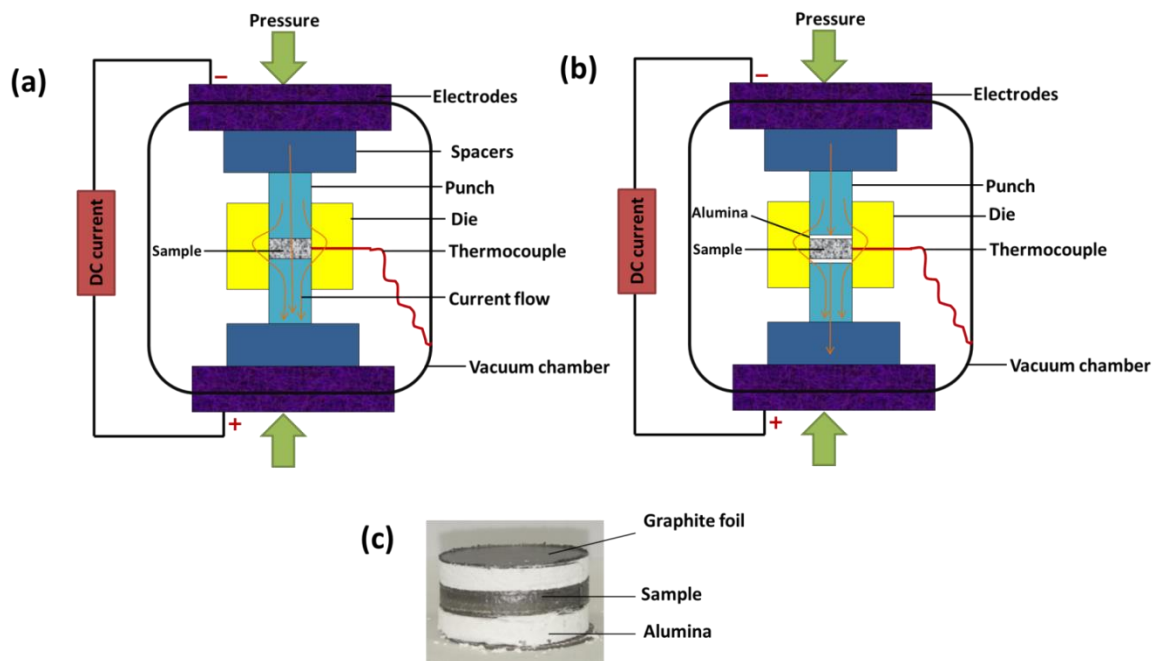


Fig. 2.5 Schematic diagram of the SPS column: (a) Normal setup (b) Current isolation using alumina (c) Sample preparation with alumina

2.3.3 Sintering of aluminium and polyaniline doped ZnO composites

Al-doped ZnO ceramics were pre-compacted at 25 MPa for 1 min thereafter sintered at varying pressure of 250 - 500 MPa and temperatures of between 550 to 700°C to ensure full densification and less concentration of secondary phases in ceramics. Detailed information about the sintering is given in Table 2.1.

The polyaniline doped ZnO and $Zn_{0.98}Al_{0.02}O$ ceramics were sintered firstly heated up to 150°C at a rate of 50°C, then kept there for 10 min to ensure polymer covers grains and thereafter applied pressure of 250 - 500 MPa at the last 2 min of the holding time. While pressing the temperature was increased to final temperature of 250°C using the same heating rate and it was held for 10 - 30 min (Table 2.1).

2.4 Characterization techniques

2.4.1 X-ray diffractometer

X-ray diffractometer (XRD Bruker D4) was used to confirm the phase structure in powder and dense ceramics by using copper cathode as a radiation source ($K\alpha$, wavelength 1.5419Å) at 40 kV and 40 mA. The diffraction patterns were recorded with a precision of 0.01° in the 2θ range of 10 - 80° and step size of 0.02°. EVA software installed with JCPDS crystallographic database was used to identify available phase(s). The background of the diffraction pattern was evaluated to observe peak-positions and intensities. Alumina powder was used to confirm peak shift in the ceramics. Crystallite sizes of < 100 nm were estimated using the Scherrer equation assuming that the grains are spherical (Eq. 2.1) [196].

$$d_{XRD} = \frac{K\lambda}{\beta \cdot \cos\theta} \quad [2.1]$$

Where K is dimensionless shape factor (0.9), λ is wavelength (nm), β is full width of the diffraction peak at half maximum height (FWHM in rads).

2.4.2 Microscopy analysis

2.4.2.1 Scanning electron microscopy

The morphology of the powders and the microstructure of the ceramics were studied by Scanning Electron Microscopy (MEB JEOL JSM65 10LV (CIRIMAT), Field Emission Gun Scanning Electron Microscopy (FEG-SEM, ZEISS SUPRA 55) (CRISMAT)) and SEM Quanta 250 FEI FEG (Faculty of Medicine, Toulouse)). The powders were mounted on carbon tape whereas the fractured sections of the dense ceramics were mounted with carbon paste; silver layer of about 150 - 300 nm was coated on the samples to prevent charge build-

up and to have high resolution images. Focused beam of high-energy electrons operating between 20 – 30 kV was used to generate variety of signals on the surface of the specimens. The signals from the sample-electron interaction revealed information about the sample's morphology, phases and with the aid of Energy dispersive X-ray spectroscopy (EDX) the estimated chemical compositions. Data and images were recorded at a working distance of about 8-10 mm and magnifications between x 1 to x 40 k. Image J software was used to measure the grain sizes. Mendeson stereological factor of 1.56 was used to transform 2D average measured length to 3D average grain size [197].

2.4.2.2 Transmission electron microscopy

Transmission electron microscopy (HT 7700 Hitachi, 120kV) was used to quantify the phase composition of polymer/ZnO ceramics. High energy of 80-100 kV and current of 12 μ m was used. The samples were ground in a mortar and then put on a grid with a film of carbon with a hole. Images were taken at magnification of x 200 – x 200 k.

2.4.3 Particle size and relative density measuring techniques

2.4.3.1 Brunauer–Emmett–Teller technique (BET)

Brunauer–Emmett–Teller technique (BET) (Micromeritics desorb 2300A) was used to determine the specific surface area of the starting powders. The powders were filled in test tubes which were heated up to 200°C while passing helium gas through it. The surface area of the powders was recorded from degassing of the powders with nitrogen. The mass of the powders before and after degassing was also recorded. The grain sizes were estimated from the specific surface area (BET) equation (Eq.2.2) [198]. This method assumes that the grains are spherical without any pores.

$$d_{BET} = \frac{6}{\rho \times S_{BET}} \quad [2.2]$$

Where d_{BET} is the crystallite size (m), ρ is the density of the sample (g/m^3) and S_{BET} is the specific surface area (m^2/g).

2.4.3.2 Mastersizer

The mastersizer (Mastersizer 2000 (CRISMAT) and 3000 (CIRIMAT)) were used to study the particle size distribution of the initial powders. Liquid analysis mode was used. The samples were stirred at the speed of 2500 tr/min.

2.4.3.3 Relative density measurement

The ZnO ceramics were polished by silicon carbide discs (P320 and P600) to remove graphite foil. The density of the ceramics was measured by Archimedes method (Kern, ARJ 220-4M) and the relative density was calculated taking the theoretical density as 5.681g/cm³. For pellets with relative density of < 92%, geometric density was calculated.

2.4.4 Thermal analysis (TGA-DSC)

The thermal behaviours of the powders were studied by Differential Thermal Analysis (DTA) and thermogravimetric analysis (TGA) (Setaram TAG16). Samples with and without polymer were heated at 400 and 1000°C applying heating rates between 3-10°C/min, respectively.

2.4.5 Spectroscopy analysis

2.4.5.1 Inductively coupled plasma-optical/atomic emission spectroscopy (ICP-OES/ICP-AES)

Chemical composition of the powders was obtained by inductively coupled plasma atomic emission spectroscopy (ICP-AES) (Ultima 2-Horiba) and ICP-optical emission spectroscopy (ICP-OES) (JY 2000). The powders were dissolved in an aqueous solution of nitric acid at room temperature, until they were fully dissolved.

2.4.5.2 Fourier Transform-Infrared Spectroscopy (FTIR)

Fourier Transform-Infrared Spectroscopy (FTIR) (Spectrometry Frontier and Microscope Spotlight 400 Series: MIR-NIR) to identify any organic structures in the powders. Ceramic sample were powdered. The recordings were done in the wavelength range of 650–4000 cm⁻¹

2.4.5.3 RAMAN

Raman Spectrometer (JobinYvon LabRAM HR800) was used to identify chemical structures of selected samples. Analysis was done using 633 nm red laser at a grating, accumulation and time of 600 tr, 3 and 30 s, respectively.

2.5 Electrical transport properties

2.5.1 Resistivity and Seebeck Coefficient measurements

Seebeck coefficient and resistivity of the dense ceramics were simultaneously measured using ZEM-3 (Ulvac-Riko, CRISMAT laboratory, Caen). The photography of the equipment is shown in Fig.2.6; the enlarged section shows the setup of the sample which is illustrated in a schematic form in Fig.2.7. The dense ceramics were cut into 9 x 3 x 3 mm bars and coated

with gold to ensure electrical ohmic contact. Graphite foil was inserted on both sides of heaters to have a good electrical and thermal contact with the sample. Seebeck coefficient was determined from $\Delta V/\Delta T$ as discussed in section 1.1 (Chapter 1). The lower heater on the hot side provides differential temperature on the sample. At set temperature T1 and T2, the voltage was measured using the electrodes (Thermocouples). The change in voltage was measured at ΔT of 10, 20 and 30°C; an average value was taken at each set point temperature. Whereas for the resistivity measurements the sample was heated and held at set point temperature. The measurement follows the four point method in which constant current is applied on both ends of the sample to measure voltage drop at T1 and T2 by eliminating thermo-electromotive force. The ceramics with and without polymer were measured at room temperature upto 500°C and 200°C, respectively. The measurement was done in low pressure of helium atmosphere to eliminate oxidation process caused by air.

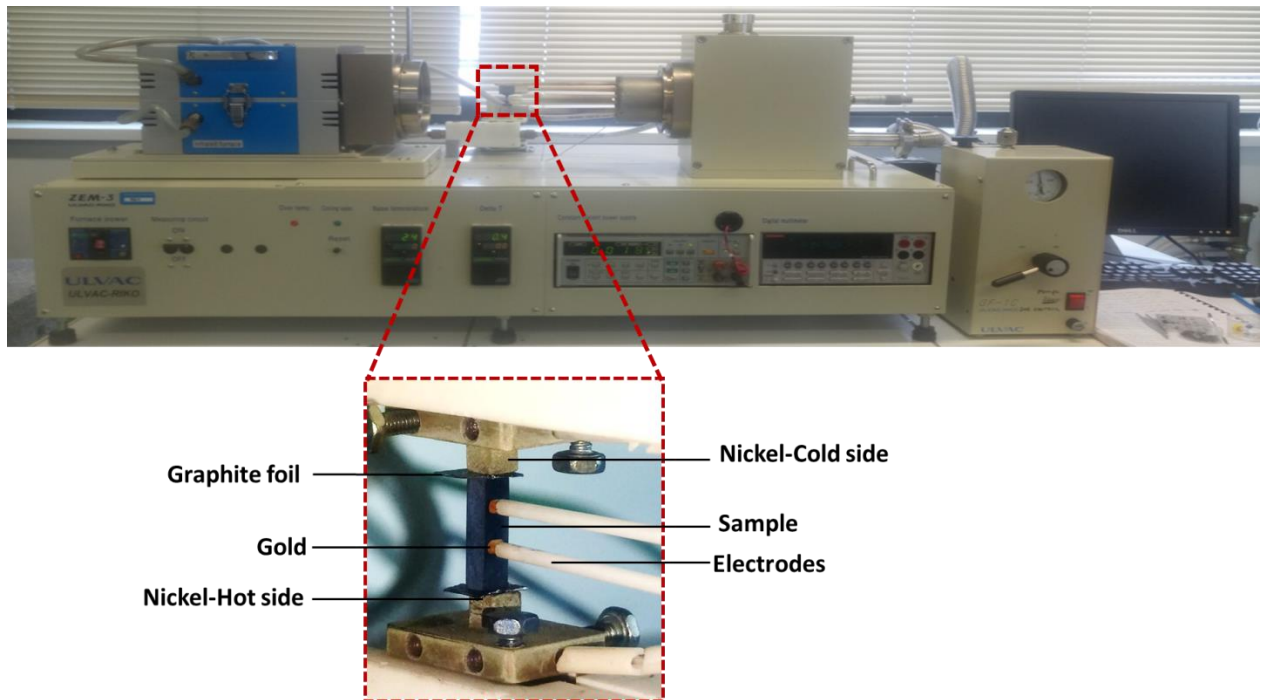


Fig. 2.6 Photo of ZEM-3 (Ulvac-Riko).

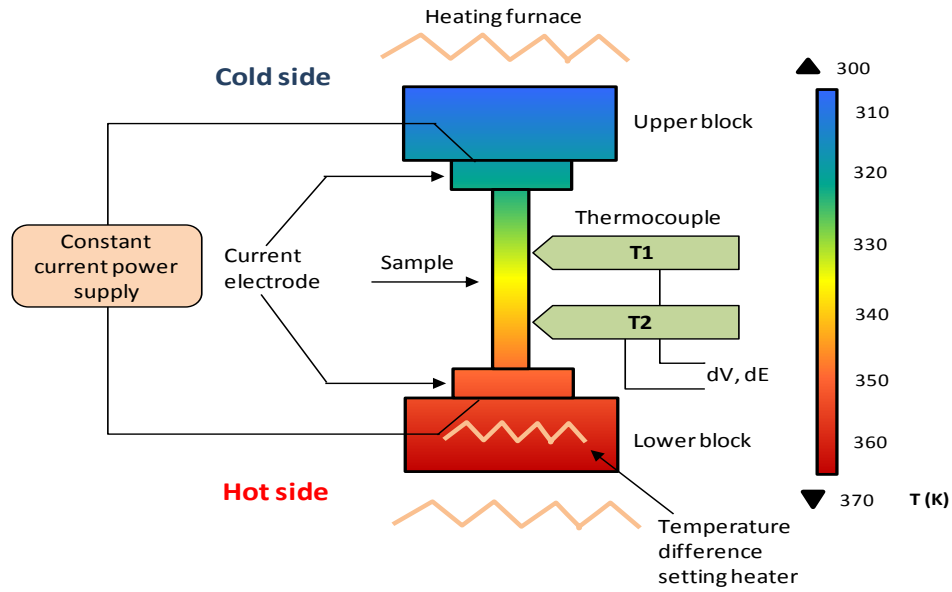


Fig. 2.7 Illustration of measurement section

2.5.2 Thermal conductivity measurement

The thermal conductivity was determined by measuring thermal diffusivity (α), ceramic density (d) (kg/m^3) and heat capacity (C_p) (J/kg) based on the following equation:

$$k = \alpha(T)C_p(T)d(T) \quad [2.3]$$

The diffusivity was measured using laser flash apparatus (LFA 457 Microflash, NETZSCH, CRISMAT), schematic diagram is shown in Fig. 2.8. The samples were cut at dimensions of $6 \times 6 \times 1$ mm; the principle behind the measurement is that the lower surface of the sample is heated by short energy laser pulse which causes a change in temperature at the upper surface of the sample, see enlarged image. This change in temperature is measured by the infrared detector and recorded as a function of time. Thus, the diffusivity is then calculated from sample thickness (x) and half time measurement ($t_{1/2}$)[199]:

$$\alpha = \frac{0.1388x^2}{t_{1/2}} \quad [2.4]$$

The diffusivity of the ceramics with and without polymer were measured at room temperature upto 500°C and 200°C , respectively. White samples (Pure ZnO) were coated with graphite spray to prevent reflection of laser beam.

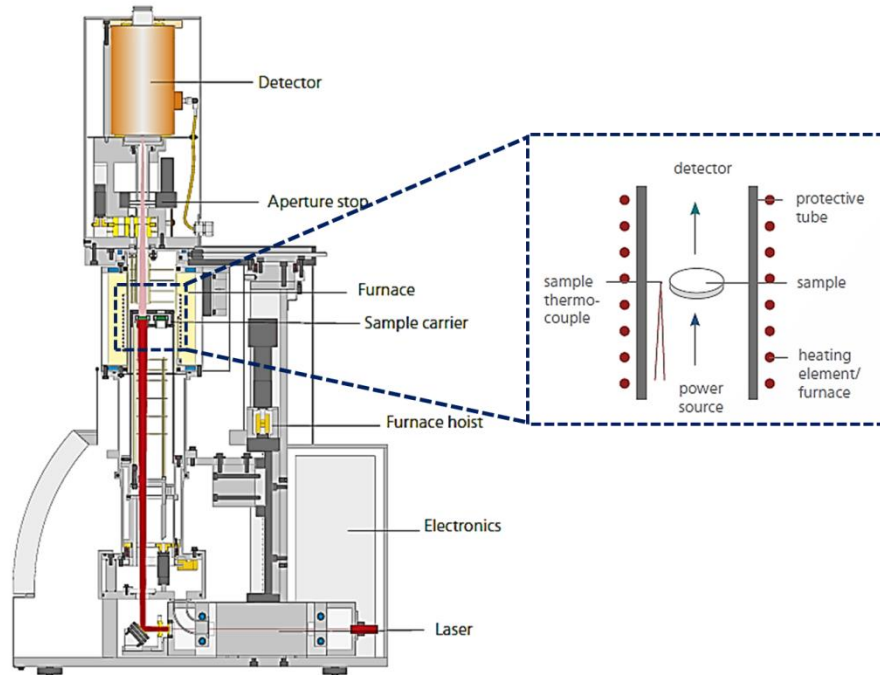


Fig. 2.8 Schematic diagram of LFA 457 MicroFlash (NETZSCH)[199]

The heat capacity was measured using thermal analyser thermogravimetric (TGA) and differential scanning calorimetry (DSC) (STA 449 F3 Jupiter, NETZSCH, CRISMAT). Similarly, ceramics with and without polymer were measured at room temperature upto 500°C and 200°C, respectively. The measurement was done in two steps, first by measuring reference sample sapphire for calibration and then followed by the specimen. For the calibration, sapphire was firstly heated at a rate of 30°C/min upto the setpoint temperature to remove moisture and ensure stability. Then for the measurement a heating rate of 10°C/min was used, firstly by measuring the reference sample followed by the specimen. Change in temperature (ΔT), mass loss (m) and heat flow (Q) were recorded, thus, heat capacity (C_p) was calculated from the heat transfer (Eq. 2.5) [200]. Typical example of C_p measured as a function of temperature is indicated in Appendix A.

$$C_p = \frac{Q}{m\Delta T} \quad [2.5]$$

2.5.3 Hall Effect measurements

Hall effect measurements were done to determine carrier concentration and hall mobility of sintered ceramics. The measurements were done using physical property measurement system (Model 7100 AC transport controller, Quantum system). Resistance was measurement using the Van der Pauw technique at room temperature and applied magnetic field up to 9

tesla. The setup of the sample is indicated in figure Fig. 2.9; the preparation of samples on to a sample holding (Fig. 2.9. (a)) and schematic view of how indium contacts were put on the samples (Fig. 2.9. (a)). To determine carrier concentration (n), resistance was plotted against magnetic field according to Eq. 2.6 [201]:

$$n = -\frac{BI}{xVe} \quad [2.6]$$

Where B is magnetic induction (tesla), I is current (A), x is thickness of sample, V is hall voltage (V) and e is electronic charge.

The hall mobility was calculated using the relationship of resistivity and carrier concentration (see Eq. 1.8); resistivity was determined from ZEM-3 measurement.

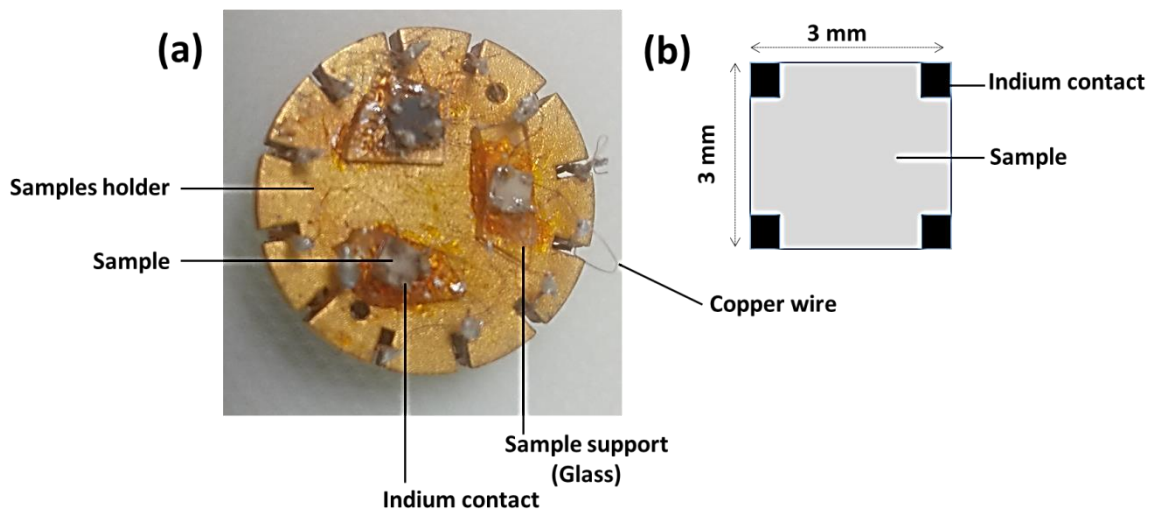


Fig. 2.9 Sample preparation for the physical property measurement: (a) Sample holder (b) arrangement of indium contacts on sample

2.5.4 Band gap measurements

The band gap measurements were done using photovoltaic route using Bentham PVE 300 PV. The equipment is composed of two probe light sources, 75 W Xenon and 100 W Quartz to provide illumination from ultraviolet (UV) to near infrared (NIR) with standard wavelength range of 300 – 1100 nm. Reflectance mode was used for these measurements with ceramics having a diameter and thickness of 2 and 0.5 mm, respectively. The equipment was first calibrated and thereafter measured the first spectrum without a sample to determine

the baseline. Lastly, the spectrums of the samples were analysed. The band gap (E_g) was determined through the Tauc's power law behaviour [202]:

$$2\alpha t = \ln \left[\frac{(R_{max} - R_{min})}{(R - R_{min})} \right] \quad [2.7]$$

Where R_{min} and R_{max} are the maximum and minimum reflectance in the reflection spectra, R is the reflection for any intermediate energy photons, α is absorption coefficient and t is time. For direct band gap, the absorption coefficient is given by:

$$\alpha h\nu = A(h\nu - E_g)^{1/2} \quad [2.8]$$

Where A is a constant which is different for different transitions, $h\nu$ is the energy of photons with frequency ν . From equation 2.7 and 2.8 the proportional relation of $\ln \frac{(R_{max} - R_{min})}{(R - R_{min})}$ and α is evident. In the case of absorption spectra a graph of $(\alpha h\nu)^2$ versus $h\nu$ is plotted, then a strainline is obtained which gives the direct band gap value. Similarly for reflectance, a graph of square of $\ln \left[h\nu \frac{(R_{max} - R_{min})}{(R - R_{min})} \right]$ versus $h\nu$ is plotted. Fig. 2.10 illustrates how the band gap is estimated.

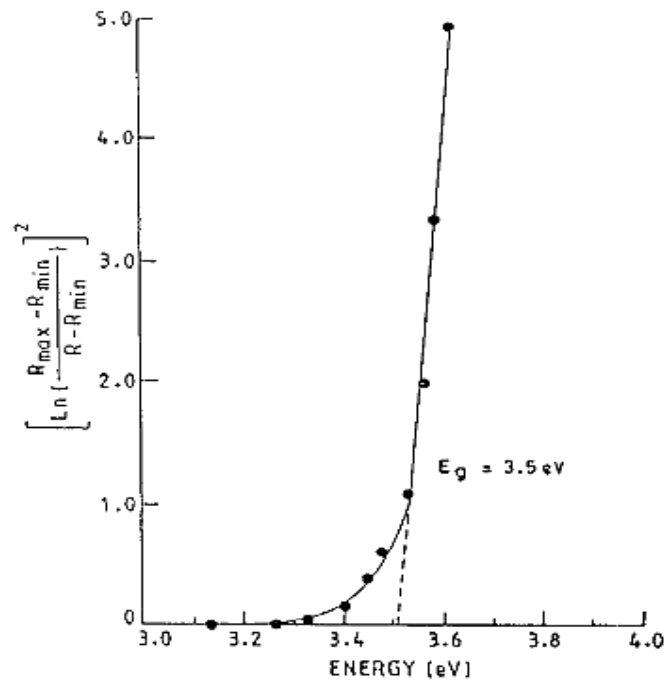


Fig. 2.10. Typical example of direct band gap estimation using ZnS film [202]

Chapter 3

Influence of processing parameters on the densification and the microstructure of pure zinc oxide ceramics prepared by spark plasma sintering

3. Influence of processing parameters on the densification and the microstructure of pure zinc oxide ceramics prepared by spark plasma sintering

3.1 Introduction

Nowadays, the use of ZnO nanoparticles is mostly in modern electro-ceramic applications, because of their large surface areas, unusual adsorptive properties, surface defects and fast diffusivities [203]. As a result, the sintering temperature could be lowered and the properties of materials improved for the small grain size ceramics. For instance, there have been reports about sintering of ZnO nanoparticles at low temperatures, less than 600°C [115-118]. This causes less grain growth which is beneficial for enhancing photocatalytic activity, nonlinear current-voltage characteristics and thermoelectric properties [83, 85, 119].

To obtain optimal properties of ZnO nanoparticles and enhance their applications, it is important to have better control of their crystallinity, particle size and morphology. Since 1990s, there has been an interest in producing specific nanoparticles with unique properties. Their efficiency and specific application highly depend on the particle size distribution and grain morphology of the materials [94, 114]. Moreover, various investigations have been focused on understanding relevant factors and optimizing the processing parameters for large scale synthesis of ZnO powders [204, 205]. Nanopowder synthesis methods such as hydrothermal and chemical precipitation have been used to prepare ZnO nanoparticles [83, 119]. Since hydrothermal technique is energy intensive, most studies have been focussed on chemical precipitation method as it is cost efficient.

One of the most crucial issues with consolidating ceramic nanopowders is obtaining full densification. Extensive studies have been done on the conventional sintering (such as hot pressing, low pressure sintering and hot isostatic sintering [100, 206] of nanopowder materials. Relative density of above 95% is reached at high temperature (800-1200°C) and long sintering periods (>2 h) when using these techniques, which causes grain growth due to diffusion of grain boundaries and Ostwald ripening [101-105]. A lot of work is currently being focused on finding ways to minimize grain growth and improve ceramic properties.

Spark plasma sintering (SPS) is a recent effective sintering technique for consolidating all kind of materials [98]. It uses rapid heating and high thermal efficiency, and as a result, it contributes to full densification of materials within minutes with retained nano/microstructure

[100, 106, 107, 207, 208]. Despite the effectiveness of SPS technology, only few publications are available on SPS of pure ZnO.

Aimable *et al.* [101] reported that 60 nm ZnO particles synthesized through a continuous Segmented Flow Tubular Reactor (SFTR) could not be fully densified by traditional methods, densification of 65% was obtained sintering at 1100°C for 4 h. Whereas, when the SPS was used densification of 99.5% with grain size of $0.2 \pm 0.8 \mu\text{m}$ was obtained at 900°C within 5 min. It is evident that the rapid heating of SPS allows lower sintering temperatures during a short period of time. Further, densification of 95.1% with grain size of $1 \pm 0.5 \mu\text{m}$ was obtained when using 250 nm commercial ZnO particles at SPS conditions of 900°C for 5 min. This indicates the influence of powder quality on the sintering mechanism of ZnO ceramics. Schwarz *et al.* [118] were able to densify nanocrystalline ZnO up to relative density (RD) of 95% at low temperature of 400°C. They also indicated that heating rates affects the sintering behaviour of nano-ZnO ceramics, the higher the heating rate the better the densification kinetics during heating ramp and holding time. Moreover, the recent reports by Virtudazo *et al.* [32] on sintering of nanoporous ZnO highlighted the influence of powder morphology on the sintering mechanism. The ceramics were only densified to 78 - 91% when sintering was performed between 550 - 950°C. Sintering above 750°C resulted in ceramic grain sizes of about 10 μm due to high surface area of the starting powder. Zhang *et al.* [34] sintered micro-nanostructured (hybrid) powders using SPS in which they got less dense ceramic of 84% at a temperature of 900°C, pressure of 50 MPa and holding time of 5 min.

Some recent work [116, 118, 179, 180] focused on the SPS sintering of ZnO nanoparticles at low temperatures (less than 400°C) by adding solvents (such as water, aqueous acetic acid, etc....) to enhance densification. Dargatz *et al.* [116, 179] were able to get a fully dense ZnO ceramic at 400°C by controlling the heating rates, water content and electric field. About 99.9% relative density was reported when using 1.6 wt% water, and morphological anisotropy was observed in the presence of bound water. The diffusion of hydrogen and hydroxide ions into the ZnO crystallite could modify the grain boundary mobility and lead to pronounced grain anisotropy perpendicular to the uniaxial applied load. The improved densification at such low temperatures is due to the adsorbed water on the surface of the ZnO particles that reduces the inter-particles friction allowing better mobility of the particles and dissolution of Zn^{2+} and O^{2-} ions on the grain's surface during sintering. Gonzalez-Julian *et al.* recently reported the lowest sintering temperature of 250°C; and densification of 97.3% was obtained using aqueous acetic acid [180].

Even though highly densified ZnO has been reported at low temperature using sintering aids, it is important to have better understanding on the sintering behaviour of dry and/or undoped ZnO ceramics. There are a few reports which mostly focus on the effect of sintering temperature on the sintering behaviour of newly synthesized powders. In this work, a commercially available ZnO powder was used to perform a systematic study on the densification characteristics and the microstructure of ZnO ceramics using spark plasma sintering technique. The influence of parameters such as temperature, pressure, current insulation, sintering atmosphere and period of pressure application were fully evaluated [209].

3.2 Experimental method and procedure

The commercial ZnO powder was densified using Spark Plasma Sintering, with 8 and 20 mm inner diameter tungsten carbide and graphite dies. The molds were lined with 0.2 mm thick graphite foil (PERMA-FOIL®Toyo Tanso). Several parameters were varied during the study with the aim to get fully dense pellets. These were namely sintering pressure (250 -850 MPa), temperature (400 to 700°C), atmosphere (Air and Vacuum), current isolation, period of pressure application and die geometry (8 and 20 mm), all were investigated with one objective to achieve minimal grain growth.

3.3 Results and discussion

3.3.1 Characterization of the commercial ZnO powder

SEM analysis of the commercial ZnO powder showed irregular morphology of the grains (Fig.3.1 (a)). The grains had elongated and spherical structures due to the low surface energy associated with high polar plane (002).The particle size distribution of the powder is given in Fig.3.1 (b), it showed that majority of the grain sizes ranges between 100 and 250 nm. A mean grain size of 193 nm was determined with a surface area of 5.8 m²/g. The XRD analysis indicated that the powder has characteristic signature of zinc oxide hexagonal wurzite structure (ICPSD No. 01-070-8070, Fig. 3.2). The elemental analysis showed that powder has low concentration of impurities (Al, Mg, K, Ta, S, and P), less than 5ppm.

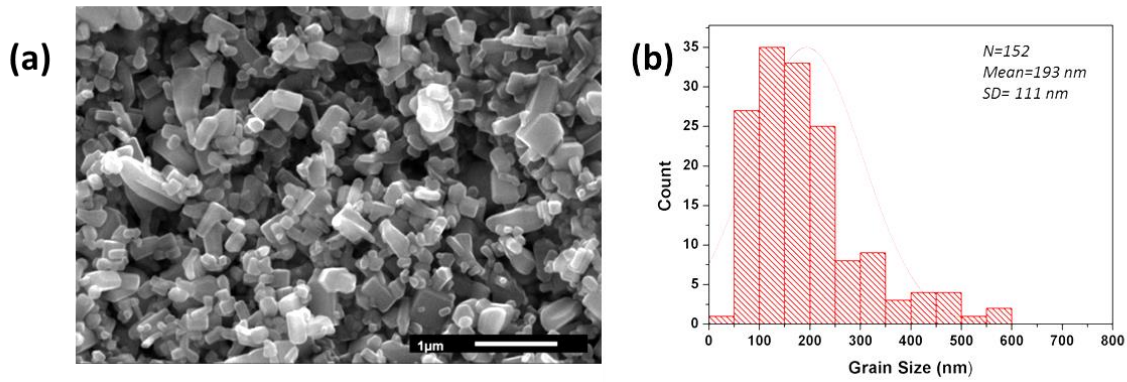


Fig. 3.1 SEM micrograph (a) of commercial zinc oxide powder and corresponding particle size distribution (b)

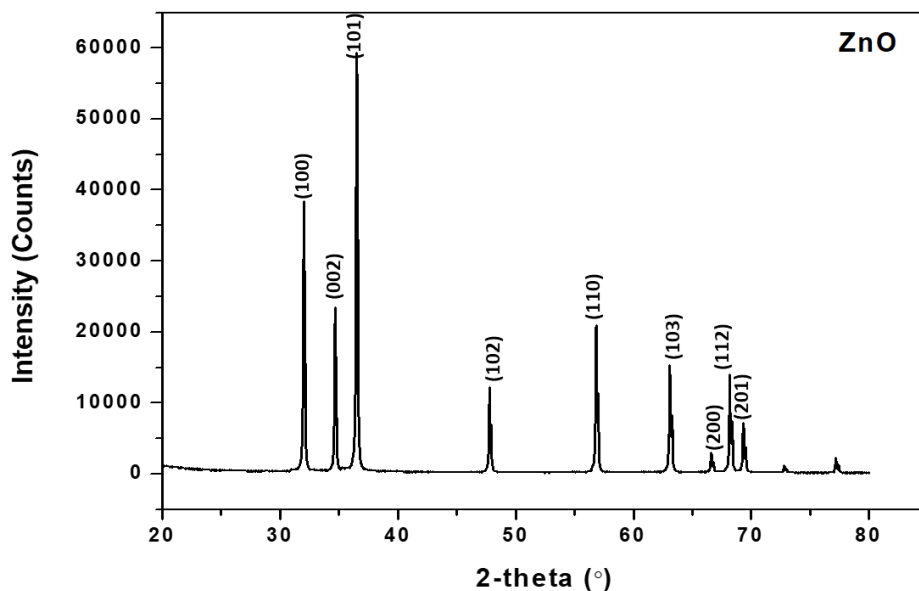


Fig. 3.2 XRD patterns of zinc oxide powder

FTIR spectroscopy has been utilised to identify eventual impurities in the ZnO powders, as shown in Fig.3.3 (a). The spectroscopic analysis indicated that the concentration of nitrates (NO_3) and hydroxides (O-H) after drying reduced from 0.015 to 0.0026 and 0.0125 to \sim 0.001, respectively. Further, a broadband around 3500 cm^{-1} in all the ZnO powders shows characteristic signature of O-H group stretching vibrations [210]. Since, ZnO nanoparticles are known to be good adsorbents for hydrogen [211], this indicates that the powders contained adsorbed moisture. The band around 2600 cm^{-1} corresponds to CO_2 . The small amount of CO_2 could arise from trapped CO_2 in the atmosphere during the FTIR analysis [30]. The two bands at 1440 cm^{-1} and 1553 cm^{-1} confirm the presence of nitrate phase [210,

212]. It is noticed that drying the powder reduces the concentration of organic components. Thermogravimetric analysis of the powder is given in Fig.3.3 (b). It is indicated that whatever the sample, mass loss occurs from room temperature till 1000°C. The total mass loss of the dried powder reduced from 0.49% to 0.26%. In zone 1 the mass loss is attributed to adsorbed moisture. Between 200°C and 300°C, the second zone, was attributed to remaining moisture. Finally, the last zone (3) probably corresponds to the evacuation of organic components, i.e. CO₂ and NO₃ groups. It was observed after 500°C the mass of dried sample becomes constant with temperature whereas the mass of undried sample continues to decrease with an increase in temperature. This implies that the loss of mass (moisture, NO₃, CO₂) was not proportional with the temperature increment for the undried sample, hence, the linear decrease in mass with temperature.

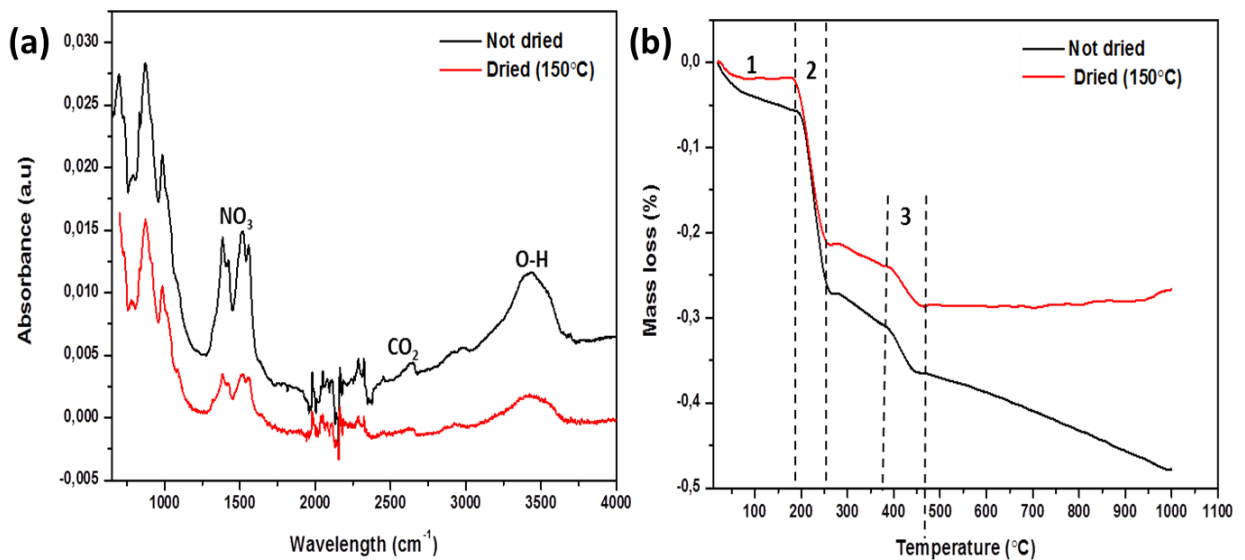


Fig. 3.3 Effect of drying ZnO powder: (a) FTIR and (b) Thermo-gravimetric analysis of commercial ZnO powder

The influence of atmosphere on the thermal behaviour of ZnO has been studied; Fig.3.4 shows the variation of mass as a function of temperature. It was observed that treating the ZnO in air could retain the stoichiometry of ZnO up to 1000°C. However, in vacuum atmosphere a gradual decrease in mass is observed from room temperature up to 800°C. Below 200°C, the mass loss could be due to removal of moisture from powder. Between 200 - 800°C, it could be due to the removal of remaining moisture and evaporation of oxygen to the atmosphere [213]. After 800°C, a sharp drop in mass was observed which could be related to the dissipation of oxygen from the ZnO structure.

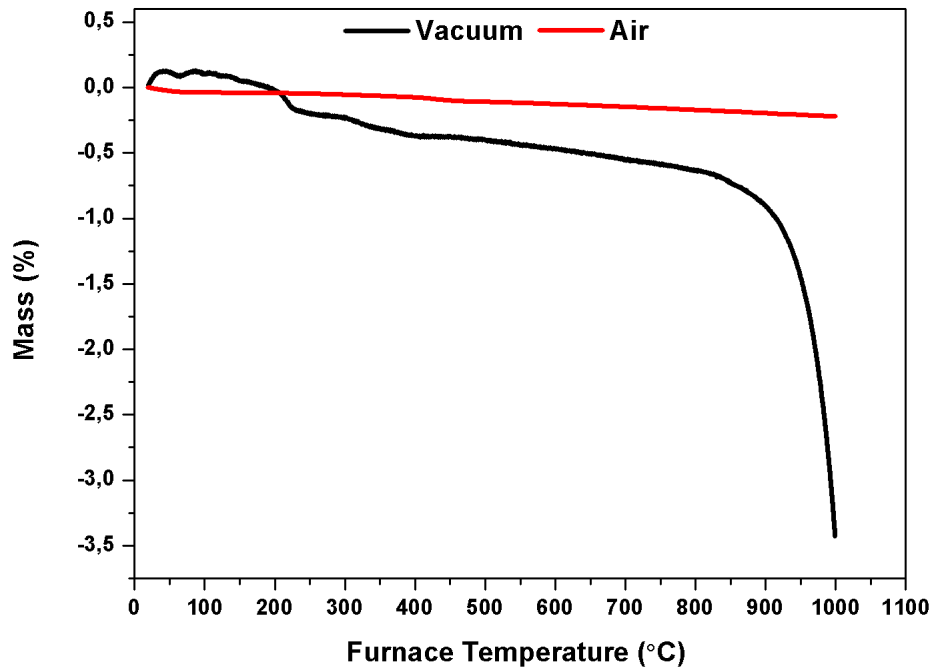


Fig. 3.4 Thermal behaviour of ZnO ceramics in air and vacuum atmospheres

3.3.2 Spark plasma sintering of ZnO ceramics

Spark plasma sintering (SPS) of pure ZnO ceramics was explored with the aim to get fully dense pellets and fine microstructure. The effect of SPS parameters on the relative density and microstructure of ZnO ceramics was extensively explored. A number of parameters were varied which are mentioned above. The summary of the relative density and grain size of the different samples are given in Table 3.1.

Table 3.1 Relative density and grain size of ceramics prepared from commercial ZnO powder for different sintering conditions [Symbols: SC is sintering cycle and RT is room temperature]

Study	Die diameter	Atmosphere	Sintering cycle	Insulation	Temperature	Pressure & when applied	Relative density	Grain size (Image J)
-	mm	-	-	-	°C	MPa	%	µm
Pressure	8	Air	SC1	Without	400	250,RT	76,5±2,2	0,38±0,13
	8	Air	SC1	Without	400	350,RT	76,9±0,7	0,36±0,13
	8	Air	SC1	Without	400	450,RT	85,2±1,2	0,29±0,13
	8	Air	SC1	Without	400	550,RT	85±1,7	0,27±0,13
	8	Air	SC1	Without	400	700,RT	89,7±1,4	0,24±0,13
Temperature	8	Air	SC1	Without	400	850,RT	92,2±1,2	0,22±0,13
	20	Air	SC1	Without	25	250,RT	64,4±2,2	0,20±0,13
	20	Air	SC1	Without	400	250,RT	76,5±2,2	0,4±0,1
	20	Air	SC1	Without	500	250,RT	95,3±0,1	0,5±0,1
	20	Air	SC1	Without	600	250,RT	99,4±0,4	3,3±1,5
Die geometry dimensions	20	Air	SC1	Without	700	250,RT	99,1 ±0,5	5,4±2,1
	8	Air	SC1	Without	700	250,RT	97,8±1,2	5,3±2,3
Sintering atmosphere	20	Vacuum	SC1	Without	700	250,RT	98,8±,9	4,3±1,9
	20	Vacuum	SC1	Without	900	100,RT	97,8±0,5	10,3±3,6
Current isolation	20	Vacuum	SC1	With	900	100,RT	98,0±1,3	5,1±1,8
Application of pressure	20	Vacuum	SC2	With	900	100, Last 2 min of heating stage	98,7±0,4	3,6±1,3

3.3.2.1 Effect of sintering pressure

The effect of sintering pressure on the microstructure and densification of zinc oxide ceramics was investigated using an 8 mm tungsten carbide die. The pressure was varied between 250 – 850 MPa at a fixed temperature of 400°C. It was observed that the relative density gradually increases from 77% to 92% as the sintering pressure is increased from 250 to 850 MPa (Fig.3.5). The improved densification is due the formation of dense nano-grain clusters and their hierarchical growth by rotation and sliding, until the closed pores form [107, 214]. Dargatz *et al.* [116, 179] previously reported on the sintering of pure ZnO at 400°C and 50 MPa in a dry and wet state. Relative densities of 59% and 100% were reported for dry and wet state (1.6 wt% water), respectively. To our knowledge, this is the first report on high relative density of 92% obtained for pure ZnO in a dry state sintered at 850 MPa at temperature as low as 400°C.

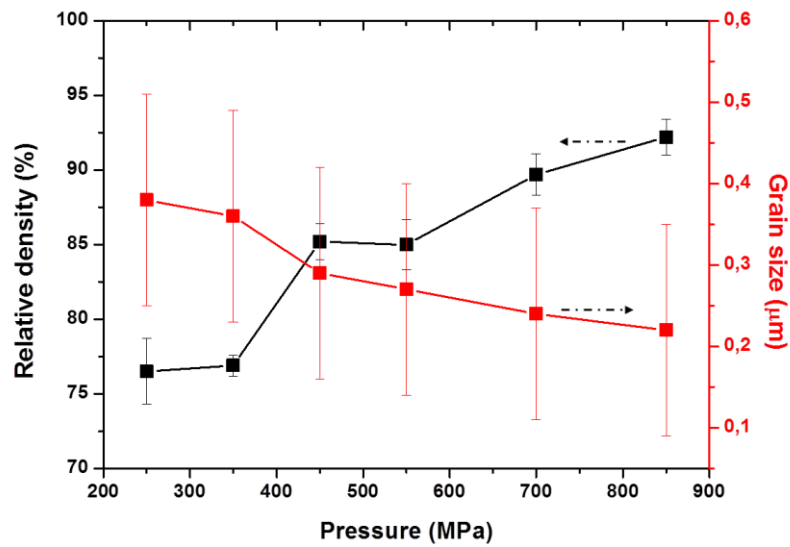


Fig. 3.5 Relative density and grain size as a function of pressure for ceramics prepared from commercial ZnO powder ($T=400^{\circ}\text{C}$)

The dense ceramics were analysed by XRD to confirm the phase structure. The XRD patterns of the sintered ZnO ceramics are given in Fig.3.6; similar characteristic signature as that of as-received powder was obtained, i.e. the wurzite structure. No phase change occurs during sintering within the range of pressure used in this work.

The fracture surface of the samples sintered at various pressures was analysed by SEM (Fig.3.7). Grain sizes determined through image J are given in Fig.3.5. It was observed that at lower pressure of 250 MPa the grain growth is more obvious compared to pressures above 350 MPa. The grains looked more defined. Increasing the sintering pressure up to 850 MPa does not cause much grain growth as quantified by the mean grain sizes (~ 220 nm) in Fig. 3.9. A review by Chaim *et al.* [107] reported on the similar behaviour from cubic zirconia [215] and magnesium aluminate spinel [216, 217]. The increase in the pressure affects the pore closure during densification. Some visible pores confirm that the ceramics are not fully dense. It is the first time reporting on the effect of pressure on pure ZnO sintered by spark plasma sintering technique.

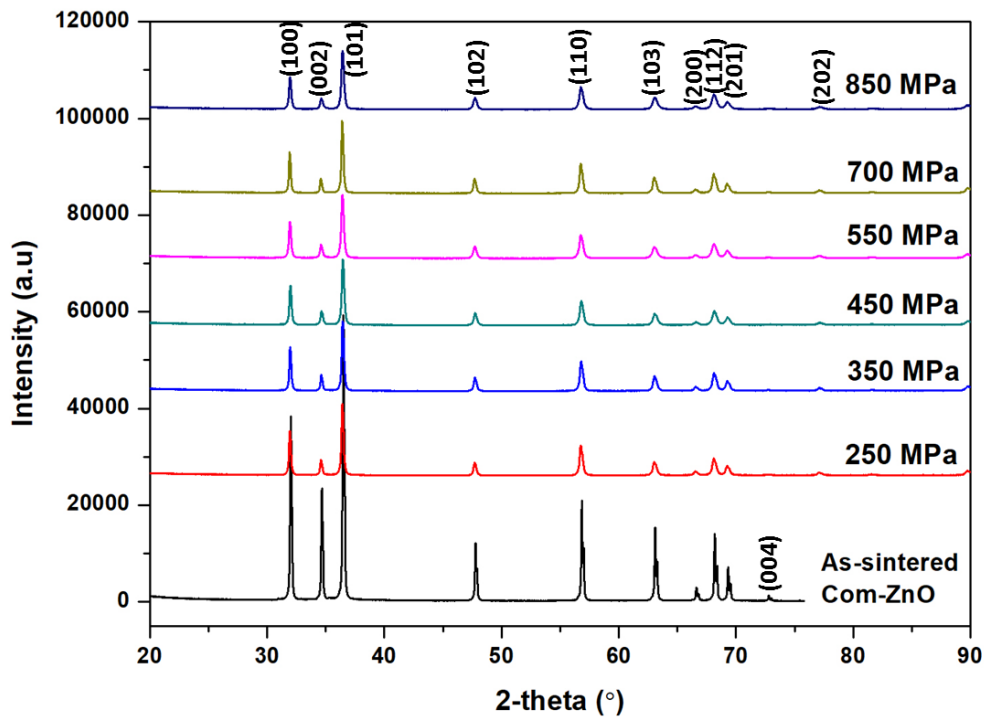


Fig. 3.6 XRD patterns of ZnO ceramics sintered at varying pressure

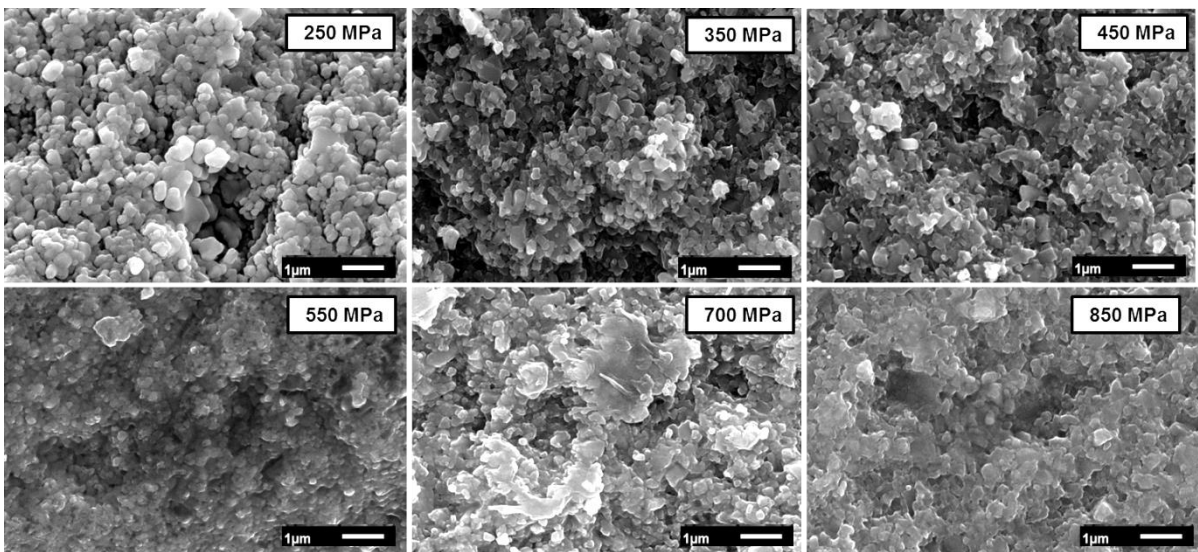


Fig. 3.7 SEM micrograph of fractured surface of ceramics prepared from commercial ZnO powder at various pressures ($T = 400\text{ }^{\circ}\text{C}$)

3.3.2.2 Effect of sintering temperature

The effect of sintering temperature on the densification of ZnO ceramics was studied under air atmosphere, using a 20 mm tungsten carbide die. A sintering pressure of 250 MPa was used to avoid deformation of tungsten carbide die at high temperatures. The relative density is shown in Fig.3.8, as a function of the sintering temperature. With an increase in sintering temperature the relative density of the ceramics was improved from 64% up to $99 \pm 0.4\%$ at temperature as low as 600°C. Between 600°C and 700°C the relative density did not change much, respectively 99.4 and 99.1 %. Gao *et al.* [24] reported a decrease in the relative density of pure ZnO ceramics from 98.5% to 97% when sintering between 550°C to 700°C in vacuum was observed. This could have been caused by the creation of pores due to grain growth [187]. The rate of grain growth relies on the initial powder quality (grain size, porosity); a powder with high specific area would result in faster reaction rates. Hence, it is vital to be cautious about preparation methods of starting powders to control the particle size.

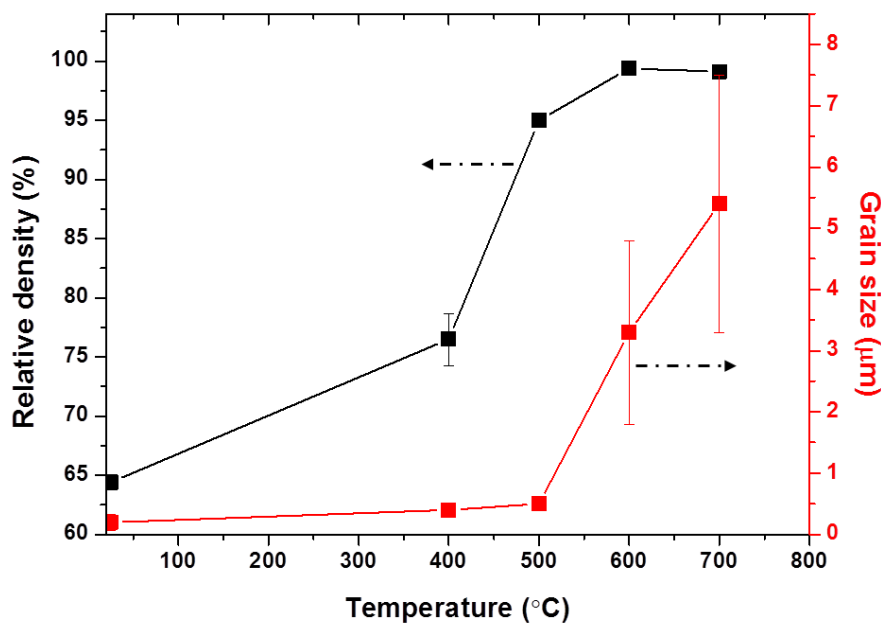


Fig. 3.8 Relative density and grain size of ceramics prepared from commercial ZnO as a function of temperature ($P = 250$ MPa)

The fracture surface micrographs of the ceramics obtained at various temperatures are given in Fig. 3.9. The corresponding grain sizes are given in Fig. 3.8, which were determined by analysis of SEM micrographs (Image J on ~27 particles). There is an increase in the grain size from initial size of 193 nm to 5.5 ± 2.2 µm, when sintering is performed at 700°C, 250 MPa. According to Aimable *et al.* [101] such grain growth is controlled by the diffusion rate

of zinc ions within the crystal structure [14]. Hence, the neighbouring grains diffuse into each other at the grain boundaries causing grain growth during sintering [193]. It is also shown that the grains become more defined and sharper at 600°C and 700°C (Fig.3.9).

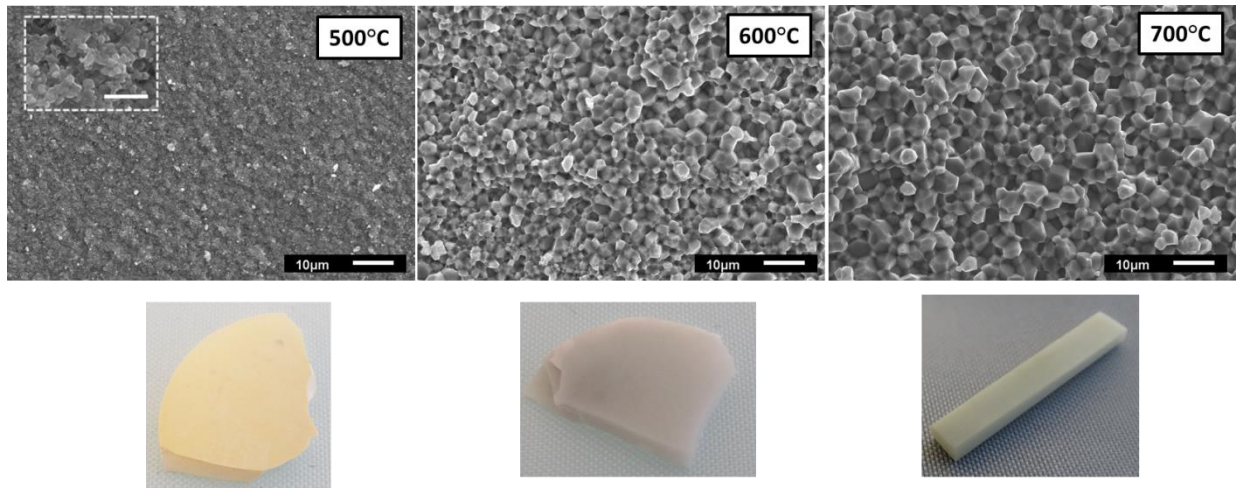


Fig. 3.9 SEM micrographs of fractured surfaces and pictures of as-sintered ceramics showing the effect of sintering temperature

The pictures of the as-sintered ZnO ceramics are given in Fig.3.9. It was noticed that there is a colour change from the initial starting white powder. The ceramics becomes yellow at 500°C, grey at 600°C and grey-whitish at 700°C. The phase structure of the as-sintered is similar to the one of the raw powder. The structure is the wurzite crystal. Han [6] attributed the colour change to oxygen deficiency in dually doped ZnO composites (Al, Cd, Ga, Sc). In the present case, the colour change is due to oxygen deficiency related to the low partial pressure of oxygen at high temperatures.

3.3.2.3 Influence of die diameter

Two tungsten carbide dies presenting different inner diameters (8 mm and 20 mm) were used in order to see if a change in dimensions could affect the microstructure and relative density of ceramics prepared from commercial powder. Sintering at 700°C and 250 MPa (air atmosphere) was chosen to ensure full densification of ZnO ceramics due to the changes in temperature distribution when a different die size is used. The relative density is 97.8% and 99.1% for 8 and 20 mm die diameter, respectively. The SEM micrographs in Fig.3.10 (a) indicated that the grain size distribution for 8 and 20 mm ceramics looks similar (Fig. 3.10 (b)). This implies that temperature distribution of the two dies does not vary much when sintering ZnO ceramics. However, electro-thermal simulations on alumina sample by finite element modelling on 10 and 20 mm inner diameter graphite dies have shown, a difference of

about 100°C for the same set point fixed at the surface of the tool [218]. Thus, densification characteristics rely on the sintered material, type and diameter of die. In this study, the change of die diameter from 8 to 20 mm does not significantly influences the densification of pure ZnO, not the grain size.

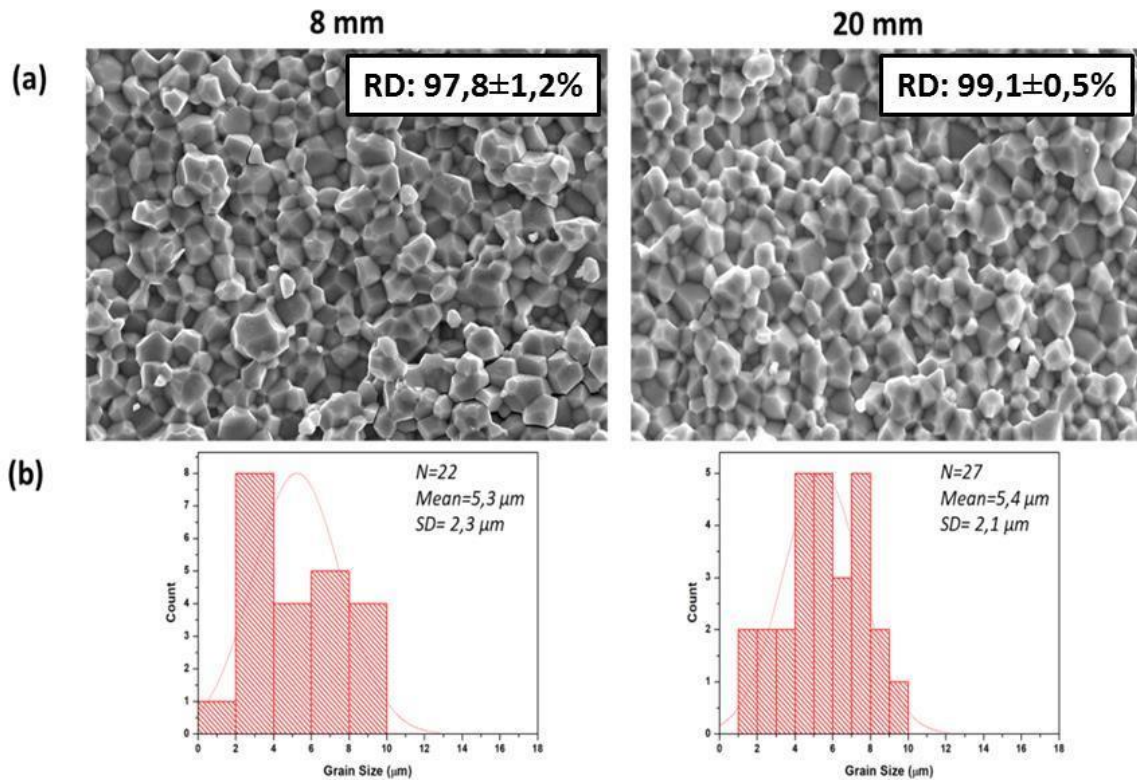


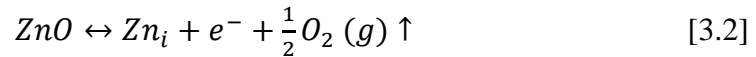
Fig. 3.10 (a) SEM micrograph of fractured surfaces (b) grain size distribution of ceramics prepared from commercial ZnO powder for 8 mm and 20 mm die

3.3.2.4 Influence of sintering atmosphere

The influence of sintering atmosphere on the relative density and grain size of ZnO ceramics was studied using 20 mm die. Since ZnO is easily reduced, the oxygen partial pressure plays a huge role on the densification of ZnO ceramics. Two different sintering atmospheres: air and vacuum were used to sinter commercial ZnO powder. These will allow changing the oxygen stoichiometry of ZnO ceramics and to evaluate its effects on the morphology and relative density. The summary of the samples characteristics for different atmospheres are given in Table 3.1. A relative density of 98.7% and 98.8% is obtained when operating in air and vacuum; respectively (700°C and 250 MPa). The SEM micrographs are given in Fig.3.13; there is only a small difference of roughly 1.7 μm between the grain sizes of the ceramics (Fig.3.11 (b)). Hence, the morphology and relative density are not affected when the

sintering is performed in air or vacuum at 700°C and 250 MPa.

For further comparison, the temperature was increased to 900°C in order to get a more oxygen deficient ceramic. In oxygen deficient environment, the first stages of densification of ZnO is controlled by the diffusion of oxygen atoms which can be easily influenced by the external oxygen partial pressure [219, 220]. In that manner, more zinc interstitials are created as shown in the general reduction oxidation reaction:



The relative density slightly decreased to 97.8% when the temperature was increased to 900°C. Previous studies on the conventional sintering of pure ZnO ceramics indicated that higher densification was obtained in oxygen rich atmosphere than in air [104, 221]. Thus, sintering occurs by means of oxidation of the excess zinc ions. The SEM micrograph is given in Fig.3.12 (un-insulated: 900°C); the grain size increases as the temperature increases: from 5.3 μm (700°C) to 10.3 μm (900°C). The inserted image showed that there are pores in the ceramic sintered at 900°C which could have been caused by grain growth [187]. This justifies the decrease in the relative density. It was also observed that the grains have some pits on them which could be due to the evaporation of ZnO above 900°C.

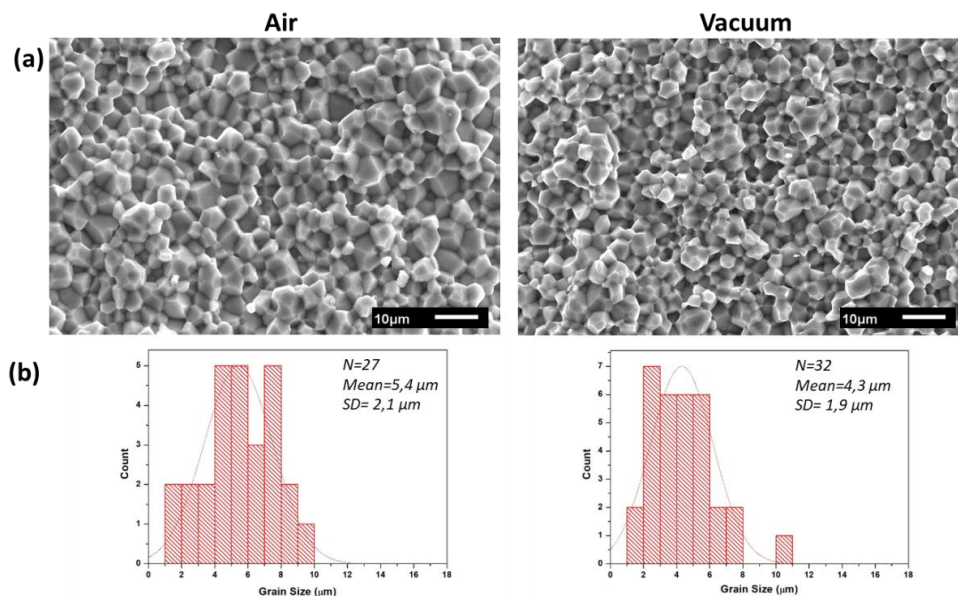


Fig. 3.11 (a) SEM micrograph of fractured surfaces (b) grain size distribution (Image J) of ceramics prepared from ZnO powder (700°C - 250 MPa)

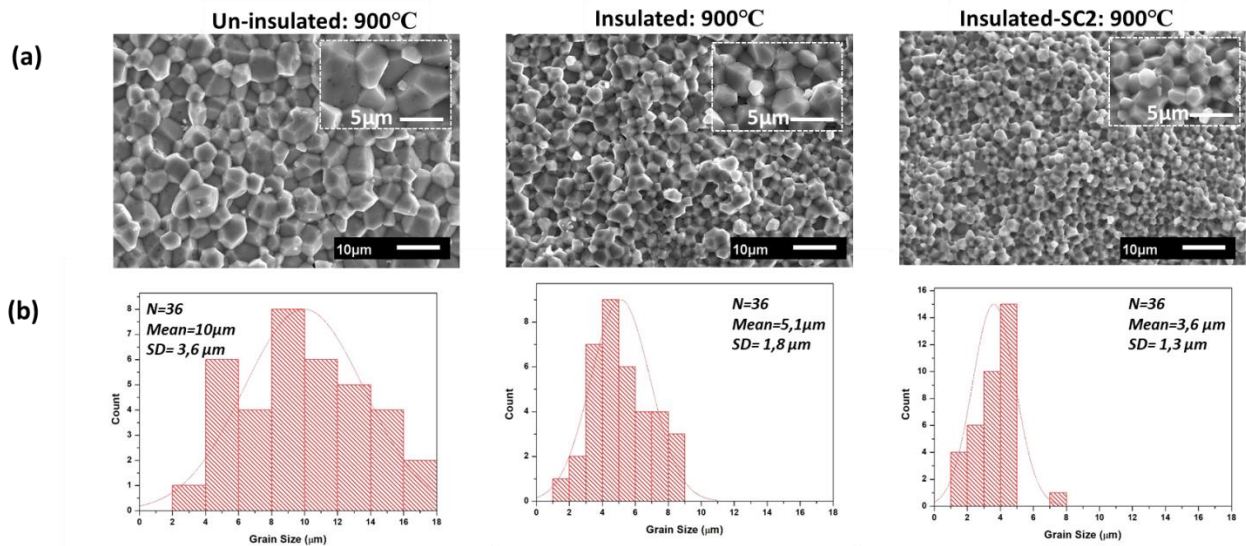


Fig. 3.12 (a) SEM micrograph of fractured surfaces (b) grain size distribution (Image J) of ceramics prepared from ZnO powder (900°C - 100 MPa)

3.3.2.5 Influence of current isolation

The effect of current on ZnO ceramics was investigated for sintering treatment performed at 900°C in vacuum. The relative density of pure ZnO ceramics with and without current is given in Table 3.1. Whatever the current condition, the relative density does not change respectively, 97.8% (without) and 98% (with). The SEM micrographs are given in Fig.3.12 (un-insulated: 900°C and insulated: 900°C). There is a decrease in the grain size to 5 μm when the sintering is done without current passing through the sample: contrary to the average value of 10.3 μm for the “un-insulated cycle”. The grain growth in the normal setup could have been contributed by Joule heating [194, 222]. While for insulated one the densification took place by heat radiation from the die surface. Retainment in the microstructure with visible grain boundaries was previously reported on sintering pure ZnO ceramic with current isolation [194]. While a ceramic sintered with current passing through did not show any grain boundaries i.e. neighbouring grains diffused into each other following the grain boundary diffusion mechanism [118]. This supports the observed results in this work.

3.3.2.6 Influence of period of pressure application

The effect of the period at which pressure is applied during sintering was investigated on the relative density and morphology of pure ZnO ceramics prepared from commercial powder. Two conditions were compared: pressure applied at room temperature (SC1) and the last two minutes of heating stage (SC2). The sample was sintered in vacuum with current isolation at

a sintering temperature and pressure of 900°C and 100 MPa, respectively. The relative density of the ceramics is given in Table 3.1. The relative density slightly improved from 98% (SC1) to 99% (SC2). The slight improvement in densification is due to easier particle sliding or rotation when the pressure is applied at high temperature [107, 192]. The SEM micrograph of the ZnO ceramics is given in Fig.3.12. The grain size decreased when SC2 was used. Moreover, the grain size distribution is smaller. An average grain size of 3.6 µm was obtained which is lesser than SC1 by 2.4 µm. This could have been caused by the difference in heat transfer between the grains; SC1 had better contact as compared to SC2.

3.3.2.7 Summary of SPS parameters influence on pure ZnO ceramics

The overall view of the influence of SPS parameters on the relative density and grain size of pure ZnO ceramics is given in Fig.3.13. High pressure sintering is desirable for maintaining the nanostructure, though the difficulty of obtaining a fully dense ceramic. Whereas, increasing the temperature from 600 - 900°C results in fully densified ceramics of about 99% which shows to have big impact on the grain size. Sintering of pure ZnO without insulation at 900°C causes bigger grains with size of about 10 µm. The application of pressure during the holding time seems to lower the grain size as compared to ceramics pressed during initial stage (RT). This figure could play as a guide towards sintering of pure ZnO depending on the properties required for the final product.

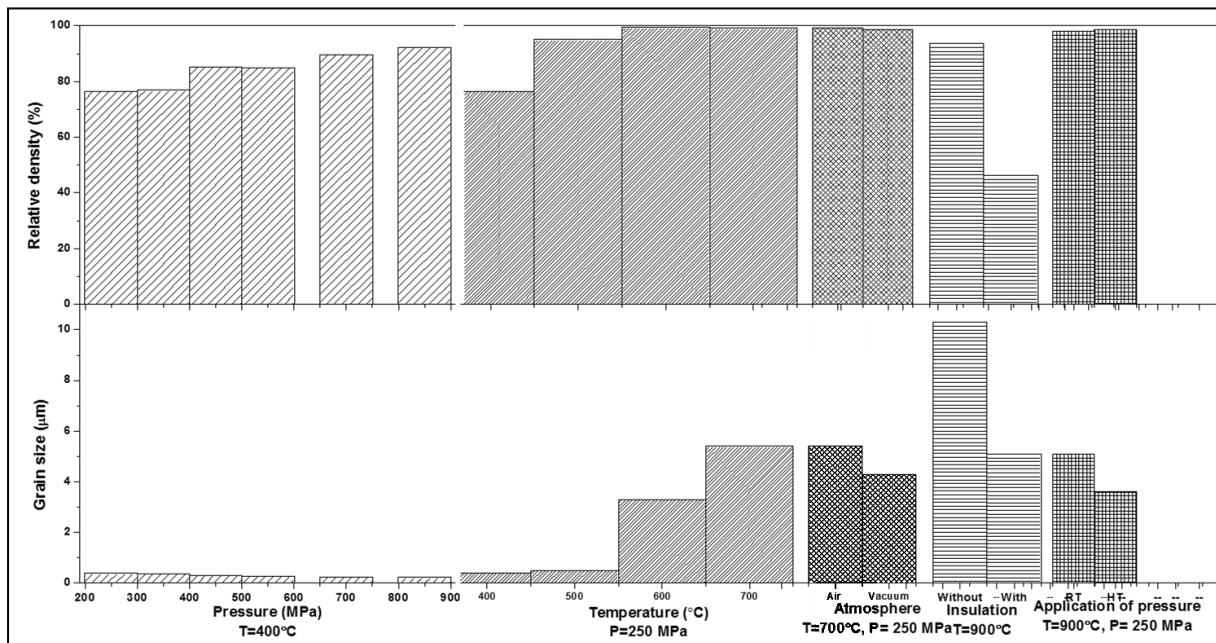


Fig. 3.13 Influence of SPS parameters on the densification and grain size of ZnO ceramics
(Note: RT is room temperature and HT is holding temperature)

3.4 Conclusions

The influence of processing parameters on the densification and the microstructure of pure zinc oxide ceramics prepared by spark plasma sintering was performed in this work. Increasing the pressure improves the relative density of ZnO ceramics due to particle rotation. A maximum relative density of 92% was obtained at a temperature as low as 400°C for an applied pressure of 850 MPa. In this case the grain size is 220 ± 0.1 nm. The increment of temperature up to 600°C with a lower pressure, 250 MPa, lead to a significant increase of the relative density and grain size, respectively 99.4% and 3.3 μm .

The sintering atmospheres (air and vacuum) did not affect the densification and microstructure of ZnO ceramics. The impact of the electric current during sintering has been evaluated through experiments performed with or without insulation. There is no change in relative density but a grain size difference of 7.8 μm was obtained for the two conditions.

This study could provide a guide for controlling the densification and the grain size of ZnO ceramics obtained by spark plasma sintering of dried powders.

Chapter 4

Thermoelectric properties of ZnO ceramics densified through spark plasma sintering

4. Thermoelectric properties of ZnO ceramics densified through spark plasma sintering

4.1 Introduction

The previous chapter (Chapter 3) focused on the influences of SPS parameters on the densification of pure ZnO ceramics. A guide for controlling densification and grain size of pure ZnO was determined, which will be beneficial when optimizing thermoelectric properties. Extensive research on ZnO ceramics has been performed on single or double doping with group 3 elements and transition metals [10, 32, 44, 95, 108, 109, 111, 112]. However, there is limited literature that focuses on the thermoelectric properties of pure (intrinsic) ZnO ceramics. The performance of ZnO relies mostly on the concentration of oxygen vacancies [223]. Therefore, it is vital to have better understanding of the electrical properties of intrinsic ZnO. Other methods which have been conducted to improve thermoelectric properties of ZnO ceramics is applying nanostructuring of the material [23, 26]. This method reduces thermal conductivity through phonon scattering at the grain boundaries. The advancements in sintering techniques from conventional pressing to spark plasma sintering have added huge value on the control of grain growth enabling more flexibility in material structuring or modifications. However, some reports have indicated that even though reducing the grain size could assist in lowering the thermal conductivity, it can also lower the electrical conductivity due to the scattering of electrons, and the latter is undesirable [23].

This chapter narrates the work done on the preparation method for ZnO powder and compares its characteristics with those of commercial powder. Microstructural studies of the sintered ceramics at various sintering conditions were also investigated. The thermoelectric properties of the ZnO ceramics were discussed for both as-sintered and annealed in air to have better understanding on the effect of oxygen vacancies.

4.2 Materials and methods

4.2.1 Synthesis of ZnO particles

Co-precipitation method followed by calcination treatment was used to synthesize ZnO powders because it produces high quality powders. Moreover this technique allows low temperature processing and has high manufacturing yield. The synthesis procedure was taken from the previous work of Guy [191] and Beynet *et al.* [115]. High purity chemicals: zinc nitrate hexahydrate ($\text{Zn}(\text{NO}_3)_2 \cdot 6\text{H}_2\text{O}$, 98%) (Sigma-Aldrich) and ammonium oxalate

monohydrate ((NH₄)₂C₂O₄.H₂O, 98%) (Molekula) were used as precursors without any further purification. A detailed experimental procedure is presented in chapter 2. Solutions of 4 M zinc nitrate hexahydrate and 0.2 M and 0.38 M ammonium oxalate monohydrate were prepared separately. At ambient temperature the solutions were mixed at subsequent time and constantly stirred. By adjusting with an ammonia solution, caution was observed to ensure that the final pH was between 6.5 and 7. A white precipitate was formed which was centrifuged and dried for 22 hrs at 80°C. The dried precipitate was calcined in a furnace in the temperature range between 500°C and 700°C to obtain the starting ZnO powder. The characteristics of the synthesized ZnO powder was compared with those of commercial available zinc oxide (Com-ZnO) of high purity (99.99%) and submicronic particle size procured from Sigma-Aldrich.

4.2.2 Densification of ZnO by Spark plasma sintering (SPS)

The commercial and synthesized ZnO powders were densified using SPS already described in chapters 2 and 3 using 8 and 20 mm inner diameter tungsten carbide and graphite dies (respectively). The moulds were lined with 0.2 mm thick graphite foil (PERMA-FOIL®Toyo Tanso). Two sintering parameters i.e. temperature (600-700) and atmosphere (air and vacuum) were investigated with the aim to produce fully dense pellets with minimal grain growth. Samples sintered in vacuum were current isolated to avoid the influences of electric field on the ZnO grains; which can affect the reactivity and diffusion during sintering [194, 195].

The uniaxial pressure of up to 250 MPa was applied at room temperature for the samples sintered at 700°C, using tungsten carbide tool for 2 min. On the other hand, the conventional graphite mould was been used under vacuum. The pressure of 100 MPa was applied for samples sintering at 900°C during the last 2 min of heating stage to improve mobility of grains. The temperature increase was achieved at ramp rate of 100°C/min, though for samples sintered at 900°C the ramp rate was reduced by 50% on the last 2 min of heating stage to avoid temperature overshoot. The isothermal time was kept for 6 min. The temperature was reduced at a rate of 100°C/min simultaneously with pressure release.

4.2.3 Electrical measurements

Seebeck coefficient and resistivity of the dense ceramics were simultaneously measured using ZEM-3 (Ulvac-Riko, CRISMAT). The dense ceramics were cut into 9x3x3 mm bars and coated with gold to ensure electrical ohmic contact. Graphite foil was inserted on both sides of heaters to have a good electrical and thermal contact with the sample. The thermal

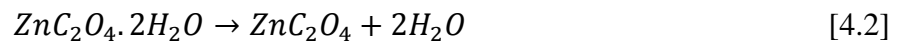
conductivity was determined by measuring separately thermal diffusivity (α), ceramic density (d) and heat capacity (C_p). And for these measurements the samples were cut to dimensions of 6x6x1 mm. The thermal conductivity was then calculated using Eq. 4.1. The band gap was determined through the photovoltaic route using Bentham PVE 300 PV.

$$k = \alpha(T)C_p(T)d(T) \quad [4.1]$$

4.3 Results and discussion

4.3.1 Characterization of synthetic zinc oxide powders

The precipitate from the co-precipitation synthesis was analysed by X-ray diffraction (XRD), Scanning electron microscopy (SEM) and thermo-analyser. The XRD results given in Fig.4.1 (a) showed that the phase structure is monoclinic zinc oxalate hydrate (ICSD No. 00-025-1029) following the given Miller indices. The SEM observations indicate that the grains of the zinc oxalate hydrate have platelet-like structures stacked on each other (Fig.4.1 (b)). Thermogravimetric analysis of the zinc oxalate hydrate (Fig.4.2) indicated that under thermal treatment the oxalate goes through two decomposition reactions respectively at 150 and 400°C. The decrease in mass at 150°C associated with an endothermic peak could be due to removal of water adsorbed at the grain's surface (Eq.4.2). The drop at 400°C associated with an exothermic peak, could result from the decomposition of organic components to form zinc oxide. These observations are in agreement with previously reported results (Eq.4.3) [191, 224, 225].



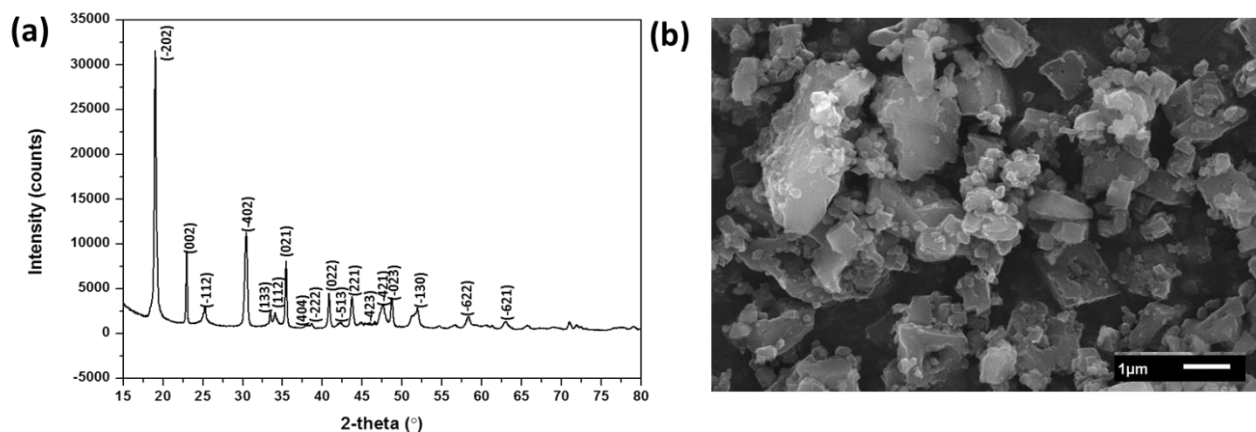


Fig. 4.1 Characterization of the precipitate (a) XRD patterns and (b) SEM micrographs of zinc oxalate hydrate

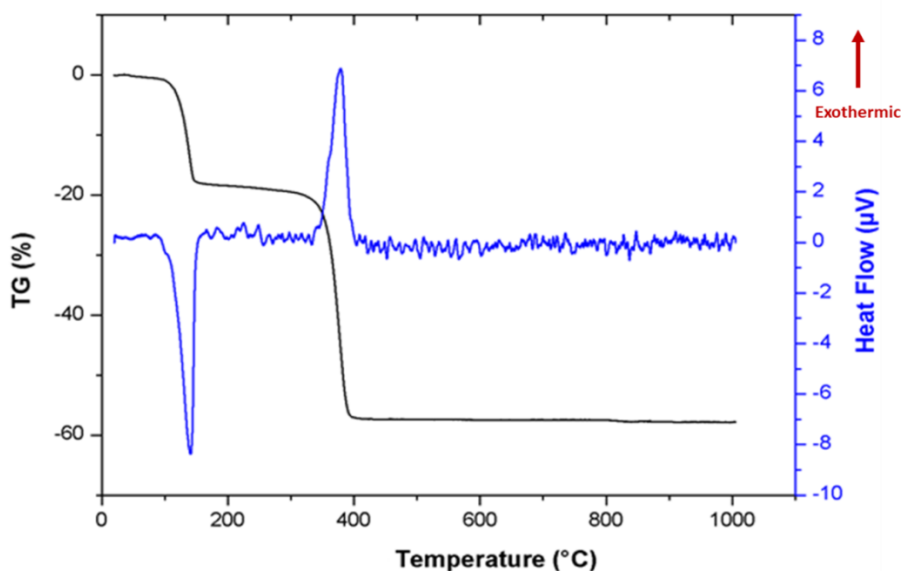


Fig. 4.2 Differential Thermal and Thermogravimetric Analysis of zinc oxalate hydrate.

Based on the TGA results, the precipitate was further calcined at temperatures between 500°C to 700°C to get ZnO phase. XRD analysis of the powder calcined at various temperatures (500-700°C) given in Fig.4.3 (a) collaborated the TGA results. These calcined zinc oxide samples were observed to have hexagonal wurzite structure (ICPSD No. 01-070-8070). Increasing the temperature from 500 to 700°C does not change the phase structure. The XRD data in Fig.4.3 (b) shows sharpening of the peaks which indicates, not surprisingly increasing grain size. The elemental analysis of both commercial and synthetic powder showed the presence of very low concentration of impurities (Al, Mg, K, Ta, S, and P), less than 5 ppm which is acceptable. The SEM analysis of the calcined powders presented in

Fig.4.4 revealed grain growth and agglomeration as the calcination was temperature increased. The formation of agglomerates is attributed to the reduction of high surface energy of the nanoparticles during thermal treatment [191, 226].

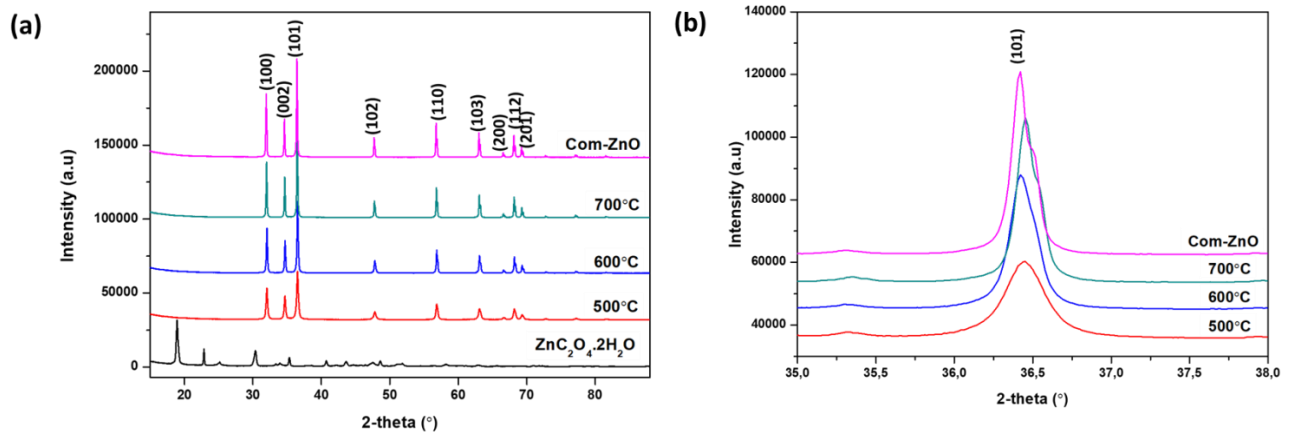


Fig. 4.3 XRD patterns of commercial zinc oxide powder and synthetic one, heat-treated at various temperatures (a) and Zoomed 101 peak (b)

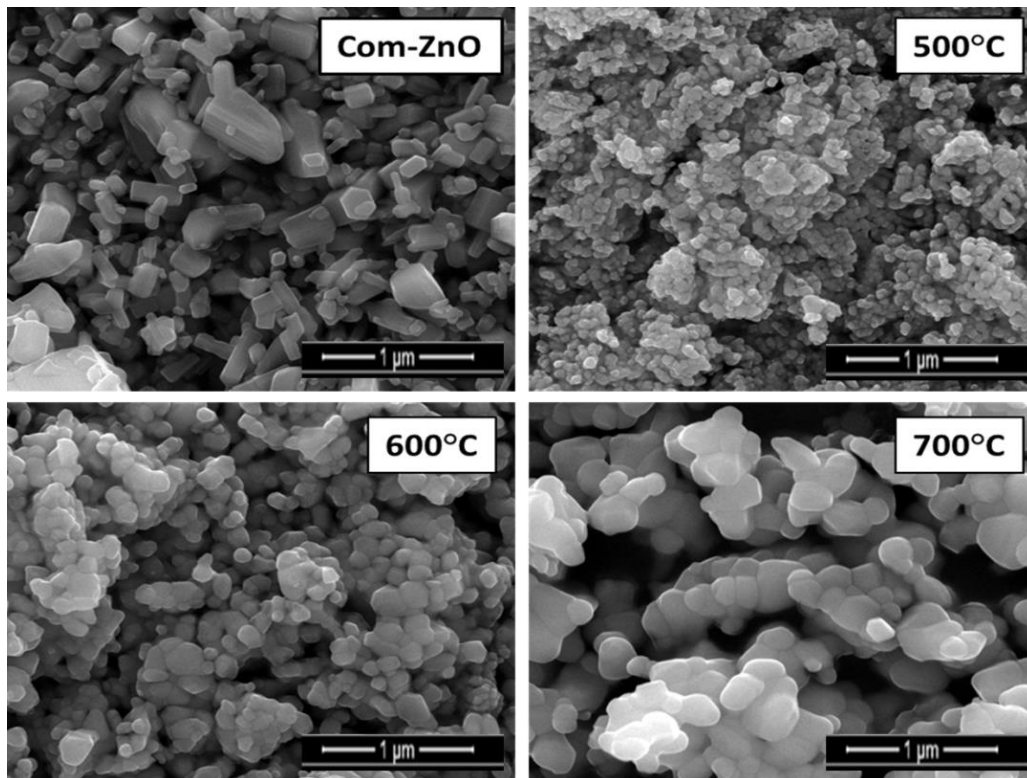


Fig. 4.4 SEM micrographs of synthetic ZnO powders obtained at various calcination temperatures

The particle size distribution of the calcined powders shown in Fig.4.5 indicated the distribution of the grains broadens as the temperature of calcination is increased. The grain size varies from 78 nm to 289 nm when the calcination temperature is increased from 500 to 700°C. The grain size and surface area of the powders are given in Table 4.1. The surface area of the powders decreases as the temperature increases, confirming the grain growth observed by SEM. The sample calcined at 500°C has the smallest average grain sizes: 73 nm (BET) and 78 nm (Image J). Each grain consists roughly of one crystallite.

Table 4.1 Specific surface area and grain size of synthetic and commercial ZnO powders

Sample	Surface area	Grain size	Grain size	Crystallite size
	(BET)	(BET)	(SEM-Image J)	(XRD)
	m^2/g	nm	nm	nm
500°C	14.5	73	78±19	53
600°C	5.9	179	177±61	-
700°C	3.3	320	289±154	-
Com-ZnO	5.8	182	193±111	-

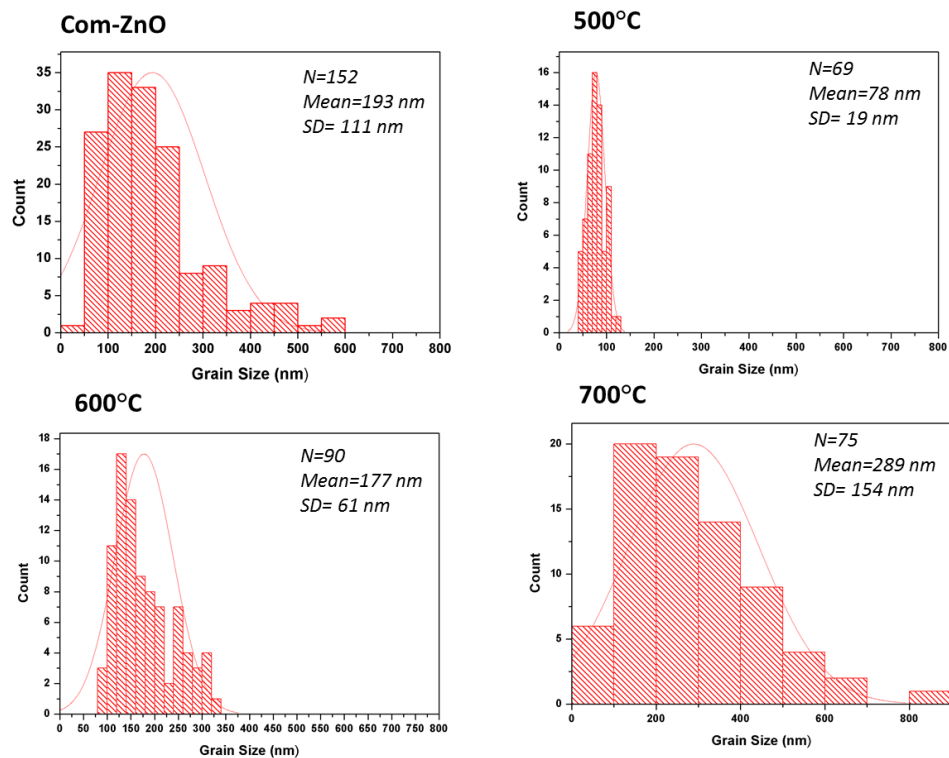


Fig. 4.5 Particle size distribution of ZnO powders (ImageJ)

FTIR and thermal analysis

FTIR spectroscopy was utilised to identify any eventual impurities in the ZnO powders, as shown in Fig.4.6 (a). It was observed that the synthesized powders contain characteristic signatures similar to those of commercial ZnO (Com-ZnO) as discussed in chapter 3 [209]: Some notable features of the graph are, the O-H group stretching vibrations at 3500cm^{-1} , CO_2 at 2600cm^{-1} and NO_3 phase at 1440cm^{-1} and 1553cm^{-1} . It was observed that increasing the calcination temperature reduced the amount of organic components in the powders. The Com-ZnO powder contained high concentration of NO_3 components as compared to the synthetic ZnO powders, the difference could have been due to unique preparation methods.

The FTIR results were supported by thermo-gravimetric analysis given in Fig.4.6 (b) which revealed that whatever the sample, mass loss occurs from room temperature till 1000°C . The amount of mass loss depends on the composition and stability of the sample. In the measured temperature range, the powder calcined at 700°C logically shows lower mass loss (0.15% mass loss). Compared with the other samples, three zones can be identified from the thermo-gravimetric curves. In zone 1, commercial powder and the sample calcined at 700°C showed slight decrease in mass, while the powders calcined at 500°C and 600°C loose approximately 0.2%, attributed to adsorbed H_2O species. Between 200°C and 300°C , a second zone, was attributed to remaining moisture. Surprisingly, commercial powder shows the highest mass loss in this region. It is difficult to give an explanation for this since we do not know the preparation conditions of the commercial powder. Finally, the last zone probably corresponds to the evacuation of organic components, i.e. CO_2 and NO_3 groups. The observed mass loss at various temperatures clearly supports the bands which were identified by FTIR.

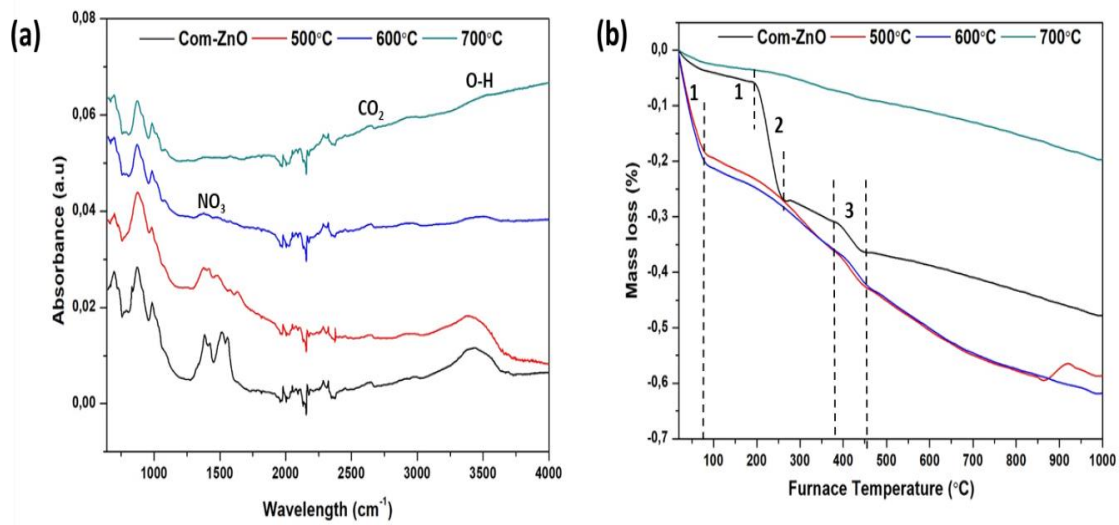


Fig. 4.6 FTIR (a) and Thermogravimetric analysis (b) of the different ZnO powders

4.3.2 Spark plasma sintering of pure ZnO ceramics

This section discusses the spark plasma sintering and its effects on commercial and synthetic ZnO powder. It was decided to investigate the influence of the starting powder characteristics on densification of sintering and microstructural evolution of the ZnO ceramics. The effect temperature and atmosphere on the sintering process were investigated, the summary of the relative density and grain size evolution of the ceramics are presented in Table 4.2. The ZnO ceramics prepared from synthetic and commercial powder are abbreviated as CSP and CCP, respectively.

4.3.2.1 Sintering behaviour of commercial and synthetic pure ZnO in air and vacuum

4.3.2.1.1 Sintering in air atmosphere

The sintering behaviour of the commercial and synthetic ZnO powders was studied in air up to a temperature of 700°C (the temperature limit of the tungsten carbide tools) while keeping a constant axial pressure of 250 MPa, without current isolation. Synthetic powder calcined at 600°C was used as it has almost the same average grain size as the commercial powder: 177±61 nm (synthetic powder) and 193±111 nm (commercial powder). The punch displacement and displacement ratio, representing respectively the shrinkage and shrinkage speed of the powder, are given in Fig.4.7 as a function of sintering time. The displacement ratio of both samples showed two peaks: sharp peaks at 100-300s (room temperature) and broad peaks at 600-1000s (300-600°C). The first peak could be attributed to the rearrangement of grains by rolling due to applied pressure at room temperature [106, 107, 209]. The second peak could be due to the densification of the ceramics at high temperature,

with grains diffusing with neighbouring grains. The influence of sintering temperature on ceramics prepared through commercial powder (CCP) has been studied in detail in chapter 3 [209].

During the heating stage, the displacement of both samples gradually increases with temperature and tend to reach a constant state after 900 s. The ceramics prepared from synthetic ZnO powder (CSP) reach higher displacement of about 3 mm as compared to the commercial powder (CCP) (2 mm). This could be due to the smaller particles size distribution and homogenous morphology, leading to better mobility of grains [105, 187, 193]. It was also observed that CSP finished sintering earlier than the CCP with a difference of $\sim 40^{\circ}\text{C}$. This indicates the importance of working with nano-sized grains that can be sintered at lower temperature. The sintering mechanism of pure ZnO in air could be controlled by the lattice and grain boundary diffusion of interstitial Zn ions (Zn_i) [100, 102, 104, 221, 227]. ZnO being a non-stoichiometric material, it is sensitive to sintering atmosphere, which could affect the densification of the ZnO ceramics. This discussion is detailed in section 4.3.2.1.2.

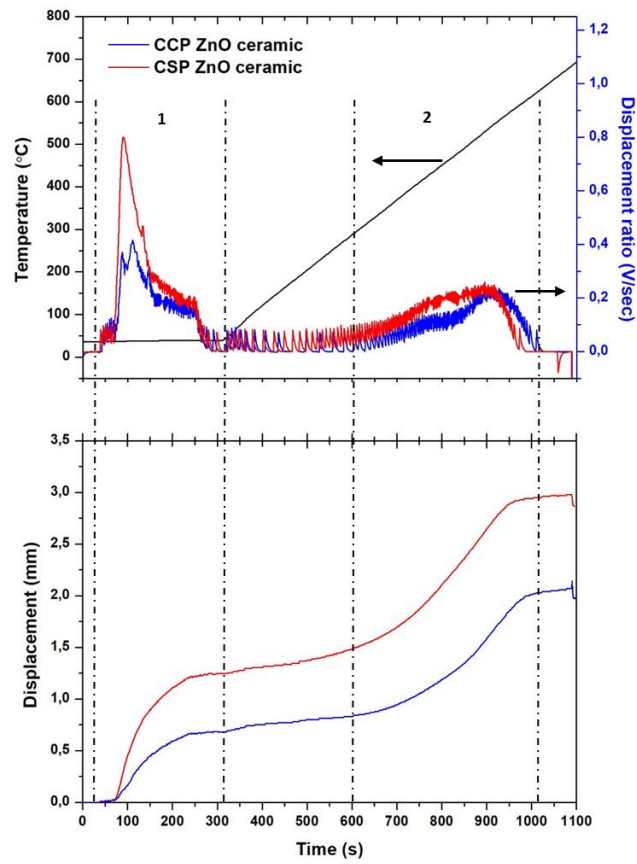


Fig. 4.7 Displacement ratio and displacement during heating of pure commercial and synthetic ZnO powder in air (700°C)

Table 4.2 Relative density and grain size of ceramics prepared from com-ZnO and synthetic ZnO powder for different sintering conditions [Symbols: CCP : ceramics prepared from commercial ZnO powder, CSP : ceramics prepared from synthetic ZnO powder, SC : sintering cycle and RT : room temperature]

Die diameter	Atmosphere	Sintering cycle	Insulation	Temperature	Pressure & when applied	Relative density	Grain size (Image J)
mm	-	-	-	°C	MPa	%	µm
Powder calcined at 500°C (C500)							
8	Air	SC1	Without	600	250,RT	100	2,2±0.6
8	Air	SC1	Without	700	250,RT	99.4±0.2	6±2
Powder calcined at 600°C (C600)							
8	Air	SC1	Without	600	250,RT	99.3±0.1	2,4±0.6
8	Air	SC1	Without	700	250,RT	99.5±0.2	5,4±1.3
20	Air	SC1	Without	700	250,RT	100	5±2
20	Vacuum	SC2	With	900	100, Last 2 min of heating stage	98.9±0.4	4±2
Powder calcined at 700°C (C700)							
8	Air	SC1	Normal	600	250,RT	99.3±0.2	3±1
8	Air	SC1	Normal	700	250,RT	100	4,2±1,6
Commercial ZnO (Com-ZnO)							
8	Air	SC1	Without	700	250,RT	97,8±1,2	5,3±2,3
20	Air	SC1	Without	700	250,RT	99,1 ±0,5	5,4±2,1
20	Vacuum	SC2	With	900	100, Last 2 min of heating stage	98.7±0,4	3,6±1,3

The CSP and CCP ceramics were sintered at a dwell time of 6 min. The relative densities are given in Table 4.2. No significant difference was observed for both powders sintered at 700°C, the relative density of CSP and CCP was 100% and 99%, respectively. The SEM micrographs of CSP and CCP ceramics are given in Fig.4.8. The same grain size distribution for both ceramics is evidenced. The grain size increased from 177 nm to 4.7 µm for CSP and from 193 nm to 5.4 µm for CCP, indicating samples had the same growth rate. The grain size distribution of both samples appeared to be similar. XRD patterns indicated no phase change after sintering.

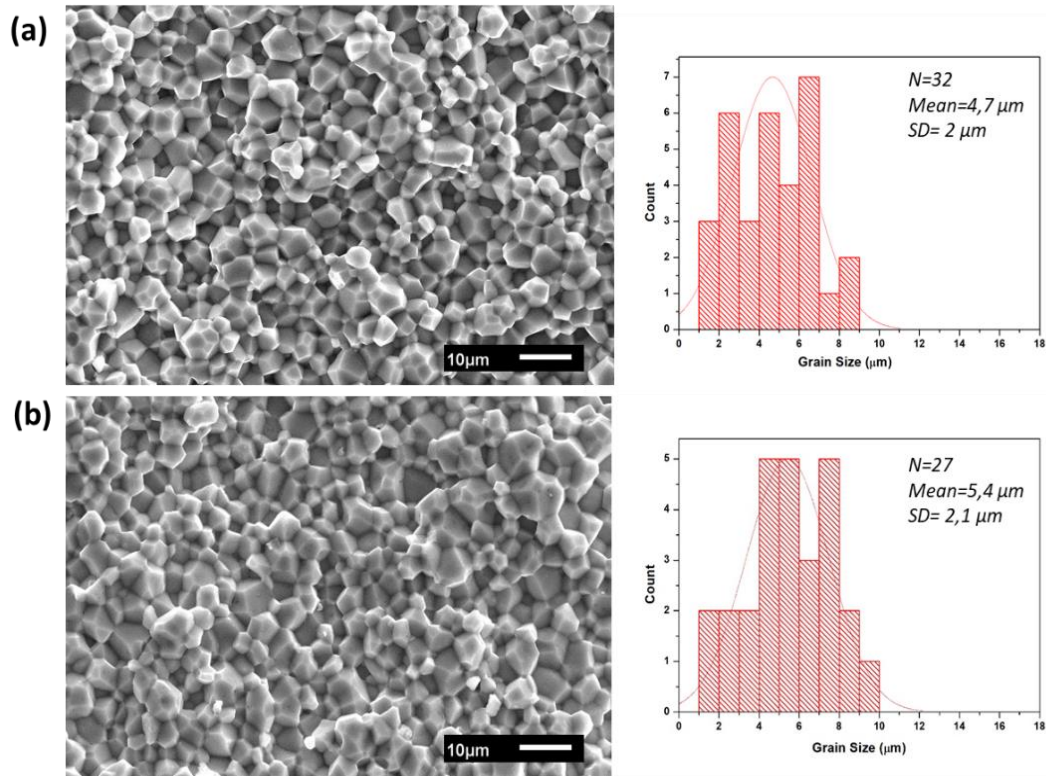


Fig. 4.8 SEM micrograph of fractured surfaces and grain size distribution (Image J) (a) CSP ceramic (b) CCP ceramic (700°C-250 MPa)

4.3.2.1.2 Sintering in vacuum atmosphere

Commercial and synthetic ZnO powders were further sintered in vacuum to evaluate the sintering behaviour of the ZnO ceramics up to a temperature of 900°C, applying axial pressure of 100 MPa during the last 2 min of heating stage, with current isolation. Insulation was used in this section to avoid the influence of electric field on the ZnO grains because sintering ZnO at high temperature creates more oxygen vacancies which could affect the consistency of current flow. The punch displacement and displacement ratio, representing respectively the shrinkage and shrinkage speed of the powder, are given in Fig.4.9 as a function of sintering time. The displacement ratio of both samples showed two broad peaks at 400-900s (200-600°C) and 1000-1250s (800-900°C). The first peak could be caused by the softening of the grains during the heating stage, as a result the grains easily rearrange [106, 107, 187]. It was observed that CSP ceramics shrinks at 400°C, 300 s earlier than CCP ceramics. This could have occurred because of differences in particle size distribution and morphology in the starting powders. Han *et al.* [33] reported about the sintering of Al-doped ZnO ceramics prepared from nanoparticles, rods and platelets powders. Similar relative densities of 90% were reported, though it was observed that the rods and platelets ceramics

have preferential orientation on miller impedance, $\langle 001 \rangle$, direction while for the nanoparticles it was prohibited. Whereas, Zhang *et al.* [34] reported on Al-doped ZnO ceramics with hybrid micro/nano structure powders. In this case, low relative density of 80% was achieved with non-preferential grain growth. These findings could support the observed unique sintering behavior of CCP and CSP ceramics due to the differences in powder quality.

The second peak (in Fig 4.9) could be caused by applied pressure. It was observed that during the heating stage, the displacement of both samples gradually increases with temperature and tend to reach a constant state after 1200 s. The CSP and CCP ceramics reached displacement of about 3 and 2.5 mm, respectively. As previously stated, the difference could be due to smaller particle size distribution and morphology of CSP powder which leads to higher mobility of grains.

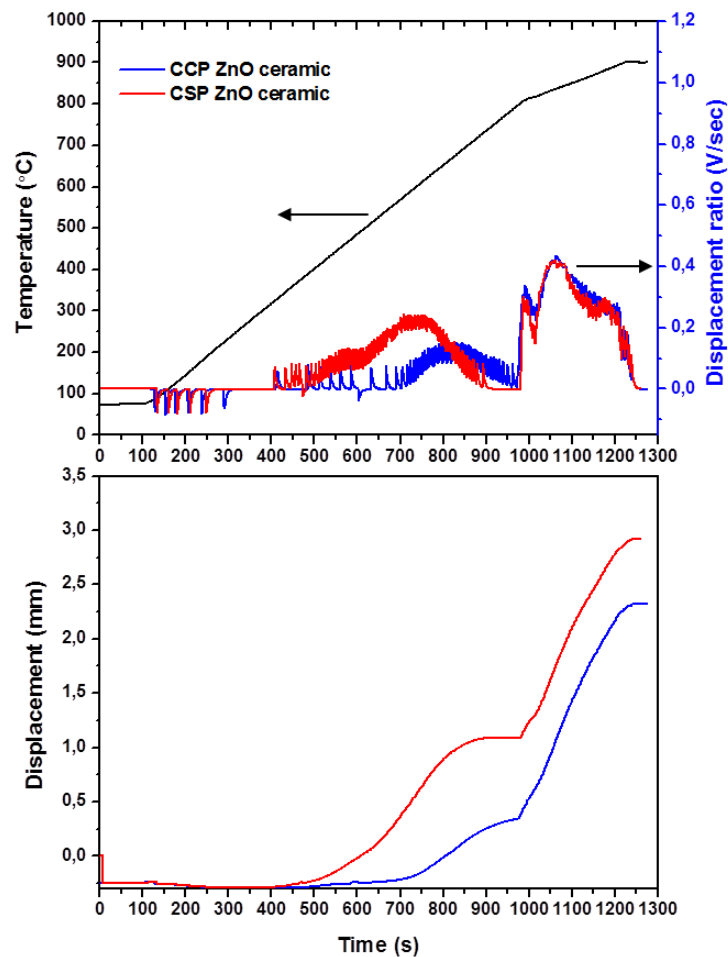


Fig. 4.9 Displacement ratio and displacement during heating of pure commercial and synthetic ZnO powder in air (900°C)

The powders were sintered under dwell period of 6 min and the relative densities are presented in Table 4.2. The relative density of CSP slightly decreased to 98.9 % when sintering in vacuum at 900°C, this could have resulted from the presence of pores in the ceramic [187]. Similar relative density was achieved for CCP. The microstructure given in Fig.4.10 revealed that there is no significant change in the grain size as well between CSP and CCP, an average mean grain size of 3.9 μm and 3.6 μm were determined, respectively. Comparing the two sintering temperatures (700°C and 900°C), CSP grain size remained at a mean of 4 μm when sintering at 700°C and 900°C. While a slight decrease in the grain size was observed in CCP, from 5.4 μm (700°C) to 3.6 μm (900°C). Smaller grain sizes were obtained at 900°C because of axial pressure was applied during the last minutes of heating stage; this delayed the diffusion of grains at the grain boundaries.

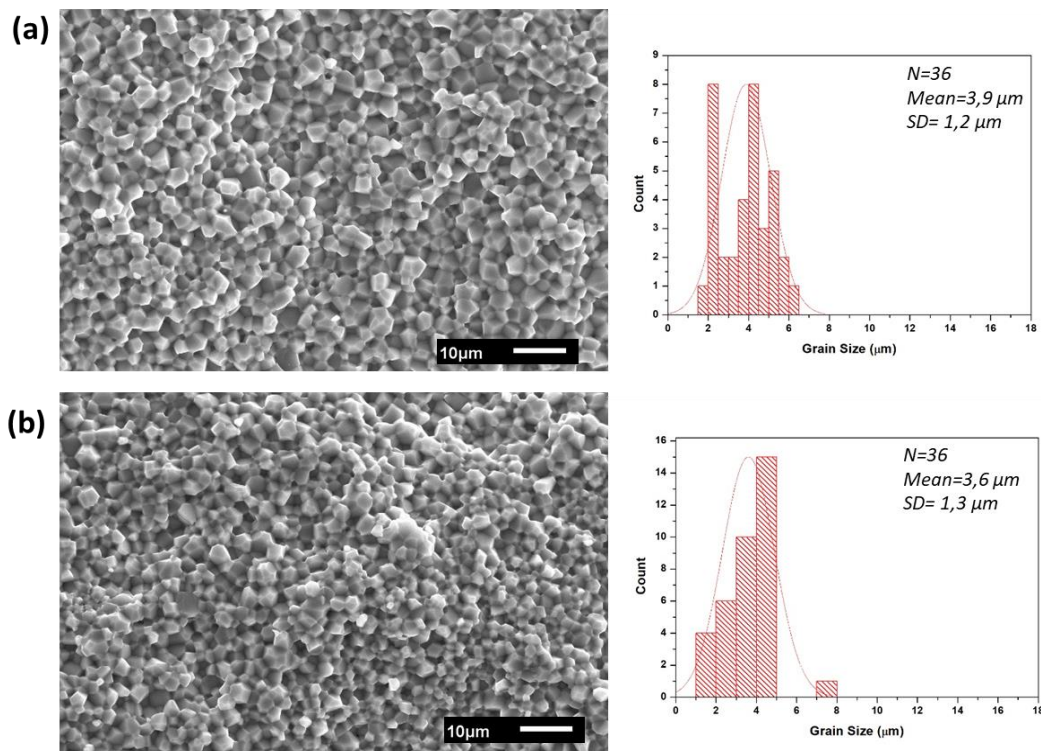


Fig. 4.10 SEM micrograph of fractured surfaces and grain size distribution (Image J) (a) CSP ceramics (b) CCP ceramic (900°C -100 MPa-SC2)

The photographs of the ceramics sintered at 900°C were taken to compare colour changes and are given in Fig.4.11. The CSP appear greenish and the CCP appear greyish after sintering. XRD analysis indicated that the dense ceramics have the same phase structure as the starting powders. The ICP analysis indicated that the powders have the same low content of impurities such as Al, Mg, K, Ta, S, and P, all less than 5ppm. This may suggest that, the

difference in the colour could probably be related to oxygen content which is dependent on synthesis method of the powders (unknown for commercial powder).

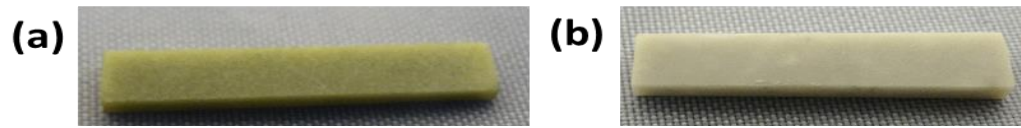


Fig. 4.11 Photographs of (a) CSP ceramic (b) CCP ceramic (900°C -100 MPa-SC2)

4.3.2.2 Effect of sintering temperature on synthetic ZnO powder calcined at different temperatures

Synthetic powders were prepared through the co-precipitation process followed by calcination. Then, the calcined samples were sintered 600°C and 700°C using 8 mm die. The samples were labelled as C500, C600 and C700 corresponding the calcination temperature. The relative densities given in Table 4.2 showed that fully dense ceramics above 99% are obtained from the ceramics prepared from synthetic powder. It was noted that the behaviour of densification differs for each powder; C500 reach 100% densification at 600°C while increasing the temperature to 700°C leads to a decrease of 0.6%. Whereas, increasing the temperature from 600°C to 700°C in C700 ceramics resulted in an increase in the relative density from 99.3 to 100%. The difference could have been caused by the difference in powder surface area; C500 had higher surface area of reaction as compared to C700. Similar results were reported by Aimable *et al.* [101] on comparative study of sintering synthesized and commercial powder. The relative density of C600 ceramics did not change much when the temperature was increased.

The XRD analysis of the ceramics presented in Fig.4.12 indicated no change in the phase structure with sintering temperature. It is a hexagonal wurzite structure of ZnO as was earlier demonstrated; similar characteristic signature was observed for all the parameters. The SEM micrographs of the fractured surfaces of the ceramics sintered at 600°C and 700°C are given in Fig.4.13. It was observed that, at both temperatures, sintering leads to homogenous morphology and an increase in the grain size for C500, C600 and C700 samples. At a sintering temperature of 600°C, grain size of 2.2, 2.4 and 3 µm were determined for C500, C600 and C700 ceramics, respectively. Further increase in the sintering temperature to 700°C caused an increase in the grains to 6, 5.4 and 4.2 µm for C500, C600 and C700 ceramics, respectively. The sample C500 sample showed bigger grains as compared to C600 and C700 samples, probably because of the high surface area of reaction it possess, surrounding grain

boundaries easily diffuse with each other [32, 101]. The photographs of the as-sintered ceramics are given in Fig.4.14; it was observed that the ceramics becomes grey after sintering as indication of oxygen deficiency as discussed in previous section. This might have an influence on the electrical properties of the ZnO ceramics as it is sensitive to defects concentration as was discussed in chapter 1.

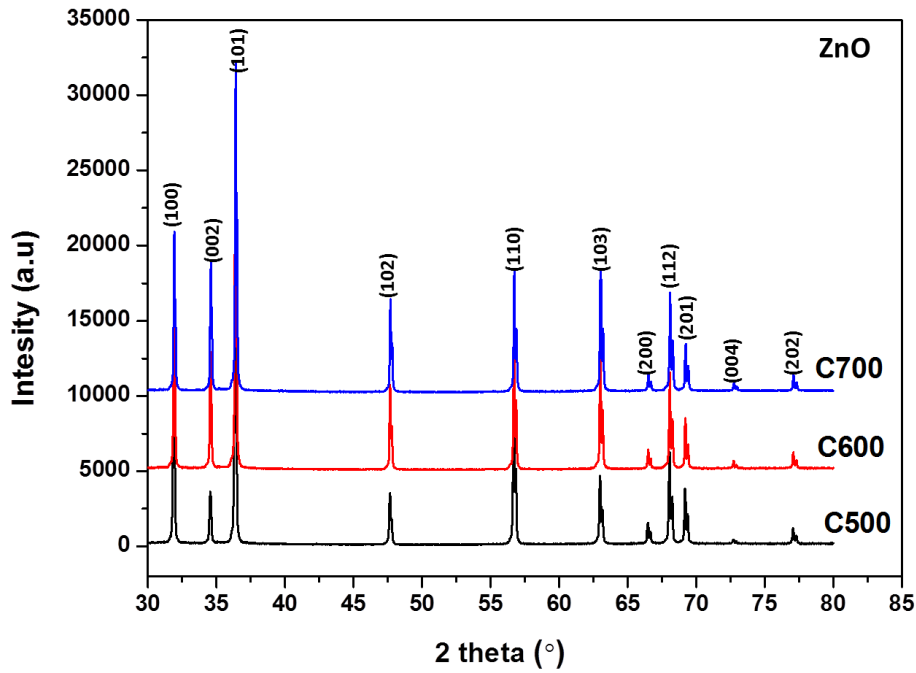


Fig. 4.12 XRD patterns of ZnO ceramics from synthesized powder sintered at 600°C

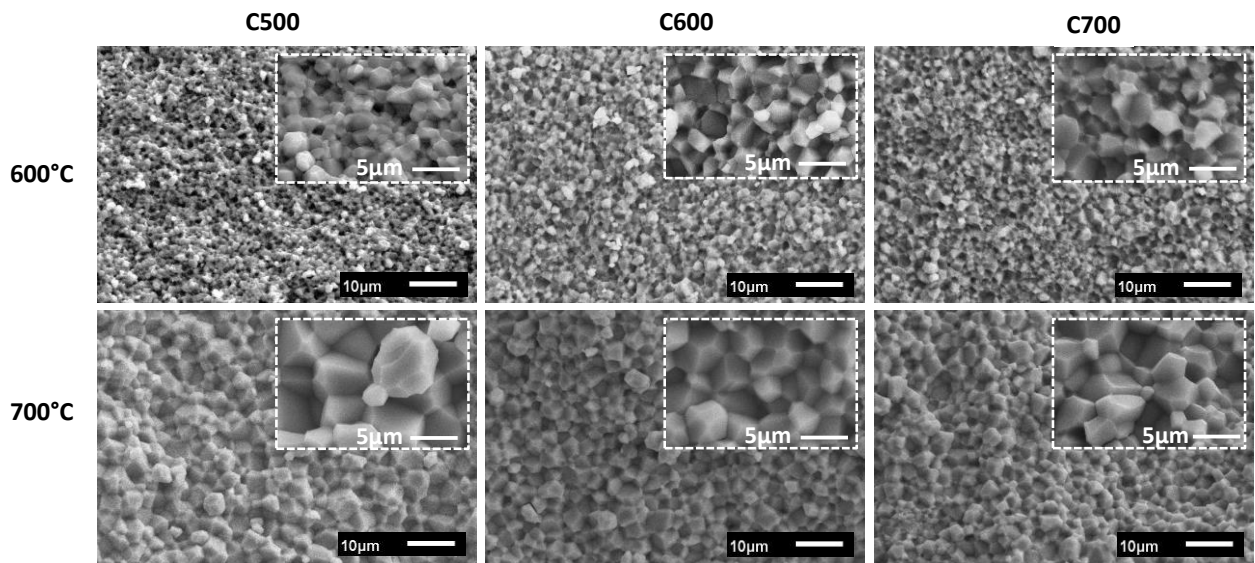


Fig. 4.13 SEM micrograph of fractured surfaces of ZnO ceramics prepared from synthesized powder (P=250 MPa)

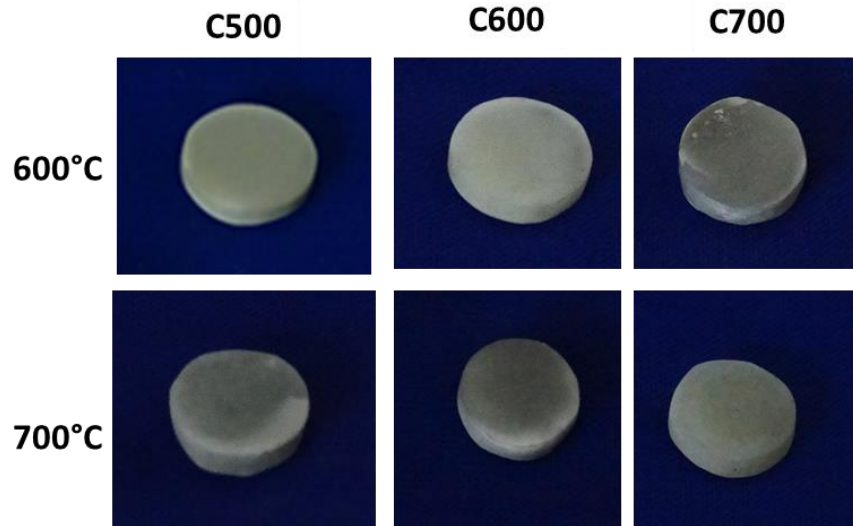


Fig. 4.14 Photos of as-sintered ZnO ceramics prepared from synthesized powder

4.3.3 Influence of annealing treatment on the microstructure of ZnO ceramics

The ZnO ceramics sintered at 700°C prepared from commercial powder (Com-ZnO) were used to study the influence of annealing on the microstructural properties. The as-sintered ZnO ceramics were annealed in air to oxidise the ceramic to have stable electrical measurements. Annealing in oxygen environment fills the available oxygen vacancies and breaks the donor complex, this improves the resistivity measurements [223]. The thermogravimetric analysis of the as-sintered ZnO ceramic shown in Fig 4.16 indicated a logarithmic increase in mass from 0 to about 0.24 % when the temperature was increased. This indicates that the oxygen from the atmosphere reacts with interstitials Zn^{2+} to form stable compound ZnO, see Eq 4.4 [219, 220]. The inserted photographs showed that the ceramic changes colour from greyish to white when it is annealed in air. Based on the TGA results, the ceramics were annealed during 24 h at 600°C in air to stabilize the stoichiometry in the ceramics. The SEM microstructure of the annealed ceramic after 24 h is presented in Fig. 4.17; it was observed that grain size difference between the as-sintered and annealed is insignificant. This will be beneficial in improving the thermal conductivity as small grain size could be quite useful in reducing the thermal conductivity due to phonon scattering at grain boundaries.



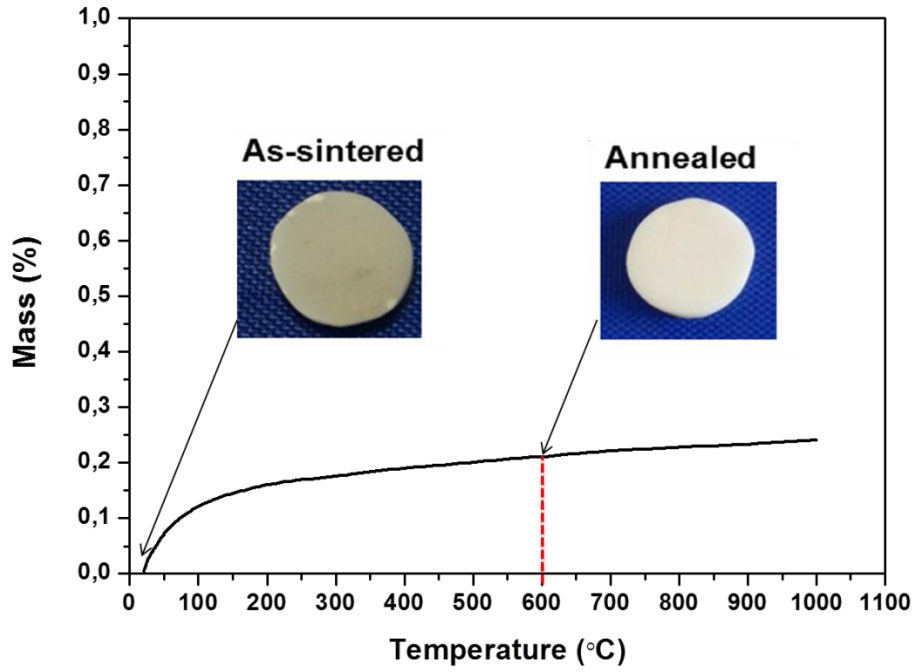


Fig. 4.15 Thermogravimetric (TGA) analysis of as-sintered CCP ceramic

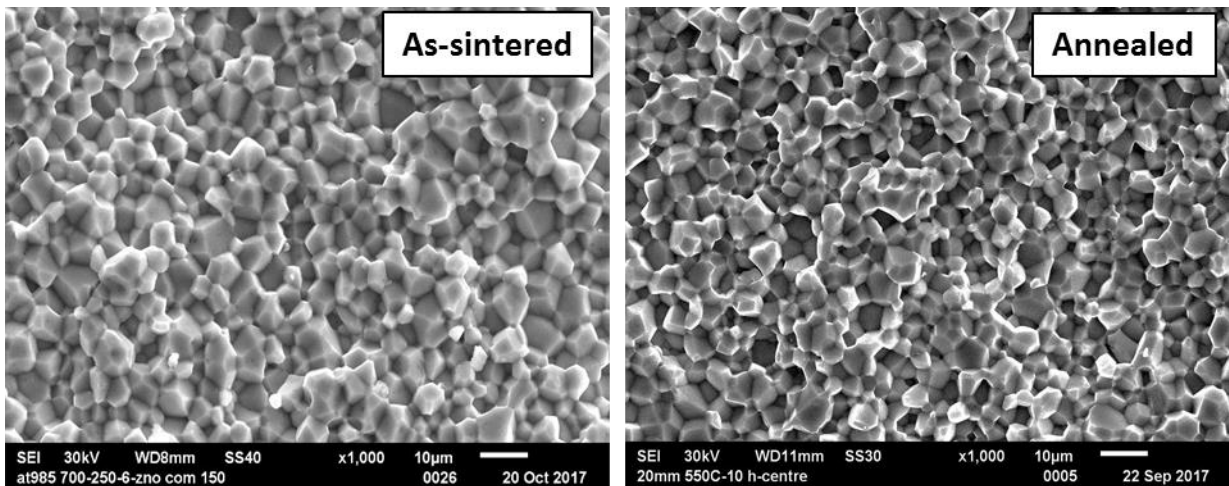


Fig. 4.16 SEM micrographs of as-sintered and annealed CCP ceramic

4.3.4 Thermoelectric properties of pure ZnO ceramics

The thermoelectric properties of as-sintered and annealed pure ZnO ceramics (both prepared from synthetic and Com-ZnO powder) were analysed and the details are given below. Ceramics prepared from commercial powder are indicated as CCP and those prepared from synthesized powder are indicated as CSP. The samples are further identified according to the corresponding sintering temperature (700°C and 900°C) and the atmospheric condition of sintering (Air or Vacuum). Additionally, CCP and CSP ceramics sintered at 900°C were compared with some experimental data from literature. The electrical properties were carried out from room temperature (RT) to 500°C under a reduced atmosphere. From additional electrical measurements (hall measurements), the carrier concentration, carrier mobility and bandgap were determined at room temperature (Table 4.3).

4.3.4.1 Influence of ZnO microstructure and defects on thermoelectric properties

4.3.4.1.1 Resistivity of ZnO ceramics

The resistivity results of various ZnO ceramics as a function of temperature are presented in Fig.4.17; all samples showed an increase in the resistivity with an increase in temperature indicating a typical metallic behaviour. Gautam *et al.* [111] observed similar electrical behaviour on pure ZnO, however, the causes of such behaviour was not reported. Similar behaviour was observed for Ni doped ZnO ceramics at temperatures between 250-450°C, the behaviour was due to thermally induced disconnection of low ohmic chains of ZnO grains by highly resistive NiO phase[228]. In this report the ceramic is pure ZnO, therefore the only plausible explanation is that the metallic behaviour could have been caused by the presence of ZnO defects formed during sintering and/or grain boundary resistance [229].

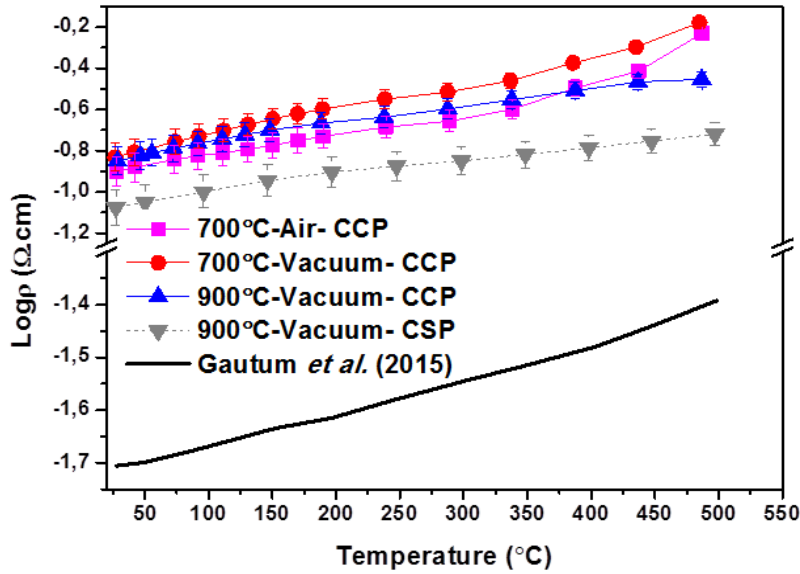


Fig. 4.17 Resistivity vs Temperature of as-sintered pure ZnO ceramics

The effect of sintering temperature on CCP ceramics sintered in a vacuum becomes evident in the resistivity behaviour. At RT both the *700°C-Vacuum-CCP* and *900°C-Vacuum-CCP* samples have the same resistivity of $\sim 0.12 \Omega.cm$ as shown in Fig 4.17. However, when the sample temperature is raised to $500^\circ C$ the resistivity's begin to deviate with that of *700°C-Vacuum-CCP* sample showing a more rapid increase when compared to *900°C-Vacuum-CCP*. This behaviour may be attributed to higher concentration of oxygen vacancies in *900°C-Vacuum-CCP* than in the *700°C-Vacuum-CCP* resulting in a slow increase in the resistivity in the former. This idea is further supported by the lower carrier mobility for the *900°C-Vacuum-CCP* sample when compared to that of *700°C-Vacuum-CCP* sample see Table 4.3. From the additional electrical parameters of the ceramics given in Table 4.3 and it is shown that there is a difference of 0.7×10^{17} in carrier concentrations between *700°C-Vacuum-CCP* and *900°C-Vacuum-CCP*, which could be another further explanation for the slow increase in the resistivity for *900°C-Vacuum-CCP*.

Table 4.3 Electrical parameters measured at room temperature of as-sintered ZnO ceramics

Sample	n (cm ⁻³)	μ (cm/V.s)	Bandgap (eV)
700°C-Air-CCP	4,3x10 ¹⁷	116	3.1
700°C-Vacuum-CCP	4,8x10 ¹⁷	90	3.2
900°C-Vacuum-CCP	5,5x10 ¹⁷	83	3.1
900°C-Vacuum-CSP	7,8x10 ¹⁷	62	2.9

From the resistivity measurements, Fig.4.17, the influence of the sintering atmosphere on the electrical behaviour on CCP ceramics is not very significant. It is noted however that between 150°C and 400°C it is observed that *700°C-Air-CCP* undergoes some chemical changes due to oxidation resulting in a lower resistivity as compared to the *700°C-Vacuum-CCP*. This process ceases above 450°C probably due to saturation and the resistivities of the two samples become comparable.

The influence of the synthesis process on the electrical behaviour was further evaluated by comparing the resistivity behaviour of two samples; commercial CCP and synthetic CSP, both sintered at 900°C in vacuum. It was observed that *900°C-Vacuum-CSP* was the most conducting of all the samples i.e. lower resistivity compared to *900°C-Vacuum-CCP* and all other samples. Although the sample still showed metallic behaviour with increase in temperature like other samples it was however always lower than all samples in resistivity. This could be because of the high carrier concentration of 7.8×10^{17} cm/Vs and even though it has low mobility caused, probably by oxygen vacancies and defects. The reported resistivity values for ZnO are higher than the ones reported in literature; this could be because of the difference in ceramic preparation conditions [31, 32, 95, 111]. The bandgaps of all the samples are in the same range and would not have significant influence on the differences observed in the resistivity data in Fig. 4.17.

4.3.4.1.2 Seebeck Coefficient of ZnO ceramics

The variation of the Seebeck Coefficient (or thermopower) as a function of temperature is given in Fig. 4.18; the negative sign indicated *n-type* conductivity. High absolute Seebeck Coefficient (|S|) values of between 550-600 μV/K were obtained for CCP samples at room temperature. Whilst for the CSP samples a lower value of |S|= 475 μV/K was obtained at

room temperature. Gautum *et al* [111] reported even lower $|S|$ value of $280 \mu\text{V/K}$ at room temperature. The differences in these experimental values are most likely as a result of differences in carrier concentrations in the different samples. The Seebeck coefficient is related to the carrier concentration in semiconductors as given by Mott's formula in Eq.4.5 [10]. It is therefore evident that different material preparation techniques have the ability to engineer materials with unique and diverse properties. In this light different sintering technique plays a huge role on the electrical properties of ceramics, as was observed in difference in values for both Seebeck Coefficient.

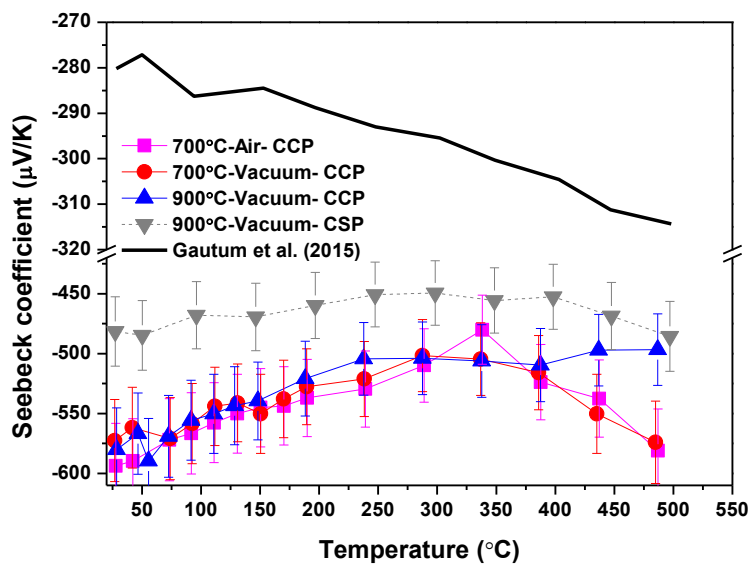


Fig. 4.18 Seebeck Coefficient vs Temperature of as-sintered pure ZnO ceramics

$$S_{bulk} = \frac{8m^* \pi^2 k_b^2}{3eh^2} T \left(\frac{\pi}{3n} \right)^{\frac{2}{3}} \quad [4.5]$$

From Fig.4.18; it was observed that when the temperature is increased from room temperature to 500°C there is a transition in $|S|$ that occurs at $\sim 325^\circ\text{C}$ for $700^\circ\text{C-Air-CCP}$ and $700^\circ\text{C-Vacuum-CCP}$ ceramics. The $|S|$ decreased from $\sim 575 \mu\text{V/K}$ at room temperature to $500 \mu\text{V/K}$ at 325°C , thereafter increased to $575 \mu\text{V/K}$ at 500°C is purely due to the increase in more electrons (i.e. charge carriers) being promoted above the Fermi level into the conduction band because of increase in temperature and hence more electrons moving from the hot junction to the cold junction. Above 325°C this promotion reaches a saturation point and further increase in temperature results in electron scattering instead due to increased lattice vibrations and hence an increase in $|S|$ back to $575 \mu\text{V/K}$ again. The increased

scattering was further supported by the increase in resistivity at high temperatures which was explained earlier.

For the 900°C -Vacuum-CCP samples $|S|$ increased up to 250°C and thereafter remained constant with an increase in temperature suggesting that after carrier saturation there is no significant scattering to lattice vibrations, any issue which will be explored when thermal conductivity is discussed.

The 900°C -Vacuum-CSP samples did not show significant changes in $|S|$ with temperature. This is somewhat surprising and this requires further experimental work not possible at the present moment. Therefore, further studies need to be done to have better understanding on the thermoelectric properties of intrinsic ZnO ceramics especially those which are oxygen deficiency.

4.3.4.1.3 Thermal conductivity of ZnO ceramics

The temperature dependence of thermal conductivity is presented in Fig. 4.19; it is evident that the thermal conductivity of all samples decreased with an increase in temperature due to phonon-phonon scattering due to increased lattice vibrations [23]. At room temperature, the initial thermal conductivity for all samples was ~ 45 W/m.K and these decreases exponentially to ~ 12 W/m.K at 500°C . The results are similar to the work reported by Gautam *et al.*[111]. However, these values are too high for improved thermoelectric applications and the reason might be due to the relatively large grain sizes of the samples. Which are namely 5.3, 5.4, 3.6, 5.4, and 3.9 μm corresponding to samples 700°C -Air-CCP, 700°C -Vacuum-CCP, 900°C -Vacuum-CCP, 700°C -Air-CSP and 900°C -Air-CSP, respectively. As a result, nanostructuring is being considered as an option to reduce the thermal conductivity.

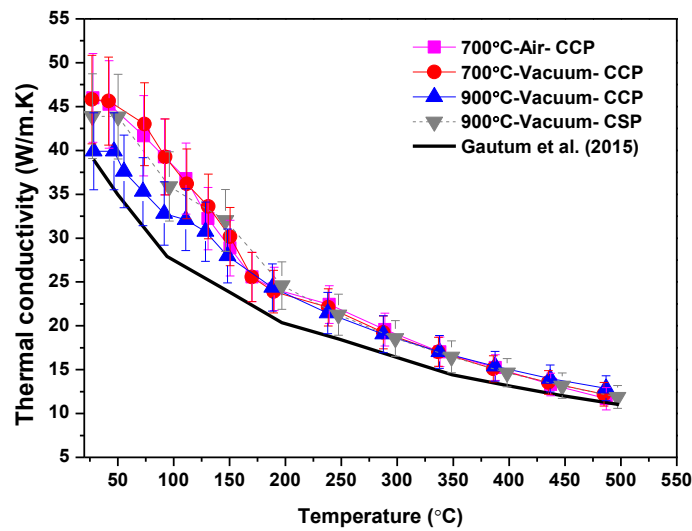


Fig. 4.19 Thermal conductivity vs Temperature of as-sintered pure ZnO ceramics: (a) resistivity (b) Seebeck Coefficient (c) thermal conductivity (d) power factor (e) ZT

4.3.4.1.4 Thermoelectric performance of ZnO ceramics

The key thermoelectric performance behaviour of the ceramics as a function of temperature is shown in Fig.4.20 in terms of power factor (Fig.4.20 (a)) and figure of merit (Fig. 4.20 (b)). The power factor measures the electrical performance of the ceramics by comparing the Seebeck Coefficient and resistivity of the ceramics. From Fig. 4.20 (a) it is observed that 700°C-Air-CCP and 900°C-Vacuum-CSP ceramics gave the highest power factor of about $2.7 \times 10^{-4} \text{ W/m}^2\text{K}$ at room temperature due to the lower electrical resistivity resulting from higher carrier concentration and higher mobility. The overall decrease in the power factor with temperature could be related to the increase in the resistivity due to phonon scattering and possibly additional oxidation of the ceramics.

The figure of merit (ZT) in Fig. 4.20 (a) shows a general increase in ZT with an increase in temperature for all the samples. This evolution can be related to the decrease in the thermal conductivity when the temperature is increased and /or alternatively due to an increase in the Seebeck coefficient particularly at higher temperatures. A maximum ZT of 8×10^{-3} at 500°C was achieved for 900°C-Vacuum-CSP ceramic this is not very far from that reported by Gautam et al. [111] a ZT of 17×10^{-3} at the same temperature. Further improvements the thermoelectric properties requires an increase in the carrier concentration of the ZnO ceramics maybe through doping with donor elements such as Al, Ga, In etc which will be shown in the next chapters.

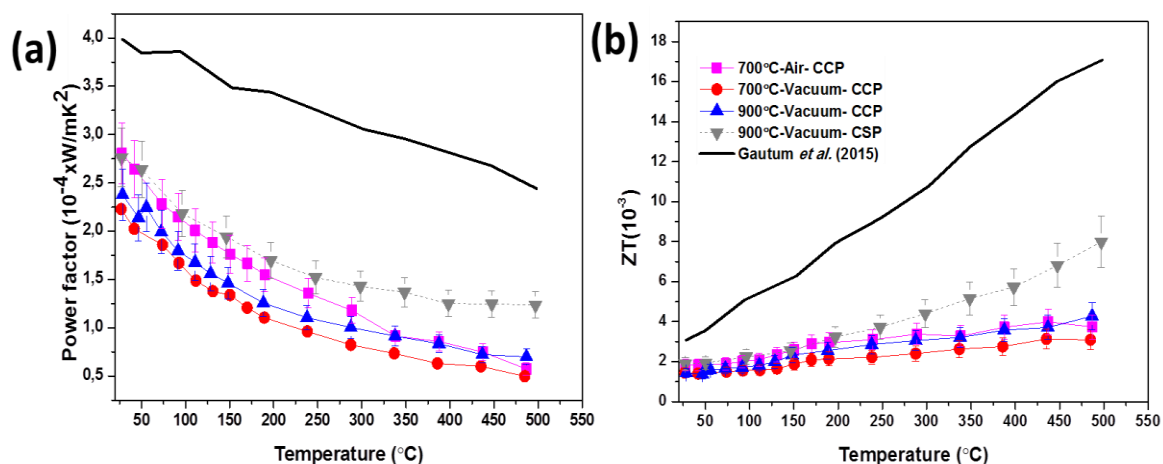


Fig. 4.20 Performance of as-sintered pure ZnO ceramics with temperature: power factor (a) ZT (b)

4.3.4.2 Influence of ZnO microstructure and defects on thermoelectric properties

Prior to attempts on doping, some work was done to try and understand the effect of annealing on the thermoelectric properties of the ZnO ceramics. CSP ZnO ceramic sintered at 900°C in Vacuum was annealed in air for 24 h at 600°C . The thermoelectric properties of as-sintered and annealed ceramics are indicated in Fig.4.21. The annealed sample expectedly became more resistive, by 4 orders of magnitude at 50°C (Fig. 4.21(a)). This is probably because of the decrease in the carrier concentration from 7.8×10^{17} to $5.5 \times 10^{13} \text{ cm}^{-3}$ as a result of ZnO oxidation when it thermally heated in air. The annealed sample indicated a semiconducting behaviour with an increase in temperature. The difference in the conduction mechanism in the samples can be attributed to differences on ZnO defects concentrations. A transition at 250°C was observed which may have been due to the non-equilibrium state of the sample. Zakutayev *et al* [230] reported a transition for annealed Ga-doped ZnO thin films at 500°C . After 350°C , the resistivity is close to that reported by Liang [95] and Sondergaard *et al.* [109].

The evolution of Seebeck Coefficient with temperature is given in Fig 4.21 (b); the $|S|$ increased from 500 V/K to $\sim 800 \text{ V/K}$ at room temperature when annealed because of the decrease in the carrier concentration. The absolute value of the Seebeck Coefficient decreased with an increase in temperature, similarly to that of as-sintered ceramics. Liang [95] reported almost constant the $|S|$ with temperature whilst Sondergaard *et al.* [109] observed an increase with temperature as expected by the Mott's equation. The increase in

|S| in this study has been explained earlier in section.

The thermal conductivity of the ceramics given in Fig.4.21 (c) indicated that the annealing conditions used in this study do not bring any significant difference on thermal conductivity. Thermal conductivity of 43 W/mK at 75°C was determined for both as-sintered and annealed ZnO ceramics, which is within previously reported values of 33-48 W/mK at 75°C [95, 109].

The figure of merit vs temperature data is given in Fig.4.21 (d) it reveals that annealing does not improve the performance of the ZnO ceramics probably because of reduced electrical conductivity. Maximum ZT of $\sim 2 \times 10^{-3}$ was obtained at 500°C for annealed ZnO ceramics. The performance of both the as-sintered and annealed is in the range of other reported ZT values in the literature.

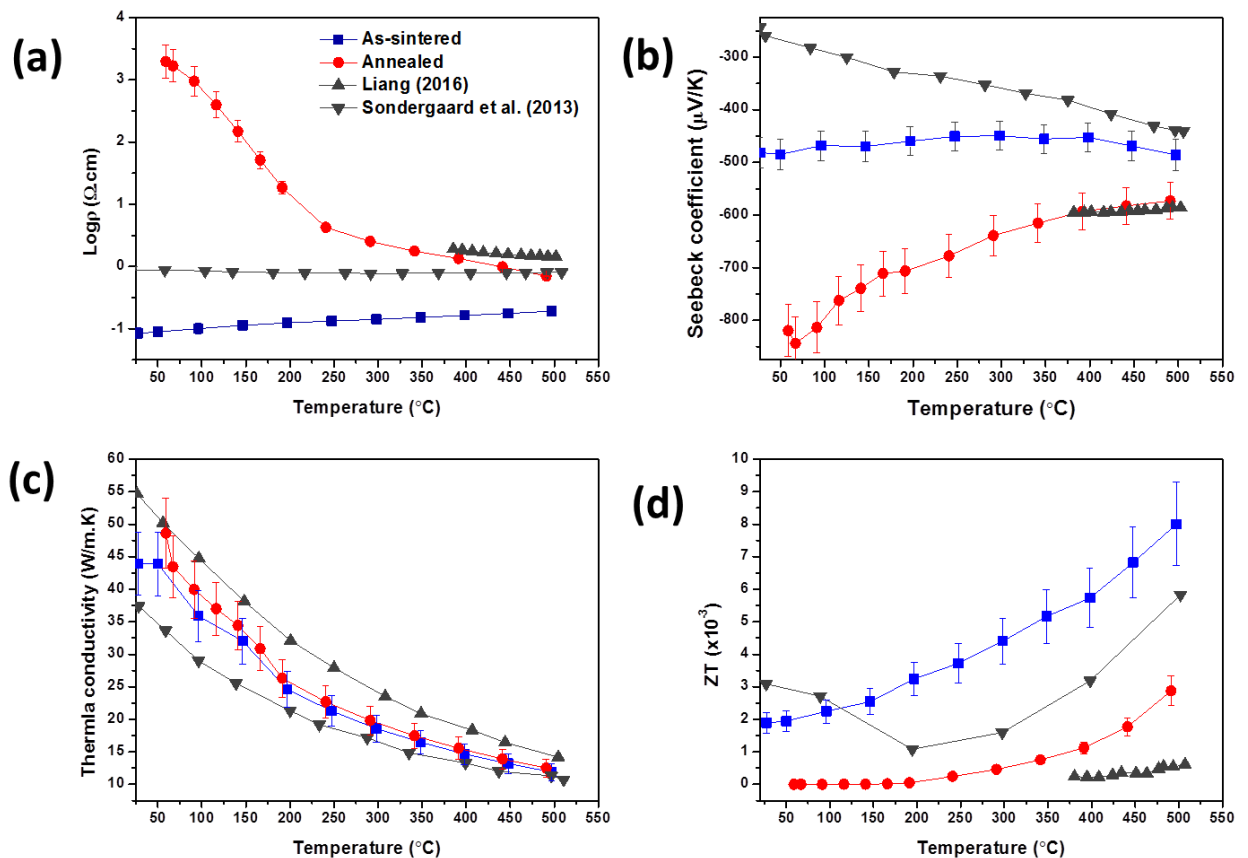


Fig. 4.21 Thermoelectric properties of annealed 900°C-Vacuum-CSP ceramic: (a) resistivity (b) Seebeck Coefficient (c) thermal conductivity (d) ZT

4.4 Conclusions

ZnO nanoparticles were successfully synthesized through co-precipitation technique followed by calcination. Increasing the calcination temperature increases the grain size of ZnO powder; calcination temperature of 500°C gave the smallest grain size of 73 nm. The effect of sintering atmosphere and temperature on the densification and microstructure evolution on ZnO ceramics prepared from commercial and synthesized powder were successfully investigated. Ceramics prepared from synthetic powder could be fully densified above 99% at temperature as low as 600°C. At temperatures around 700°C the ZnO ceramics indicated to be sensitive to the powder's specific surface area, ceramic's grain sizes of 6 ± 2 μm and 4.2 ± 1.6 μm were obtained for surface areas of 14 m^2/g (C500) and 3.3 m^2/g (C700), respectively. This study has illustrated that SPS can sinter to high densities irrespective of starting powder. However, to maintain a nanostructured ceramic it is important to look into low temperature sintering and/or modification of starting powder.

Annealing at 600°C did not show any significant change on the microstructure of ZnO ceramics but changed the oxygen stoichiometry. And this had an effect on the electrical conduction mechanism as annealed samples became semiconducting while the as-sintered ceramics showed metallic behaviour.

A somewhat unique behaviour was observed on Seebeck Coefficient variation with temperature and attempts to explain this unique behaviour was given which however might need further work to confirm this behaviour.

The thermal conductivity of ZnO ceramics was found to be still too high for more efficient thermoelectric applications. And as such there is need to look into reducing the thermal conductivity by doping with donor elements such as Al, Ga, In etc as shall be shown the subsequent chapters. Annealing did not improve thermoelectric properties of the ZnO ceramics because it reduced the electrical conductivity significantly.

In conclusion from this work it became apparent that sample preparation technique is important in determining the electrical conductivity and thermoelectric properties of materials. Ceramics prepared from synthetic powder showed higher carrier concentration than the commercial bought ceramics. As a result, as-sintered ceramics prepared from synthetic powder gave the best and highest performance with a ZT of 8×10^{-3} which is far much better than that from commercial samples.

Chapter 5

Microstructure and thermoelectric properties of Al-doped ZnO ceramics prepared through spark plasma sintering

5 Microstructure and thermoelectric properties of Al-doped ZnO ceramics prepared through spark plasma sintering

5.1 Introduction

The previous chapter (Chapter 4) discussed the thermoelectric properties of pure zinc oxide (ZnO) and it was found that it is too resistive for the applications envisaged. It was proposed in the introduction that doping with group 3 elements (such as aluminium (Al), gallium (Ga), indium (In)) can lead to enhanced electrical properties because dopants can modify the band gap of the oxide and furthermore their ionic radius are close to that of Zn ($\text{Al}^{3+}=0.054$ nm, $\text{In}^{3+}=0.08$ nm, $\text{Ga}^{3+}=0.062$ nm, $\text{Zn}^{2+}=0.074$ nm) [126, 127].

Thus far, the highest ZT reported for doped ZnO composites is from dual doping of Al and Ga; $\text{ZT} = 0.45@1000$ K and $\text{ZT} = 0.65@1247$ K using conventional sintering [28]. Al-doped ZnO ceramics were extensively investigated with ZTs of ~ 0.17 to 0.47 at 1000 K from ceramics prepared through hot press [28, 110, 128, 129], microwave [130] and spark plasma sintering [6, 33, 34, 37, 111, 131]. The substitution of Al on the zinc site of ZnO helps to improve thermoelectric properties through enhanced electrical conductivity and reduced thermal conductivity caused by nanostructuring. Aluminium is known to be a grain growth inhibitor [231, 232].

However, these properties can be easily affected by the preparation methods of the powders. In most reported work, the authors have prepared solid reactions of ZnO and Al_2O_3 powders which could cause inhomogeneity in the material [233]. The most reliable technique is the synthesis of the powders by wet chemical methods that lead to homogenous mixture [115, 191]. Nowadays, consolidation is being conducted using spark plasma sintering (SPS) technique; resulting in full densification which is attained in a short period which minimizes grain growth [100, 234]. Smaller grains are effective for reducing thermal conductivity through phonon scattering [235].

In this chapter, 2 mol% Al was doped in pure ZnO powder because of the previously reported high ZT of between $0.3 - 38$ due to high electrical conductivity and reduced thermal conductivity for this precise amount of aluminium [28, 34, 131]. The characterizations of $\text{Zn}_{0.98}\text{Al}_{0.02}\text{O}$ powder which was synthesized through co-precipitation followed by calcination are discussed in detail in this chapter. The sintering was done using SPS at varying temperatures, pressures and periods of pressure application to find suitable microstructure.

This discussion includes characterization of the powders and ceramics, densification characteristics and thermoelectric properties of the Al-doped ZnO ceramics.

5.2 Materials and methodology

5.2.1 Synthesis of $Zn_{0.98}Al_{0.02}O$ powder

Al-doped ZnO powder was synthesized through co-precipitation techniques followed by calcination, similarly to procedures previously done by Guy *et al.* [236] and Beynet *et al.* [115]. Solutions of 4 M concentration of zinc nitrate hexahydrate and aluminium nitrate, and 0.2 M and 0.38 M ammonium oxalate monohydrate were prepared. Aluminium nitrate was added at an excess of 10 % to ensure final aluminium concentration of 2 mol%. At ambient temperature, zinc nitrate hexahydrate/aluminium nitrate solution was mixed with 0.2 M ammonium oxalate monohydrate solution to initiate nucleation. At a subsequent time and constant stirring, 0.38 M ammonium oxalate monohydrate solution was added into the mixture to promote particle growth. The pH was adjusted using ammonia solution to a pH around 6.5 - 7. A white precipitate was formed which was centrifuged and dried for 22 hrs at 80°C, thereafter, calcined in a furnace at 600°C to form $Zn_{0.98}Al_{0.02}O$ powder.

5.2.2 Spark plasma sintering of the $Zn_{0.98}Al_{0.02}O$ powder

Al-doped ZnO ceramics were pre-compacted at 25 MPa for 1 min thereafter sintered using spark plasma sintering with an 8 and 20 mm inner diameter tungsten carbide dies. The influence of sintering temperature (550-700°C), pressure (250-500 MPa) and period of pressure application (room temperature (RT) or holding time (HT)) was investigated. The sintered ceramics were polished by silicon carbide discs (P320 and P600) to remove graphite foil for further analytical analysis.

5.3 Results and discussion

5.3.1 Characterization of synthetic Al-doped ZnO powders

In this report, pure and Al-doped ZnO are represented as 0 at% and 2 at%, respectively. Normalized XRD patterns of the precipitate given in Fig.5.1 showed single phase structure of zinc oxalate, when doped with Al, which is similar to the patterns of the undoped zinc oxalate. However, there was an increment in the intensity of the peaks: 25°, 33°, 42.5° and others for 2 at% as compared to 0 at%. The increment of intensity could have been caused by the slight presence of Al in the ZnO powder. The SEM image of the precipitates given in Fig.5.2 indicated no difference in the morphology between 0 at% and 2 at%. Thermogravimetric analysis of zinc oxalate and Al doped zinc oxalate show the same behavior (Fig.5.3).

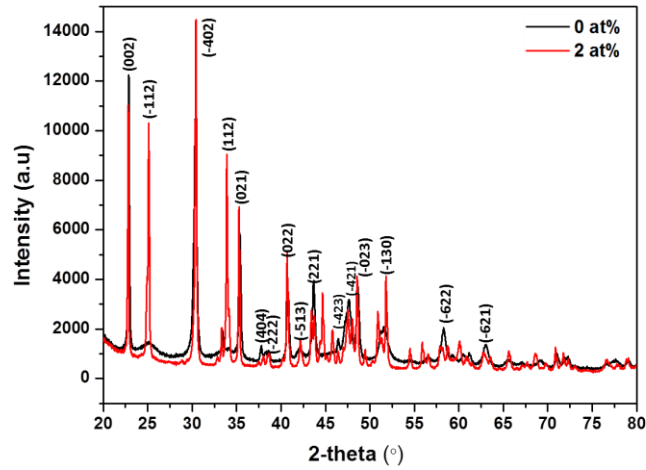


Fig. 5.1 XRD patterns of pure and Al-doped ZnO oxalate powder

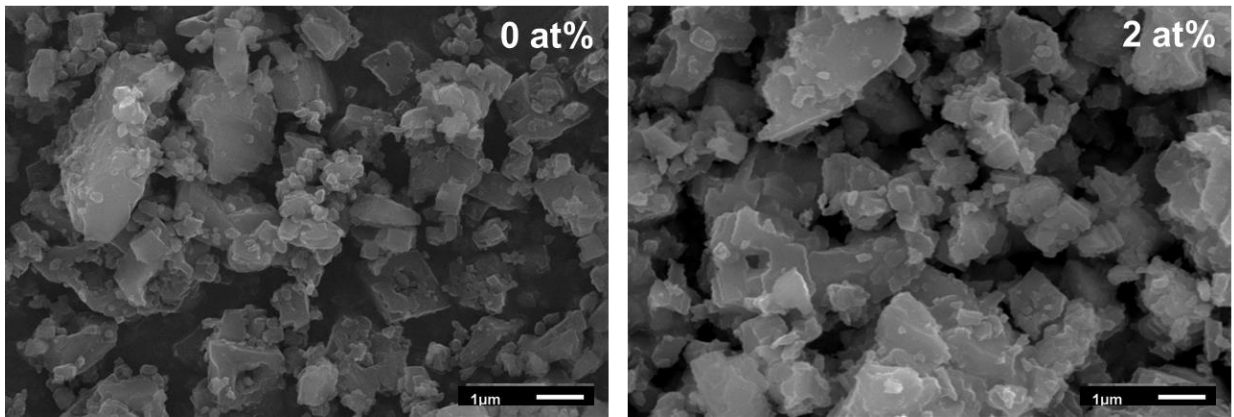


Fig. 5.2 SEM images of pure and Al-doped ZnO oxalate powder

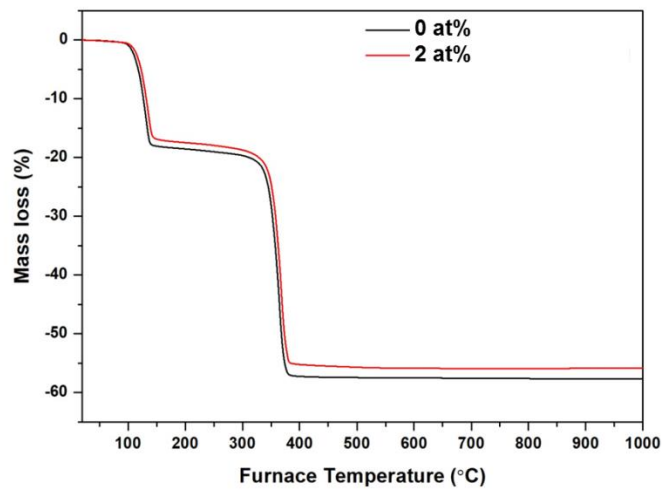


Fig. 5.3 Thermogravimetric analysis of pure and Al-doped ZnO powder

The calcined powder was analyzed by ICP (check Chapter 2 for analysis details) to confirm the amount of Al in the powder. 2 at% Al were determined, which is in perfect agreement with the target value. The XRD patterns of 0 at% and 2 at% powder presented in Fig.5.4 showed that the 2 at% powder has similar wurzite hexagonal structure as the undoped sample (Reference sample, 0 at%). The presence of additional phases was not detected and the lattice parameters did not show any considerable changes possibly due to small concentration of Al in the powder, indicating homogenous distribution of Al in ZnO powder.

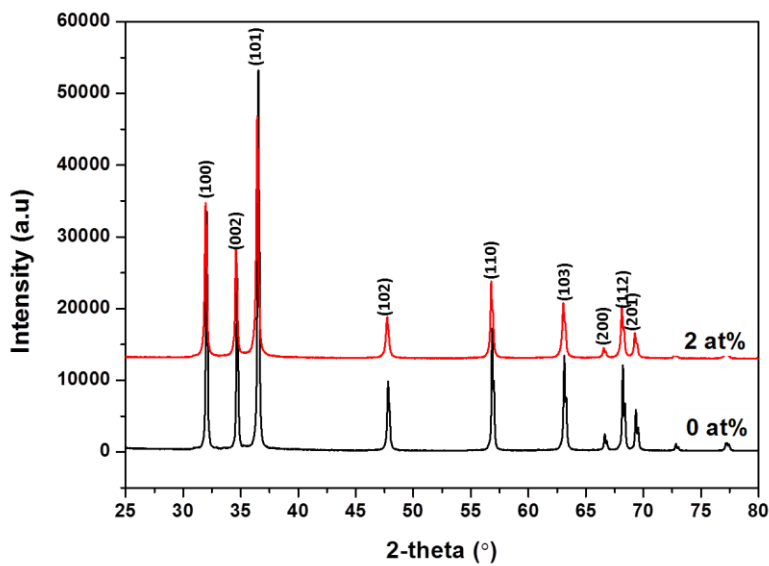


Fig. 5.4 XRD patterns of pure and Al-doped ZnO powder

The SEM micrographs of the powders given in Fig.5.5 show a decrease in the grain size for 2 at%. This is not surprising since Al is known to be a grain growth inhibitor. Further, image J analysis on the SEM micrographs determined that the powder had aggregate sizes of 525 ± 169 nm. The particle and crystallite size of the powders given in Table 5.1 showed that 2 at% has particle sizes of about 75 ± 13 nm with crystallite sizes of about 40 nm. The total surface area of the powder increased from 5.9 to $11 \text{ m}^2/\text{g}$ when Al was added into ZnO structure, supporting the SEM observations. The particle size distribution curve in Fig.5.6 indicated that the 2 at% has two populations of particles at 1 and 10 μm which could have resulted from the agglomeration. These results have indicated the influence of Al doping in ZnO powder especially on the morphology that could have later affect the electrical properties of the ceramics.

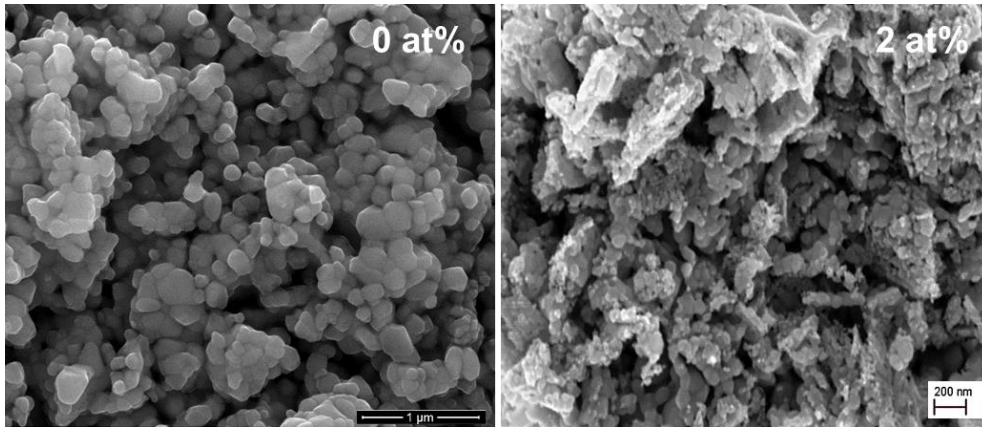


Fig. 5.5 SEM micrographs of pure and Al-doped ZnO powder

Table 5.1 Surface area distribution and particle size of pure and Al-doped ZnO powders

Sample	S_{BET} m ² /g	d_{BET} nm	d_{SEM} nm	d_{XRD} nm
0 at%	5.9	179	177±61	-
2 at%	11	100	75±13	40

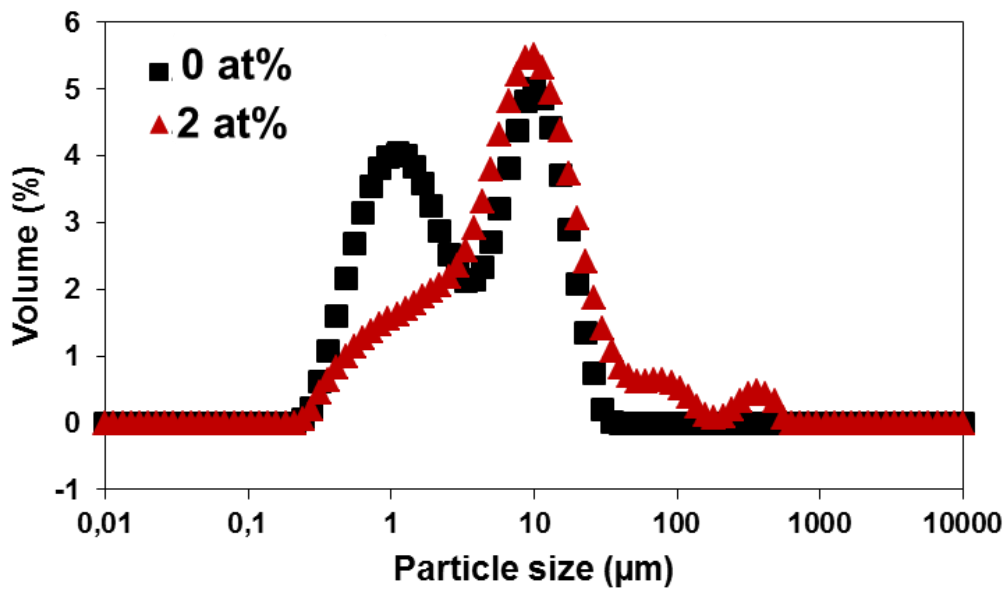


Fig. 5.6 Particle size distribution of pure and Al-doped ZnO powder

5.3.2 Spark plasma sintering of Al-doped ZnO powder

Al-doped ZnO powder ($\text{Zn}_{0.98}\text{Al}_{0.02}\text{O}$) was spark plasma sintered in air at various parameters such as temperature, pressure and period of pressure application to get a fully dense ceramic. The summary of the ceramics characteristics for different sintering conditions are given in Table 5.2.

5.3.2.1 Sintering behavior of Al-doped ZnO ceramics

The sintering curve of 0 at% and 2 at% are given in Fig. 5.7. The sintering steps of 2 at% Al-doped ZnO are divided into three segments; the first stage is the rearrangement of the nanoparticles due to applied pressure. The displacement of 2 at% was slow, and reached only 0.7 mm as compared to 1.2 mm for 0 at%, could be related to the aggregates present in the powder. The second stage could be related to the neck formations between the particles due to localized heating caused by spark discharge [100, 106, 115, 209]. The displacement of the 2 at% sample gradually increased to the same level as that of 0 at%. The third stage is the pore elimination in which the necks between the particles are gradually developed and there is progression of plastic transformation. Both samples finished sintering at 550°C; however, the total displacement differed by 0.5mm. The 2 at% sample gave total displacement of 2.5 mm while 0 at% gave 3 mm. This indicates the influences of grain size on the sintering behavior of the ceramics. The high density of grain boundaries could have enhanced the diffusion rate of 2at% sample [237], due to the high surface area of 2 at%. As a result, the sintering temperature decreased. The reduction in the sintering temperature has been reported on the sintering of nanoparticles materials such as ZnO [100, 116]. Reduced temperature implies less grain growth which will be beneficial for improving thermoelectric properties.

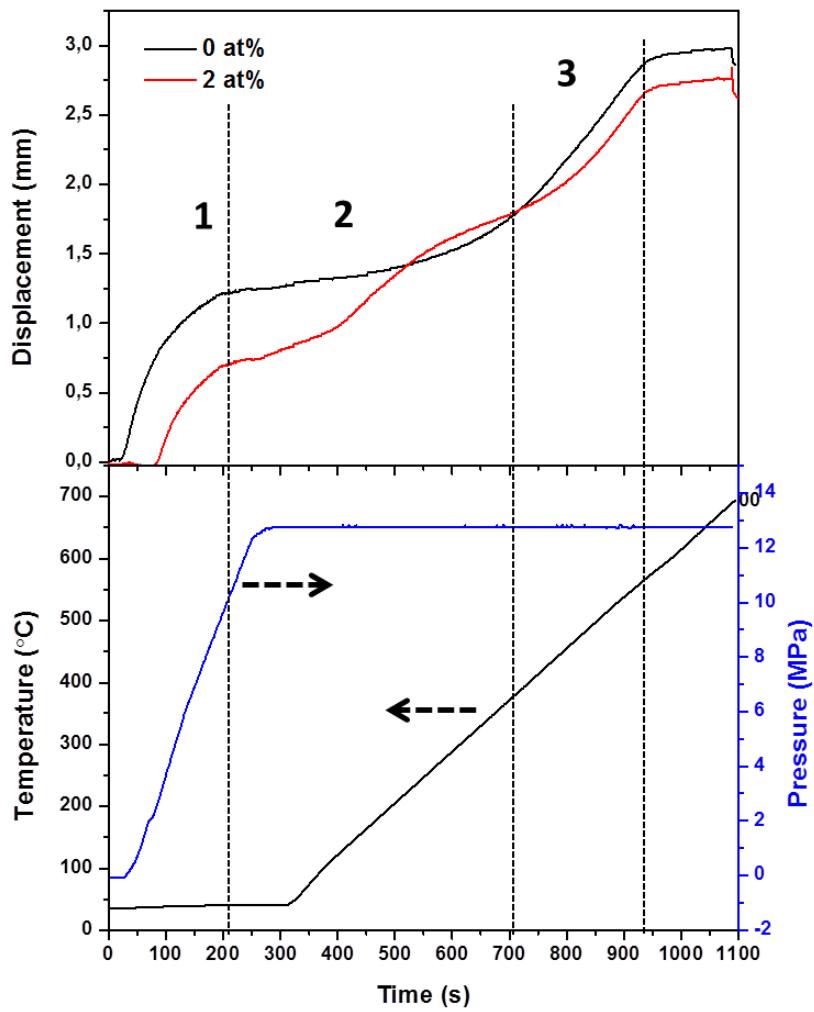


Fig. 5.7 Sintering behavior of pure ZnO and Al-doped ZnO using spark plasma sintering

Table 5.2 Summary of pure and Al-doped ZnO ceramics characteristics for varied SPS parameters (*Note: RT-Room temperature, HT- Holding time*)

Ref.	Temp eratu re	Initial Pressur e	Final Pressure	Point of Pressure Application	Atmosphere	RD %	Grain size μm
	$^{\circ}\text{C}$	MPa	MPa	$^{\circ}\text{C}$			
ZnO							
1	600	25	250	RT	Air	99.3 \pm 0.1	2.4 \pm 0.6
2	700	25	250	RT	Air	100	5 \pm 2
Zn_{0.98}Al_{0.02}O							
3	RT	250	250	RT	Air	57 \pm 0.2	-
4	550	250	250	RT	Air	79.9 \pm 0.5	-
5	600	250	250	RT	Air	84.9 \pm 0.2	-
6	650	250	250	RT	Air	98.9 \pm 0.1	0.46 \pm 0.01
7	700	25	250	RT	Air	98.1 \pm 0.1	0.76 \pm 0.26
8	600	25	250	HT	Air	84.3 \pm 0.2	-
9	650	25	250	HT	Air	98.6 \pm 0.1	0.09 \pm 0.02
10	600	100	500	HT	Air	98.5 \pm 0.1	-
Bibliography [Zn_{0.98}Al_{0.02}O]							
Ma et al. [238]	900	50	50	-	Vacuum	99.9	-
Nam et al. [131]	900	50	50	-	Vacuum	94	0.2
Han et al.[33]	950	50	50	-	Vacuum	90	-

5.3.2.2 Effect of sintering temperature s

The influence of the sintering temperature between 550-700°C on the structure, the microstructure and the density of Al-doped ZnO ceramics was studied. Relative density versus temperature given Fig. 5.8 showed an increase in the relative density with an increment in the temperature. Maximum relative density of 98.9% was achieved at 650°C from initial relative green density of 57% at room temperature. Beyond 650°C a decrease in the relative density was observed which could be due to the presence of pores and/or decrease in the ceramic density related to the physical properties such as the density of the individual materials [107, 238]. Ma et al. [238] reported a high densification of 99.9%, however, at a very high temperature of 900°C. While, Nam *et al.* [131] and Han et al. [33] found low relative densities of 94% and 90% at temperatures of 900°C and 950°C, respectively. Other reports includes, relative densities of 99% at temperatures between 800-1200°C and 65-93% sintering between 700-900°C for Al-doped ceramics [111, 239]. The results from the present study indicated that at a temperature of 650°C and pressure of 250 MPa a relative density of 98.9% is obtained. The achievement of high relative densities at very low temperatures could be due to better rearrangement of the grains at high pressures.

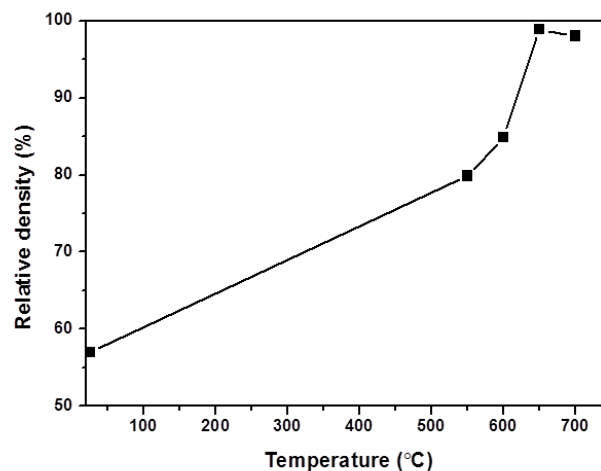


Fig. 5.8 Relative density versus temperature of Al-doped ZnO ceramics

The XRD analysis of some of the ceramics (Fig.5.9) showed that the main phase for the Al-doped ZnO ceramics is ZnO hexagonal wurzite structure. It was observed that as the sintering temperature was increased the XRD peaks of the ceramics are sharpened which is related to the crystallization of the grains. The zoomed inserted image indicated the presence of spinel phase (ZnAl_2O_4) at 37, 35, 32.5 and 31.5°. Other phases in small compositions are alumina (Al_2O_3) at 33.4° and some unknown phase at 30.9°. This implies that Al did not dissolve fully

in the ZnO structure because of the solubility limit. As a result, excess Al reacts with ZnO to form ZnAl_2O_4 and Al_2O_3 . To date, there is not exact value of the solubility limit of Al into ZnO, solubility limits of between 0.3-0.5 mol% Al have been reported thus far [240, 241]. It is possible that these secondary phases present in higher quantity at higher temperature could have contributed to the decrease in the relative density at 700°C due to their physical properties, the density of Al_2O_3 and ZnAl_2O_4 phases are 3.95 and 4.61 g/cm^3 , respectively, at room temperature [242, 243]. Also, more pores could have been formed because ZnAl_2O_4 acts an insulator. The localization at ZnO grain boundaries restricts grain growth [6, 33, 37, 244]. Nunes and Bradt [244] report on conventionally sintered $\text{ZnO/Bi}_2\text{O}_3/\text{Al}_2\text{O}_3$ ceramics found that the majority of the activation energy (400 kJ/mol) was related to the transport of the ZnAl_2O_4 spinel particles which are most probably controlled by the diffusion of O^{2-} in the ZnAl_2O_4 spinel structure. It is also observed in Fig. 5.9 that decreasing the temperature below 650°C reduces the presence of the spinel phase.

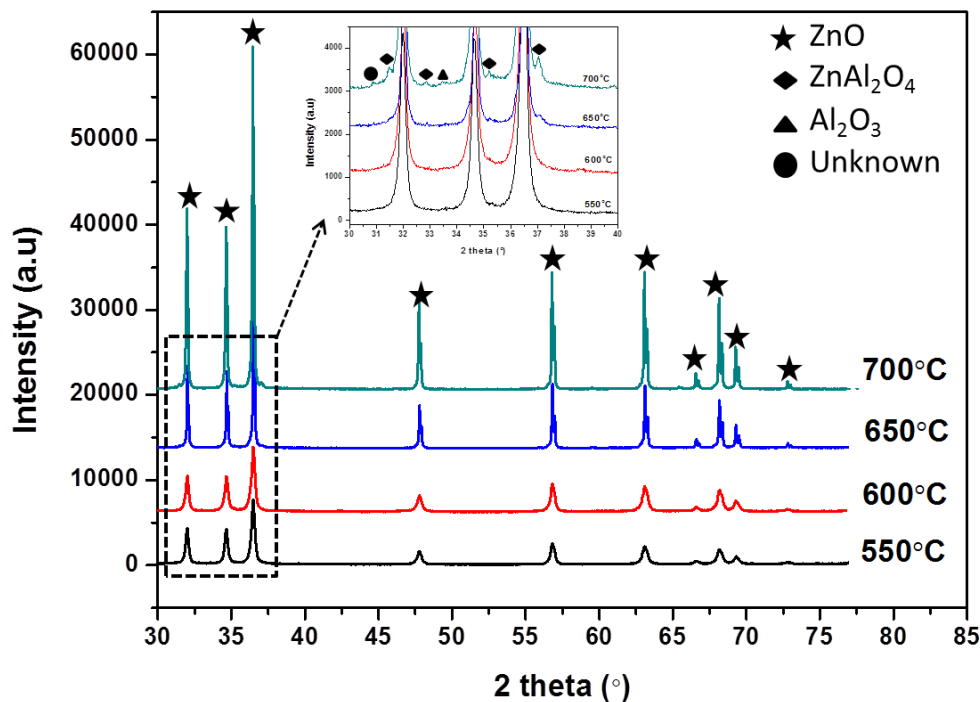


Fig. 5.9 XRD patterns of Al-doped ZnO ceramics at varying temperature

The SEM micrograph of 0 at% and 2 at% ceramics sintered at 700°C are given in Fig.5.10. It is shown that there is a decrease in the grain size when 2 at% Al is doped in the ZnO. The grains decreased from 5.8 μm for 0 at% to 0.76 μm for 2 at% with nano-precipitates of 104 nm that can be due to grain growth inhibiting effect as discussed in previous sections. Further

studies were done to understand the influence of sintering temperature on the microstructure of 2 at% Al doped ZnO, given in Fig. 5.11. It was observed that sintering at 550°C and 600°C did not change the grain size of the ceramics. However, at a temperature of 650°C and 700°C the grain size increased from initial grain size of 75 nm to 457 nm and 760 nm, respectively. EDS analysis on the sample sintered at 700°C indicated that the light phase is Al rich and the dark phase is Zn rich. This can be supported by the XRD results because the ZnAl_2O_4 and Al_2O_3 peaks are Al rich phases. Therefore, the light phase in the SEM analysis is the spinel phase of ZnAl_2O_4 and Al_2O_3 as determined by the XRD analysis. This is in conformity with the ZnAl_2O_4 peak observed in XRD results of Jood *et al.* [130], when fine nanoparticles of ZnAl_2O_4 were dispersed on ZnO grains in the SEM analysis. It was noticed that the spinel phase is in homogeneously distributed across the sample. The spinel phase may be beneficial or detrimental for the electrical properties such as resistivity and carrier mobility. Some reports indicated that it could lead to a decrease of the thermal conductivity while on the other hand it could be a hindrance in improving the electrical conductivity (scatters electrons) [33, 110, 111, 130, 131, 233]. EDS analysis of the sample sintered at 650°C did not indicate any secondary phases which may be attributed to the low concentration of ZnAl_2O_4 and Al_2O_3 . Further studies were conducted to reduce the concentration of secondary phase in the ceramics with full densification.

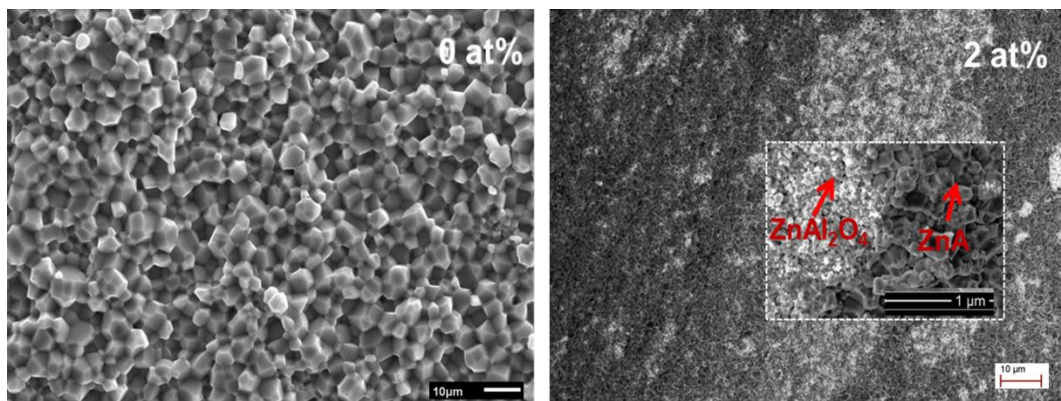


Fig. 5.10 SEM micrographs of 0 at% and 2 at% Al ZnO ceramic sintered at 700°C

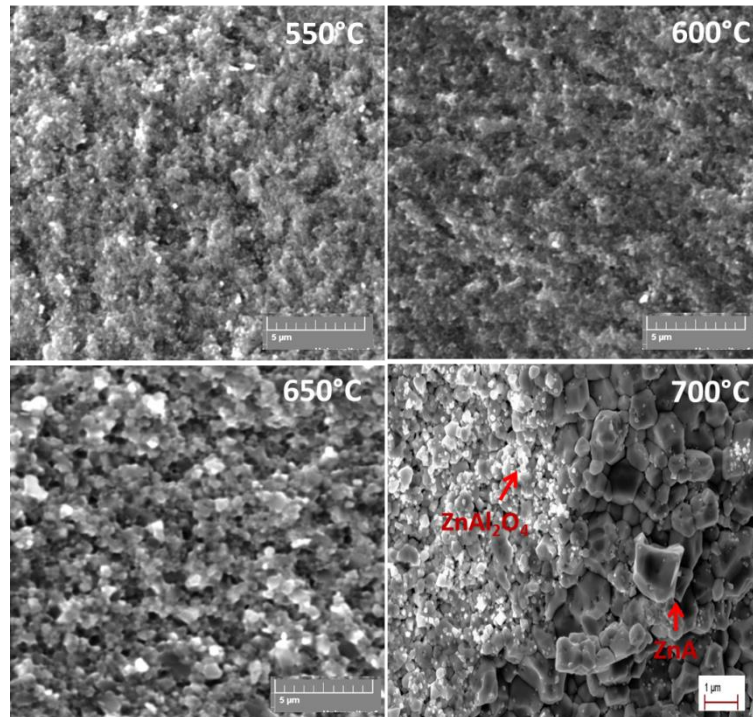


Fig. 5.11 SEM micrograph of Al-doped ZnO ceramic at different sintering temperatures

5.3.2.3 Reduction of the amount of spinel phase in Al-doped ZnO ceramics

In the previous section it was indicated that sintering at temperature above 650°C with a pressure of 250 MPa applied at room temperature causes the formation of the secondary phases that can be a hindrance in improving thermoelectric properties. It was proposed to apply the pressure immediately on the initial stages of holding time and to double the pressure while reducing the temperature, to avoid the presence of spinel phase in the sintered ceramics. At first the influence of the changes in sintering conditions on the densification was determined. As presented in Table 5.2 the relative density is constant at 84% when a pressure of 250 MPa is applied at room temperature or at 600°C. An increase in the relative density from 84 to 98.5% was observed when the sintering pressure was increased to 500 MPa during heating stage at a temperature of 600°C. However, the sintered ceramic cracked at this pressure due to distribution of residual stresses during cooling of sintered ceramic [245]. As a result, a densification of 98.6% was achieved at 650°C and 250 MPa without cracks. This will be beneficial in improving the electrical conductivity and better thermoelectric properties.

The XRD patterns of the ceramics sintered at different temperature, pressure and period of pressure application are indicated in Fig.5.12 and Fig. 5.13. For all the samples the major

phase structure is hexagonal ZnO structure. It was noted that applying the pressure at room temperature (RT) and decreasing the temperature from 650°C to 600°C the presence of secondary phases reduced in the ceramic, as they were not visible on the XRD patterns. It is possible that the concentration of the secondary phases was below the XRD detection limit. Whereas, when the pressure is applied during holding time (HT) for both 600°C and 650°C, the secondary phases were not detected as well. Similarly, when the pressure was increased from 250 to 500 MPa, the secondary phases were not observed (Fig.5.13).

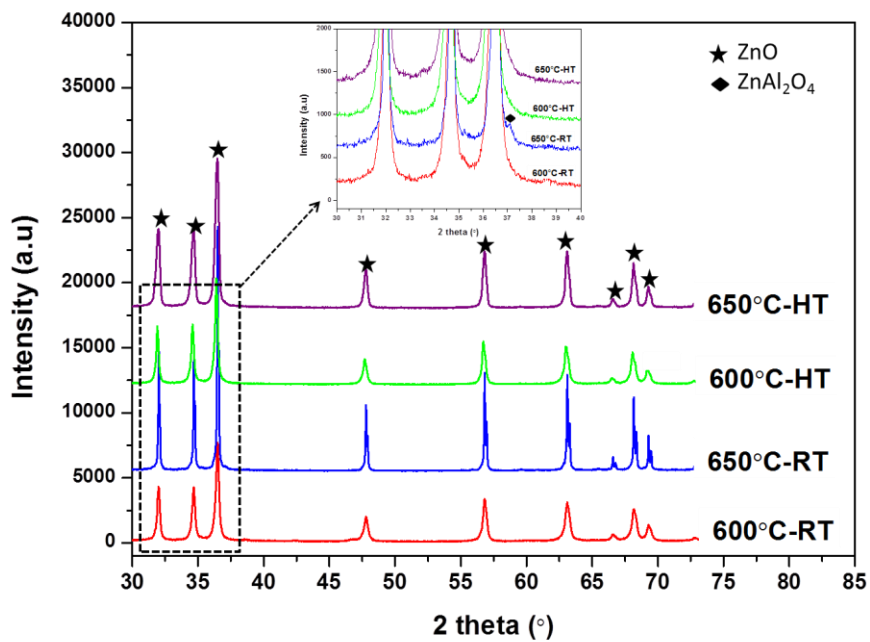


Fig. 5.12 XRD patterns of Al-doped ZnO ceramics sintered at 600C and 650C with a pressure of 250 MPa using RT and HT mode

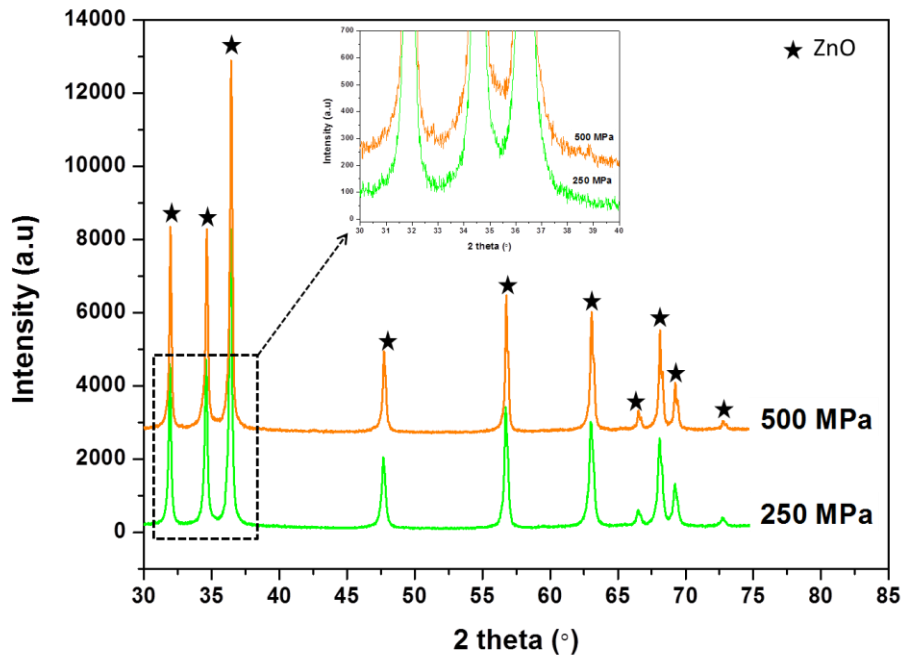


Fig. 5.13 XRD patterns of Al-doped ZnO ceramics sintered at 250 MPa and 500 MPa with a temperature of 600°C using HT mode

The SEM micrograph of the sample sintered at 650°C using HT mode is presented in Fig. 5.14. It was revealed that the nanostructure of the sample is maintained and there is no secondary phase detected in the ceramic. This sample was further annealed in air at 600°C for 24 h to obtain fully oxidized ceramic in order to ensure stable measurement and reproducibility of electrical properties. The influence of the annealing treatment on the microstructure of Al-doped ZnO ceramics in Fig.5.15 indicated an increase in the grain size from 90 nm to 140 nm. Additionally, the secondary phases were not present possibly because the amount is below the detection limit. XRD analysis of the annealed sample did not show any secondary phases.

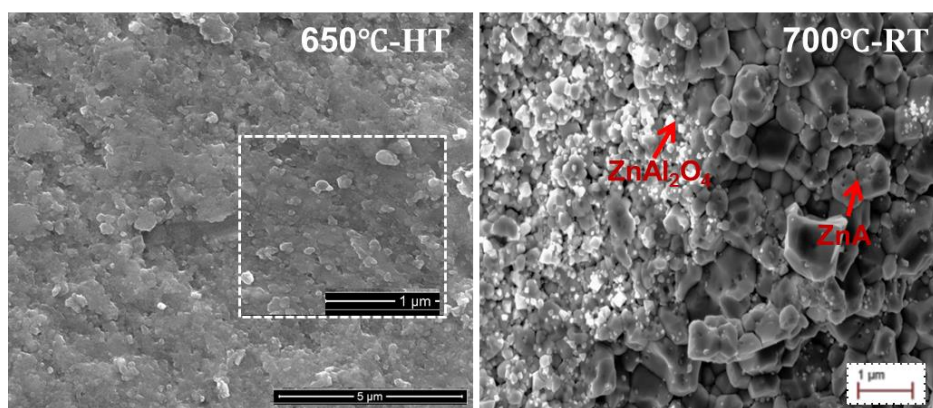


Fig. 5.14 SEM micrograph of Al-doped ZnO ceramics sintered at 650°C (HT) and 700°C (RT)

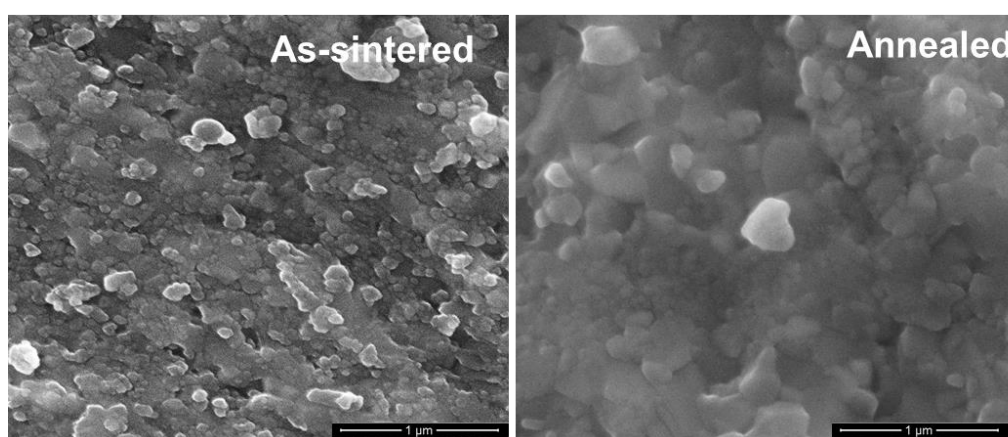


Fig. 5.15 SEM micrograph of annealed Al-doped ZnO ceramics sintered at 650°C (HT)

5.3.3 Thermoelectric properties

The thermoelectric properties were determined for the annealed ceramic sintered at 650°C (HT) as it had minimal/no secondary phase and densification of 98.6%. The resistivity as a function of temperature is given in Fig. 5.16; for the samples 0 at% and 2 at%. It is shown that addition of Al in ZnO reduces the resistivity especially at low temperature, less than 200°C. At 50°C the resistivity reduced from ~1960 Ω.cm to ~50 Ω.cm for 0 at% and 2 at%, respectively. This could be due to the substitution of Al³⁺ ions on the Zn²⁺ site creating extra free electrons [6, 33, 34, 37, 111, 131]. It is observed that the resistivity of both samples decreases with an increase in temperature which is significant of a semiconducting behavior. At high temperature the valence electrons gain enough energy to reach the conduction band, hence, the lowest resistivity of about 1 Ω.cm at 500°C [53]. Sondergaard *et al.* [109] reported the lowest resistivity as compared to our samples for the same Al content, i.e. resistivity values of 0.005 and 0.0015 Ω.cm at room temperature were obtained for samples sintered at

850°C and 900°C, respectively. This difference could be due to high carrier concentration caused by differences in preparation methods and sintering procedures creating more oxygen vacancies.

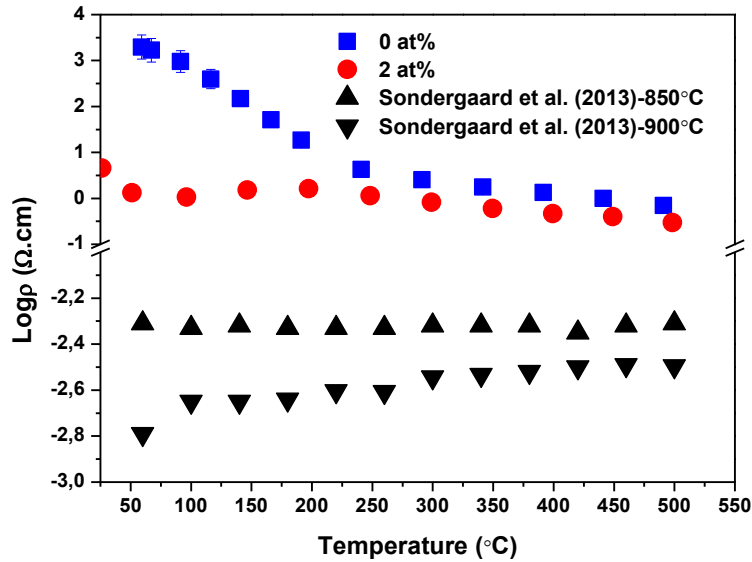


Fig. 5.16 Resistivity versus temperature for annealed pure and Al-doped ZnO ceramics sintered at 650°C (HT)

The Seebeck Coefficient as a function of temperature is given in Fig.5.17. The negative sign indicates n-type conductivity. Adding 2 at% Al reduced the Seebeck coefficient value from 800 to 175 $\mu\text{V/K}$ at 50°C. This decrease could be caused by the increase in the carrier concentration. The broadband equation (Eq.5.1) indicates inverse relationship between Seebeck coefficient and carrier concentration [10].

$$S_{bulk} = \frac{8m^* \pi^2 k_b^2}{3eh^2} T \left(\frac{\pi}{3n} \right)^{\frac{2}{3}} \quad [5.1]$$

The absolute Seebeck Coefficient, $|S|$, for the 2 at% sample increases with an increase in temperature from 50°C to 500°C; which is related to the scattering of the electrons at high temperature. The behaviour is different from pure ZnO which showed a decrease in the $|S|$ with temperature increment. Sondergaard *et al.*[109] reported similar behaviour to that of 2at% Al-doped ZnO with $|S|$ of about 125 $\mu\text{V/K}$ at 50°C for sintering at 850°C and 900°C.

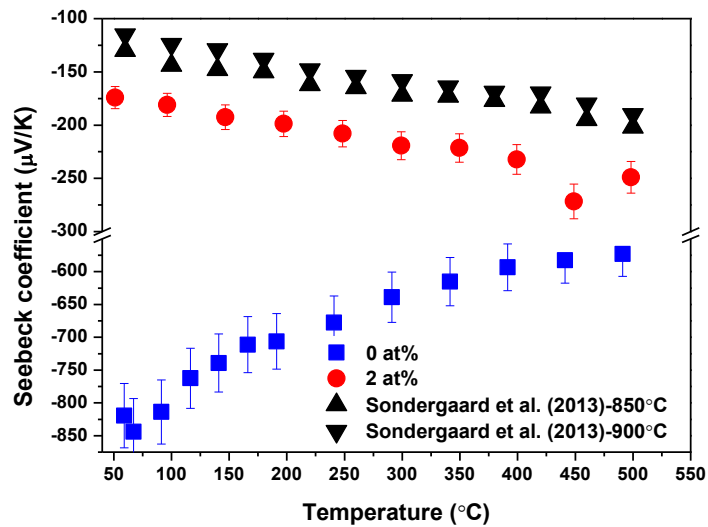


Fig. 5.17 Seebeck Coefficient versus temperature for annealed pure and Al-doped ZnO ceramics sintered at 650°C (HT)

The thermal conductivity versus temperature of the sintered ceramic presented in Fig.5.18 revealed that doping with Al into ZnO ceramic reduces the thermal conductivity from 50 W/m.K (0at%) to 27 W/m.K (2at%) at 50°C. This was caused by phonon scattering at the grain boundaries because of reduced grain size [6, 33, 34, 37, 111, 131]. It is shown that the thermal conductivity determined in this present work is almost similar to that reported by Sondergaard *et al.*[109] that could be due to the close proximity of the grain sizes values. A grain size difference of 20 nm was determined between the present study and that of Sondergaard *et al.* [109].

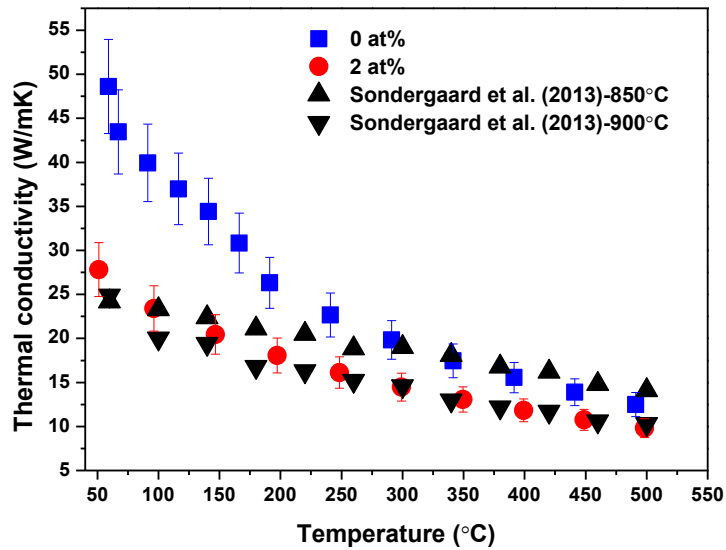


Fig. 5.18 Thermal conductivity versus temperature of annealed pure and Al-doped ZnO ceramics sintered at 650°C (HT)

The performance of the ceramics was determined using figure of merit, ZT , given in Fig.5.19. An increase in ZT was observed with temperature increment for all samples. It was observed that $0 \text{ at}\%$ performs better than the $2 \text{ at}\%$ ceramic by a ZT value of 1.5×10^{-3} at a temperature of 500°C. The improved performance is because of high Seebeck Coefficient shown by $0 \text{ at}\%$ ceramics. The performance of the $2 \text{ at}\%$ can be enhanced by improving the solubility of Al in ZnO through process manipulations such as sintering temperature increment and operating in vacuum to increase the electrical conductivity. Also, new materials could be incorporated with the Al-doped ZnO ceramic to enhance the electrical conductivity while maintaining the nanostructure of ceramic.

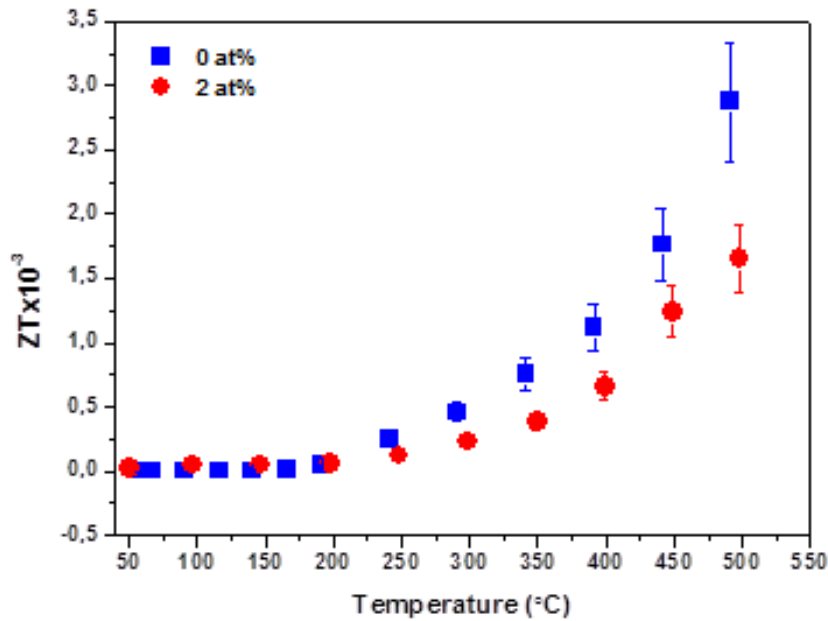


Fig.5.19 Figure of merit (ZT) of annealed pure and Al-doped ZnO ceramics sintered at 650°C (HT)

5.4 Conclusions

The synthesis and spark plasma sintering of Al-doped ZnO powder was studied in this chapter. The addition of 2 at% Al in ZnO powder reduces the grain size from 177 to 75 nm. The relative density of Al-doped ZnO sintered at a temperature of 650°C reaches high relative density of 98.9%. Sintering above 650°C causes an increase in the grain size which consequently decreases the relative density due to pores. The addition of Al into the ZnO ceramics caused a decrease in the grain size from 5.4 μm (without Al) to <1 μm (with 2 at% Al). Sintering above 650°C and applying the axial pressure during room temperature causes the presence of spinel phase, ZnAl_2O_4 , which is unwanted for thermoelectric properties. Applying the pressure during holding time prevents the formation of spinel phase. Annealing increased the grain size of the Al-doped ZnO ceramics by 50 nm. The resistivity of the Al-doped ZnO ceramics slightly reduces, which causes a decrease in the absolute Seebeck Coefficient as a result of increased carrier concentration. The reduction in the grain size leads to a decrease in the thermal conductivity due to phonon scattering at the grain boundaries. As a result, ZT value of 1.5×10^{-3} at 500°C, smaller than the one of pure ZnO ceramics was obtained. The low Seebeck Coefficient and electrical conductivity value of Al-doped ZnO ceramic caused the decrease in the performance. Even so, these results revealed the

importance of reduced thermal conductivity and low resistivity in improving thermoelectric properties of Al-doped ZnO ceramics. It is advised to do further experiments to optimize the amount of Al dopants in ZnO ceramics are required to improve thermoelectric properties either by incorporating new materials to develop new composites and/or optimize the sintering parameters.

Chapter 6

Spark plasma sintering of polyaniline dispersed in Al-doped ZnO ceramics for thermoelectric application

6 Spark plasma sintering of polyaniline dispersed in Al-doped ZnO ceramics for thermoelectric application

6.1 Introduction

The previous chapter (Chapter 5) discussed the thermoelectric properties of Al-doped ZnO ceramics. It was found that the ceramics were still resistive and have high thermal conductivity which affected their efficiency. The approach in this chapter is to incorporate new materials into the Al-doped ZnO ceramics to generate unique properties that could enhance the power factor ($S^2\sigma$).

Nowadays, conducting polymers (such as Polyaniline (PANI), polypyrrole, Polyethylenedioxythiophene (PEDOT) etc...) have attracted researchers attention as they are environmentally friendly, easy to synthesize, simple and reversible doping/dedoping chemistry, modifiable electrical conductivity and intrinsically low thermal conductivity [144, 147, 152, 246]. Among the various organic polymers, PANI is one of the most widely studied semiconducting organics that possess chemical stability and exceptional electrical properties [151, 153, 156, 157, 177]. Metal oxide/polymer composites are regarded as future candidates for thermoelectric application because they are light weight, cheaper and non-toxic [177, 246]. Metal oxide/polymer implies that the polymer is incorporated into the metal oxide in small quantities whereas polymer/metal oxide means that the metal oxide is added into the polymer. Composites such as BiCuSeO/PANI [247], $\text{Ca}_3\text{Co}_4\text{O}_9$ /PANI [248], TiO_2 /polymer based [150], $\text{Li}_{0.5}\text{Ni}_{0.5}\text{Fe}_2\text{O}_4$ /polyparaphenylene (PPP) [30] etc.... have also been investigated. The highest ZT of 0.54 at 1200K was obtained for 9wt% PPP/ $\text{Zn}_{0.95}\text{Ni}_{0.05}\text{O}$ composites prepared through spark plasma sintering [135]. It was because of reduced thermal conductivity as a result of drastic mismatch in the vibrational spectra of organic and inorganic materials [135, 139]. Also, the simultaneous improvement of Seebeck Coefficient and electrical conductivity due to selective scattering of charge carriers with low energy through energy filtering contributed to the enhanced ZT [178]. The behaviour of the nano-junctions in these composites provides unique properties that cannot be attained in either organic or inorganic materials individually.

At present there is no reported literature on the dispersion of PANI in Al-doped ZnO ceramics. Available work reports on the PANI composites explores the incorporation of ZnO nanocomposites in the polyaniline matrix, the ZT improved from 0.00075 to 0.0035 at room

temperature for pure PANI and 15 wt% Al doped ZnO nanorods [177], respectively. In this work, an attempt to understand microstructural and thermoelectric properties of PANI dispersed in Al-doped ZnO ceramics was carried out. Al-doped ZnO powder was prepared through co-precipitation route and thereafter mixed with activated PANI emeraldine salt. The composites were spark plasma sintered at low temperatures to obtain full densification by the studying the effect of the parameters: temperature, pressure, holding time and point of pressure application.

6.2 Materials and methodology

6.2.1 Preparation of $Zn_{0.98}Al_{0.02}O$ /Polyaniline powder

Al-doped ZnO ($Zn_{0.98}Al_{0.02}O$) powder was synthesised through co-precipitation technique followed by calcination at 600°C for one hour. It was incorporated with activated PANI Emeraldine salt prepared from PANI Emeraldine base (Sigma-Aldrich) using 1 M hydrochloric acid (HCl). PANI concentrations of 0.75 wt%, 5 wt% and 9 wt% labelled as 0.75PANI, 5PANI and 9PANI, respectively, were investigated.

6.2.2 Spark plasma sintering of $Zn_{0.98}Al_{0.02}O$ /Polyaniline powder

ZnO composites were consolidated using Dr. Sinter 2080 unit (SPS Syntex Inc., Japan) available at the Plateforme Nationale de Frittage Flash (PNF2) located at the Université Toulouse 3 Paul Sabatier using 8 and 20 mm inner diameter tungsten carbide die. The ceramics were sintered at a heating rate of 50°C up to 250°C to avoid degradation of polyaniline, at axial pressures of 250-850 MPa and dwell time of 10-30 min.

6.2.3 Characterization of $Zn_{0.98}Al_{0.02}O$ /Polyaniline powders and ceramics

The microstructure analysis of the ZnO composites was done using Scanning Electron Microscopy (MEB JEOL JSM65 10LV) while an X-ray diffractometer (XRD Bruker D4) was used to analyze the phase structure. A combination of Differential Thermal Analysis (DTA) and thermogravimetric analysis (DAT GTA) (Setaram TAG16) was used to study the thermal behaviour of the powders at a heating rate of 3°C/min up to 1000°C. In addition to the above characterizations, Fourier Transform-Infrared Spectroscopy (FTIR) (Spectrometry Frontier and Microscope Spotlight 400 Series: MIR-NIR) spectra were recorded at a wavelength range of 650–4000 cm^{-1} . Raman Spectrometer (JobinYvon LabRAM HR800) was used to identify chemical structures of selected samples. Analysis was done using 633 nm red laser at a grating, accumulation and time of 600 tr, 3 and 30s, respectively.

6.2.4 Electrical properties of $Zn_{0.98}Al_{0.02}O$ /Polyaniline ceramics

Seebeck coefficient and resistivity measurements of the dense ceramics were simultaneously performed using ZEM-3 (Ulvac-Riko, CRISMAT). The dense ceramics were cut into 9x3x3 mm bars and coated at their extremities with gold to ensure electrical ohmic contacts. Graphite foil was inserted on both sides of heaters to have a good electrical and thermal contact with the sample. The thermal conductivity (k) (W/m.K) was determined using equation 6.1 by measuring thermal diffusivity (α) (m^2/s), ceramic density (d) (g/cm^3) and heat capacity (C_p) (J/K). The samples were cut into dimensions of 6x6x1 mm bars for the thermal conductivity measurements. The bandgap of the ceramics were determined using the photovoltaic measurements (Bentham PVE 300 PV).

$$k = \alpha(T)C_p(T)d(T) \quad [6.1]$$

6.3 Results and discussion

6.3.1 Characterization of mixed powders of Al-doped ZnO and Polyaniline

As alluded earlier, Polyaniline (PANI) emeraldine base was activated using 1 M hydrochloric (HCl) acid to Polyaniline (PANI) emeraldine salt to make it to be more electrically conductive [151]. The analysis presented here begins with that of PANI only before adding it into the metal oxide. XRD analysis of the polyaniline powders given in Fig.6.1 showed that both PANI emeraldine base and salt have two broad peaks which diffracted at 2-theta angles of 20° and 24° due to the parallel and perpendicular periodicity of the PANI chains [249-251]. The partial crystallinity is as a result of the repetitive rings of benzenoid and quinoid in the PANI. The addition of HCl in the PANI emeraldine base caused a depreciation of the intensity at 20° and sharpening of the peak at 24° which could be related to the crystallization of the polymer [252]. The SEM micrographs of the polyaniline emeraldine powders given in Fig.6.2 indicated that polyaniline emeraldine base powder has platelet like structures. The addition of the HCl solution induces the formation of aggregates with small crystallites (Fig.6.2 (b)), confirming the XRD results.

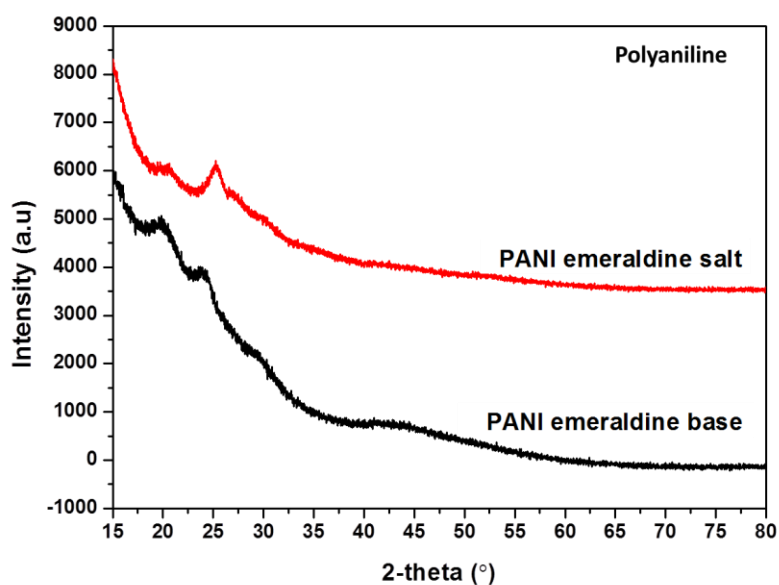


Fig. 6.1 XRD patterns of polyaniline emeraldine powder

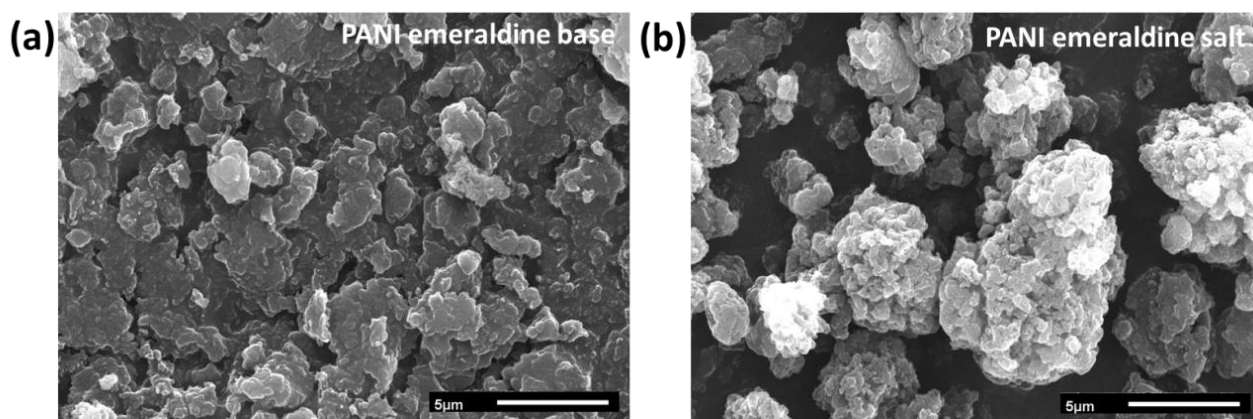
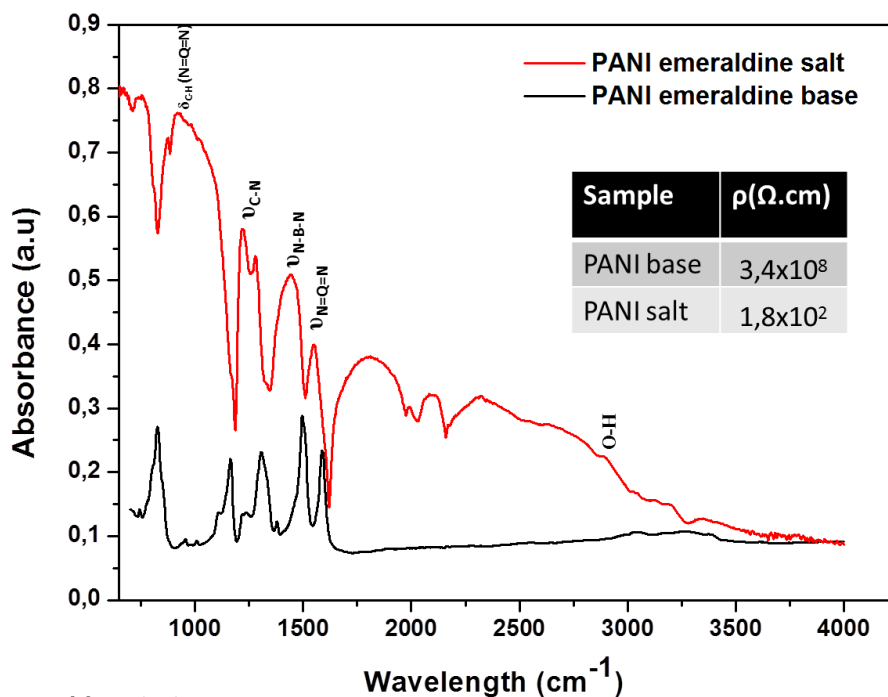


Fig. 6.2 SEM micrographs of polyaniline emeraldine powder before (a) and after (b) addition of HCl.

After phase and morphology analysis, the molecular structure of the polymers was studied using FTIR and the results are given in Fig.6.3. It was observed that there is a red-shift of the spectrum of PANI emeraldine salt as compared to that of PANI emeraldine base which could be as a result of enhanced charge delocalization and formation of conjugation structure [151]. The absorption band observed at 1450 cm^{-1} for PANI emeraldine base shifted to a lower frequency by $\sim 450\text{ cm}^{-1}$ and became more broadened ascribing to the aromatic C-H-in plane bending vibrations of the quinoid structure. This is a characteristic peak for conductive PANI, and it is normally considered to be an electronic-like band in which there is a measure of the

degree of delocalised electrons in PANI. These delocalised electrons may account for the drop in resistivity by 6 orders of magnitude for PANI salt [151], shown in the table inserted inside the Fig. 6.3.



Abbreviations:

ν - stretching vibrations; δ - bending vibrations; B- benzenoid unit; Q- quinoid unit

Fig. 6.3 FTIR spectrum of polyaniline powders with inserted table of resistivity at room temperature

Thermal stability studies of the conducting polymer were carried using thermogravimetric analysis (TGA). The results from the TGA analysis of the PANI powders are given in Fig.6.4. The mass loss of the PANI emeraldine base slightly decreases due to moisture content from room temperature to 300°C, thereafter sharply decreases at 400°C as a result of degradation of the organic components. It was observed that the PANI emeraldine salt losses more mass by 15% as compared to PANI emeraldine base, which could be due to the removal of chlorine ions. Similarly to the PANI emeraldine base, sharp decrease was observed at 400°C.

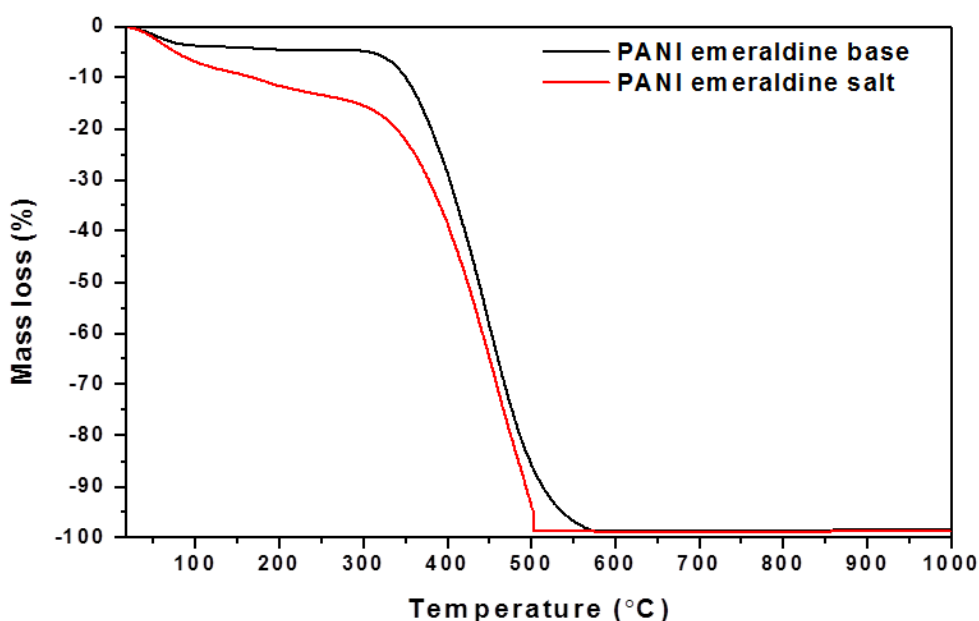


Fig. 6.4 Thermogravimetric analysis of polyaniline powder before and after acid activation

After the above basic and fundamental characterisation of the activated polyaniline, the salt was dispersed in Al-doped ZnO powder at concentrations between 0.75 wt% to 9 wt% to investigate its effect on the thermoelectric properties of the doped metal oxide. Prior to the electrical measurements, XRD analysis of the Al-doped ZnO/PANI powders was done and the results are given in Fig. 6.5. It was observed that the phase structure did not change and is hexagonal ZnO, similarly to reference samples (ZnO and ZnA). However, there were little peaks broadening which could be as a result of the amorphous nature of the polymer.

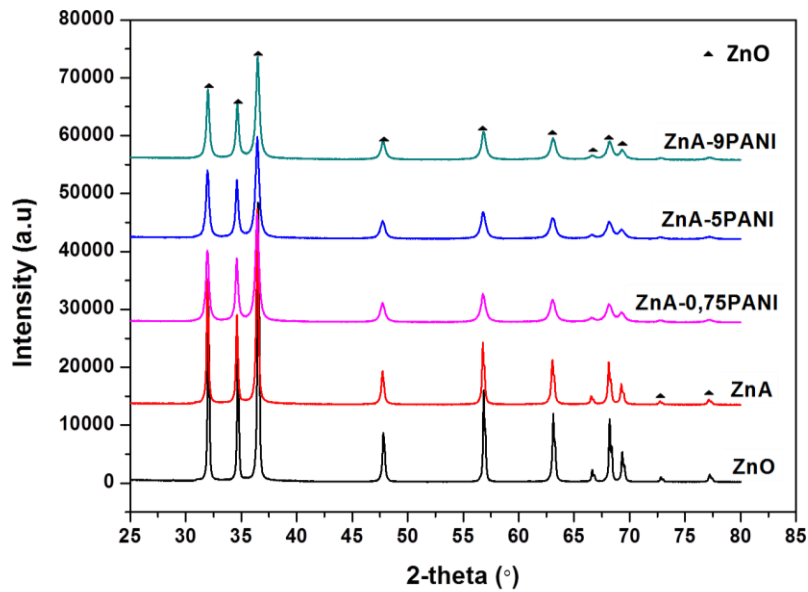


Fig. 6.5 XRD patterns of Al-doped ZnO powders and PANI composites.

Morphology studies (using SEM) of the Al-doped ZnO/PANI powders showed that addition of the polyaniline binds the grains together as shown in Fig.6.6. The increase in the concentration from 0.75 wt% to 9 wt% causes increase in the aggregates size.

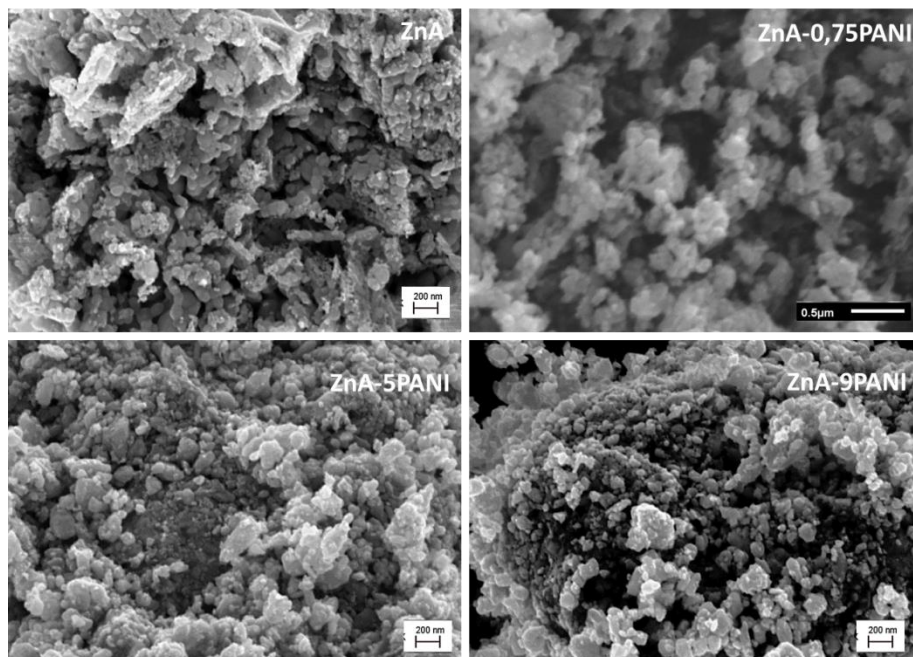


Fig. 6.6 SEM micrographs of Al-doped ZnO powders doped with polyaniline powder
FTIR analysis given in Fig.6.7 was done to confirm the presence of polyaniline in the powders. Compared to the reference sample, ZnA, it was observed that the powders incorporated with PANI have new peaks between 1000 and 1750 cm^{-1} , an indication of PANI

presence in the powders. The peak 1000 cm^{-1} shifted to the right by 112 cm^{-1} , which may be related to the changes in the PANI structure due to the presence of Al-doped ZnO nanoparticles. The Al-doped ZnO nanoparticles could have enhanced charge delocalization and the formation of conjugation structure [151], which are responsible for red shift in absorption bands in PANI.

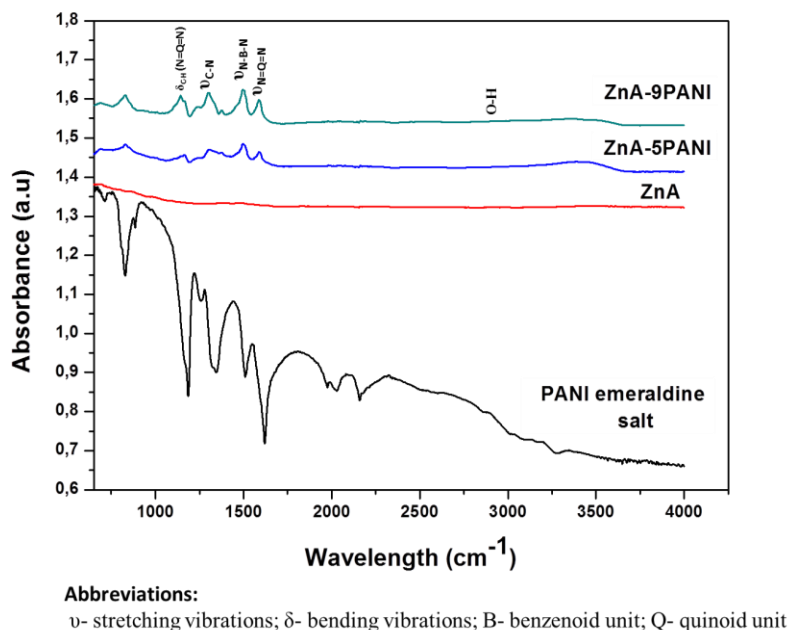


Fig. 6.7 FTIR spectrum of Al-doped ZnO powders doped with polyaniline powder

As a matter of principle, to check thermal stability of the doped oxide-PANI composite, thermogravimetric analysis of Al-ZnO/PANI powder (Fig.6.8) was done. It was observed that there was more mass loss in the Al-ZnO/PANI composites as compared to the reference sample, ZnA. Mass difference of about 2% at 320°C was observed. ZnA-5PANI and ZnA-9PANI indicated to have the same decrease in mass from room temperature up to 320°C . Between 320°C and 400°C , a sharp decrease in mass is observed for both samples. ZnA-5PANI had total 4% mass loss whilst ZnA-9PANI had 5.5%. This analysis shows that to avoid the loss of polyaniline during sintering, it is advisable to sinter below 300°C .

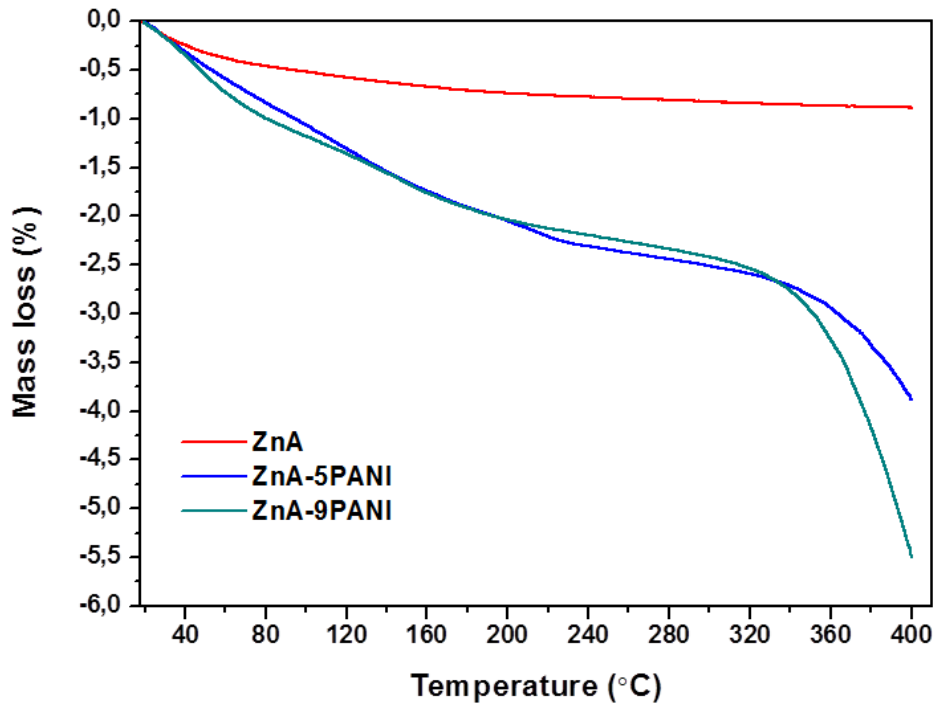


Fig. 6.8 Thermogravimetric analysis Al-doped ZnO powders doped with polyaniline powder

6.3.2 Characterization of sintered Al-doped ZnO/PANI ceramics

The Al-doped ZnO/PANI powders were sintered using spark plasma sintering at a temperature of 250°C to avoid degradation of the polyaniline powder. The amount of polyaniline was varied between 0.75 - 9 wt%. A concentration of 9 wt% was used because of reported high ZT value of ~0.54 on Zn_{0.95}Ni_{0.05}O/9wt% Polyparaphenylene ceramics [135]. However, it is ideal to start with a lower concentration to have an overview on the effect of polyaniline without affecting the properties of Al-doped ZnO. The effect of holding time, pressure and point of pressure application were studied on 0.75 wt% PANI. The relative density of the ceramics given in Table 6.1 showed that the relative density of ZnA-0.75PANI ceramics slightly improved the relative density by 3.9 % when the holding time was increased from 10 to 30 min. Further, when the pressure was increased from 500 to 850 MPa the relative density increased from 69.9% to 79.6%, respectively. Surprisingly, when the 850 MPa pressure was applied at room temperature, the relative density was enhanced to 97%. However, cracks were observed on the ceramic. The high increase in relative density at room temperature could have been caused by the coverage of the polymer around the grains.

To obtain high density and un-cracked ceramic, the concentration of PANI was manipulated. Previous studies by Wu *et al.* [135] reported the highest ZT of 0.54 at 1200 K for ZnO/polymer based ceramics using 9 wt% PPP. In the light of this previous work, an attempt to improve the relative density was done by using PANI concentration of 9 wt% (*ZnA-9PANI*). For this sample, applying a low pressure of 250 MPa at room temperature allowed to get a relative density of 95.4%. Furthermore, applying the pressure during first holding stage using 8 mm die increased the relative density to 97.3%, and for 20 mm dies relative density of 95.9% was obtained. The concentration of PANI was decreased to 5 wt% (*ZnA-5PANI*) to improve the densification for 20 mm die; a high relative density of 98.5% was obtained at lowest temperature of 250°C and a pressure of 250 MPa. Unlike in the report of Wu *et al.* [139] and Wu *et al.* [135] who densified at high temperatures of 827°C and 900°C, respectively, we were able to obtain full densification at very low temperature of 250°C.

The XRD patterns of the ceramics given in Fig. 6.9 did not show any presence of second phase after sintering. Rather, a broadening of ZnA-5PANI and ZnA-9PANI peaks was observed as compared to ZnO and ZnA, which could have been caused by the amorphous nature of the polymer and/or retained nanostructure of the ceramic. Sintering at low temperature decreases grain growth rate [100, 107, 209], as a result the nano-grains are retained.

Table 6.1 Relative density of sintered Al-doped ZnO/PANI ceramics

No.	Die diameter	Temperature	Initial pressure	Initial holding time	Final pressure	Final Holding time	Relative density
	mm	(°C)	MPa	min	MPa	min	%
ZnA-0.75PANI							
1.	8	250	-	-	500, HT	10	69.9±0.9
2.	8	250	-	-	500, HT	30	73.8±1.8
3.	8	250	-	-	850, HT	10	79.6±0.6
4.	8	250	-	-	850, RT	10	97.4±0.1
ZnA-5PANI							
5.	20	250	150, RT	10	250, HT	10	98.5±0.1
ZnA-9PANI							
6.	8	250	-	-	250,RT	10	95.4±0.1
7.	8	250	150, RT	10	250,HT	10	97.3±0.1
8.	20	250	150, RT	10	250, HT	10	95.9±0.1

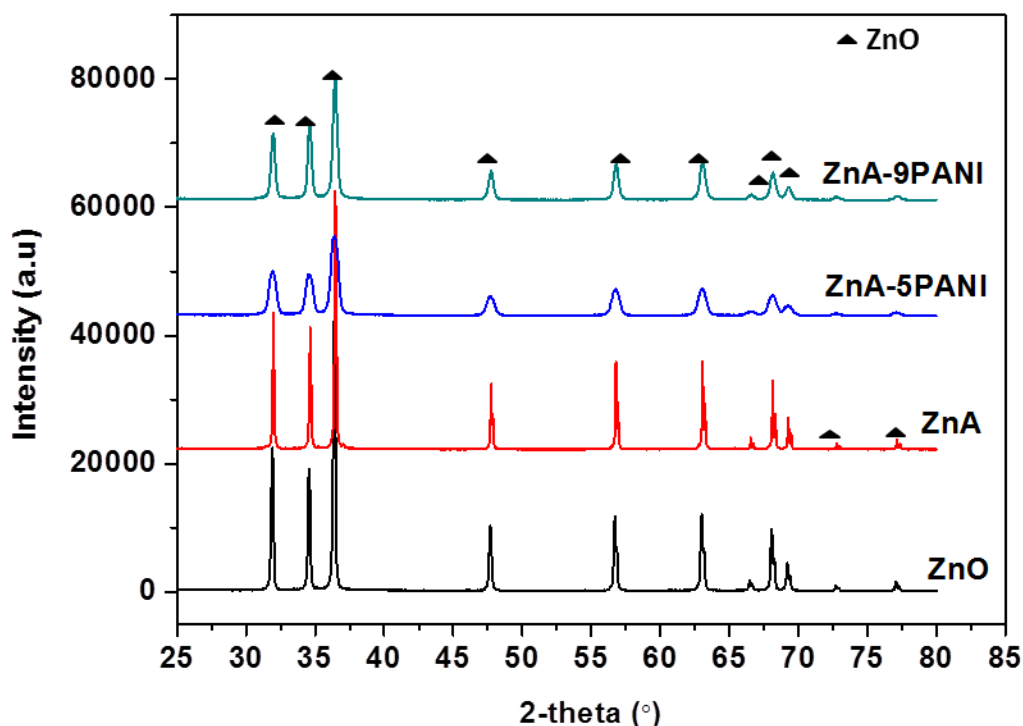


Fig. 6.9 XRD patterns of pure ZnO, ZnA, ZnA-5PANI and ZnA-ZA9PANI ceramics

The SEM micrographs in Fig. 6.10 revealed a decrease in the grain sizes from 140 nm of annealed *ZnA* ceramics to 86 nm and 50 nm for *ZA5P* and *ZA9P* ceramics, respectively. The presence of PANI in the ceramics was confirmed by TEM analysis (Fig. 6.11); the dark shade corresponds to ZnA grains while the light shade corresponds to polyaniline. From the TEM micrographs it could be suggested that the polyaniline covers the grains of the ZnA which could be beneficial in lowering the thermal conductivity by introducing a barrier to the flow of phonons [30, 135, 139].

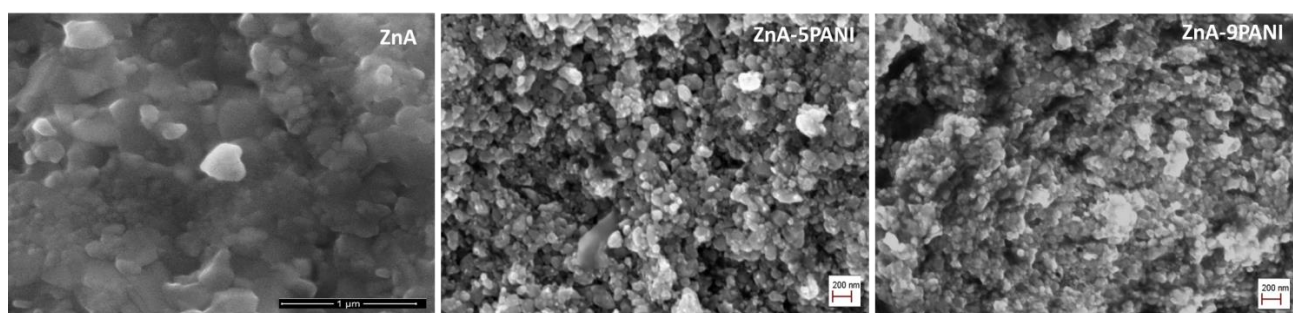


Fig. 6.10 SEM micrographs of ZnA, ZnA-0,75PANI ZnA-5PANI and ZnA-ZA9PANI ceramics

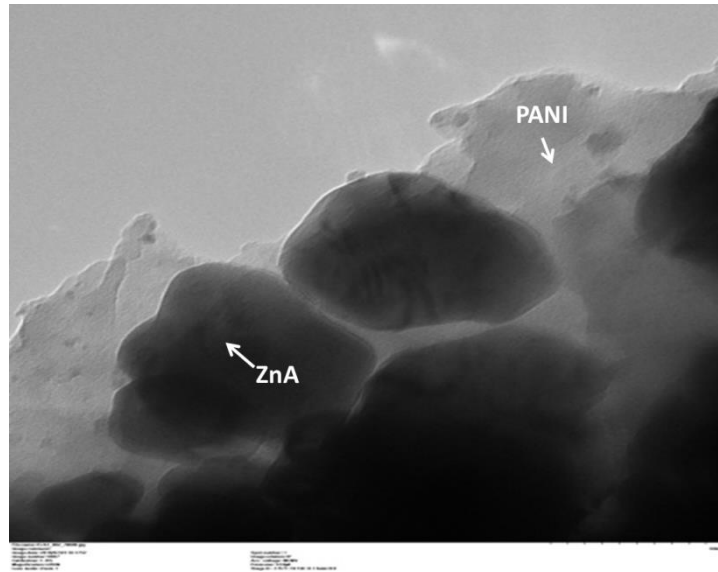


Fig. 6.11 TEM micrographs of ZnA-ZA9PANI ceramic

Raman analysis was conducted on the as-sintered ZnO composite ceramics to confirm the presence of PANI after sintering. The Raman spectrum given in Fig. 6.12 showed that a reference sample, ZnA, has sharp peak at 430 cm^{-1} which is related to the non-optical phonon E_{2H} mode of ZnO due to vibrations of O and Zn sublattice [253, 254]. The weak peak 380 cm^{-1} is multi-phonons scattering process of E_{2H} - E_{2L} and A1 phonons, respectively [253]. The peaks 1250 and 1300 cm^{-1} on the ZnA spectrum could be due to CO_2 from the atmosphere. It was noticed that the incorporation of polyaniline into ZnA caused the development of new peaks related to the vibrations of the PANI chains. The bands appearing between 1100 - 1600 cm^{-1} correspond to the stretching modes of PANI structure [255, 256]: 1600 cm^{-1} could be ascribed to C-C stretching vibration of benzene ring, 1470 - 1590 cm^{-1} could be the deformation vibrations of N-H, 1340 - 1390 cm^{-1} could be telling information about carrier vibrations in PANI in C-N polaronic structure. 1220 cm^{-1} could be ascribed to C-N stretching mode of polaronic unit. 1180 cm^{-1} may be related to C-H vibrations of aromatic rings. The bands between 400 - 1010 cm^{-1} could give information about the deformation vibrations of the benzene rings. The raman analysis has confirmed the presence of PANI in the ceramics as observed in the TEM results. The influence of the deformed structure of the PANI on thermoelectric properties will be discussed in detail.

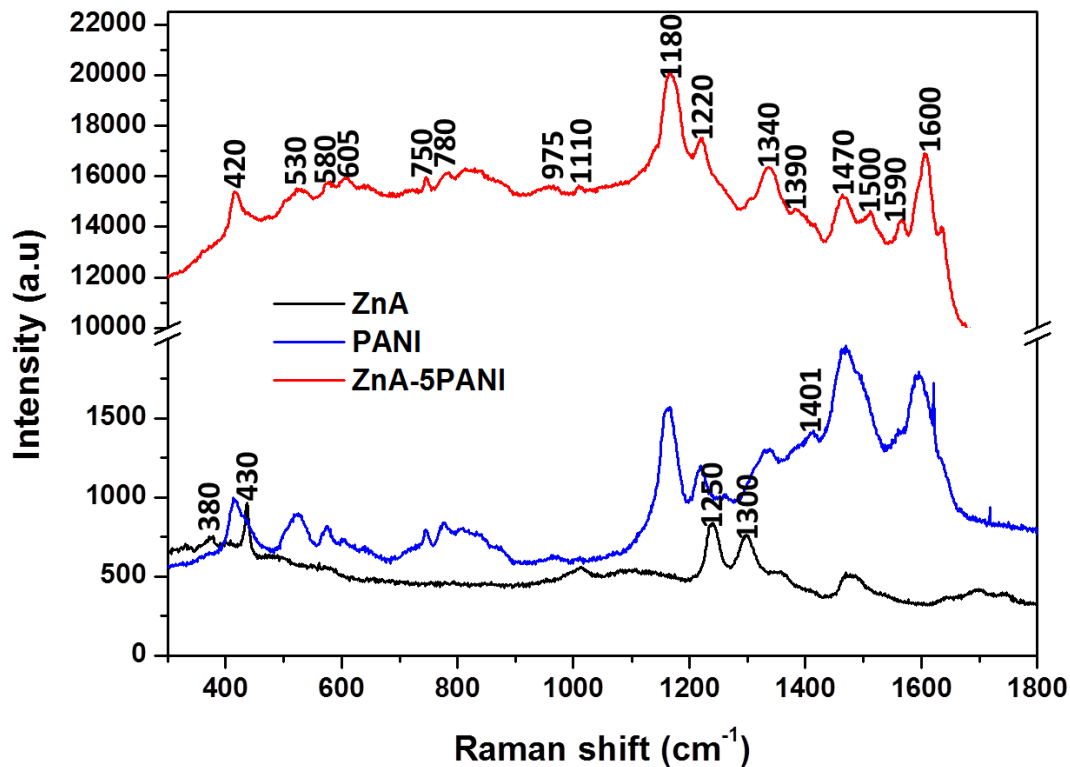


Fig. 6.12 Raman spectrum of ZnA and ZnA-5PANI ceramics and PANI pellet

6.3.3 Thermoelectric properties of sintered ceramics

6.3.3.1 Thermal conductivity

The objective of introducing Polyaniline (PANI) was used to reduce the thermal conductivity of ZnO ceramics while maintaining high Seebeck Coefficient. We were successful in this regard as the thermal conductivity decreased from 25 W/mk in the ceramic with 0 wt% to 6 W/mk and 3 W/m.k in 5 and 9 wt% samples respectively. These results are shown in Fig 6.13. The achievement was great in that it was below the target value of 5 W/mk. This value was set based on the best performing materials (such as Bi composites, Se composites etc...) with thermal conductivities between 2-3 W/m.K [257]. The drastic decrease is most likely due to the mismatch in phonon vibrations in PANI and ZnA (see Fig 6.14) [135, 139]. The thermal vibrations of PANI and ZnA are different, at the interface there is a clash of phonon flow see illustration in Fig 6.14. It was also observed that the thermal conductivity does not change much with temperature increase. The behaviour is different from those reported by

Wu *et al.* [135, 139], they observed expected decrease in the thermal conductivity with an increase in temperature. The difference could be related to the material properties (such as grain size) and processing procedures (such as type of polymer, sintering technique).

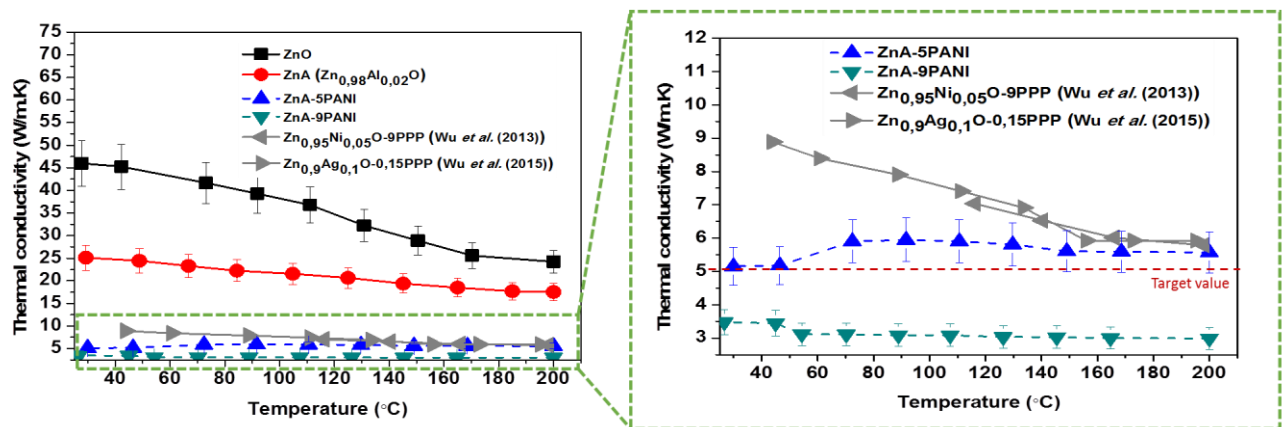


Fig. 6.13 Thermal conductivity of ZnO, ZnA, ZnA-5PANI and ZnA-ZA9PANI ceramics

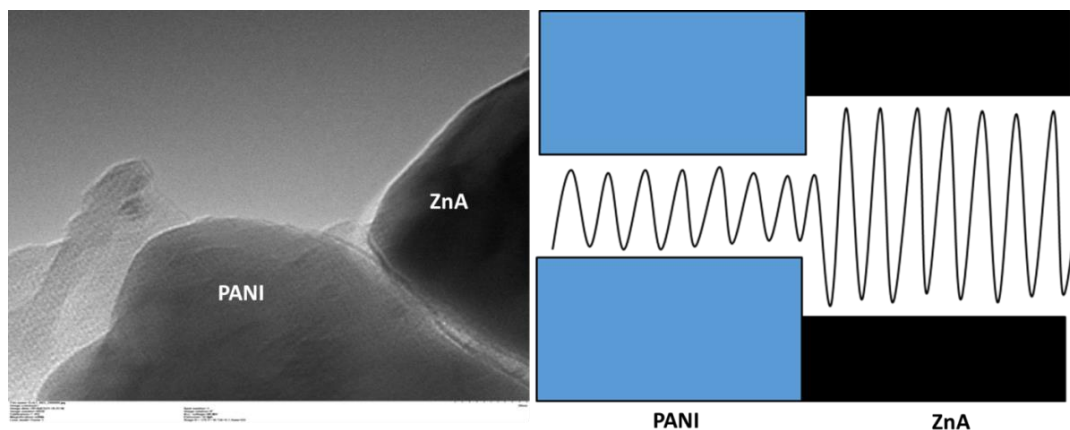


Fig. 6.14 Illustration of thermal vibrations of ZnA-ZA9PANI ceramic at the interface[150]

6.3.3.2 Resistivity and Seebeck Coefficient

Figure 6.15, shows the resistivity variation of the sintered ceramics as a function of temperature. It is evident that incorporating polyaniline into the samples lowered the resistivity when compared to the reference samples (*ZnA and ZnO*). The addition of polyaniline caused a decrease in the resistivity from 5.62 $\Omega\cdot\text{cm}$ (*sample ZnA*) to 0.78 and 0.67 $\Omega\cdot\text{cm}$ for 5 wt% and 9 wt% PANI, respectively, at room temperature. The decrease in the resistivity could have been caused by the high mobility of charge carriers determined through Hall measurements: 26162 $\text{cm}^2\text{V}^{-1}\text{s}^{-1}$ and 834 $\text{cm}^2\text{V}^{-1}\text{s}^{-1}$ for 5wt% and 9wt% PANI,

respectively. Wu *et al* [135, 139] reported resistivity values of 0.008 and 0.006 $\Omega\cdot\text{cm}$ for $\text{Zn}_{0.9}\text{Ag}_{0.1}\text{O}-0.15\text{PPP}$ and $\text{Zn}_{0.95}\text{Ni}_{0.05}\text{O}-9\text{PPP}$, respectively. The dissimilarities in resistivity could have been caused by the different powder preparation and sintering methods. The enlarged image of resistivity vs temperature indicated that there is a transition after 120°C , this could be due to material instability or phase changes, thermogravimetric analysis showed continued decomposition of the material even after 120°C (Fig.6.8). As a result, the electrical conduction mechanism changed after 120°C , The Arrhenius plot for the temperature range 120°C to 190°C of ZnA-5PANI and ZnA-9PANI is given in Fig. 6.16 and it indicates an almost a linear fit. This proves that the conduction mechanism of the charge carriers is thermally driven when charge carriers first acquire certain amount of energy heat energy before they move from one point to the other, this is the typical mechanism common in semiconductors. This mechanism is different from what happens in the low temperature range from 30°C to 100°C , in which the conduction mechanism is typical of a material in the insulating regime.

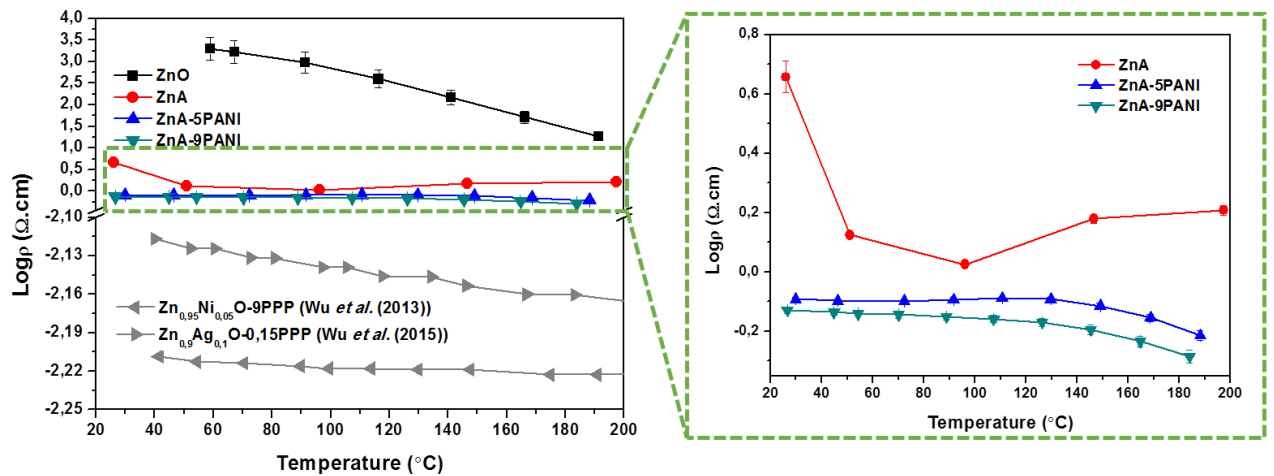


Fig. 6.15 Resistivity of ZnO, ZnA, ZnA-5PANI and ZnA-9PANI ceramics

Table 6.2 Determined physical properties of Al-doped ZnO/PANI ceramics

Sample	n (cm^{-3})	μ ($\text{cm}^2\text{V}^{-1}\text{s}^{-1}$)	bandgap (eV)
ZnA-5PANI	2.25×10^{15}	26162	~3
ZnA-9PANI	9.14×10^{15}	834	~3

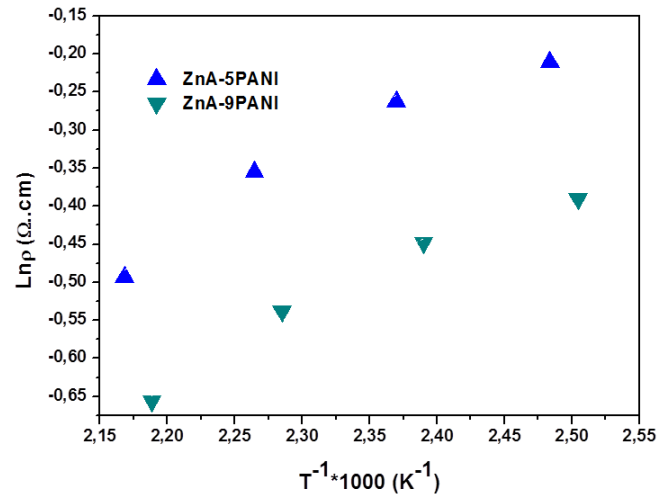


Fig. 6.16 Arrhenius plot of ZnA-5PANI and ZnA-9PANI

The Seebeck Coefficient versus temperature is given in Fig. 6.17; it was observed that for all the samples the Seebeck Coefficient values are negative which indicates n-type conductivity behaviour. We observed that doping ZnA with PANI caused a decrease in the absolute value of Seebeck Coefficient from 175 to 140 $\mu\text{V/K}$ at room temperature for both polymer samples. The decrease could have been caused by the large effective mass of the polymers [258]. Increasing the concentration of PANI from 5 wt% to 9 wt% gave insignificant change of the Seebeck Coefficient of the ceramics, absolute Seebeck Coefficient of 150 $\mu\text{V/K}$ was obtained at room temperature. At 40°C, the Seebeck Coefficient was 144 and 149 $\mu\text{V/K}$ for 5 and 9 wt% PANI, respectively. It was noticed that the Seebeck Coefficient remained almost the same with an increase in temperature similar to those reported by Wu *et al.* [135, 139] for polyparaphenylene doped ZnO based ceramics.

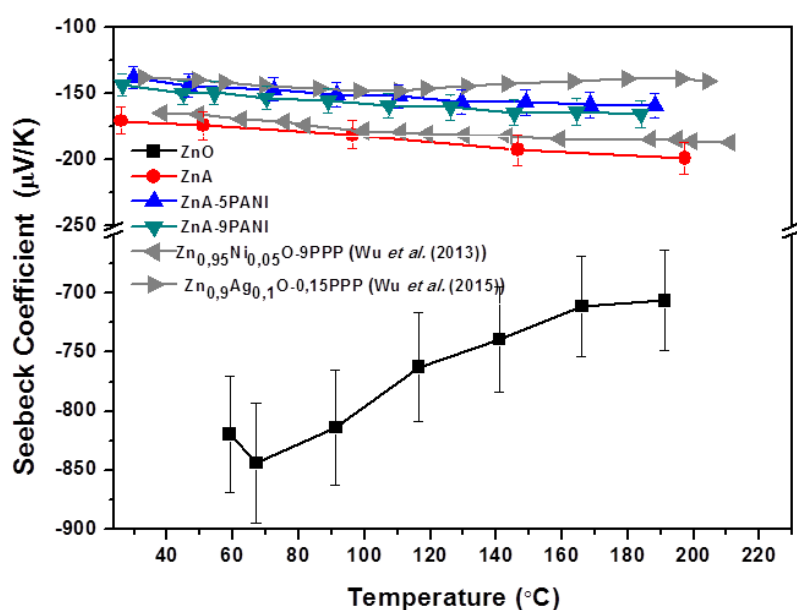


Fig. 6.17 Seebeck Coefficient of Al-doped ZnO/PANI ceramics

6.3.3.3 Performance of Al-doped ZnO/PANI ceramics

The performance of the ceramics as a function of temperature was evaluated using the power factor (PF) and figure of merit (ZT) respectively reported in Fig. 6.18.a and b. As presented in Fig. 6.18 (a and b), an increase in the PF and ZT was observed with an increase in temperature for all the samples. The power factor of the ceramics given in Fig. 6.18 (a), revealed that the addition of PANI into Al-doped ZnO composites improved the electrical performance of the ceramics. This may be due to improved electrical conductivity and stable Seebeck Coefficient. At 60°C, the power factor for ZnO, ZnA, ZnA-5PANI and ZnA-9PANI were 0, 0.022, 0.025, 0.031 W/mK², respectively. Maximum power factor of 0.05 and 0.035 W/mK² was obtained for 5 and 9 wt% PANI, respectively. The figure of merit (ZT) presented in Fig. 6.18 (b) indicated that the incorporation of PANI into the ceramics improved the ZT by 0.004x10⁻³ for every 20°C increment due to reduced thermal conductivity. Maximum performance was obtained from ZnA-9PANI with a ZT of 0.8x10⁻³ at 190°C. Table 6.3 compares the ZT of different materials at 190°C, higher ZT values of 37x10⁻³ and 39x10⁻³ were reported for Zn_{0.9}Ag_{0.1}O-0.15PPP[139] and Zn_{0.95}Ni_{0.05}O-9PPP[135], respectively. These materials reported by Wu et al [135, 139] performed better than the ones reported in this work because of their higher electrical conductivity they possess, which could be influenced by the different methods of ceramic's preparation techniques such as sintering conditions, powder synthesis methods.

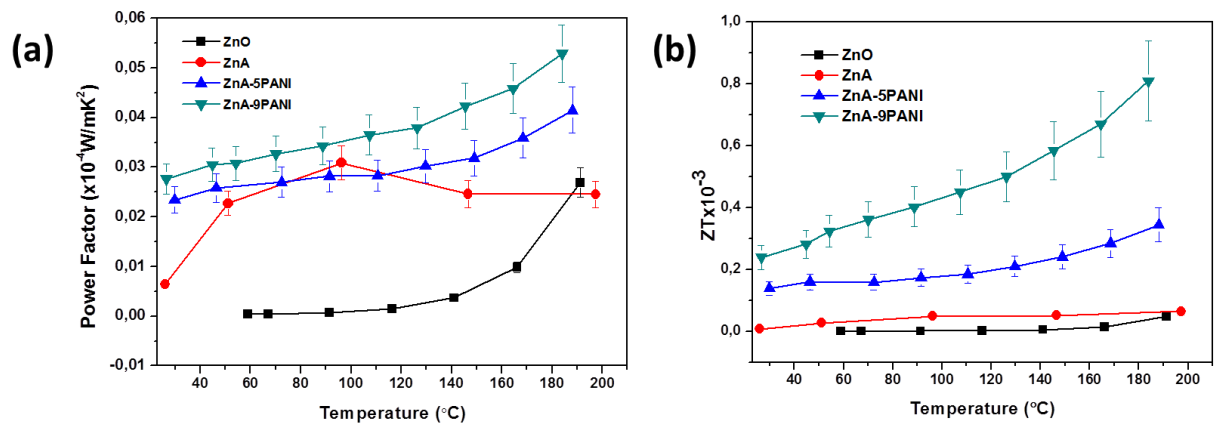


Fig. 6.18 Performance of Al-doped ZnO/PANI ceramics: (a) Power factor (b) Figure of merit

Table 6.3 Figure of merit of ZnO based polymer composites at 190°C

Ref.	ZT $\times 10^{-3}$
ZnO	0,05
ZnA	0,06
ZnA-5PANI	0,34
ZnA-9PANI	0,81
Zn _{0.95} Ni _{0.05} O-9PPP[135]	39
Zn _{0.9} Ag _{0.1} O-0.15PPP[139]	37

6.4 Conclusions

The influence of the incorporation of polyaniline in Al-doped ZnO, sintered by spark plasma sintering, was studied in this chapter. Full densification of 98.5% and 97.3% was achieved for ZnA-5PANI and ZnA-9PANI, respectively, at very low temperatures of 250°C. Because of the reduced sintering temperature, the nanometric size (~40nm) of the ceramic grains were maintained. As a result, low thermal conductivity below 5 W/mK was achieved with the incorporation of PANI into the ZnA. The resistivity was also slightly improved and stable high Seebeck Coefficient of ~150 $\mu\text{V/K}$ was determined. A maximum ZT value of 0.8×10^{-3} was achieved at 190°C using ZnA-9PANI as compared to ZT of 0.05 and 0.06 for pure ZnO and ZnA, respectively. Even though the performance is not surpassing the already reported ones in the literature, this has opened opportunities for development of ZnO based polymer composites at low temperatures using spark plasma sintering.

Conclusions and Recommendations

Conclusions and recommendations

Conclusions

The objective of this work was to synthesize and sinter, using spark plasma sintering, pure ZnO, Al-doped ZnO and polyaniline incorporated Al-doped ZnO. We show that sample preparation and spark plasma sintering technique are core steps towards improving the thermoelectric properties of ZnO based ceramics. First-, a guide for the densification and grain size of dried ZnO ceramics was developed. It was illustrated that SPS can sinter to high densities irrespective of starting powder. Ceramics prepared from both synthetic and commercial ZnO powder could be fully densified above 99% at a temperature as low as 600°C. Annealing at 600°C does not have significant effect on the microstructure of ZnO ceramics, however, changes the oxygen stoichiometry, and the resistivity of pure ZnO ceramics of increased by three order of magnitude.

The addition of 2 at% Al doping reduced the grain size of the ZnO ceramics by 100 nm which consequently decreased the thermal conductivity by 18 W/mK at room temperature. The technique/procedure used in spark plasma sintering of Al-doped ZnO ceramics was found effective for changes in the phase structure. Application of axial pressure at room temperature and sintering above 650°C was found to cause secondary phases such as spinel phase (ZnAl_2O_4) that could affect the resistivity. Aluminum doping resulted in reduced Seebeck Coefficient value of the doped ZnO ceramic when compared to the pure ZnO ceramics, maximum ZT value of 1.5×10^{-3} at 500°C was achieved.

Regarding PANI incorporation, full densification at low temperature of 250°C and axial pressure of 250 MPa was achieved for 5 and 9 wt% PANI dispersed in the Al-doped ZnO ceramics (ZnA). Due to the reduced sintering temperature, the nanostructure of the ceramics was maintained, which helped to reduce thermal conductivity to less than 6 W/mK. This is probably one of the big milestones from this work. The Seebeck Coefficient was able to be maintained at $\sim 150 \mu\text{V/K}$ with a slight improvement in the resistivity. Improved ZT value of 0.8×10^{-3} was achieved at 190°C using ZnA-9PANI as compared to ZT value of 0.06×10^{-3} for ZnA ceramics. Even though the performance is not surpassing the already reported ones in the literature, this has opened opportunities for development of ZnO based polymer composites at low temperatures using spark plasma sintering.

Recommendations

The thermoelectric properties of pure ZnO ceramics were explored but more work still needs to be done to bring them to a level of commercialization. However this work has laid up a good framework for additional improvements. It is advisable to do an in-depth study on the electronic structure and energy band analysis of pure ZnO dense ceramics, doped and PANI incorporated, to have better understanding of their electrical behaviour. One of the main problems with the Al-doped ZnO ceramics is the high resistivity in the ceramics. It is recommended to sinter in a reduced atmosphere (vacuum); this will increase the concentration of oxygen vacancies as these are known to enhance the electrical conductivity by reducing the resistivity. Additionally, it is advised to increase the sintering temperature to above 800°C, at high temperature the kinetic energy of particles increases, thus, increasing the chances of collision of the grains and rate of reaction of Al in to the ZnO. Hence, higher probabilities of Zn²⁺ displacement by Al³⁺ in the ZnO structure. Also, at high temperature the grain size will be increased which will improve the mobility of charge carriers to reduce the resistivity.

This study has shown that polymer inclusion in ZnO based ceramics is beneficial in improving the thermal conductivity and Seebeck Coefficient; however, the low resistivity in the ceramics is affecting its performance. This is an important direction for future work when all doping experiments have been optimised. It was noted in this study that the reduction in the sintering temperature decreases the presence of the secondary phases, so, it is possible sintering at a temperature of 250°C and high concentration of Al the secondary phases could be avoided another important consideration for future work.

References

- [1] Zheng X, Liu C, Yan Y, Wang Q. A review of thermoelectrics research—Recent developments and potentials for sustainable and renewable energy applications. *Renewable and sustainable energy reviews*2014. p. 486-503.
- [2] Maciá-Barber E. *Thermoelectric Materials: Advances and Applications*. Pan Stanford; 2015.
- [3] Koumoto K, Mori T. *Thermoelectric nanomaterials*. Springer; 2015.
- [4] Nolas GS, Sharp J, Goldsmid J. *Thermoelectrics: basic principles and new materials developments*. Springer Science & Business Media; 2013.
- [5] Zhang X, Zhao L-D. Thermoelectric materials: Energy conversion between heat and electricity. *Journal of Materiomics*2015. p. 92-105.
- [6] Han L. *High Temperature Thermoelectric Properties of ZnO Based Materials: Department of Energy Conversion and Storage, Technical University of Denmark*; 2014.
- [7] Tritt TM, Subramanian M. Thermoelectric materials, phenomena, and applications: a bird's eye view. *MRS bulletin*2006. p. 188-98.
- [8] Madsen GK, Singh DJ. BoltzTraP. A code for calculating band-structure dependent quantities. *Computer Physics Communications*2006. p. 67-71.
- [9] Scheidemantel T, Ambrosch-Draxl C, Thonhauser T, Badding J, Sofo J. Transport coefficients from first-principles calculations. *Physical Review B*2003. p. 125210.
- [10] Walia S, Balendhran S, Nili H, Zhuiykov S, Rosengarten G, Wang QH, et al. Transition metal oxides—Thermoelectric properties. *Progress in Materials Science*2013. p. 1443-89.
- [11] Walia S, Weber R, Balendhran S, Yao D, Abrahamson JT, Zhuiykov S, et al. ZnO based thermopower wave sources. *Chemical Communications*2012. p. 7462-4.
- [12] Walia S, Balendhran S, Yi P, Yao D, Zhuiykov S, Pannirselvam M, et al. MnO₂-based thermopower wave sources with exceptionally large output voltages. *The Journal of Physical Chemistry C*2013. p. 9137-42.
- [13] Fergus JW. Oxide materials for high temperature thermoelectric energy conversion. *Journal of the European Ceramic Society*2012. p. 525-40.
- [14] Snyder GJ, Toberer ES. Complex thermoelectric materials. *Materials For Sustainable Energy: A Collection of Peer-Reviewed Research and Review Articles from Nature Publishing Group*: World Scientific; 2011. p. 101-10.

- [15] Zebarjadi M, Esfarjani K, Dresselhaus M, Ren Z, Chen G. Perspectives on thermoelectrics: from fundamentals to device applications. *Energy & Environmental Science*2012. p. 5147-62.
- [16] Furlong RR, Wahlquist EJ. US space missions using radioisotope power systems. *Nuclear news*1999. p. 26-35.
- [17] Zhao D, Tan G. A review of thermoelectric cooling: materials, modeling and applications. *Applied Thermal Engineering*2014. p. 15-24.
- [18] Rowe DM. *Thermoelectrics handbook: macro to nano*. CRC press; 2005.
- [19] Zhao L-D, Lo S-H, Zhang Y, Sun H, Tan G, Uher C, et al. Ultralow thermal conductivity and high thermoelectric figure of merit in SnSe crystals. *Nature*2014. p. 373.
- [20] Olvera A, Moroz N, Sahoo P, Ren P, Bailey T, Page A, et al. Partial indium solubility induces chemical stability and colossal thermoelectric figure of merit in Cu₂Se. *Energy & Environmental Science*2017. p. 1668-76.
- [21] Dughaish Z. Lead telluride as a thermoelectric material for thermoelectric power generation. *Physica B: Condensed Matter*2002. p. 205-23.
- [22] Hong M, Chen Z-G, Zou J. Fundamental and progress of Bi₂Te₃-based thermoelectric materials. *Chinese Physics B*2018. p. 048403.
- [23] Minnich A, Dresselhaus M, Ren Z, Chen G. Bulk nanostructured thermoelectric materials: current research and future prospects. *Energy & Environmental Science*2009. p. 466-79.
- [24] Gao L, Li Q, Luan W, Kawaoka H, Sekino T, Niihara K. Preparation and electric properties of dense nanocrystalline zinc oxide ceramics. *Journal of the American Ceramic Society*2002. p. 1016-8.
- [25] Li J-F, Liu W-S, Zhao L-D, Zhou M. High-performance nanostructured thermoelectric materials. *NPG Asia Materials*2010. p. 152.
- [26] Lan Y, Minnich AJ, Chen G, Ren Z. Enhancement of thermoelectric figure-of-merit by a bulk nanostructuring approach. *Advanced Functional Materials*2010. p. 357-76.
- [27] Vineis CJ, Shakouri A, Majumdar A, Kanatzidis MG. Nanostructured thermoelectrics: big efficiency gains from small features. *Advanced Materials*2010. p. 3970-80.
- [28] Ohtaki M, Araki K, Yamamoto K. High thermoelectric performance of dually doped ZnO ceramics. *Journal of Electronic Materials*2009. p. 1234-8.
- [29] Zhang X, Chang C, Zhou Y, Zhao L-D. BiCuSeO thermoelectrics: an update on recent progress and perspective. *Materials*2017. p. 198.

- [30] Wu Z, Xie H. Thermoelectric performance of polyparaphenylene/Li_{0.5}Ni_{0.5}Fe₂O₄ nanocomposites. *Materials Research Innovations*2014. p. 120-4.
- [31] Cramer CL, Gonzalez-Julian J, Colasuonno PS, Holland TB. Continuous functionally graded material to improve the thermoelectric properties of ZnO. *Journal of the European Ceramic Society*2017. p. 4693-700.
- [32] Virtudazo RVR, Guo Q, Wu R, Takei T, Mori T. An alternative, faster and simpler method for the formation of hierarchically porous ZnO particles and their thermoelectric performance. *RSC Advances*2017. p. 31960-8.
- [33] Han L, Van Nong N, Zhang W, Hung LT, Holgate T, Tashiro K, et al. Effects of morphology on the thermoelectric properties of Al-doped ZnO. *RSC Advances*2014. p. 12353-61.
- [34] Zhang D-B, Li H-Z, Zhang B-P, Liang D-d, Xia M. Hybrid-structured ZnO thermoelectric materials with high carrier mobility and reduced thermal conductivity. *RSC Advances*2017. p. 10855-64.
- [35] Lei Y, Li Y, Xu L, Yang J, Wan R, Long H. Microwave synthesis and sintering of TiNiSn thermoelectric bulk. *Journal of Alloys and Compounds*2016. p. 166-70.
- [36] Noudem J, Lemonnier S, Prevel M, Reddy E, Guilmeau E, Goupil C. Thermoelectric ceramics for generators. *Journal of the European ceramic society*2008. p. 41-8.
- [37] Han L, Van Nong N, Hung LT, Holgate T, Pryds N, Ohtaki M, et al. The influence of α - and γ -Al₂O₃ phases on the thermoelectric properties of Al-doped ZnO. *Journal of Alloys and Compounds*2013. p. 291-6.
- [38] Sootsman JR, Chung DY, Kanatzidis MG. New and old concepts in thermoelectric materials. *Angewandte Chemie International Edition*2009. p. 8616-39.
- [39] Nolas G, Morelli D, Tritt TM. Skutterudites: A phonon-glass-electron crystal approach to advanced thermoelectric energy conversion applications. *Annual Review of Materials Science*1999. p. 89-116.
- [40] Kleinke H. New bulk materials for thermoelectric power generation: clathrates and complex antimonides. *Chemistry of Materials*2009. p. 604-11.
- [41] Lei Y, Cheng C, Li Y, Wan R, Wang M. Microwave synthesis and enhancement of thermoelectric figure of merit in half-Heusler TiNiSbxSn_{1-x}. *Ceramics International*2017. p. 9343-7.
- [42] Hicks L, Dresselhaus MS. Effect of quantum-well structures on the thermoelectric figure of merit. *Physical Review B*1993. p. 12727.

- [43] Chen G, Dresselhaus M, Dresselhaus G, Fleurial J-P, Caillat T. Recent developments in thermoelectric materials. *International Materials Reviews*2003. p. 45-66.
- [44] Kinemuchi Y, Nakano H, Mikami M, Kobayashi K, Watari K, Hotta Y. Enhanced boundary-scattering of electrons and phonons in nanograined zinc oxide. *Journal of Applied Physics*2010. p. 053721.
- [45] He J, Tritt TM. Advances in thermoelectric materials research: Looking back and moving forward. *Science*2017. p. eaak9997.
- [46] Popescu A, Woods L, Martin J, Nolas G. Model of transport properties of thermoelectric nanocomposite materials. *Physical Review B*2009. p. 205302.
- [47] He J, Sootsman JR, Girard SN, Zheng J-C, Wen J, Zhu Y, et al. On the origin of increased phonon scattering in nanostructured PbTe based thermoelectric materials. *Journal of the American Chemical Society*2010. p. 8669-75.
- [48] Scheele M, Oeschler N, Meier K, Kornowski A, Klinke C, Weller H. Synthesis and thermoelectric characterization of Bi₂Te₃ nanoparticles. *Advanced Functional Materials*2009. p. 3476-83.
- [49] Yamashita O, Tomiyoshi S, Makita K. Bismuth telluride compounds with high thermoelectric figures of merit. *Journal of Applied Physics*2003. p. 368-74.
- [50] Gelbstein Y, Dashevsky Z, Dariel M. High performance n-type PbTe-based materials for thermoelectric applications. *Physica B: Condensed Matter*2005. p. 196-205.
- [51] Fu T, Yue X, Wu H, Fu C, Zhu T, Liu X, et al. Enhanced thermoelectric performance of PbTe bulk materials with figure of merit $zT > 2$ by multi-functional alloying. *Journal of Materiomics*2016. p. 141-9.
- [52] Heremans JP, Jovovic V, Toberer ES, Saramat A, Kurosaki K, Charoenphakdee A, et al. Enhancement of thermoelectric efficiency in PbTe by distortion of the electronic density of states. *Science*2008. p. 554-7.
- [53] Pei Y, Shi X, LaLonde A, Wang H, Chen L, Snyder GJ. Convergence of electronic bands for high performance bulk thermoelectrics. *Nature*2011. p. 66.
- [54] Joshi G, Lee H, Lan Y, Wang X, Zhu G, Wang D, et al. Enhanced thermoelectric figure-of-merit in nanostructured p-type silicon germanium bulk alloys. *Nano letters*2008. p. 4670-4.
- [55] Favier K, Bernard-Granger G, Navone C, Soulier M, Boidot M, Leforestier J, et al. Influence of in situ formed MoSi₂ inclusions on the thermoelectrical properties of an N-type silicon–germanium alloy. *Acta Materialia*2014. p. 429-42.

- [56] Lan Y, Wang D, Ren Z. Silicon–Germanium Alloys. *Advanced Thermoelectrics: Materials, Contacts, Devices, and Systems*2017. p. 353.
- [57] Peng K, Lu X, Zhan H, Hui S, Tang X, Wang G, et al. Broad temperature plateau for high ZT s in heavily doped p-type SnSe single crystals. *Energy & Environmental Science*2016. p. 454-60.
- [58] Hong M, Chen ZG, Yang L, Liao ZM, Zou YC, Chen YH, et al. Achieving $zT > 2$ in p-Type AgSbTe_{2-x}Sex Alloys via Exploring the Extra Light Valence Band and Introducing Dense Stacking Faults. *Advanced Energy Materials*2018. p. 1702333.
- [59] Hong M, Chen ZG, Yang L, Zou YC, Dargusch MS, Wang H, et al. Realizing zT of 2.3 in Ge_{1-x-y}SbxInyTe via Reducing the Phase-Transition Temperature and Introducing Resonant Energy Doping. *Advanced Materials*2018. p. 1705942.
- [60] Biswas K, He J, Blum ID, Wu C-I, Hogan TP, Seidman DN, et al. High-performance bulk thermoelectrics with all-scale hierarchical architectures. *Nature*2012. p. 414.
- [61] Wu D, Zhao L-D, Tong X, Li W, Wu L, Tan Q, et al. Superior thermoelectric performance in PbTe–PbS pseudo-binary: extremely low thermal conductivity and modulated carrier concentration. *Energy & Environmental Science*2015. p. 2056-68.
- [62] Sakurada S, Shutoh N. Effect of Ti substitution on the thermoelectric properties of (Zr, Hf) NiSn half-Heusler compounds. *Applied Physics Letters*2005. p. 082105.
- [63] Sakurada S, Shutoh N, Hirono S. Thermoelectric material and thermoelectric device. Google Patents; 2010.
- [64] Saramat A, Svensson G, Palmqvist A, Stiewe C, Mueller E, Platzek D, et al. Large thermoelectric figure of merit at high temperature in Czochralski-grown clathrate Ba₈Ga₁₆Ge₃₀. *Journal of Applied Physics*2006. p. 023708.
- [65] Yang J, Shi X, Bai S, Zhang W, Chen L. Thermoelectric material including a filled skutterudite crystal structure. Google Patents; 2010.
- [66] Gayner C, Kar KK. Recent advances in thermoelectric materials. *Progress in Materials Science*2016. p. 330-82.
- [67] Pickett WE. Electronic structure of the high-temperature oxide superconductors. *Reviews of Modern Physics*1989. p. 433.
- [68] Kieslich G, Cerretti G, Veremchuk I, Hermann RP, Panthöfer M, Grin J, et al. A chemists view: Metal oxides with adaptive structures for thermoelectric applications. *physica status solidi (a)*2016. p. 808-23.

- [69] Funahashi R, Urata S, Sano T, Kitawaki M. Thermoelectric Properties of Ca₃Co₄O₉ Single Crystals/powder Composite. *Journal of the Japan Society of Powder and Powder Metallurgy*2003. p. 485-9.
- [70] Van Nong N, Pryds N, Linderoth S, Ohtaki M. Enhancement of the Thermoelectric Performance of p-Type Layered Oxide Ca₃Co₄O_{9+δ} Through Heavy Doping and Metallic Nanoinclusions. *Advanced materials*2011. p. 2484-90.
- [71] Wang Y, Sui Y, Cheng J, Wang X, Su W. Comparison of the high temperature thermoelectric properties for Ag-doped and Ag-added Ca₃Co₄O₉. *Journal of Alloys and Compounds*2009. p. 817-21.
- [72] Ito M, Furumoto D. Microstructure and thermoelectric properties of Na_xCo₂O₄/Ag composite synthesized by the polymerized complex method. *Journal of Alloys and Compounds*2008. p. 517-20.
- [73] Zhao L-D, He J, Berardan D, Lin Y, Li J-F, Nan C-W, et al. BiCuSeO oxyselenides: new promising thermoelectric materials. *Energy & Environmental Science*2014. p. 2900-24.
- [74] Wang Y, Sui Y, Wang X, Su W. Enhancement of thermoelectric efficiency in (Ca, Dy) MnO₃–(Ca, Yb) MnO₃ solid solutions. *Applied Physics Letters*2010. p. 052109.
- [75] Kabir R, Tian R, Zhang T, Donelson R, Tan TT, Li S. Role of Bi doping in thermoelectric properties of CaMnO₃. *Journal of Alloys and Compounds*2015. p. 347-51.
- [76] Bocher L, Aguirre M, Logvinovich D, Shkabko A, Robert R, Trottmann M, et al. CaMn_{1-x}Nb_xO₃ (x≤0.08) Perovskite-Type Phases As Promising New High-Temperature n-Type Thermoelectric Materials. *Inorganic chemistry*2008. p. 8077-85.
- [77] Liu Y, Xu W, Liu D-B, Yu M, Lin Y-H, Nan C-W. Enhanced thermoelectric properties of Ga-doped In₂O₃ ceramics via synergistic band gap engineering and phonon suppression. *Physical Chemistry Chemical Physics*2015. p. 11229-33.
- [78] Wang N, He H, WAN C, KOUMOTO K. Thermoelectric properties of Nb-doped SrTiO₃ ceramics enhanced by potassium titanate nanowires addition. *Journal of the Ceramic Society of Japan*2010. p. 1098-101.
- [79] Wang HC, Wang CL, Su WB, Liu J, Sun Y, Peng H, et al. Doping effect of La and Dy on the thermoelectric properties of SrTiO₃. *Journal of the American Ceramic Society*2011. p. 838-42.
- [80] Xiong L-B, Li J-L, Yang B, Yu Y. Ti³⁺ in the surface of titanium dioxide: generation, properties and photocatalytic application. *Journal of Nanomaterials*2012. p. 9.
- [81] Hashimoto S, Poulsen FW, Mogensen M. Conductivity of SrTiO₃ based oxides in the reducing atmosphere at high temperature. *Journal of alloys and compounds*2007. p. 232-6.

- [82] Molinari M, Tompsett DA, Parker SC, Azough F, Freer R. Structural, electronic and thermoelectric behaviour of CaMnO_3 and $\text{CaMnO}_{3-\delta}$. *Journal of Materials Chemistry A*2014. p. 14109-17.
- [83] Janotti A, Van de Walle CG. Fundamentals of zinc oxide as a semiconductor. *Reports on progress in physics*2009. p. 126501.
- [84] Klingshirn CF, Waag A, Hoffmann A, Geurts J. Zinc oxide: from fundamental properties towards novel applications. Springer Science & Business Media; 2010.
- [85] Willander M, Zhao Q, Hu Q-H, Klason P, Kuzmin V, Al-Hilli S, et al. Fundamentals and properties of zinc oxide nanostructures: optical and sensing applications. *Superlattices and Microstructures*2008. p. 352-61.
- [86] Moezzi A, McDonagh AM, Cortie MB. Zinc oxide particles: Synthesis, properties and applications. *Chemical Engineering Journal*2012. p. 1-22.
- [87] Krasil'nikov V, Dyachkova T, Tyutyunnik A, Gyrdasova O, Melkozerova M, Baklanova I, et al. Magnetic and optical properties as well as EPR studies of polycrystalline ZnO synthesized from different precursors. *Materials Research Bulletin*2018. p. 553-9.
- [88] Gupta TK. Application of zinc oxide varistors. *Journal of the American Ceramic Society*1990. p. 1817-40.
- [89] Kołodziejczak-Radzimska A, Jesionowski T. Zinc oxide—from synthesis to application: a review. *Materials*2014. p. 2833-81.
- [90] Sawada H, Wang R, Sleight AW. An electron density residual study of zinc oxide. *Journal of Solid State Chemistry*1996. p. 148-50.
- [91] Kohan A, Ceder G, Morgan D, Van de Walle CG. First-principles study of native point defects in ZnO. *Physical Review B*2000. p. 15019.
- [92] Sirelkhatim A, Mahmud S, Seeni A, Kaus NHM, Ann LC, Bakhori SKM, et al. Review on zinc oxide nanoparticles: antibacterial activity and toxicity mechanism. *Nano-Micro Letters*2015. p. 219-42.
- [93] Wu X, Lee J, Varshney V, Wohlwend JL, Roy AK, Luo T. Thermal conductivity of wurtzite zinc-oxide from first-principles lattice dynamics—a comparative study with gallium nitride. *Scientific reports*2016. p. 22504.
- [94] Olorunyolemi T, Birnboim A, Carmel Y, Wilson Jr OC, Lloyd IK, Smith S, et al. Thermal conductivity of zinc oxide: from green to sintered state. *Journal of the American Ceramic Society*2002. p. 1249-53.

- [95] Liang X. Thermoelectric transport properties of naturally nanostructured Ga–ZnO ceramics: Effect of point defect and interfaces. *Journal of the European Ceramic Society*2016. p. 1643-50.
- [96] Lu L, Wong M. The resistivity of zinc oxide under different annealing configurations and its impact on the leakage characteristics of zinc oxide thin-film transistors. *IEEE Transactions on Electron Devices*2014. p. 1077-84.
- [97] Schmidt-Mende L, MacManus-Driscoll JL. ZnO – nanostructures, defects, and devices. *Materials Today*2007. p. 40-8.
- [98] Orru R, Licheri R, Locci AM, Cincotti A, Cao G. Consolidation/synthesis of materials by electric current activated/assisted sintering. *Materials Science and Engineering: R: Reports*2009. p. 127-287.
- [99] Langer J, Hoffmann MJ, Guillon O. Electric Field-Assisted Sintering and Hot Pressing of Semiconductive Zinc Oxide: A Comparative Study. *Journal of the American Ceramic Society*2011. p. 2344-53.
- [100] Chaim R, Levin M, Shlayer A, Estournès C. Sintering and densification of nanocrystalline ceramic oxide powders: a review. *Advances in Applied Ceramics*2008. p. 159-69.
- [101] Aimable A, Goure Doubi H, Stuer M, Zhao Z, Bowen P. Synthesis and Sintering of ZnO Nanopowders. *Technologies*2017. p. 28.
- [102] Senda T, Bradt RC. Grain Growth in Sintered ZnO and ZnO-Bi₂O₃ Ceramics. *Journal of the American Ceramic Society*1990. p. 106-14.
- [103] Gupta TK, Coble RL. Sintering of ZnO: I, Densification and Grain Growth*. *Journal of the American Ceramic Society: Blackwell Publishing Ltd*; 1968. p. 521-5.
- [104] Lee V, Parravano G. Sintering reactions of zinc oxide. *Journal of Applied Physics*1959. p. 1735-40.
- [105] Rahaman MN. Sintering of ceramics. Nee York: CRC Press; 2008.
- [106] Chaim R, Marder R, Estournés C, Shen Z. Densification and preservation of ceramic nanocrystalline character by spark plasma sintering. *Advances in Applied Ceramics*2012. p. 280-5.
- [107] Chaim R, Chevallier G, Weibel A, Estournès C. Grain growth during spark plasma and flash sintering of ceramic nanoparticles: a review. *Journal of Materials Science*2018. p. 3087-105.

- [108] Colder H, Guilmeau E, Harnois C, Marinel S, Retoux R, Savary E. Preparation of Ni-doped ZnO ceramics for thermoelectric applications. *Journal of the European Ceramic Society*2011. p. 2957-63.
- [109] Søndergaard M, Bøjesen ED, Borup KA, Christensen S, Christensen M, Iversen BB. Sintering and annealing effects on ZnO microstructure and thermoelectric properties. *Acta Materialia*2013. p. 3314-23.
- [110] Tsubota T, Ohtaki M, Eguchi K, Arai H. Thermoelectric properties of Al-doped ZnO as a promising oxide material for high-temperature thermoelectric conversion. *Journal of Materials Chemistry*1997. p. 85-90.
- [111] Gautam D, Engenhorst M, Schilling C, Schierning G, Schmechel R, Winterer M. Thermoelectric properties of pulsed current sintered nanocrystalline Al-doped ZnO by chemical vapour synthesis. *Journal of Materials Chemistry A*2015. p. 189-97.
- [112] Kim KH, Shim SH, Shim KB, Niihara K, Hojo J. Microstructural and thermoelectric characteristics of zinc oxide-based thermoelectric materials fabricated using a spark plasma sintering process. *Journal of the American Ceramic Society*2005. p. 628-32.
- [113] Carter CB, Norton MG. *Ceramic materials: science and engineering*. Springer; 2007.
- [114] Tarkhanyan RH, Niarchos DG. Effect of Pore Size on Reduction of the Lattice Thermal Conductivity of Nano to Micro-Scale Porous Materials. *Journal of electronic materials*2014. p. 3808-11.
- [115] Beynet Y, Izoulet A, Guillemet-Fritsch S, Chevallier G, Bley V, Pérel T, et al. ZnO-based varistors prepared by spark plasma sintering. *Journal of the European Ceramic Society*2015. p. 1199-208.
- [116] Dargatz B, Gonzalez-Julian J, Bram M, Jakes P, Besmehn A, Schade L, et al. FAST/SPS sintering of nanocrystalline zinc oxide—Part I: Enhanced densification and formation of hydrogen-related defects in presence of adsorbed water. *Journal of the European Ceramic Society*2016. p. 1207-20.
- [117] Guillon O, Gonzalez-Julian J, Dargatz B, Kessel T, Schierning G, Räthel J, et al. Field-assisted sintering technology/spark plasma sintering: mechanisms, materials, and technology developments. *Advanced Engineering Materials*. 2014;16:830-49.
- [118] Schwarz S, Thron AM, Rufner J, Benthem K, Guillon O. Low temperature sintering of nanocrystalline zinc oxide: effect of heating rate achieved by field assisted sintering/spark plasma sintering. *Journal of the American Ceramic Society*2012. p. 2451-7.
- [119] Schmidt-Mende L, MacManus-Driscoll JL. ZnO—nanostructures, defects, and devices. *Materials today*2007. p. 40-8.

- [120] Zhang S, Wei S-H, Zunger A. Intrinsic n-type versus p-type doping asymmetry and the defect physics of ZnO. *Physical Review B*2001. p. 075205.
- [121] Kohan AF, Ceder G, Morgan D, Van de Walle CG. First-principles study of native point defects in ZnO. *Physical Review B: American Physical Society*; 2000. p. 15019-27.
- [122] Pengshou X, Yuming S, Chaoshu S, Faqiang X, Haibin P. Electronic structure of ZnO and its defects. *Science in China Series A: Mathematics*2001. p. 1174-81.
- [123] Batsanov SS. Van der Waals radii of elements. *Inorganic materials*2001. p. 871-85.
- [124] Metallurgy and Material science. In: Kanpur I, editor. *Module 2: Defect Chemistry and Defect Equilibria*. India: NPTEL; 2012.
- [125] Kamarulzaman N, Kasim MF, Rusdi R. Band gap narrowing and widening of ZnO nanostructures and doped materials. *Nanoscale research letters*2015. p. 346.
- [126] Jayaraman VK, Álvarez AM, Kuwabara YM, Koudriavstev Y. Effect of co-doping concentration on structural, morphological, optical and electrical properties of aluminium and indium co-doped ZnO thin films deposited by ultrasonic spray pyrolysis. *Materials Science in Semiconductor Processing*2016. p. 32-6.
- [127] Look DC. Progress in ZnO materials and devices. *Journal of electronic materials*2006. p. 1299-305.
- [128] Ohtaki M, Tsubota T, Eguchi K, Arai H. High-temperature thermoelectric properties of $(\text{Zn}_{1-x}\text{Al}_x)\text{O}$. *Journal of applied physics*1996. p. 1816-8.
- [129] Fujishiro Y, Miyata M, Awano M, Maeda K. Effect of Microstructural Control on Thermoelectric Properties of Hot-Pressed Aluminum-Doped Zinc Oxide. *Journal of the American Ceramic Society*2003. p. 2063-6.
- [130] Jood P, Mehta RJ, Zhang Y, Peleckis G, Wang X, Siegel RW, et al. Al-doped zinc oxide nanocomposites with enhanced thermoelectric properties. *Nano letters*2011. p. 4337-42.
- [131] Nam WH, Lim YS, Choi S-M, Seo W-S, Lee JY. High-temperature charge transport and thermoelectric properties of a degenerately Al-doped ZnO nanocomposite. *Journal of Materials Chemistry*2012. p. 14633-8.
- [132] Jood P, Mehta RJ, Zhang Y, Borca-Tasciuc T, Dou SX, Singh DJ, et al. Heavy element doping for enhancing thermoelectric properties of nanostructured zinc oxide. *RSC Advances*2014. p. 6363-8.
- [133] Wang C, Wang Y, Zhang G, Peng C, Yang G. Theoretical investigation of the effects of doping on the electronic structure and thermoelectric properties of ZnO nanowires. *Physical Chemistry Chemical Physics*2014. p. 3771-6.

- [134] Wu Z-H, Xie H-Q, Zhai Y-B. Preparation and thermoelectric properties of Co-doped ZnO synthesized by Sol–Gel. *Journal of nanoscience and nanotechnology*2015. p. 3147-50.
- [135] Wu Z-H, Xie H-Q, Zhai Y-B. Enhanced thermoelectric figure of merit in nanostructured ZnO by nanojunction effect. *Applied Physics Letters*2013. p. 243901.
- [136] Zakharchuk K, Widenmeyer M, Alikin DO, Xie W, Populoh S, Mikhalev SM, et al. Self-forming nanocomposite concept for ZnO-based thermoelectrics. *Journal of Materials Chemistry A*2018.
- [137] Tian T, Cheng L, Xing J, Zheng L, Man Z, Hu D, et al. Effects of sintering on the microstructure and electrical properties of ZnO-based thermoelectric materials. *Materials & Design*2017. p. 479-85.
- [138] Tsubota T, Ohtaki M, Eguchi K, Arai H. Transport properties and thermoelectric performance of $(\text{Zn}_{1-y}\text{Mg}_y)_{1-x}\text{Al}_x\text{O}$. *Journal of Materials Chemistry*1998. p. 409-12.
- [139] Wu Z-H, Hua-Qing X, Yuan-Yuan W, Jiao-Jiao X, Jian-Hui M. Nanojunctions Contributing to High Performance Thermoelectric ZnO-Based Inorganic-Organic Hybrids. *Chinese Physics Letters*2015. p. 117303.
- [140] Han L, Christensen DV, Bhowmik A, Simonsen SB, Hung L, Abdellahi E, et al. Scandium-doped zinc cadmium oxide as a new stable n-type oxide thermoelectric material. *Journal of Materials Chemistry A*2016. p. 12221-31.
- [141] Liang X. Thermoelectric transport properties of Fe-enriched ZnO with high-temperature nanostructure refinement. *ACS applied materials & interfaces*2015. p. 7927-37.
- [142] Zhu B, Li D, Zhang T, Luo Y, Donelson R, Zhang T, et al. The improvement of thermoelectric property of bulk ZnO via ZnS addition: Influence of intrinsic defects. *Ceramics International*2018. p. 6461-5.
- [143] Nam WH, Kim BB, Seo SG, Lim YS, Kim J-Y, Seo W-S, et al. Structurally nanocrystalline-electrically single crystalline zno-reduced graphene oxide composites. *Nano letters*2014. p. 5104-9.
- [144] Du Y, Shen SZ, Cai K, Casey PS. Research progress on polymer–inorganic thermoelectric nanocomposite materials. *Progress in Polymer Science*2012. p. 820-41.
- [145] Gerard M, Chaubey A, Malhotra B. Application of conducting polymers to biosensors. *Biosensors and bioelectronics*2002. p. 345-59.
- [146] Skotheim TA. *Handbook of conducting polymers*. CRC press; 1997.
- [147] Zhang L, Du W, Nautiyal A, Liu Z, Zhang X. Recent progress on nanostructured conducting polymers and composites: synthesis, application and future aspects. *Science China Materials*2018. p. 1-50.

- [148] Bubnova O, Khan ZU, Malti A, Braun S, Fahlman M, Berggren M, et al. Optimization of the thermoelectric figure of merit in the conducting polymer poly (3, 4-ethylenedioxythiophene). *Nature materials*2011. p. 429.
- [149] Aïch RB, Blouin N, Bouchard A, Leclerc M. Electrical and thermoelectric properties of poly (2, 7-carbazole) derivatives. *Chemistry of Materials*2009. p. 751-7.
- [150] Wu Z-H, Xie H-Q, Zhai Y-B, Gan L-H, Liu J. Enhanced thermoelectric performance of TiO₂-based hybrid materials by incorporating conducting polymer. *Chinese Physics B*2015. p. 034402.
- [151] Li J, Tang X, Li H, Yan Y, Zhang Q. Synthesis and thermoelectric properties of hydrochloric acid-doped polyaniline. *Synthetic Metals*2010. p. 1153-8.
- [152] Culebras M, Gómez CM, Cantarero A. Review on polymers for thermoelectric applications. *Materials*2014. p. 6701-32.
- [153] Jun L, Lian-meng Z, Li H, Xin-feng T. Synthesis and thermoelectric properties of polyaniline. *Journal of Wuhan University of Technology-Mater Sci Ed*2003. p. 53-5.
- [154] Yakuphanoglu F, Şenkal BF, Saraç A. Electrical conductivity, thermoelectric power, and optical properties of organo-soluble polyaniline organic semiconductor. *Journal of Electronic Materials*2008. p. 930-4.
- [155] Mateeva N, Niculescu H, Schlenoff J, Testardi L. Correlation of Seebeck coefficient and electric conductivity in polyaniline and polypyrrole. *Journal of Applied Physics*1998. p. 3111-7.
- [156] Yan H, Sada N, Toshima N. Thermal transporting properties of electrically conductive polyaniline films as organic thermoelectric materials. *Journal of Thermal Analysis and Calorimetry*2002. p. 881-7.
- [157] Sun Y, Wei Z, Xu W, Zhu D. A three-in-one improvement in thermoelectric properties of polyaniline brought by nanostructures. *Synthetic Metals*2010. p. 2371-6.
- [158] Hiraishi K, Masuhara A, Nakanishi H, Oikawa H, Shinohara Y. Evaluation of thermoelectric properties of polythiophene films synthesized by electrolytic polymerization. *Japanese Journal of Applied Physics*2009. p. 071501.
- [159] Yue R, Chen S, Lu B, Liu C, Xu J. Facile electrosynthesis and thermoelectric performance of electroactive free-standing polythieno [3, 2-b] thiophene films. *Journal of Solid State Electrochemistry*2011. p. 539-48.
- [160] Shinohara Y, Imai Y, Isoda Y, Hiraishi K, Nakanishi H. A new challenge of polymer thermoelectric materials as ecomaterials. *Materials science forum: Trans Tech Publ*; 2007. p. 2329-32.

- [161] Bao-Yang L, Cong-Cong L, Shan L, Jing-Kun X, Feng-Xing J, Yu-Zhen L, et al. Thermoelectric performances of free-standing polythiophene and poly (3-methylthiophene) nanofilms. *Chinese Physics Letters*2010. p. 057201.
- [162] Jiang Q, Liu C, Song H, Shi H, Yao Y, Xu J, et al. Improved thermoelectric performance of PEDOT: PSS films prepared by polar-solvent vapor annealing method. *Journal of Materials Science: Materials in Electronics*2013. p. 4240-6.
- [163] Kong F, Liu C, Xu J, Huang Y, Wang J, Sun Z. Thermoelectric performance enhancement of poly (3, 4-ethylenedioxythiophene): poly (styrenesulfonate) composite films by addition of dimethyl sulfoxide and urea. *Journal of electronic materials*2012. p. 2431-8.
- [164] Maddison D, Unsworth J, Roberts R. Electrical conductivity and thermoelectric power of polypyrrole with different doping levels. *Synthetic metals*1988. p. 99-108.
- [165] Lee W, Park Y, Choi Y. Metallic electrical transport of pf6-doped polypyrrole: Dc conductivity and thermoelectric power. *Synthetic metals*1997. p. 841-2.
- [166] Kemp N, Kaiser A, Liu CJ, Chapman B, Mercier O, Carr A, et al. Thermoelectric power and conductivity of different types of polypyrrole. *Journal of Polymer Science Part B: Polymer Physics*1999. p. 953-60.
- [167] Kemp N, Kaiser A, Trodahl H, Chapman B, Buckley R, Partridge A, et al. Effect of ammonia on the temperature-dependent conductivity and thermopower of polypyrrole. *Journal of Polymer Science Part B: Polymer Physics*2006. p. 1331-8.
- [168] Wu J, Sun Y, Pei W-B, Huang L, Xu W, Zhang Q. Polypyrrole nanotube film for flexible thermoelectric application. *Synthetic Metals*2014. p. 173-7.
- [169] Park Y, Yoon C, Lee C, Shirakawa H, Suezaki Y, Akagi K. Conductivity and thermoelectric power of the newly processed polyacetylene. *Synthetic Metals*1989. p. D27-D34.
- [170] Pukacki W, Płocharski J, Roth S. Anisotropy of thermoelectric power of stretch-oriented new polyacetylene. *Synthetic Metals*1994. p. 253-6.
- [171] Choi E, Suh D, Kim G, Kim D, Park Y. Magneto thermoelectric power of the doped polyacetylene. *Synthetic metals*1999. p. 375-6.
- [172] Yue R, Chen S, Liu C, Lu B, Xu J, Wang J, et al. Synthesis, characterization, and thermoelectric properties of a conducting copolymer of 1, 12-bis (carbazolyl) dodecane and thieno [3, 2-b] thiophene. *Journal of Solid State Electrochemistry*2012. p. 117-26.
- [173] Reddy P, Jang S-Y, Segalman RA, Majumdar A. Thermoelectricity in molecular junctions. *Science*2007. p. 1568-71.

- [174] Swartz ET, Pohl RO. Thermal boundary resistance. *Reviews of modern physics*1989. p. 605.
- [175] Lu P-X, Qu L-B. Electronic structure, lattice dynamics and thermoelectric properties of PbTe from first-principles calculation. *Chinese Physics Letters*2013. p. 017101.
- [176] Holland E, Pomfret S, Adams P, Abell L, Monkman A. Doping dependent transport properties of polyaniline-CSA films. *Synthetic metals*1997. p. 777-8.
- [177] Mitra M, Kargupta K, Ganguly S, Goswami S, Banerjee D. Facile synthesis and thermoelectric properties of aluminum doped zinc oxide/polyaniline (AZO/PANI) hybrid. *Synthetic Metals*2017. p. 25-31.
- [178] Narducci D, Selezneva E, Cerofolini G, Frabboni S, Ottaviani G. Impact of energy filtering and carrier localization on the thermoelectric properties of granular semiconductors. *Journal of Solid State Chemistry*2012. p. 19-25.
- [179] Dargatz B, Gonzalez-Julian J, Bram M, Shinoda Y, Wakai F, Guillon O. FAST/SPS sintering of nanocrystalline zinc oxide—Part II: Abnormal grain growth, texture and grain anisotropy. *Journal of the European Ceramic Society*2016. p. 1221-32.
- [180] Gonzalez-Julian J, Neuhaus K, Bernemann M, da Silva JP, Laptev A, Bram M, et al. Unveiling the mechanisms of cold sintering of ZnO at 250° C by varying applied stress and characterizing grain boundaries by Kelvin Probe Force Microscopy. *Acta Materialia*2018. p. 116-28.
- [181] Guo J, Legum B, Anasori B, Wang K, Lelyukh P, Gogotsi Y, et al. Cold Sintered Ceramic Nanocomposites of 2D MXene and Zinc Oxide. *Advanced Materials*2018. p. 1801846.
- [182] Zhao X, Guo J, Wang K, Herisson De Beauvoir T, Li B, Randall CA. Introducing a ZnO–PTFE (Polymer) Nanocomposite Varistor via the Cold Sintering Process. *Advanced Engineering Materials*2018. p. 1700902.
- [183] de Beauvoir TH, Sangregorio A, Cornu I, Elissalde C, Josse M. Cool-SPS: an opportunity for low temperature sintering of thermodynamically fragile materials. *Journal of Materials Chemistry C*2018. p. 2229-33.
- [184] Gonzalez-Julian J, Neuhaus K, Bernemann M, Pereira da Silva J, Laptev A, Bram M, et al. Unveiling the mechanisms of cold sintering of ZnO at 250 °C by varying applied stress and characterizing grain boundaries by Kelvin Probe Force Microscopy. *Acta Materialia*2018. p. 116-28.

- [185] Funahashi S, Guo J, Guo H, Wang K, Baker AL, Shiratsuyu K, et al. Demonstration of the cold sintering process study for the densification and grain growth of ZnO ceramics. *Journal of the American Ceramic Society*2017. p. 546-53.
- [186] Guo J, Zhao X, Herisson De Beauvoir T, Seo JH, Berbano SS, Baker AL, et al. Recent Progress in Applications of the Cold Sintering Process for Ceramic–Polymer Composites. *Advanced Functional Materials*2018. p. 1801724.
- [187] German RM. *Sintering theory and practice*1996.
- [188] Bhadra S, Khastgir D. Glass–rubber transition temperature of polyaniline: experimental and molecular dynamic simulation. *Synthetic Metals*2009. p. 1141-6.
- [189] Fosong W, Jinsong T, Lixiang W, Hongfang Z, Zhishen M. Study on the Crystallinity of Polyaniline. *Molecular Crystals and Liquid Crystals*1988. p. 175-84.
- [190] Mory J-E, Guy I, Schneider D, Rousset A, Legros R, Peigney A. Poudre d'oxyde de zinc dope, procede de fabrication et ceramique obtenue a partir de ladite poudre. In: FRANCE PCD, editor. *IFI CLAIMS PATENT SERVICES*. France: Jean-Eudes MoryIsabelle GuyDidier SchneiderAbel RoussetRenee LegrosAlain PeigneyPharmacie Centrale De France 1993.
- [191] Guy I. *Elaboration and characterization of powders and varistors based on zinc oxide dope [Doctorate]: Universite Paul Sabatier; 1995.*
- [192] Santanach JG, Weibel A, Estournès C, Yang Q, Laurent C, Peigney A. Spark plasma sintering of alumina: Study of parameters, formal sintering analysis and hypotheses on the mechanism (s) involved in densification and grain growth. *Acta Materialia*2011. p. 1400-8.
- [193] Tokita M. Mechanism of spark plasma sintering. *Proceeding of NEDO International Symposium on Functionally Graded Materials: Japan; 1999.* p. 22.
- [194] Misawa T, Shikatani N, Kawakami Y, Enjoji T, Ohtsu Y, Fujita H. Observation of internal pulsed current flow through the ZnO specimen in the spark plasma sintering method. *Journal of materials science*2009. p. 1641-51.
- [195] Yang S, Chen F, Shen Q, Zhang L. Microstructure and electrical property of aluminum doped zinc oxide ceramics by isolating current under spark plasma sintering. *Journal of the European Ceramic Society*2016. p. 1953-9.
- [196] Monshi A, Foroughi MR, Monshi MR. Modified Scherrer equation to estimate more accurately nano-crystallite size using XRD. *World Journal of Nano Science and Engineering*2012. p. 154-60.

- [197] Manière C, Durand L, Weibel A, Estournès C. A predictive model to reflect the final stage of spark plasma sintering of submicronic α -alumina. *Ceramics International*2016. p. 9274-7.
- [198] Zielinski JM, Chemicals I. *Pharmaceutical Physical Characterization: Surface Area and Porosity*. Manchester: Intertek2013.
- [199] NETZSCH. *Laser Flash Apparatus LFA 457 MicroFlash*. Germany: NETZSCH-Gerätebau GmbH.
- [200] Bergman TL, Incropera FP, Lavine AS, Dewitt DP. *Introduction to heat transfer*. John Wiley & Sons; 2011.
- [201] Runyan WR, Shaffner TJ. *Semiconductor measurements and instrumentation*. McGraw-Hill New York; 1975.
- [202] Kumar V, Sharma SK, Sharma T, Singh V. Band gap determination in thick films from reflectance measurements. *Optical materials*1999. p. 115-9.
- [203] El-Shall MS, Graiver D, Pernisz U, Baraton M. Synthesis and characterization of nanoscale zinc oxide particles: I. laser vaporization/condensation technique. *Nanostructured Materials*1995. p. 297-300.
- [204] Liu K-K, Shan C-X, Zhou R, Zhao Q, Shen D-Z. Large-scale synthesis of ZnO nanoparticles and their application as phosphors in light-emitting devices. *Optical Materials Express*2017. p. 2682-90.
- [205] Wang Y-m, Li J-h, Hong R-y. Large scale synthesis of ZnO nanoparticles via homogeneous precipitation. *Journal of Central South University*2012. p. 863-8.
- [206] Langer J, Quach DV, Groza JR, Guillon O. A comparison between FAST and SPS apparatuses based on the sintering of oxide ceramics. *International Journal of Applied Ceramic Technology*2011. p. 1459-67.
- [207] Noudem JG, Kenfaui D, Quetel-Weben S, Sanmathi CS, Retoux R, Gomina M. Spark Plasma Sintering of n-Type Thermoelectric $\text{Ca}_{0.95}\text{Sm}_{0.05}\text{MnO}_3$. *Journal of the American Ceramic Society*2011. p. 2608-12.
- [208] Kenfaui D, Bonnefont G, Chateigner D, Fantozzi G, Gomina M, Noudem JG. $\text{Ca}_3\text{Co}_4\text{O}_9$ ceramics consolidated by SPS process: Optimisation of mechanical and thermoelectric properties. *Materials Research Bulletin*2010. p. 1240-9.
- [209] Radingoana P, Guillemet-Fritsch S, Olubambi P, Chevallier G, Estournès C. Influence of processing parameters on the densification and the microstructure of pure zinc oxide ceramics prepared by spark plasma sintering. *Ceramics International*2019.

- [210] Vijayaprasath G, Murugan R, Hayakawa Y, Ravi G. Optical and magnetic studies on Gd doped ZnO nanoparticles synthesized by co-precipitation method. *Journal of Luminescence*2016. p. 375-83.
- [211] Wahab R, Khan F, Ahmad N, Shin H-S, Musarrat J, Al-Khedhairi AA. Hydrogen adsorption properties of nano-and microstructures of ZnO. *Journal of Nanomaterials*2013. p. 101.
- [212] Yayapao O, Thongtem T, Phuruangrat A, Thongtem S. Ultrasonic-assisted synthesis of Nd-doped ZnO for photocatalysis. *Materials Letters*2013. p. 83-6.
- [213] Secco E. DECOMPOSITION OF ZING OXIDE. *Canadian Journal of Chemistry*1960. p. 596-601.
- [214] Chaim R. Grain coalescence by grain rotation in nano-ceramics. *Scripta Materialia*2012. p. 269-71.
- [215] Quach DV, Avila-Paredes H, Kim S, Martin M, Munir ZA. Pressure effects and grain growth kinetics in the consolidation of nanostructured fully stabilized zirconia by pulsed electric current sintering. *Acta Materialia*2010. p. 5022-30.
- [216] Sokol M, Halabi M, Mordekovitz Y, Kalabukhov S, Hayun S, Frage N. An inverse Hall-Petch relation in nanocrystalline MgAl₂O₄ spinel consolidated by high pressure spark plasma sintering (HPSPS). *Scripta Materialia*2017. p. 159-61.
- [217] Sokol M, Halabi M, Kalabukhov S, Frage N. Nano-structured MgAl₂O₄ spinel consolidated by high pressure spark plasma sintering (HPSPS). *Journal of the European Ceramic Society*2017. p. 755-62.
- [218] Manière C. Spark plasma sintering: couplage entre les approches: modélisation, instrumentation et matériaux: Université Paul Sabatier-Toulouse III; 2015.
- [219] Lin C, Wang B, Xu Z, Peng H. Densification and Electrical Properties of Zinc Oxide Varistors Microwave-Sintered Under Different Oxygen Partial Pressures. *Journal of Electronic Materials*2012. p. 3119-24.
- [220] Chen Z, Yamamoto S, Maekawa M, Kawasuso A, Yuan X, Sekiguchi T. Postgrowth annealing of defects in ZnO studied by positron annihilation, x-ray diffraction, Rutherford backscattering, cathodoluminescence, and Hall measurements. *Journal of applied physics*2003. p. 4807-12.
- [221] Gupta T, Coble R. Sintering of ZnO: I, Densification and grain growth. *Journal of the American Ceramic Society*1968. p. 521-5.

- [222] Orrù R, Licheri R, Locci AM, Cincotti A, Cao G. Consolidation/synthesis of materials by electric current activated/assisted sintering. *Materials Science and Engineering: R: Reports*2009. p. 127-287.
- [223] Mahmood K, Asghar M, Ali A, Ajaz-Un-Nabi M, Arshad MI, Amin N, et al. Enhancement of thermoelectric properties of MBE grown un-doped ZnO by thermal annealing. *ADVANCES IN ENERGY RESEARCH*2015. p. 117-24.
- [224] Dollimore D. The thermal decomposition of oxalates. A review. *Thermochimica Acta*1987. p. 331-63.
- [225] Hu C, Mi J, Shang S, Shangguan J. The study of thermal decomposition kinetics of zinc oxide formation from zinc oxalate dihydrate. *Journal of Thermal Analysis and Calorimetry*2014. p. 1119-25.
- [226] Salahuddin NA, El-Kemary M, Ibrahim EM. Synthesis and Characterization of ZnO Nanoparticles via Precipitation Method: Effect of Annealing Temperature on Particle Size. *Nanoscience and Nanotechnology*2015. p. 82-8.
- [227] Luo W, Pan J. Effects of Surface Diffusion and Heating Rate on First-Stage Sintering That Densifies by Grain-Boundary Diffusion. *Journal of the American Ceramic Society*2015. p. 3483-9.
- [228] Lisjak D, Zajc I, Drogenik M, Jamnik J. Investigation of the PTCR effect in ZnO–NiO two-phase ceramics. *Solid State Ionics*1997. p. 125-35.
- [229] Roy TK, Sanyal D, Bhowmick D, Chakrabarti A. Temperature dependent resistivity study on zinc oxide and the role of defects. *Materials Science in Semiconductor Processing*2013. p. 332-6.
- [230] Zakutayev A, Perry NH, Mason TO, Ginley DS, Lany S. Non-equilibrium origin of high electrical conductivity in gallium zinc oxide thin films. *Applied Physics Letters*2013. p. 232106.
- [231] Zhang Y, Wang W, Tan R, Yang Y, Zhang X, Cui P, et al. The Solubility and Temperature Dependence of Resistivity for Aluminum-Doped Zinc Oxide Ceramic. *International Journal of Applied Ceramic Technology*2012. p. 374-81.
- [232] Teranishi T, Mori Y, Hayashi H, Kishimoto A. Thermoelectric Property of Polycrystalline Aluminum-Doped Zinc Oxide Enhanced by Micropore Foaming. *Journal of the American Ceramic Society*2012. p. 690-5.
- [233] Cai K, Müller E, Drašar C, Mrotzek A. Preparation and thermoelectric properties of Al-doped ZnO ceramics. *Materials Science and Engineering: B*2003. p. 45-8.

- [234] Guillon O, Gonzalez-Julian J, Dargatz B, Kessel T, Schierning G, Räthel J, et al. Field-assisted sintering technology/spark plasma sintering: mechanisms, materials, and technology developments. *Advanced Engineering Materials*2014. p. 830-49.
- [235] Holland M. Phonon scattering in semiconductors from thermal conductivity studies. *Physical Review*1964. p. A471.
- [236] Guy I. Elaboration et caractérisation de poudres et de varistances à base d'oxyde de zinc dopé: Toulouse 3; 1995.
- [237] Ewsuk KG, Ellerby DT, DiAntonio CB. Analysis of nanocrystalline and microcrystalline ZnO sintering using master sintering curves. *Journal of the American Ceramic Society*2006. p. 2003-9.
- [238] Ma N, Li J-F, Zhang B, Lin Y, Ren L, Chen G. Microstructure and thermoelectric properties of Zn_{1-x}Al_xO ceramics fabricated by spark plasma sintering. *Journal of Physics and Chemistry of Solids*2010. p. 1344-9.
- [239] Díaz-Chao P, Giovannelli F, Lebedev O, Chateigner D, Lutterotti L, Delorme F, et al. Textured Al-doped ZnO ceramics with isotropic grains. *Journal of the European Ceramic Society*2014. p. 4247-56.
- [240] Shirouzu K, Ohkusa T, Hotta M, Enomoto N, Hojo J. Distribution and solubility limit of Al in Al₂O₃-doped ZnO sintered body. *Journal of the Ceramic Society of Japan*2007. p. 254-8.
- [241] Serier H, Gaudon M, Ménétrier M. Al-doped ZnO powdered materials: Al solubility limit and IR absorption properties. *Solid State Sciences*2009. p. 1192-7.
- [242] Auerkari P. Mechanical and physical properties of engineering alumina ceramics. Technical Research Centre of Finland Espoo; 1996.
- [243] Parmelee CW, Badger AE, Ballam GA. A study of a group of typical spinels. University of Illinois at Urbana Champaign, College of Engineering ...; 1932.
- [244] Nunes SI, Bradt RC. Grain Growth of ZnO in ZnO-Bi₂O₃ Ceramics with Al₂O₃ Additions. *Journal of the American Ceramic Society*1995. p. 2469-75.
- [245] Tomaszewski H. Residual stresses in layered ceramic composites. *Journal of the European Ceramic Society*1999. p. 1329-31.
- [246] Lan Y, Wang X, Wang C, Zebarjadi M. Organic/Inorganic Hybrid Nanostructured Materials for Thermoelectric Energy Conversion. *Functional Organic and Hybrid Nanostructured Materials: Fabrication, Properties, and Applications*2018.
- [247] Zheng B, Liu Y, Zhan B, Lin Y, Lan J, Yang X. Enhanced thermoelectric properties of BiCuSeO/polyaniline composites. *Journal of electronic materials*2014. p. 3695-700.

- [248] Zheng B, Lin Y, Lan J, Yang X. Thermoelectric properties of Ca₃Co₄O₉/polyaniline composites. *Journal of Materials Science & Technology*2014. p. 423-6.
- [249] Khalid M, Acuna JJ, Tumelero MA, Fischer JA, Zoldan VC, Pasa AA. Sulfonated porphyrin doped polyaniline nanotubes and nanofibers: synthesis and characterization. *Journal of Materials Chemistry*2012. p. 11340-6.
- [250] Mostafaei A, Zolriasatein A. Synthesis and characterization of conducting polyaniline nanocomposites containing ZnO nanorods. *Progress in Natural Science: Materials International*2012. p. 273-80.
- [251] Vadiraj T, Belagali S. Characterization of polyaniline for optical and electrical properties. *IOSR Journal of Applied Chemistry*2015. p. 53-6.
- [252] Butoi B, Groza A, Dinca P, Balan A, Barna V. Morphological and structural analysis of polyaniline and poly (o-anisidine) layers generated in a DC glow discharge plasma by using an oblique angle electrode deposition configuration. *Polymers*2017. p. 732.
- [253] Navaneethan M, Mani GK, Ponnusamy S, Tsuchiya K, Muthamizhchelvan C, Kawasaki S, et al. Influence of Al doping on the structural, morphological, optical, and gas sensing properties of ZnO nanorods. *Journal of Alloys and Compounds*2017. p. 555-64.
- [254] Ponnusamy R, Sivasubramanian D, Sreekanth P, Gandhiraj V, Philip R, Bhalerao G. Nonlinear optical interactions of Co: ZnO nanoparticles in continuous and pulsed mode of operations. *RSC Advances*2015. p. 80756-65.
- [255] Shakoor A, Rizvi TZ. Raman spectroscopy of conducting poly (methyl methacrylate)/polyaniline dodecylbenzenesulfonate blends. *Journal of Raman Spectroscopy: An International Journal for Original Work in all Aspects of Raman Spectroscopy, Including Higher Order Processes, and also Brillouin and Rayleigh Scattering*2010. p. 237-40.
- [256] Rohom AB, Londhe PU, Mahapatra S, Kulkarni S, Chaure N. Electropolymerization of polyaniline thin films. *High Performance Polymers*2014. p. 641-6.
- [257] Terasaki I. Thermal Conductivity and Thermoelectric Power of Semiconductors. *Comprehensive Semiconductor Science and Technology*, Elsevier; 2011. p. 326-58.
- [258] Pei Y, LaLonde AD, Wang H, Snyder GJ. Low effective mass leading to high thermoelectric performance. *Energy & Environmental Science*2012. p. 7963-9.

Appendix

Appendices A : Heat capacity measurements

Instrument: TGA-DSC (STA 449 F3 Jupiter, NETZSCH)

Conditions: Bulk pure ZnO, heating rate 10°C/min, RT-500°C

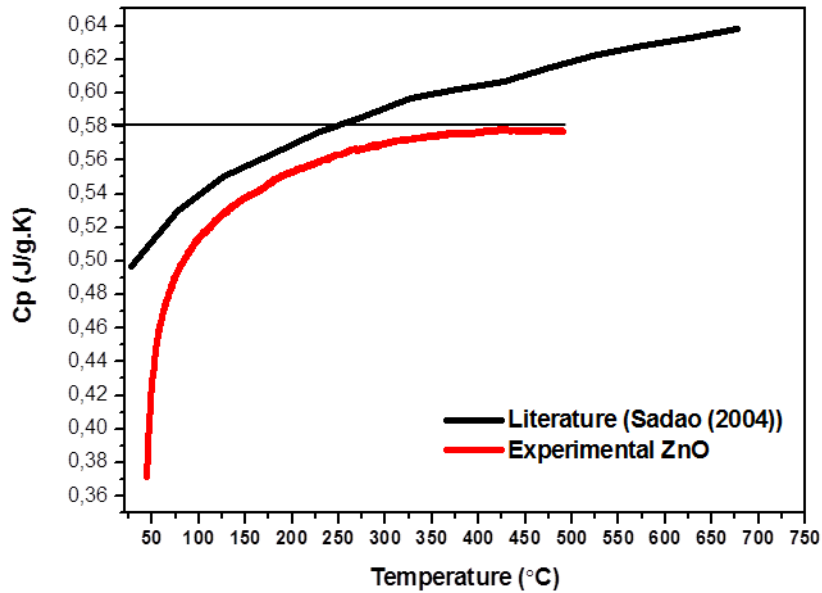


Figure A1 : Heat capacity versus temperature of pure ZnO comparig literature and experimental measurements

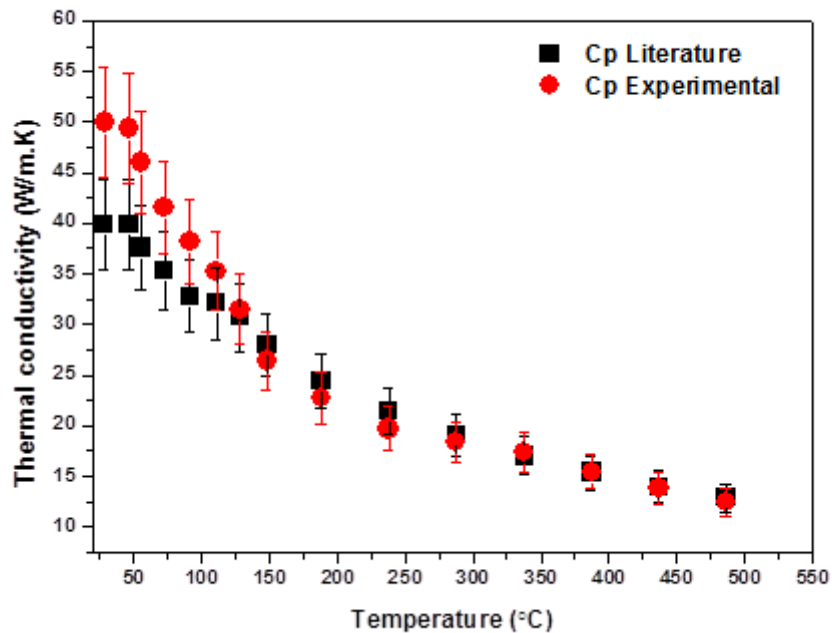


Figure A2 : Thermal conductivity versus temperature of pure ZnO comparig literature and experimental measurements

Extended abstract
[Résumé étendu]

Résumé étendu

La demande mondiale croissante en énergie et la nécessité de créer des environnements et des économies plus écologiques en réduisant l'utilisation de combustibles fossiles entraînent un large éventail de recherches et de développement de sources d'énergie durables et alternatives. Les dispositifs thermoélectriques (TE) sont une de ces alternatives qui peuvent être utilisées pour la conversion directe de la chaleur en électricité. Ils sont préférés en raison du manque de pièces mobiles, de leur robustesse dans les environnements rudes et de la non nécessité de fluides à haute température. Actuellement, leurs limites sont dues à l'efficacité du transfert de chaleur et au coût, ce qui les relègue au second plan pour leur application aux procédés de manipulation morphologique de conversion d'énergie à grande échelle.

Actuellement, de nombreuses recherches ont été consacrées à l'amélioration et au développement de nouveaux matériaux thermoélectriques écologiques, peu coûteux et contenant des éléments naturellement abondants. De ce fait, l'utilisation d'oxyde métallique comme matériau TE s'est avérée une meilleure option et de nombreuses études ont été réalisées au cours des dernières années. Pour cette étude, l'oxyde de zinc ZnO a été choisi en raison de son coefficient de Seebeck très élevé et de sa mobilité de porteurs de charges, ce qui en fait un matériau idéal pour l'amélioration des performances thermoélectriques. Cependant, le principal problème avec le ZnO pur est la conductivité thermique et la résistivité électrique élevées qui réduisent le rendement thermoélectrique. Par conséquent, dans cette étude, on s'intéresse à l'amélioration des propriétés thermoélectriques du ZnO en optimisant les paramètres de synthèse, la température de calcination et le dopage de la poudre de ZnO, ainsi que les paramètres du cycle de frotage par SPS. La thèse se résume comme suit:

Dans le **chapitre 1**, une revue de la littérature sur les principes et les propriétés thermoélectriques de différents matériaux est discutée en détail. L'accent est mis sur l'oxyde de zinc et de ses composites. L'une des principales conclusions est que le perfectionnement des techniques de traitement a permis de réduire la température de frittage à moins de 400°C, ce qui a entraîné une diminution de la taille des grains de ~30 µm à moins de 10 µm [1-4]. Par conséquent, des conductivités thermiques inférieures à 12 W/m.K ont été obtenues pour une céramique de ZnO totalement dense à 700K. Il est connu que la nanostructuration permet de diminuer la conductivité thermique. Par ailleurs, ZnO étant non stoechiométrique et semi-conducteur, ses propriétés électriques sont facilement affectées par la température et l'atmosphère de frittage. Il a donc été noté que la qualité de la poudre et les techniques de

frittage jouent un rôle crucial dans l'amélioration des propriétés thermoélectriques des céramiques à base de ZnO. Un ZT maximal de 0,06 a été rapporté pour la céramique de ZnO pure préparée à partir de particules nanoporeuses frittées à 950°C, avec une résistivité de 0,002 Ω .cm, un coefficient Seebeck de -123 μ V/K et une conductivité thermique de 11 W/mK [5]. Les matériaux thermoélectriques (TE) avec un $ZT > 1$ sont considérés comme des matériaux à haute performance avec un potentiel de commercialisation [6, 7]. Ainsi, ZnO pur, simplement ou doublement dopé avec des éléments du groupe III (Al, Ga, In et B) et des métaux de transition (Ni, Co, Cd, Sc, etc.) présente un comportement thermoélectrique intéressant [8, 9].

Jusqu'ici, le double dopage de l'aluminium et du gallium a montré un ZT élevé de 0,66 à 1250K dans les céramiques au ZnO [10]. L'interdépendance des paramètres reste un frein à l'amélioration des propriétés thermoélectriques des composites ZnO dopés à l'aluminium, notamment entre la résistivité et la conductivité thermique. L'ajout de polymères conducteurs (tels que poly (3,4-éthylènedioxythiophène), polythionates, polypropylène, polyaniline, polyacétylène, polypyrrole, polyéthylène et polyparaphynélène (PPP)) dans des céramiques à base de ZnO a permis d'améliorer simultanément la résistivité et le coefficient de Seebeck tout en maintenant la conductivité thermique à son point minimal [9, 11-14]. Un ZT de 0,54 a été atteint pour la céramique $Zn_{0.95}Ni_{0.05}O$ incorporée avec 9% en masse de PPP [9]. Les auxiliaires de frittage et les phases secondaires pourraient aider à densifier complètement les composites de ZnO à des températures inférieures à 400°C, permettant ainsi de produire des céramiques dotées de propriétés thermoélectriques uniques.

Dans ce travail, l'accent a été mis sur la synthèse du ZnO en poudre et sur l'influence des paramètres de frittage flash (tels que la température, la pression, l'isolation du courant, l'atmosphère de frittage et la pression) sur la densification et les performances thermoélectriques de la céramique. L'indicateur de performance ZT compris entre 4×10^{-4} et 2×10^{-3} a pu être obtenu à 700K par d'autres chercheurs. La poudre de ZnO a également été dopée à l'Al pour améliorer ses propriétés électriques. L'influence de la synthèse de la poudre et des paramètres de frittage sur les propriétés thermoélectriques a été évaluée. La conductivité thermique des céramiques ZnO dopées à l'aluminium a encore été réduite par l'incorporation de polyaniline. Le frittage en dessous de 300°C, à une température inférieure à la température de frittage, en utilisant la technique de frittage flash a été étudié. La céramique

à base de ZnO/Polymère présentent un ZT d'environ 0,5 à 500K. On s'attendait donc à une amélioration du ZT en raison de la conductivité thermique réduite.

Le chapitre 2 traite du matériel et des méthodes utilisés pour mener à bien cette étude. Des poudres de ZnO pur et de ZnO dopé à l'Al ont été synthétisées par la méthode de co-précipitation suivie de la calcination à des températures comprises entre 500 et 700°C. La voie de synthèse de la poudre utilisée dans ce travail a été décrite par Mory *et al.* [15] dans le cadre des travaux de thèse de Guy [16] au Centre interuniversitaire de recherche et d'ingénierie des matériaux (CIRIMAT). Une composition en aluminium de 2 % atomique a été utilisée, car la limite de solubilité de Al dans le cristal de ZnO est <2 mol% et en plus des propriétés thermoélectriques prometteuses ont été rapportées pour cette concentration [10, 17]. Le ZnO dopé Al (ZnA) a été mélangé avec de la poudre de polyaniline activée à des concentrations de 0,75, 5 et 9 wt% en masse en utilisant un mélangeur TURBULAe suivi d'un broyage à billes pour assurer une homogénéité.

Les poudres ont été frittées au frittage flash (unité Dr. Sinter 2080 (SPS Syntex Inc., Japon)) dans une matrice en carbure de tungstène et graphite de 8 et 20 mm de diamètre. La figure 1 illustre le schéma de principe de la configuration de la chambre SPS. La section transversale de la matrice indique la position de l'échantillon et le revêtement du moule avec une feuille de graphite de 0,2 mm d'épaisseur (PERMA-FOIL®Toyo Tanso). Le principe de la technique de frittage flash est que le frittage a lieu par application simultanée d'un courant électrique et d'une pression axiale sur un échantillon. Comme le montre l'image agrandie de l'échantillon, lorsqu'un courant électrique passe à travers, il y a une décharge par étincelle entre les grains [18, 19]. De cette manière, il se produit un chauffage par effet Joule, entraînant le transport de masse des grains pour former une céramique dense [18-21]. Pour chaque échantillon considéré, la pression de frittage (250-850 MPa), la température (250 à 700°C), l'atmosphère (Air et Vide), l'isolation du courant et le cycle de frittage (SC) ont été étudiés.

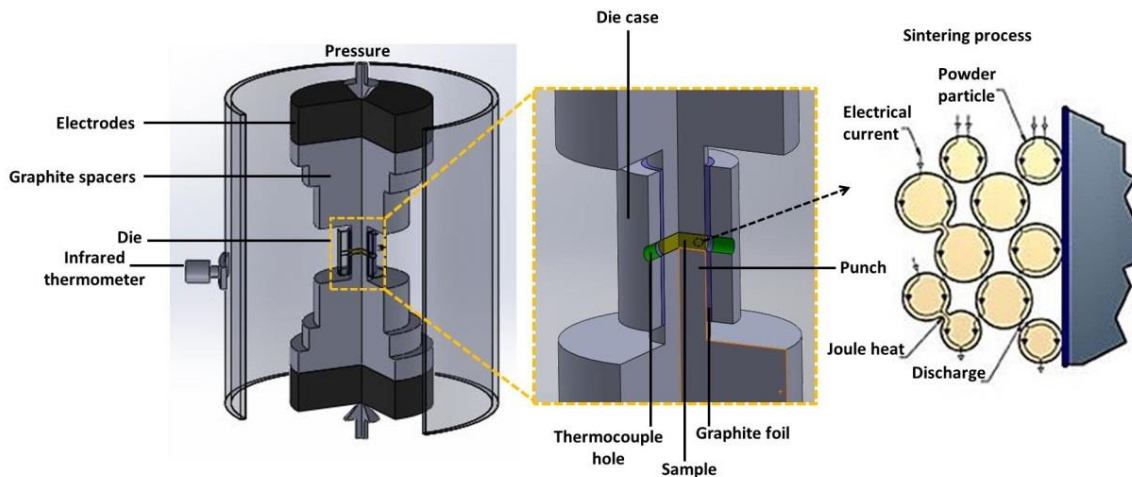


Fig.1. Configuration de la chambre SPS et processus de frittage

Les céramiques en poudre et denses ont été caractérisées à l'aide de méthodes analytiques telles que SEM, XRD, ICP, FTIR, Thermogravimétrie, etc. Le coefficient Seebeck et la résistivité des céramiques denses ont été simultanément mesurés en utilisant ZEM-3 (Ulvac-Riko, CRISMAT). Les céramiques denses ont été découpées en barres de 9x3x3 mm et recouvertes d'or pour assurer le contact ohmique. Une feuille de graphite a été insérée des deux côtés des éléments chauffants pour assurer un bon contact électrique et thermique avec l'échantillon. La conductivité thermique a été déterminée en mesurant séparément la diffusivité thermique (α), la densité de la céramique (d) et la capacité thermique (C_p). Et pour ces mesures, les échantillons ont été découpés à des dimensions de 6x6x1 mm. La conductivité thermique a ensuite été calculée en utilisant Eq. 01. Les mesures par effet Hall ont été effectuées à l'aide du système de mesure des propriétés physiques (contrôleur de transport modèle 7100, système Quantum).

$$k = \alpha(T)C_p(T)d(T) \quad [01]$$

L'influence des paramètres de traitement sur la densification et la microstructure des céramiques à l'oxyde de zinc pur préparées par frittage flash a été étudiée au **chapitre 3**. La densification et la taille des grains de ZnO dans diverses conditions de frittage sont présentées à la Fig. 2. Il a été noté que la pression améliore la densité relative des céramiques en ZnO grâce à la rotation des particules [22, 23]. Une densité relative maximale de 92% a été obtenue à une température aussi basse que 400°C pour une pression appliquée de 850 MPa. Dans ce cas, la taille des grains était de $220 \pm 0,1$ nm. L'augmentation de la température jusqu'à 600°C avec une pression plus basse, 250 MPa, conduit à une augmentation significative de la densité et de la taille du grain de 99,4% et 3,3 μ m, respectivement.

Les atmosphères de frittage (air et vide) n'affectent pas la densification et la microstructure des céramiques de ZnO. L'impact du courant électrique lors du frittage a été évalué par des expériences réalisées avec ou sans isolation. La densité relative n'a pas changé, mais une différence de taille de grain de 7,8 μm a été observée dans les deux conditions. Cette étude pourrait servir de référence pour le contrôle de la densification et de la taille des grains de céramique ZnO obtenue par frittage flash de poudres sèches.

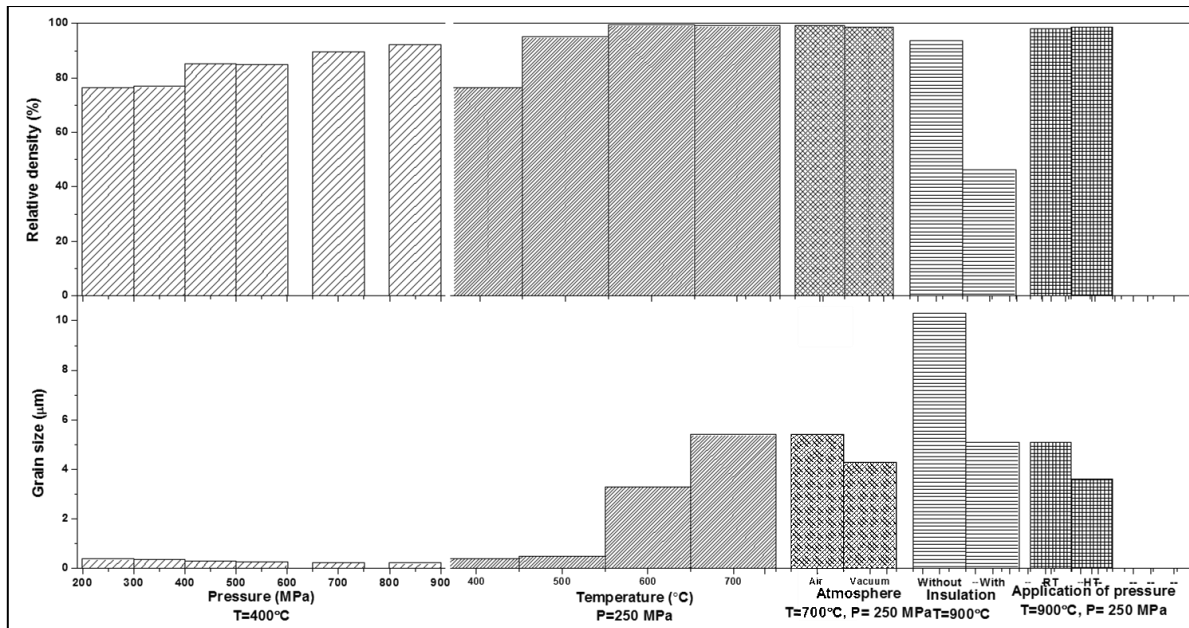


Fig.2. Influence des paramètres SPS sur la densification et la granulométrie des céramiques au ZnO (Remarque: RT correspond à la température ambiante et HT à la température de frittage)

Le **chapitre 4** était consacré à la synthèse de particules de ZnO pur en utilisant la méthode de co-précipitation, et à la compréhension des propriétés thermoélectriques des céramiques en ZnO pur. Les nanoparticules de ZnO ont été synthétisées avec succès par la méthode de co-précipitation suivie de la calcination. L'augmentation de la température de calcination conduit à une augmentation de la taille des grains de particules de ZnO. La température de calcination de 500°C a permis d'obtenir la plus petite taille de grains, 73 nm. L'effet de l'atmosphère et de la température de frittage sur la densification et l'évolution de la microstructure sur des céramiques de ZnO préparées à partir de poudre commerciale et de poudre synthétisée a été étudié avec succès. Les céramiques préparées à partir de poudre synthétisée peuvent être entièrement densifiées à plus de 99% à une température aussi basse que 600°C. Aux températures voisines de 700°C, les céramiques au ZnO se sont révélées sensibles à la surface spécifique de la poudre. Des tailles de grains de céramique de $6 \pm 2 \mu\text{m}$ et $4,2 \pm 1,6 \mu\text{m}$ ont

été obtenues pour des surfaces de 14 m²/g (C500) et 3,3 m²/g (C700), respectivement. La taille des grains du C500 était supérieure à celle du C700 en raison de sa grande surface spécifique, et donc de la facilité de la diffusion intergranulaire [5, 24].

Le recuit à 600°C n'a montré aucun changement significatif sur la microstructure des céramiques au ZnO, mais a modifié la stoechiométrie de l'oxygène. Et cela a eu un effet sur le mécanisme de conduction électrique car les échantillons recuits sont de type semi-conducteurs tandis que les céramiques obtenues après frittage SPS présentaient un comportement métallique (voir la Fig. 3 (a)). Un comportement unique de l'évolution du coefficient Seebeck avec l'augmentation de la température a été observé (voir Fig. 3 (b)). Il peut être dû à la variation de la circulation des porteurs de charge le long du niveau de Fermi. Cependant des études supplémentaires seraient nécessaires pour confirmer cette hypothèse.

Une conductivité thermique de 15 W / mK à 500°C a été mesurée pour les céramiques ZnO frittées et recuites (voir Fig.3 (c)), qui se sont révélées encore trop élevées pour des applications thermoélectriques plus efficaces. Ainsi, il est nécessaire d'envisager de réduire la conductivité thermique en dopant avec des éléments donneurs tels que Al, Ga, In, etc. Le recuit n'a pas amélioré les propriétés thermoélectriques des céramiques au ZnO car il a considérablement réduit la conductivité électrique (voir la figure 3 (a)).

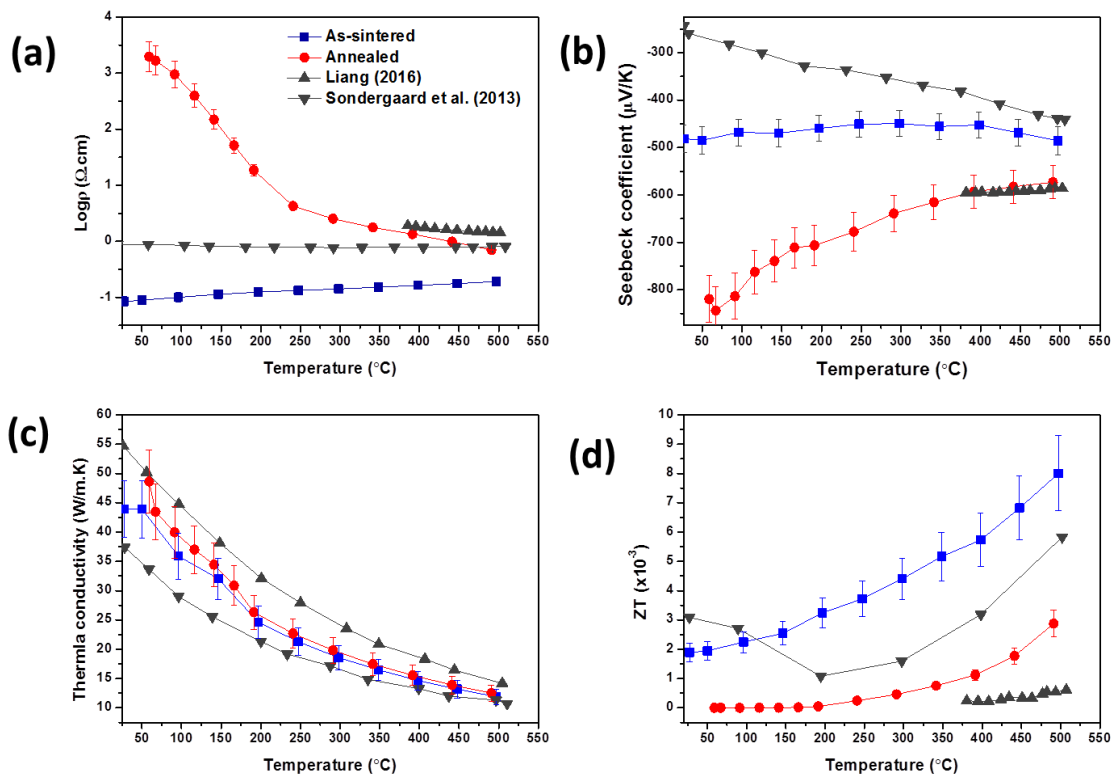


Fig.3. Propriétés thermoélectriques de la céramique recuite à 900°C (CSP): (a) résistivité (b) coefficient de Seebeck (c) conductivité thermique (d) ZT

Il est évident que la technique de préparation des échantillons est importante pour déterminer la conductivité électrique et les propriétés thermoélectriques des matériaux. Les céramiques préparées à partir de poudre synthétisée présentaient une concentration en porteurs supérieure à celle des céramiques préparées à partir de poudre commerciale. Par conséquent, les céramiques frittées préparées à partir de poudre synthétisée ont donné les meilleures performances avec un ZT de 8×10^{-3} , plus élevé que celui des échantillons commerciaux.

La synthèse et le frittage flash de poudre de ZnO dopée à l'aluminium ont été étudiés dans le **chapitre 5**. L'addition de 2 % atomique dans la poudre de ZnO a réduit la taille de grains de 177 à 75 nm; Al est connu pour être un inhibiteur de croissance [25, 26]. La densité relative du ZnO dopé à l'aluminium est passée d'une densité brute de 57% à une valeur élevée de 98,9% lors du frittage jusqu'à une température de 650°C. Un frittage au-dessus de 650°C a entraîné une augmentation de la taille des grains, ce qui a réduit la densité de 0,8%. L'ajout d'Al dans les céramiques au ZnO a entraîné une diminution de la taille des grains de 5,4 μm (sans Al) à $<1 \mu\text{m}$ (avec 2 % atomique d'Al), comme indiqué sur les micrographies MEB sur la Fig.4. Le frittage au-dessus de 650°C et l'application de la pression axiale à la température ambiante provoquent la présence d'une phase secondaire, comme le montre la figure 4. L'analyse EDS sur l'échantillon fritté à 700°C a montré que la phase claire est riche en Al et la phase sombre en Zn (Fig.4). Ceci a été confirmé par les résultats de DRX car les pics de ZnAl_2O_4 et Al_2O_3 sont riches en Al. Par conséquent, la phase claire dans l'analyse MEB est la phase spinelle ZnAl_2O_4 et la phase Al_2O_3 , telle que déterminée par l'analyse DRX. Ceci est conforme au pic de ZnAl_2O_4 observé dans les résultats de DRX de Jood et al. [27], lors de l'analyse par MEB, lorsque de fines nanoparticules de ZnAl_2O_4 ont été dispersées sur des grains de ZnO. La phase spinelle, ZnAl_2O_4 , est indésirable pour l'amélioration des propriétés thermoélectriques.

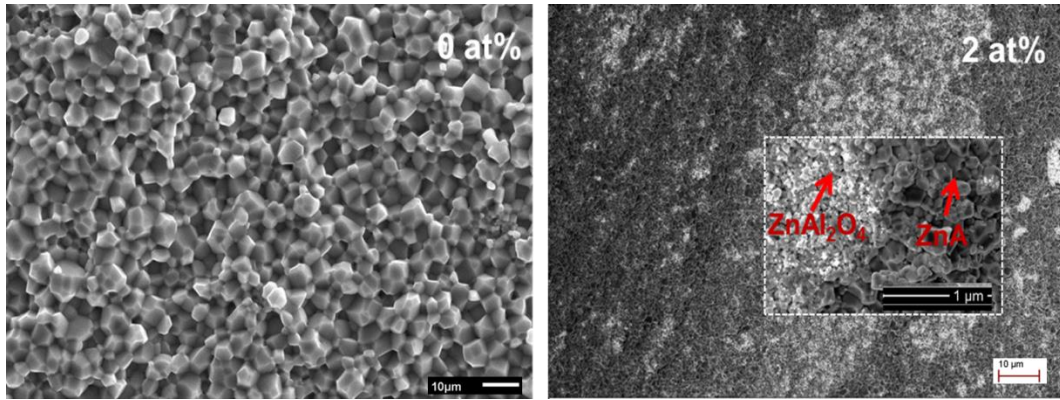


Fig.4. Micrographies au MEB de la céramique de ZnO à 0% et 2% atomique à l'Al frittée à 700 °C

Il a été découvert que l'application de la pression pendant le temps de maintien empêche la formation de la phase spinelle, une densité de 98,6% et une taille de grain de 90 nm ont été déterminées. Le recuit a augmenté la taille des grains de la céramique ZnO dopée à l'Al de 50 nm. La résistivité des céramiques ZnO dopées à l'aluminium a légèrement diminué, ce qui a entraîné une diminution du coefficient de Seebeck absolu en raison de la concentration accrue de porteurs. La relation entre le coefficient de Seebeck et la concentration de porteurs est de nature inverse selon l'équation de Mott [28]. La réduction de la taille des grains a entraîné une diminution de la conductivité thermique de moitié à la température ambiante (Fig. 5), en raison de la diffusion de phonons aux joints des grains. On obtient ainsi un ZT de $1,5 \times 10^{-3}$ à 500°C, inférieure à celui des céramiques au ZnO pur. Le faible coefficient de Seebeck et la valeur de la conductivité électrique de la céramique de ZnO dopée à l'aluminium ont provoqué une diminution des performances. Malgré tout, ces résultats ont révélé l'importance d'une conductivité thermique réduite et d'une faible résistivité dans l'amélioration des propriétés thermoélectriques des céramiques de ZnO dopé à l'Al. Il est conseillé d'effectuer d'autres expériences pour optimiser la quantité de dopants Al dans les céramiques à base de ZnO afin d'améliorer les propriétés thermoélectriques: en incorporant de nouveaux éléments afin de développer de nouveaux composites et / ou d'optimiser les paramètres de frittage.

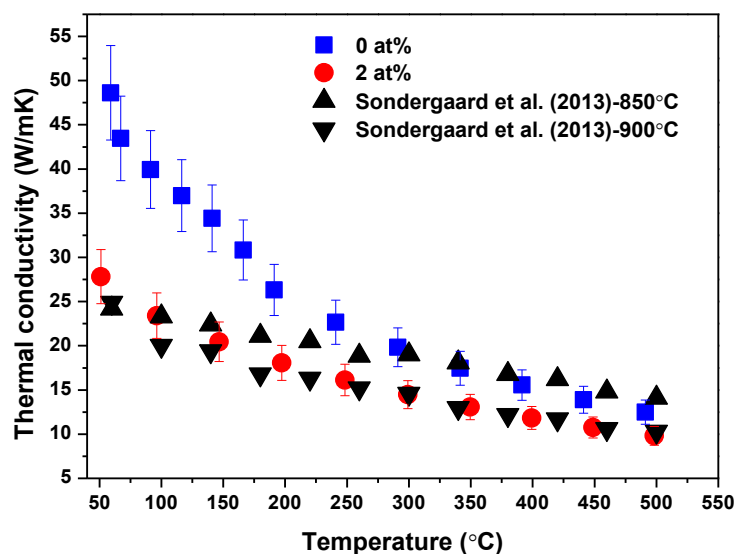


Fig.5. Conductivité thermique de 0 et 2% atomique de céramique de ZnO dopé Al

Le **chapitre 6** traite de l'incorporation de polyaniline (PANI) dans des céramiques au ZnO dopé à l'aluminium préparées par frittage flash. Il a été observé que l'inclusion de polyaniline n'affectait pas la structure de la phase ZnO. Cependant, une augmentation de la taille des agrégats de poudre a été observée lorsque la concentration en PANI augmente de 0,75% à 9% en masse. Des densités maximales de 98,5% et 97,3% ont été obtenues pour des concentrations de PANI de 5% en masse (ZnA-5PANI) et de 9% en masse (ZnA-9PANI), respectivement, à de très basses températures de 250 °C et à une pression de 250 MPa. En raison de la température de frittage réduite, la taille nanométrique des grains de céramique a été maintenue. La taille des grains a été réduite de 140 nm (céramique ZnA recuite) à 86 nm et 50 nm pour les céramiques ZnA-5PANI et ZnA-9PANI, respectivement. En conséquence, de faibles conductivités thermiques de 6 W/mK et de 3 W/mK à température ambiante pour des concentrations de PANI de 5% et de 9% en masse, respectivement, a été déterminée, comme indiqué sur l'image agrandie à la Fig. 6. La diminution drastique de conductivité thermique est très probablement due au déphasage des vibrations des phonons du PANI et du ZnA (voir Fig. 7) [9, 11]. Les vibrations thermiques de PANI et de ZnA sont différentes, il y a un choc entre flux de phonons à l'interface, voir illustration sur la Fig.7.

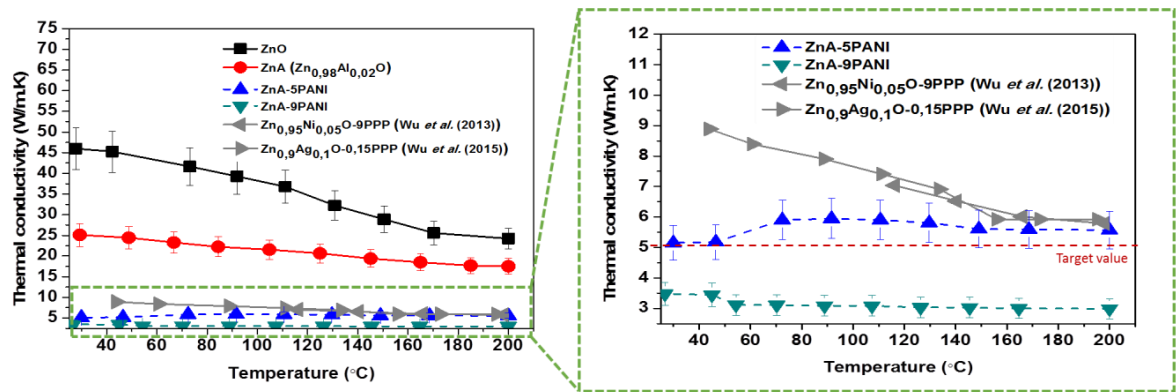


Fig.6. Conductivité thermique des céramiques ZnO, ZnA, ZnA-5PANI et ZnA-ZA9PANI

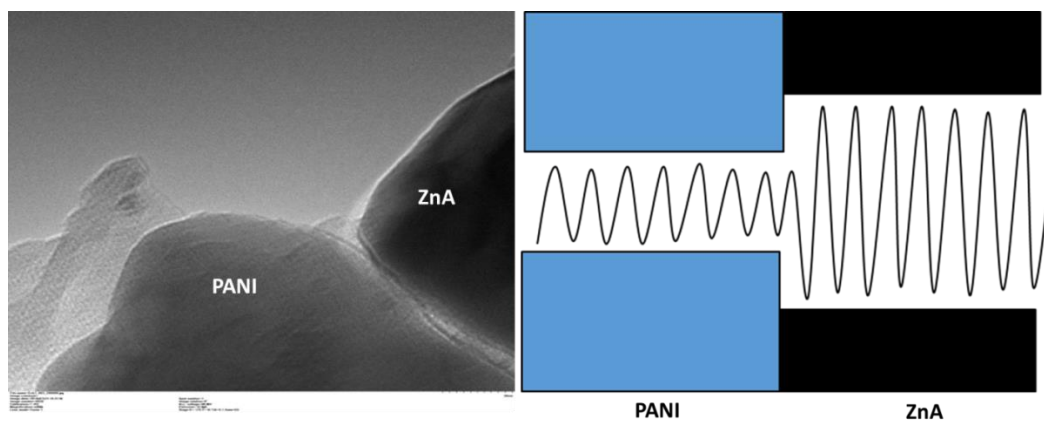


Fig.7. Illustration des vibrations thermiques de la céramique ZnA-ZA9PANI à l'interface [29]

Une analyse plus approfondie des propriétés électriques a montré que la résistivité était également légèrement améliorée avec le maintien d'un coefficient de Seebeck élevé autour de $\sim 150 \mu\text{V/K}$. Une valeur ZT maximale de $0,8 \times 10^{-3}$ a été atteinte à 190°C pour le ZnA-9PANI contre $0,05 \times 10^{-3}$ et de $0,06 \times 10^{-3}$ pour le ZnO pur et le ZnA, respectivement (voir figure 8).

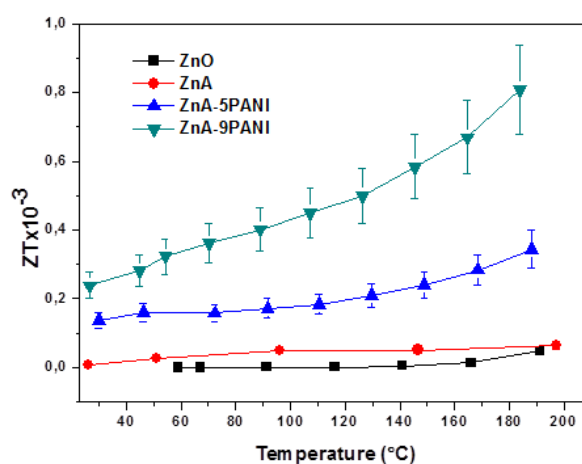


Fig.8. Figure of merit of Al-doped ZnO/PANI ceramics

Ce dernier paragraphe propose une conclusion du travail et les recommandations pour les travaux futurs. La synthèse et le frittage flash de ZnO pure, de ZnO dopé à l'Al et de polyaniline incorporant des céramiques ZnO dopées à l'Al ont été étudiés en détail avec succès. Il est devenu évident que la préparation des échantillons et la technique de frittage flash sont des étapes essentielles pour l'amélioration des propriétés thermoélectriques des céramiques à base de ZnO. Dans ce travail, un procédé de contrôle de la densification et de la granulométrie des céramiques de ZnO séchées a été élaboré. Il a été démontré que le frittage par SPS peut conduire à des densités élevées, indépendamment de la qualité de la poudre de départ. Les céramiques préparées à partir de poudre de ZnO synthétisée et commerciale peuvent être entièrement densifiées à plus de 99% à une température aussi basse que 600°C. Le recuit à 600°C n'a pas eu d'effet significatif sur la microstructure des céramiques au ZnO, mais a modifié la stoechiométrie de l'oxygène, la résistivité des céramiques au ZnO pur étant augmentée de deux ordres de grandeur.

L'ajout de 2% atomique d'Al a réduit la taille des grains de la céramique ZnO, ce qui a eu pour effet la réduction de la conductivité thermique. Une technique / procédure utilisée dans le frittage flash de céramiques de ZnO dopé par Al pourrait affecter la structure de la phase. En effet l'application de la pression axiale à la température ambiante et le frittage à une température supérieure à 650°C font apparaître des phases secondaires telles que le spinelle ($ZnAl_2O_4$) pouvant affecter la résistivité. La diminution de la valeur du coefficient Seebeck de la céramique de ZnO dopée à l'aluminium s'est traduite par des performances médiocres

par rapport à la céramique de ZnO pure; une valeur ZT maximale de $1,5 \times 10^{-3}$ à 500°C a été atteinte.

Une densification complète à basse température de 250°C et à une pression axiale de 250 MPa a été obtenue pour 5 et 9% en masse de PANI dispersé dans la céramique ZnO dopée à l'aluminium (ZnA). En raison de la température réduite, la nanostructure de la céramique a été maintenue et par conséquent, une conductivité thermique inférieure à 6 W/mK a été obtenue. Le coefficient Seebeck a pu être maintenu à environ $150 \mu\text{V/K}$ avec une légère amélioration de la résistivité. L'amélioration de la valeur de ZT ($0,8 \times 10^{-3}$) a été obtenue à 190°C avec du ZnA-9PANI contre $0,06 \times 10^{-3}$ pour les céramiques au ZnA. Même si la performance n'est pas supérieure à celles déjà rapportées dans la littérature, cela a ouvert des possibilités de développement de composites polymères à base de ZnO à basse température en utilisant le frittage flash.

Les propriétés thermoélectriques de la céramique de ZnO pure ont été expliquées à notre niveau de connaissances; il est conseillé de procéder à une étude approfondie de la structure électronique et de l'analyse de la bande d'énergie des céramiques denses en ZnO pur afin de mieux comprendre leur comportement électrique. Il est également recommandé de réaliser des études d'optimisation sur le recuit de la céramique ZnO dans le but d'améliorer les propriétés thermoélectriques. Le problème principal des céramiques au ZnO dopé à l'Al est la résistivité électrique élevée de la céramique. Il est recommandé de fritter dans une atmosphère réduite (vide) et à haute température au-dessus de 800°C pour améliorer la vitesse de réaction; cela pourrait augmenter les probabilités de déplacement de Zn^{2+} par Al^{3+} dans la structure de ZnO.

Cette étude a montré que l'inclusion de polymères dans les céramiques à base de ZnO est bénéfique pour l'amélioration de la conductivité thermique et du coefficient Seebeck; cependant, la faible résistivité de la céramique affecte ses performances. Il est recommandé d'augmenter la concentration d'Al dans les particules de ZnO, ce qui fera accroître la concentration des porteurs de charges et, par conséquent, améliorera la conductivité électrique nécessaire à la haute performance des céramiques.

References

- [1] Cramer CL, Gonzalez-Julian J, Colasuonno PS, Holland TB. Continuous functionally graded material to improve the thermoelectric properties of ZnO. *Journal of the European Ceramic Society*2017. p. 4693-700.
- [2] Kim KH, Shim SH, Shim KB, Niihara K, Hojo J. Microstructural and thermoelectric characteristics of zinc oxide-based thermoelectric materials fabricated using a spark plasma sintering process. *Journal of the American Ceramic Society*2005. p. 628-32.
- [3] Colder H, Guilmeau E, Harnois C, Marinel S, Retoux R, Savary E. Preparation of Ni-doped ZnO ceramics for thermoelectric applications. *Journal of the European Ceramic Society*2011. p. 2957-63.
- [4] Gautam D, Engenhorst M, Schilling C, Schiering G, Schmechel R, Winterer M. Thermoelectric properties of pulsed current sintered nanocrystalline Al-doped ZnO by chemical vapour synthesis. *Journal of Materials Chemistry A*2015. p. 189-97.
- [5] Virtudazo RVR, Guo Q, Wu R, Takei T, Mori T. An alternative, faster and simpler method for the formation of hierarchically porous ZnO particles and their thermoelectric performance. *RSC Advances*2017. p. 31960-8.
- [6] Zebarjadi M, Esfarjani K, Dresselhaus M, Ren Z, Chen G. Perspectives on thermoelectrics: from fundamentals to device applications. *Energy & Environmental Science*2012. p. 5147-62.
- [7] Zheng X, Liu C, Yan Y, Wang Q. A review of thermoelectrics research—Recent developments and potentials for sustainable and renewable energy applications. *Renewable and sustainable energy reviews*2014. p. 486-503.
- [8] Han L, Christensen DV, Bhowmik A, Simonsen SB, Hung L, Abdellahi E, et al. Scandium-doped zinc cadmium oxide as a new stable n-type oxide thermoelectric material. *Journal of Materials Chemistry A*2016. p. 12221-31.
- [9] Wu Z-H, Xie H-Q, Zhai Y-B. Enhanced thermoelectric figure of merit in nanostructured ZnO by nanojunction effect. *Applied Physics Letters*2013. p. 243901.
- [10] Ohtaki M, Araki K, Yamamoto K. High thermoelectric performance of dually doped ZnO ceramics. *Journal of Electronic Materials*2009. p. 1234-8.
- [11] Wu Z-H, Hua-Qing X, Yuan-Yuan W, Jiao-Jiao X, Jian-Hui M. Nanojunctions Contributing to High Performance Thermoelectric ZnO-Based Inorganic-Organic Hybrids. *Chinese Physics Letters*2015. p. 117303.

- [12] Jun L, Lian-meng Z, Li H, Xin-feng T. Synthesis and thermoelectric properties of polyaniline. *Journal of Wuhan University of Technology-Mater Sci Ed*2003. p. 53-5.
- [13] Lan Y, Wang X, Wang C, Zebarjadi M. *Organic/Inorganic Hybrid Nanostructured Materials for Thermoelectric Energy Conversion. Functional Organic and Hybrid Nanostructured Materials: Fabrication, Properties, and Applications*2018.
- [14] Zhang L, Du W, Nautiyal A, Liu Z, Zhang X. Recent progress on nanostructured conducting polymers and composites: synthesis, application and future aspects. *Science China Materials*2018. p. 1-50.
- [15] Mory J-E, Guy I, Schneider D, Rousset A, Legros R, Peigney A. Poudre d'oxyde de zinc dope, procede de fabrication et ceramique obtenue a partir de ladite poudre. In: FRANCE PCD, editor. *IFI CLAIMS PATENT SERVICES*. France: Jean-Eudes MoryIsabelle GuyDidier SchneiderAbel RoussetRenee LegrosAlain PeigneyPharmacie Centrale De France 1993.
- [16] Guy I. *Elaboration and characterization of powders and varistors based on zinc oxide dope [Doctorate]: Universite Paul Sabatier*; 1995.
- [17] Han L, Van Nong N, Zhang W, Hung LT, Holgate T, Tashiro K, et al. Effects of morphology on the thermoelectric properties of Al-doped ZnO. *RSC Advances*2014. p. 12353-61.
- [18] Santanach JG, Weibel A, Estournès C, Yang Q, Laurent C, Peigney A. Spark plasma sintering of alumina: Study of parameters, formal sintering analysis and hypotheses on the mechanism (s) involved in densification and grain growth. *Acta Materialia*2011. p. 1400-8.
- [19] Tokita M. Mechanism of spark plasma sintering. *Proceeding of NEDO International Symposium on Functionally Graded Materials: Japan*; 1999. p. 22.
- [20] Chaim R, Chevallier G, Weibel A, Estournès C. Grain growth during spark plasma and flash sintering of ceramic nanoparticles: a review. *Journal of Materials Science*2018. p. 3087-105.
- [21] Chaim R, Marder R, Estournés C, Shen Z. Densification and preservation of ceramic nanocrystalline character by spark plasma sintering. *Advances in Applied Ceramics*2012. p. 280-5.
- [22] Chaim R. Grain coalescence by grain rotation in nano-ceramics. *Scripta Materialia*2012. p. 269-71.
- [23] Chaim R, Levin M, Shlayer A, Estournès C. Sintering and densification of nanocrystalline ceramic oxide powders: a review. *Advances in Applied Ceramics*2008. p. 159-69.

- [24] Aimable A, Goure Doubi H, Stuer M, Zhao Z, Bowen P. Synthesis and Sintering of ZnO Nanopowders. *Technologies*2017. p. 28.
- [25] Zhang Y, Wang W, Tan R, Yang Y, Zhang X, Cui P, et al. The Solubility and Temperature Dependence of Resistivity for Aluminum-Doped Zinc Oxide Ceramic. *International Journal of Applied Ceramic Technology*2012. p. 374-81.
- [26] Teranishi T, Mori Y, Hayashi H, Kishimoto A. Thermoelectric Property of Polycrystalline Aluminum-Doped Zinc Oxide Enhanced by Micropore Foaming. *Journal of the American Ceramic Society*2012. p. 690-5.
- [27] Jood P, Mehta RJ, Zhang Y, Peleckis G, Wang X, Siegel RW, et al. Al-doped zinc oxide nanocomposites with enhanced thermoelectric properties. *Nano letters*2011. p. 4337-42.
- [28] Walia S, Balendhran S, Nili H, Zhuiykov S, Rosengarten G, Wang QH, et al. Transition metal oxides–Thermoelectric properties. *Progress in Materials Science*2013. p. 1443-89.
- [29] Wu Z-H, Xie H-Q, Zhai Y-B, Gan L-H, Liu J. Enhanced thermoelectric performance of TiO₂-based hybrid materials by incorporating conducting polymer. *Chinese Physics B*2015. p. 034402.